UNIVERSITY OF MANITOBA

Biomechanical Modeling of Acoustic Wave Propagation through Bone-like Porous Materials Using the Biot-JKD Theory

By

MOHAMMAD HODAEI

A thesis submitted to the Faculty of Graduate Studies of
The University of Manitoba
in fulfillment of the requirements for the degree of

Doctor of Philosophy

The Graduate Program in Biomedical Engineering
University of Manitoba
Winnipeg, Manitoba, Canada

Abstract

Osteoporosis is a degenerating disease which may cause a bone to break eventually. A way of monitoring the situation is to employ X-ray Absorptiometry (XA) to assess if a difference has happened in bone's mineral density. XA tests have been widely used as a bone density test for the hip and spine, which can be a predictor of the likelihood of future breaks in other bones. Bone density in other bones such as the lower arm, wrist, finger, or heel can be measured through peripheral tests, also called screening tests, such as quantitative ultrasound (QUS). The results of screening tests for osteoporosis diagnosis are much less accurate and cannot be compared with the results of an XA test. One of the reasons for the limitations of QUS techniques in diagnosing bone loss is the lack of understanding of the mechanism of ultrasound wave propagation through a porous, complex bone structure. Despite these issues, some features of the QUS technique make it yet very appealing for bone loss detection. For instance, QUS packages are smaller and portable in comparison to bulky MRI or X-ray techniques. Also, they are relatively cheap, do not utilize harmful radiations, and are recognized as a non-invasive technique.

This research aims to pave the way to understanding the biomechanical behavior of bone-like porous materials, i.e. cancellous bones, subject to different types of acoustical waves.

First, the transient acoustic wave propagation in a bone-like porous material saturated with a viscous fluid is investigated using Biot's theory. Due to the interaction between the viscous fluid and solid skeleton, the damping behavior is proportional to a fractional power of frequency, i.e. the dynamic tortuosity was written in terms of fractional power of frequency. Furthermore, to describe the viscous interaction of fluid and solid in the time domain, the fractional derivative is used. The fast and slow waves, which are the solutions to Biot's equations, are described by fractional calculus in the time domain. The reflection and transmission operators are expressed in the Laplace domain and inverted into the time domain using Durbin's numerical inversion. Once the numerical implementation is validated, the effects of porosity and viscosity on the stress, and reflected and transmitted waves are investigated. The results show that by increasing the porosity, the stress in a bone-like material filled with either air or bone marrow increases. The transmitted pressure decreases by increasing the porosity. The reflected pressure decreases for low viscous fluid when the porosity increases while it increases when the viscosity of the fluid is high. In addition, the results show the importance of taking into account the fractional derivatives in the transient wave propagation in such porous media.

Next, the effects of transverse acoustic waves in characterizing a bone-like porous medium filled with a viscous fluid are analyzed for the first time. Scattering operators along with stress fields are derived by using the standard Biot-JKD model. A short duration acoustical pulse is applied to one side of a bone-like, porous medium so that both longitudinal and transverse waves travel through the intermediate medium which is filled with a viscous fluid. The reflection and transmission operators along with stresses in the medium are expressed in terms of these waves. The numerical implementation is validated for the longitudinal wave by comparison with the numerical simulation data found in the literature. The effects of the transverse waves on the reflection and transmission coefficients as well as the stress field are studied by considering different viscosities and porosities. It is shown that when the fluid viscosity in the medium is relatively high (such as bone marrow), the effect of the transverse wave dominates. However, this effect is negligible when the medium is filled with a relatively low viscous fluid (such as air). Furthermore, it is shown that the role of transverse waves in characterizing bone structures and bone loss is imperative since the acoustical response of such media at specific frequencies can be triggered only by considering the effects of transverse waves.

Then, a three-dimensional (3D) analytical solution is developed to study the acoustic wave propagation through cancellous bone-like materials saturated with a viscous fluid. The effect of dynamic tortuosity, especially in clinically relevant ultrasound frequency range, is considered to investigate the effect of viscous exchange between the fluid and solid interactions. The solution includes the effects of both fast and slow longitudinal waves as well as transverse waves propagating through the medium. The scattering operators and radial displacements are derived in terms of ultrasonic waveforms by applying the Helmholtz decomposition. The effect of different porosities, wall thickness ratios, and frequencies of incident waves on the radial displacement and scattering operators are investigated by considering various incident wave angles at forward and sideward directions. The results demonstrate that the incident wave angle has a significant effect on the radial displacement and scattering operators regardless of the porosity, wall thickness ratio, and viscosity of pore fluid. Furthermore, the distribution pattern of the radial displacement and scattering operators in relatively low frequency ranges is almost symmetric while asymmetric in relatively high frequency ranges. It is also shown that the bone characterization using ultrasonic techniques is not only based on the mineral density, as used currently by electromagnetic wave-based tools, but also other biomechanical factors such as the porosity, viscosity of pore fluid, and wall thickness ratio of a cancellous bone structure. Also, the pattern of the reflected pressure can be an

iv

indicator of the state (healthy versus osteoporosis) of a cancellous bone.

Keywords

Acknowledgements

I would like to give credits to the individuals whose impact, advice, comments, influence, and support are so invaluable to me. I am honored to receive their words of wisdom.

- Dr. Pooneh Maghoul: As a talented-passionate scientist, for her weekly involvement, meetings, meticulous comments on the dissertation and supports. I am so pleased by her encouragement to commercialize my research findings and start a company.

- Dr. Neil Popplewell: For accepting to help me through my research, his guidance, and answering my conceptual questions. He is truly inspirational.

- Dr. Joe LoVetri and Dr.Mohammad Jafari Jozani: For their comments to help me stay on track and improve this research in the capacity of the advisory committee members.

- External Reviewer : For taking time and reviewing my dissertation.

- My friend: Mr. Vahid Rabbani for providing a friendly work environment in the sound and vibration laboratory and sharing his knowledge.

I am grateful for the scholarships and awards that I received during this program. These include Natural Sciences and Engineering Research Council of Canada (NSERC), Mitacs Research Training award, the University of Manitoba Graduate Enhancement of Tri-Council Stipends (GETS), Edward R. Toporeck Graduate Fellowship in Engineering, Fellowships for education purposes, FGS Research Completion Scholarship, the University of Manitoba Travel Awards, and the Excellent Paper Award from the International Conference on Medical and Biosciences in Montreal, Canada.

I would like sincerely thank my parents for giving me such amazing opportunities throughout my life.

Last but not least, I would like to appreciate my best friend and beautiful-amazing wife, Nika, for her unconditional love and support which made this journey as a great opportunity, and my lovely son, Michael, for the joy he brings into my life.

Publications

The chapters of this thesis are reproduced, with modifications, from the following publications:

- M. Hodaei, & P. Maghoul, 2021. *Ultrasonic characterization of human cancellous bone using a physics-aware neural network and a modified Biot's theory*, Under review.

- M. Hodaei, P. Maghoul, & N. Wu, 2020. *Three-dimensional biomechanical modeling of acoustic wave propagation through cylindrical bone-like porous materials*, Under review.

- M. Hodaei, P. Maghoul, & N. Popplewell, 2020. *An overview of the acoustic studies of bone-like porous materials, and the effect of transverse acoustic waves*, International Journal of Engineering Science (Elsevier), vol.147, 103189.
DOI: 10.1016/j.ijengsci.2019.103189

- M. Hodaei, V. Rabbani & P. Maghoul, 2020. *Transient acoustic wave propagation in bone-like porous materials using the theory of poroelasticity and fractional derivative: a sensitivity analysis*, Acta Mechanica (Springer), vol.231(1), 179-203.
DOI: 10.1007/s00707-019-02513-9

- M. Hodaei, V. Rabbani, P. Maghoul, & N. Wu, 2018. *Transient study of an acoustic sound field for a human cancellous bone using the Biot theory of poroelasticity*, International Conference on Medical and Biosciences (ICMBS), Montreal, Canada.

Contributions of Authors

Chapter 3: M. Hodaei, V. Rabbani, & P. Maghoul

- M. Hodaei: project conceptualization, methodology development, deriving analytical solution, numerical implementation, modelling simulations, results interpretation, original drafting and revising the paper.
- V. Rabbani: modelling simulations, results interpretation, review and edit.
- P. Maghoul: project conceptualization, criticized methodology, supervision of the analytical solution, numerical implementation, and modelling simulations, funding acquisition, review and edit.

Chapter 4: M. Hodaei, P. Maghoul, & N. Popplewell

- M. Hodaei: project conceptualization, methodology development, deriving analytical solution, numerical implementation, modelling simulations, results interpretation, original drafting and revising the paper.
- P. Maghoul: project conceptualization, criticized methodology, supervision of the analytical solution, numerical implementation, and modelling simulations, funding acquisition, review and edit.
- N. Popplewell: criticized methodology, supervision of the results interpretation, review and edit.

Chapter 5: M. Hodaei, P. Maghoul, & N. Wu

- M. Hodaei: project conceptualization, methodology development, deriving analytical solution, numerical implementation, modelling simulations, results interpretation, original drafting and revising the paper.
- P. Maghoul: project conceptualization, criticized methodology, supervision of the analytical solution, numerical implementation, and modelling simulations, funding acquisition, review and edit.
- N. Wu: criticized methodology, supervision of the results interpretation, review and edit.

Contents

x

List of Figures

List of Tables

List of Abbreviations

BUA	**Broadband ultrasonic attenuation**
SPA	**Single photon absorptiometry**
QCT	**Quantitative computed tomography**
QUS	**Quantitative ultrasound**
FDTD	**Finite-difference time-domain**
MBA	**Modified Biot-Attenborough**
DXA	**Dual energy X-ray absorptiometry**
pDXA	**Peripheral dual energy x-ray absorptiometry**
JKD	**Johnson, David Linton and Koplik, Joel and Dashen, Roger**
Biot-JKD	**Modified Biot's theory by JKD**
FEM	**Finite Element Method**
TL	**Transmission Loss**
SBS	**Stiff bone structure**
MSE	**Mean square error**

List of Nomenclature

u	displacement vector of a solid skeleton
U	absolute displacement vector of a pore fluid
P,Q,R	generalized elastic constants
L	length of a porous medium
K_f	bulk modulus of pore fluid
K_s	bulk modulus of solid
K_b	bulk modulus of a porous skeletal frame
N	shear modulus of a skeletal frame
ρ_s, ρ_f	density of solid and pore fluid, respectively
$\rho_{11}, \rho_{12}, \rho_{22}$	effective densities
ϕ	volume fraction of voids (porous space)
α_∞	tortuosity
$\mathring{\imath}$	Imaginary unit
∇	gradient operator
$\nabla \times$	curl operator
∇^2	Laplacian operator
ε	Green-Lagrange strain tensor
η	viscosity of a fluid
b_0	drag coefficients relevant to a fluid's viscosity
V_b, V_f	volume of bulk and pore, respectively
E_s, E_b	modulus of elasticity of solid and skeleton medium, respectively
v_b, v_s	Poisson's ratio of skeleton and solid medium , respectively
Λ	characteristic length of a viscous medium
$H_n^2(x)$	Hankel function of the second kind
$H_n^1(x)$	Hankel function of the first kind
$J_n(x)$	Bessel function of the first kind
Π_I	Incident acoustic power
Π_T	Transmitted acoustic power

$\tilde{\alpha}$	dynamic tortuosity
θ	angular location of cylinder
ϕ_s, ϕ_f	scalar potential of solid and fluid wave, respectively
Ψ_s, Ψ_f	vector potential of solid and fluid wave, respectively
k_0	permeability of a porous medium
ω	angular frequency, rad/s
K_s, K_f	bulk modulus of a solid and fluid, respectively
σ_s, σ_f	normal solid and fluid stress tensors, respectively
τ	shear stress tensor
δ	thickness of a viscous layer
ϕ_1, ϕ_2	scalar potential of a fast and slow wave, respectively
λ_i	eigenvalue operator
V_i	eigenvector operator
P^{inc}	pressure field of an incident wave
P^{ref}, P^{tr}	reflected and transmitted wave pressure fields, respectively
P^{left}, P^{right}	total pressure at the left and right sides of the medium, respectively
$R(\tau)$, $T(\tau)$	reflection and transmission coefficients, respectively
$\tilde{\varphi}$	Fourier transform of an incident wave
f_c	transition frequency
a	characteristic of the pore's geometry
I	second-order isotropic tensor
a_1, a_2, a_3	radial components of the wavenumber characteristic length of a viscous medium
$\sigma_{rr}, \sigma_{r\theta}, \sigma_{rz}$ and σ_f	solid and fluid stress tensors, respectively
$\tilde{\delta}_i^2(\omega)$	eigenvalue operator
p_0	amplitude of the incident waver
P_1^I	pressure field of an incident wave
$P_1^R(r,\theta,z,t)$, $P_3^T(r,\theta,z,t)$	reflected and transmitted wave pressure fields, respectively
P_{1n}^R, P_{3n}^T	reflection and transmission coefficients, respectively
γ	incident wave angle

To All passengers of Ukraine International Airlines Flight 752

Chapter 1

Introduction

1.1   The Big Picture

The structure of the bone is porous and spongy. It consists of a solid skeleton and pores which are filled with a viscous bone marrow. More precisely, the main formation of the bone structure is composed of a compact layer, which is a dense tissue found on the outside of a bone, and a spongy layer (cancellous bone) inside the bone structure, which is filled with bone marrow. This combination of a dense tissue, spongy tissue and fluid make bone a unique biological material.

Osteoporosis is recognized as a *silent epidemic* that reduces a bone's tissue and mass and increases its fragility. It mainly affects the spongy part of the bone particularly in hips, heels, and vertebrae (Osterhoff et al., 2016). So, early detection of this pathological condition is of paramount importance to ensure a proper treatment. In current practice, the only diagnostic tool for osteoporosis is a bone density test. The bone density test measures approximately the amount of bone mineral in the spine, hip, and sometimes other bones. The measured bone density can be an indicator of the state of a bone: normal bone density or low bone density (osteoporosis-osteopenia). Dual-energy X-ray absorptiometry (DXA) has been widely used as a bone density test for the hip and spine (Ott, Kilcoyne, and Chesnut III, 1987). Measuring bone density in the hip and spine is of paramount importance since the fracture risk for these bones is greater. This can cause more serious health issues such as greater pain, longer recovery time, and even permanent disability. Furthermore, DXA tests on the hip and spine can be a predictor of the likelihood of future breaks in other bones. Bone density in other bones such as the lower arm, wrist, finger, or heel can be measured through peripheral tests, also called screening tests, such as peripheral dual-energy x-ray absorptiometry (pDXA) or quantitative ultrasound (QUS). The results of screening tests for osteoporosis diagnosis are much less accurate and cannot be compared with the results of a DXA test.

One of the reasons for the limitations of QUS techniques in diagnosing osteoporosis is the lack of understanding of the mechanism of ultrasound wave propagation through a porous,

complex bone structure. Despite these issues, some features of the QUS technique make it yet very appealing for bone loss detection. For instance, QUS packages are smaller and potable relative to bulky MRI or X-ray techniques. Also, they are relatively cheap, do not utilize harmful radiations, and are recognized as a non-invasive technique.

In order to understand the mechanism of ultrasound wave propagation through the complex structure of a cancellous bone, the biomechanical models considering the viscous interchange between the viscous pore fluid and the solid skeletal frame should be developed. One of the most prominent theories to study the wave propagation in porous materials saturated with a fluid is the Biot theory of poroelasticity originally developed in the 1950s-1960s (Biot, 1956d; Biot, 1941; Biot, 1955; Biot, 1956b; Biot, 1962b). Biot's theory has been widely used in oil and gas applications and geo-science testings. It has been also applied to model the bone structure in several studies. For example, (Fellah et al., 2004a) studied wave propagation in human cancellous bone at high frequency ranges based on the Biot-JKD theoery. They used a slab immersed in water to model a bone. It should be noted that they only investigated the effect of longitudinal wave propagating in porous media and neglected the effect of transverse waves in their model. They considered the effect of porosity, density, shear modulus and viscosity on their scattering coefficients, describing the importance of these parameters in the fast and slow waves. (Fellah et al., 2013) developed a temporal model to describe wave propagation in porous media saturated with fluid using the Biot-JKD theory by applying the dynamic tortuosity and fractional calculus to describe the viscous exchange between the pore fluid and solid skeletal frame. They also did not apply the effect of transverse waves in their model and only investigated the effect of longitudinal waves in solid and fluid phases. In addition, they just considered wave propagation in one direction by using a slab as the bone model. (Sadouki, 2020) considered ultrasonic characteristic of human cancellous bone using the Biot-JKD theory. They used inverse problem to estimate three physical parameters such as porosity, tortuosity and viscous characteristic length, as well as the mechanical parameters such as Young's modulus and Poisson's ratio of the solid skeleton. They performed the tests on two samples of trabecular bone saturated with water. They modeled bone as a slab in their theoretical model and they did not consider the effects of transverse waves in their theoretical expression.

This research aims to specifically study

- the effect of transverse waves, in addition to longitudinal waves, on the acoustical response of a bone-like porous material filled with a viscous fluid such as bone marrow.

- the effect of both three-dimensional (3D) bone geometry and longitudinal and transverse acoustical waves on the response of a cylindrical cancellous bone-like porous material saturated with a viscous fluid by presenting a 3D biomechanical semi-analytical model.

1.2 Thesis Statement and Contributions

1.2.1 Thesis Statement

The aims of this research is to consider the wave propagation in bone-like porous media saturated with a viscous fluid using the Biot-JKD theory. The research has been implemented in time and frequency domains. Due to the tortuosity effect on the viscous exchange between the solid skeletal frame and pore fluid in high frequency ranges, the fractional calculus is used to describe such viscous interactions. The modeling development carried out in this research is divided into three parts. First, a transient biomechanical model is presented by considering only the propagation of longitudinal acoustic waves in 1D. A sensitivity analysis is performed to investigate the effect of biomechanical properties on acoustical response of a bone-like porous slab. Then, the effect of transverse waves, in addition to longitudinal waves, on ultrasonic response of a bone-like porous material when it is filled with a viscous fluid is studied in 1D. To study the effect of bone's geometry on acoustical response, a 3D biomechanical model is developed for ultrasonic wave propagation within a bone-like porous cylinder saturated with a viscous fluid.

1.2.2 Contributions

The contributions of this research are categorized into mathematical development and modeling, and investigation for bone characterization as follows:

1.2.3 Mathematical Development and Modeling

- Develop the 1D and 3D semi-analytical solutions for wave propagation in bone-like porous materials saturated with a viscous fluid such as bone marrow in order to consider the effect of transverse waves in addition to longitudinal waves on acoustical response of such materials.

- Develop an ultrasonic analytical solution for bone-like porous materials by considering the effect of tortuosity on viscous exchange between the viscous pore fluid and solid skeletal frame in high frequency ranges by using fractional calculus.

1.2.4   Investigations

- Investigate the effect of transverse waves, in addition to longitudinal waves, on acoustical response of bone-like porous materials.

- Investigate the sensitivity of bone's transmission and reflection coefficients on physical and mechanical properties of bone-like porous materials such as porosity, tortuosity, viscous characteristic length, Poisson's ratio, and elastic modulus.

- Investigate the effect of tortuosity in high frequency ranges on frequency responses of bone-like porous materials.

Chapter 2

Literature Survey

In this chapter, a brief description of the pertinent literature of wave propagation in bone structure is presented. Also, the structure of thesis for each chapter is explained.

The literature review is divided into three categories. First, the experimental work is considered. Then the experimental and analytical work are investigated. Next, the description of the experimental work compared with numerical work is explained. Subsequently, the gaps in the literature regarding bone characterization using acoustic waves are identified and the significance of this thesis in considering wave propagation within bone-like porous materials filled with a viscous fluid and bone characterization is highlighted.

2.0.1   Experimental Studies

Ultrasonic techniques have been widely utilized for the diagnosis of bone loss. The initial application of ultrasonic technique in clinical medicine dated back 1932 by considering the pattern produced by reflection ultrasonic energy in bone tissues. However, the first in-vitro study was carried out in 1953 by studying the bone conduction using ultrasonic technique (Anast, Fields, and Siegel, 1958). (Siegel, Anast, and Fields, 1958) measured the velocity of longitudinal waves across a broken bone by ultrasonic technique. (Horn and Robinson, 1965) studied the ultrasonic measurement and concluded that the bone condition cannot be clearly determined by the sound delay between measurements in intact and broken bones. So, they suggested to study the effect of transverse waves to get more valuable information. Other studies focused on determining the relationships between the resonant frequency and density of a bone (Selle and Jurist, 1966), the speed of sound and elasticity of a bone (Floriani, Debervoise, and Hyatt, 1967), the amount of calcium inside the bone and its transmission coefficients (Rich et al., 1966). The first studies on wave propagation in cancellous bones in order to find a correlation between the ultrasonic parameters and physical-mechanical properties of a bone has been performed by (Abendschein and Hyatt, 1970). A large number of

in-vitro and in-vivo ultrasonic tests on bones has been performed in the literature. The experiments can be divided into two categories: the velocity measurements and the attenuation measurements.

The speed of sound in cortical and cancellous bones was reported in a series of in-vitro studies by (Lang, 1970; Shalanskii et al., 1976; Yoon and Katz, 1976; Barger, 1979; Lakes, Yoon, and Katz, 1983) and in-vivo studies by (Jurist, 1970; Shalanskii et al., 1976; André et al., 1980; Greenfield et al., 1981; Behari and Singh, 1981; McCartney and Jeffcott, 1987; Fry and Barger, 1978). The evaluation of correlation between the velocity and other parameters has been extensively studied in the literature as well. As an example, (Evans and Tavakoli, 1990) considered the correlation of calcium content of the bone with the speed of sound. They obtained a correlation of 0.99 between the bone's speed of sound and calcium content for one of their samples while the correlation was so poor for other six samples. (Meunier et al., 1982) investigated the correlation between the longitudinal wave velocity and the modulus of elasticity of a cortical bone as well as its density. (Avioli, 1988) compared the speed of sound measured in a patella (kneecap) and its radius and found an identical correlation between them. (Rossman et al., 1989) measured the speed of sound on os calcis when the bone is intact and with mild bone loss. They compared their results with bone mineral density (BMD) obtained using photon absorptiometry on the proximal femur. It was shown that in osteoporosis bone whose its BMD is significantly reduced, the speed of sound is lower.

(Garcia et al., 1978) measured the attenuation in a cortical bone for a frequency range of $2 - 8$ MHz. They used short pulses as an incident wave and analyzed the transmitted signals using the Fourier transform. (Fry and Barger, 1978) measured the insertion loss, sound speed, and reflection loss of the cancellous part of human skulls. Measurements were performed in a frequency range from 0.25 to 6 MHz. The results showed that the selection of an appropriate frequency range from 0.5 to 1 MHz, has significant influence on diagnostic imaging and interrogation in the adult human skulls. Following their experiments, (Smith et al., 1979) found that the attenuation increases to 1 MHz for $10 - 20$ dB/cm and increases to 2 MHz for $50 - 60$ dB/cm. (Langton, Palmer, and Porter, 1984) developed an ultrasonic method to measure the attenuation of a bone sample. Their technique is known as the Broadband Ultrasonic Attenuation (BUA). They measured the transmission signals in bone samples immersed in the water tank. The difference between these two types of signals is attributed to the bone attenuation. Their results showed that the slope of the attenuation versus frequency for a bone sample with bone loss (osteoporosis) is higher than that of a healthy bone.

(Poll, Cooper, and Cawley, 1986) studied the BUA and the single photon absorptiometry

(SPA) tests on a wide range of patients with rheumatoid disease. They found a good correlation of 0.8 between these two methods. (Hosie et al., 1987) evaluated the BUA technique and found a correlation of 0.66 between the quantitative computed tomography (QCT) and BUA of the distal radius. (Saha and Shafkey, 1987) found a correlation of 0.7 between the density and attenuation of cadaver tibia. (Baran et al., 1988) experimentally showed that the BUA can be effectively used for bone loss risk prediction in the hip and spine. (Evans et al., 1988) compared the results obtained by the BUA with those obtained by the SPA and QCT tests. The results showed a correlation of 0.45 between the BUA and the SPA for the Radius and a correlation of 0.64 between the BUA and the QCT for the spine. (Rossman et al., 1989) performed the same experiments for the radius and spine as they found a correlation of 0.65 between the BUA and the QCT for spine and BUA and SPA for radius. (McCloskey et al., 1990) found a correlation of 0.66 between BUA and SPA and correlation of 0.72 between BUA and QCT by considering normal and abnormal groups.

Due to the potentials of ultrasonic testing to assess non-invasively bone quality, a significant attention to quantitative ultrasound has been made since 1990 (Williams, 1992; Williams et al., 1996; Hosokawa and Otani, 1997; Hosokawa and Otani, 1998; Hughes et al., 1999; Padilla and Laugier, 2000; Kaczmarek, Kubik, and Pakula, 2002; Lee, Roh, and Yoon, 2003; Hughes et al., 2003; Fellah et al., 2004a; Kaczmarek, Kubik, and Pakula, 2005; Wear et al., 2005; Sebaa et al., 2006b; Wear, 2007; Hughes et al., 2007; Pakula et al., 2008). (Cepollaro et al., 2005; Otani, 2005; Pakula, Padilla, and Laugier, 2009) developed a method to evaluate the detection of bone loss. They worked on trabecular bones and measured the speed of sound and reducing attenuation as a function of frequency which is correlated with density. Their work was accepted as a criterion for osteoporosis diagnosis. Other groups measured the fast and slow longitudinal waves in trabecular bones (Langton, Palmer, and Porter, 1984; Cepollaro et al., 2005; Otani, 2005; Mano et al., 2006). A lot of experimental tests regarding wave propagation in bone has been performed. Some of them are influenced by the physical properties of the pore fluid (fluid filled the pores) (Alves et al., 1996; Nicholson and Bouxsein, 2002; Kaczmarek, Kubik, and Pakula, 2002), mechanical properties of porous medium (Haïat et al., 2007b; Hoffmeister, Whitten, and Rho, 2000; Riekkinen et al., 2007), bone's anisotropy (Wear, 2000; Hughes et al., 2007; Wear, 2010), physical properties of porous structure (Chaffaı et al., 2002; Padilla et al., 2008) and tortuosity of the medium and viscous characteristic length (Pakula et al., 2008; Fellah et al., 2004a).

In addition to experimental methods, numerical simulations and analytical approaches have a great potential in modeling of wave propagation in cancellous bone. In the next

section, a brief history of the application of analytical approaches in ultrasonic modeling of cancellous bone is described.

2.0.2   Analytical Studies

Due to anisotropic and heterogeneous structure of the bone, especially, cancellous part of a bone, characterizing bone, in-vivo or in-vitro, is difficult. As mentioned previosuly, the most comprehensive theory for modeling wave propagation in porous media saturated with a fluid is Biot's theory. Biot's theory has been widely used in oil and gas and geo-science applications (Biot and Willis, 1957; Biot, 1962b; Biot, 1962a) or in sound-proofing (Depollier, Allard, and Lauriks, 1988). This theory has been also applied to model wave propagation in porous bone structure. (Berryman, 1980) compared Biot's theory with the measured speed of fast longitudinal wave, slow wave, and shear wave in porous media saturated with water. There is a good agreement between the results predicted by Biot's theory with the results of experiments. (McKelvie and Palmer, 1991) compared the attenuation of healthy bone and osteoporotic bone versus frequency. The results showed that the attenuation in healthy bone is much more than osteoporotic bone and also the attenuation in both increases by increasing frequency. (Williams, 1992) used Biot's theory to calculate the speed of sound in tibia and femoral bovine cancellous bone. The results obtained by Biot's theory showed a good agreement with experimental results. (Lauriks et al., 1994) compared the fast longitudinal wave in cancellous bone obtained by experiments to Biot's theory. Their result showed a good agreement between Biot's theory and their experiments. (Hosokawa and Otani, 1997; Hosokawa and Otani, 1998) modeled wave propagation through bovine cancellous bone in order to determine the fast and slow waves by experiments. They also estimated the fast and slow wave using Biot's theory. While the measured speeds for fast and slow waves showed a good agreement in both theory and experiments, some differences were observed in the attenuation between Biot's theory and the experimental results.

The analytical expression introduced by Biot is a relatively comprehensive approach for elastic materials, but it still encountered some problems. For example, the thermal effect in porous media has not considered in original Biot's theory. In addition, it needs a large number of parameters that need to be measured or estimated. (Attenborough, 1983) proposed a theory to consider the thermal effect in porous media, but it did not include the effect of the fast wave because the solid skeletal frame was considered as a rigid material. Later on, (Roh, Lee, and Yoon, 2003) proposed a new theoretical model named modified Biot-Attenborough (MBA) model. The model, in addition to fast and slow waves, is able to

consider the viscous and thermal effect as well. It is expected that the MBA model can be used to study the diagnosis of osteoporosis in cancellous bone. It should be noted that they did not consider the effect of tortuosity in their model. (Schoenberg, 1984) proposed the theoretical approach to model wave propagation in porous media. Schoenberg's theory requires less parameters to be estimated or measured with respect to Biot's theory which is an advantage for computational costs. But Schoenberg's theory assumes the fluid is inviscid and there is no prediction for viscous absorption. (Hughes et al., 1999) used a new stratified model to model wave propagation in cancellous bone. They used Schoenberg's theory in their approach to predict wave properties. They perfomed in-vitro experiments on bovine bone samples. Their results showed a qualitative agreement with Schoenberg's theory.

Among the above-mentioned analytical predictions using Biot's theory, it can be seen that the experimental results showed a good agreement with Biot's theory in predicting the speed of fast or slow waves in cancellous bones. But, it still showed limitations related to the viscous dissipation in porous media filled with viscous fluids. The original Biot's theory was modified by (Johnson, Koplik, and Dashen, 1987) in the late 1980s to address the limitations of original Biot's theory in this regard. This is of significant importance when it is aimed to model the energy dissipation in the medium at different frequency ranges. The modified theory, called Biot-JKD, introduces the concept of dynamic tortuosity, viscous characteristic length, and dynamic permeability to describe the viscous dissipation occurring in the pores. (Williams et al., 1996) expanded Biot's theory using JKD formulation to consider the attenuation versus porosity at frequencies of 0.2 MHz and 0.6 MHz for cancellous bone when it is filled with a relatively low and high viscous fluid. The results showed that the attenuation increases by increasing the frequency and porosity. The rate of increase in relatively high viscous fluid is much more then that of a relatively low viscous fluid. (Leclaire, Glorieux, and Thoen, 1997) used Biot's theory to determine acoustic parameters in high frequency by discrepancy between experimental and analytical results for the attenuation. They did not consider the JKD formulation in their analytical modeling. Also, they did not perform any validation between their analytical and experimental results. (Fellah et al., 2004a) considered reflection and transmission coefficients in human cancellous bone in one direction in frequency domain. They used a slab as a porous medium with two infinite dimensions filled with water to model cancellous bone. They used Biot's theory modified by the JKD formulation to consider the effect of viscous exchange between the fluid and solid. They did not consider the effect of transverse wave in their theoretical prediction. The experimental results for fast and slow waves transmitted thorough the slab showed a good agreement with

the theoretical prediction. (Sebaa et al., 2006a) considered transient wave propagation in the porous slab using Biot-JKD's theory. Fractional calculus was used to describe the viscous interactions between fluid and solid structure. The porous slab had two infinite dimensions and filled with water. They did not consider the effect of the transverse wave. They mentioned a good agreement between their experimental results and theoretical prediction. (Sebaa et al., 2006b) estimated the ultrasonic characteristics of cancellous bone by solving inverse problem using experimental data. They used the slab filled with water to model cancellous bone and used Biot's theory for their theoretical prediction. They also expanded Biot's theory using JKD formulation ((Johnson, Koplik, and Dashen, 1987)) to consider the effect of viscous exchange between fluid and solid. They solved inverse problem numerically by the least square method. They performed the minimization of the discrepancy between the transmitted signals obtained by experiments and theory to estimate five parameters related to physical-mechanical properties of the medium. (Hughes et al., 2007) considered wave propagation in anisotropic tortuosity in cancellous bone. They used Biot's theory and Schoenberg's model to consider the effect of viscosity and anisotropy, respectively. They generated Stratified Biot Model by applying an angle-dependent tortuosity for the layered structure. Their proposed model showed a good agreement in fast wave velocity between measured data and simulation results. (Fellah et al., 2013) developed a temporal model to describe wave propagation in the slab as a porous medium saturated with water using the Biot-JKD theory by applying dynamic tortuosity and fractional calculus to describe the viscous exchange between the pore fluid and solid skeletal frame. They also did not apply the effect of transverse wave in their model and only investigated the effect of longitudinal waves in solid and fluid phases. They used Green's functions for fast and slow waves and compared them with their experimental work. Their theoretical results showed a good agreement with the experimental results. in the next section, the application of numerical simulations in modeling of wave propagation in cancellous bone is discussed.

2.0.3   Numerical Studies

Computational techniques and tools helped researchers further analyze the mechanism of wave propagation in complex bone structures and verify the robustness of their experimental setup. Most of numerical simulations performed on cancellous bone has been carried out by employing either finite-difference time-domain (FDTD) or finite element methods (FEM). (Luo et al., 1999) considered wave propagation in cancellous bone using microCT model. They found the wave speed as well as its attenuation, but they did not differentiate fast waves

from slow waves in bone samples. (Hosokawa, 2005) applied finite-difference method using Biot's theory and considered the fast and slow waves propagation through bone samples. The generation of fast and slow longitudinal waves using finite-difference time domain (FDTD) simulation have been reported by (Bossy et al., 2005; Padilla et al., 2005; Padilla, Bossy, and Laugier, 2006). They used 3D Synchrotron microtomography of trabecular bone for their FDTD simulation. (Haïat et al., 2007b) used numerical solution to consider the effect of microsctructure of trabecular bone as well as its material properties on QUS parameters. (Nagatani et al., 2006; Nagatani et al., 2008) tried to confirm the capability of the FDDT method in order to simulate wave propagation in cancellous bone using 3D x-ray CT images. They also confirmed that the peak amplitude of the fast and slow waves showed accordance with the experimental results. (Cardoso et al., 2003) expressed that the fast wave propagation in trabecular bone is more dominant than slow wave and it can provide more information on the trabecular structure. (Luo et al., 1999) analyzed 2-D visco-elastic wave propagation in the bone. (Kaufman, Luo, and Siffert, 2003) studied 3D micro-tomography of human cancellous bone in order to characterize material properties. (Bossy et al., 2005) computed 3-D wave propagation in human cancellous bone saturated with water using a finite-difference time-domain. They used 31 human specimens to obtain the material property needed for their simulations. Their results show the monotonic increase of BUA and speed of sound (SOS) with respect to the bone volume fraction and negative velocity dispersion. Following by their work, (Haïat et al., 2007a) explained that negative velocity dispersion can be described by multiple scattering effect. (Nagatani et al., 2008) examined the generation of fast wave by experimental measurements and numerical solution using the FDTD method. They used X-ray CT image to provide the bovine bone in their numerical simulation. Their experimental and numerical results express that the attenuation of fast wave is higher in early state of propagation. Then, it decreases gradually when wave propagates further in the bone. (Hosokawa, 2005) used finite-difference method in order to simulate the transient wave propagation in bovine cancellous bone in two dimensions. They compared the speed of fast and slow waves obtained by their FDTD with those of pertinent experiments by (Hosokawa and Otani, 1997). There is a good agreement between the experimental and simulated values of the speeds of fast and slow waves. (Nguyen and Naili, 2012) presented a finite element model to consider anisotropic porous media filled with viscous fluid. Their results show the effect of anisotorpy of bone on the reflection and transmission coefficients in cancellous bone specimen.

Micro-scale modeling of the wave propagation in bones using finite-difference time-domain, especially, in cancellous bone, has been accepted as one of the applicable solutions,

but there are still two disadvantages: (*i*) forming a new wave aircraft at the interface between the solid skeletal frame and pore fluid; (*ii*) lack of a perfect-slip condition at the interface between the solid skeletal frame and pore fluid. Therefore, another approach which can be more efficient than FDTD in wave propagation for solid-fluid interaction in the cancellous bone media would be the finite element method (FEM). The FEM has more advantages in the analysis of elastic wave propagation in comparison with the FDTD (Marfurt, 1984; Zhang and Verschuur, 2002). Also, it is worth nothing that the FEM has been used by several researchers to model wave propagation in bone structures (Niebur et al., 2000; Adachi et al., 2001; Goossens et al., 2008; Ridha and Thurner, 2013; Zhang, Tozzi, and Tong, 2014). (Nguyen, Naili, and Sansalone, 2010) used FEM to model the transient wave propagation in cancellous bone submerged in an acoustic fluid. Their FEM numerical results showed that anisotropy of bone influences strongly the reflection and transmission coefficients. (Ilic, Hackl, and Gilbert, 2010) used FEM modeling to consider the attenuation of wave propagation in cancellous bone. Their numerical results show that the attenuation increases if excitation frequency and material density increases. In addition, their results endorse the results obtained by experiments as well. (Vafaeian et al., 2014) used FEM to model 6 samples of cancellous bone in order to calculate the speed of sound and broadband ultrasound attenuation. The evaluation of their numerical results with experimental results demonstrate the capability of the FEM in modeling ultrasound wave propagation in water-saturated cancellous bone. (Niebur et al., 2000) used FEM to simulate the reproduction of microstructure of bone to consider bone failure or fracture. There are many reports in the literature regarding the FEM application in different areas of wave propagation in multi-scale structure (Miehe, Schotte, and Lambrecht, 2002; Ilić and Hackl, 2004; Pahr and Zysset, 2008).

While the numerical methods such as FEM and FDTD are powerful tools in modeling of wave propagation in cancellous bones, they also have disadvantages. For example, the tortuosity is a function of fractional exponent of time and it needs to be considered in the modeling of transient wave propagation in porous media saturated with a viscous fluid. The commercially available FEM software such as COMSOL uses a constant value for the tortuosity effect in this regard. Moreover, there is a partial reflection of acoustic waves from perfect matching layers to the model that provides a systematic error in results. The FDTD also shows deficiencies in modeling of wave propagation in complex porous materials. In addition, the FEM and FDTD require meshing the entire computational domain and it must be sufficiently fine to solve both acoustics wavelength and geometrical features, which can lead to an extensively large computational costs. Consequently, to the best of the author's

knowledge, it is impertinent to simulate wave propagation in bone-like porous material using either experimental work alone or the numerical solutions such as FDTD or FEM. So, in this study several closed-form frameworks based on the Biot-JKD theory are developed to analytically investigate the acoustic response of porous bone-like materials.

2.1 Structure of the Thesis

The style of each chapter is similar to a journal paper starting with an introduction which includes literature review. Then, mathematical formulations, computational details, results and discussion, and conclusion. References and appendices follow the conclusion. Since a part of the mathematical development is common among all the chapters, so it is presented in the corresponding appendices. A brief description of future work based on this research are presented at the end. The outlines of the five chapters of this dissertation are as follows:

- **Chapter 3** *Transient Acoustic Wave Propagation in Bone-Like Porous Materials Using the Theory of Poroelasticity and Fractional Derivative: A Sensitivity Analysis*

  In this chapter, the transient acoustic wave propagation in a bone-like porous material saturated with a viscous fluid is investigated using Biot's theory. Due to the interaction between the viscous fluid and solid skeleton, the damping behavior is proportional to a fractional power of frequency. Thus, the dynamic tortuosity is written in terms of the fractional power of frequency. Furthermore, to describe the viscous interaction of fluid and solid in the time domain, the fractional derivative is used. The fast and slow waves, which are the solutions to Biot's equations, are described by fractional calculus in the time domain. The reflection and transmission operators are expressed in the Laplace domain and inverted into the time domain using Durbin's numerical inversion. Once the numerical implementation is validated, the effects of porosity and viscosity on the stress, and reflected and transmitted waves are investigated. The results show that by increasing the porosity the stress in a bone-like material filled with either air or bone marrow increases. The transmitted pressure decreases by increasing the porosity. The reflected pressure decreases for low viscous fluid when the porosity increases while it increases when the viscosity of the fluid is high. In addition, the results show the importance of considering the fractional derivatives in the transient wave propagation in such porous materials.

- **Chapter 4** *An overview of the acoustic studies of bone-like porous materials, and the effect of transverse acoustic waves*

The model presented in chapter 3 considers only the propagation of longitudinal waves within the porous media. In this chapter, the effects of transverse acoustic waves in characterizing a bone-like, porous medium filled with a viscous fluid are analyzed for the first time. Scattering operators along with stress fields are derived by using the standard Biot-JKD model. A short duration acoustical pulse is applied to one side of a bone-like, porous medium so that both longitudinal and transverse waves travel through the intermediate medium which is filled with a viscous fluid. The reflection and transmission operators along with stresses in the medium are expressed in terms of these waves. The numerical implementation is validated for the longitudinal wave by comparison with the numerical simulation performed by (Fellah et al., 2004a). The effects of the transverse waves on the reflection and transmission coefficients as well as the stress field are studied by considering different viscosities and porosities. It is shown that when the fluid viscosity in the medium is relatively high (such as bone marrow), the effect of the transverse wave dominates. However, this effect is negligible when the medium is filled with a relatively low viscous fluid (such as air). Furthermore, it is shown that the role of transverse waves in characterizing bone structures and bone loss is imperative since the acoustical response of such media at specific frequencies can be triggered only by considering the effects of transverse waves.

- **Chapter 5**   *Three-Dimensional Biomechanical Acoustics Modeling of Wave Propagation through Cylindrical Bone-Like Porous Materials Saturated with Viscous Fluid*
  The acoustical analytical models presented in chapter 3 and chapter 4 are one dimensional while in this chapter a three-dimensional acoustical model for bone is considered. In fact, chapter 5 describes a three-dimensional (3D) analytical solution for the acoustic wave propagation through cancellous bone-like materials saturated with a viscous fluid for the first time. The effect of dynamic tortuosity in high frequency ranges is considered. The solution includes the effects of both longitudinal fast- and slow-waves as well as transverse waves propagating through the medium. The scattering operators and radial displacements are derived in the form of ultrasonic waveforms by applying the Helmholtz decomposition. The effect of different porosities, wall thickness ratios, and frequencies of incident waves on the radial displacement and scattering operators are investigated by considering various incident wave angles at forward and sideward directions. The results demonstrates that the incident wave angle has a significant effect on the radial displacement and scattering operators regardless of the porosity, wall thickness ratio, and viscosity of pore fluid. Furthermore, the distribution pattern of the

radial displacement and scattering operators in relatively low frequency ranges is almost symmetric while asymmetric in relatively high frequency ranges. It is shown that the bone characterization using ultrasonic techniques is not only based on the mineral density, as used currently by electromagnetic wave-based tools, but also other biomechanical factors such as the porosity, viscosity of pore fluid, and wall thickness ratio of a cancellous bone structure. Also, the pattern of the reflected pressure can be an indicator of the state (healthy versus osteoporosis) of a cancellous bone.

- **Chapter 6** *Conclusion and Potential of Future Research Plan* In this chapter, the contributions of this research along with the conclusions as well as the future research plan are outlined.

Chapter 3

Transient Acoustic Wave Propagation in Bone-like Porous Materials Using the Theory of Poroelasticity and Fractional Derivative: A Sensitivity Analysis

Abstract

The transient acoustic wave propagation in a bone-like porous material saturated with a viscous fluid is investigated using Biot's theory. Due to the interaction between the viscous fluid and solid skeleton, the damping behavior is proportional to a fractional power of frequency, i.e. the dynamic tortuosity was written in terms of fractional power of frequency. Furthermore, to describe the viscous interaction of fluid and solid in the time domain, the fractional derivative was used. The fast and slow waves, which are the solutions to Biot's equations, were described by fractional calculus in the time domain. The reflection and transmission operators were expressed in the Laplace domain and inverted into the time domain using Durbin's numerical inversion. Once the numerical implementation was validated, the effects of porosity and viscosity on the stress, and reflected and transmitted waves were investigated. The results showed that by increasing the porosity, the stress in a bone-like material filled with either air or bone marrow increases. The transmitted pressure decreases by increasing the porosity. The reflected pressure decreases for low viscous fluid when the porosity increases while it increases when the viscosity of the fluid is high. In addition, the results showed the importance of taking into account the fractional derivatives in the transient wave propagation in such porous materials.

3.1 Introduction

Bone is a rigid organ that supports and protects other organs, stores minerals, produces red blood cells in its marrow, and supports mobility. This organ is very dynamic and metabolically active with the ability for self-repair. The actual structure of the bone is porous and spongy, consisting of a solid skeleton and pores filled with fluids. One of the most important quantities in characterizing the bone structure is its porosity, which varies between 5% to 95% (Fritsch and Hellmich, 2007). Pores in a bone are not evenly distributed. Consequently, any realistic model must be able to take into account the variation in porous properties of the bone structure for reliable assessment of bone fracture risk under normal conditions (Ogam et al., 2011; Fritsch and Hellmich, 2007).

One of the most popular theories in the literature to study the transient wave propagation in porous media saturated with a viscous fluid, such as bones, is the theory of poroelasticity originally proposed by (Biot, 1956d; Biot, 1941; Biot, 1955; Biot, 1956b; Biot, 1962b). The Biot theory is able to model the interaction between two phases such as a solid skeleton and a fluid by considering the viscous coupling effect. Biot's theory considered the frictional drag at the pore surface and included the inertia term.

The interaction between the bone marrow and solid skeleton in a bone subjected to a transient acoustic wave incident leads to a complex solution. Wave propagation in a trabecular porous bone saturated with a viscous fluid using Biot's theory has been studied by several researchers (Hosokawa and Otani, 1997; Hosokawa and Otani, 1998; Haire and Langton, 1999; Cardoso and Cowin, 2011; Fellah et al., 2004a; Sebaa et al., 2006b; Marutyan, Holland, and Miller, 2006; Hughes et al., 2007; Pakula et al., 2008; Anderson et al., 2008; Mizuno et al., 2009; Wear, 2010; Nelson et al., 2011). Furthermore, any change in bone characteristic due to bone loss or osteoporosis can be diagnosed by the speed of ultrasonic wave and its attenuation (Langton, Palmer, and Porter, 1984). (Cardoso et al., 2003) studied the wave propagation in cancellous bones for bone characterization. They demonstrated a correlation between the velocities of fast and slow waves with the porosity. They also mentioned that the presence of two waves is necessary to obtain the accurate results and failure in accounting any of them may lead to an inaccurate determination of bone properties.

Several studies related to the reflection and transmission of acoustic waves in cancellous bone have been performed in the frequency domain. (Buchanan, Gilbert, and Ou, 2012) considered a cancellous bone immersed in water and insonified by the acoustic pulse. As a result, they derived the transfer function for reflection and transmission of both fast and slow

waves. (Buchanan, Gilbert, and Khashanah, 2002; Buchanan, Gilbert, and Khashanah, 2004; Buchanan and Gilbert, 2007; Sebaa et al., 2006b) investigated the recovery of a specimen of cancellous bone immersed in water under an ultrasonic pulse. (Belhocine, Derible, and Franklin, 2007) used a transition term method to compare the experimental and analytical results of reflection and transmission of a porous plate saturated with a fluid. (Johnson, Plona, and Kojima, 1994) considered the ultrasonic properties such as reflection, transmission, attenuation, and speed of waves in porous media saturated with water using two slabs with different thicknesses.

It is more desirable to describe the transient wave propagation in porous media directly in the time domain because of its suitable consistency with experimental measurements taken by pulses of finite bandwidth and synthesizing pulse signals via Fourier transform. Some work on the reflection and transmission of acoustic waves in porous media saturated with a viscous fluid is performed in the time domain. (Caviglia and Morro, 2004) considered the reflection and transmission of a multilayer slab. They assumed the layers are linearly elastic, anisotropic, and homogeneous. (Szabo, 1994) investigated the attenuation of acoustic waves propagating in a wide variety of lossy media. The results express that dispersion and attenuation in a linear medium are accountable for the linear wave equation when the effect of a causal convolutional propagation operator is included. Their work was restricted in media with power-low attenuation, but it was shown that their approach is applicable to a broader class of media (Norton and Novarini, 2003; Waters et al., 2000).

Due to the viscous interaction between the fluid and solid skeleton in a bone-like material, the fractional derivatives must be used. A group of experimental observations relevant to the phase interaction between the fluid and solid in a porous medium illustrates the significant role of fractional derivative in the description of their mechanical properties (Bagley and Torvik, 1986; Rossikhin and Shitikova, 1997; Caputo, 1976). (Fellah, Depollier, and Fellah, 2002) considered the wave propagation in rigid porous materials. They applied the fractional calculus to describe the tortuosity of a medium and compressibility of the air in porous media. (Fellah and Depollier, 2000) studied wave propagation in porous media composed of a rigid frame filled with air. They determined the porous medium parameters using direct and inverse scattering problems. (Fellah et al., 2003) investigated the transient wave propagation in a porous rigid frame slab which was isotropic and homogeneous. The transient model took into account the thermal loss and viscosity of the medium. Finally, The transmission and reflection responses of the medium to an incident pulse were derived. (Fellah et al.,

2005) considered the transient wave propagation in a double-layered porous model. They investigated the tortuosity, viscosity, and thermal loss in their model using a time convolution interpreted by the fractional derivative. (Fellah et al., 2010) used the fractional derivative to describe the behavior of waves in a rigid porous structure. (Fellah et al., 2004b; Hanyga and Rok, 2000; Fellah, Fellah, and Depollier, 2008) also showed that the damping and stiffness of a porous material saturated with a viscous fluid are proportional to a fractional power of frequency.

This chapter aims to investigate analytically the effects of porosity, and viscosity on the stress, and reflected and transmitted pressures of a bone-like material using transient acoustic waves. This is a preliminary step to diagnose bone loss using Quantitative Ultrasound techniques. In fact, any change in bone characteristics can be caused by a bone disease such as osteoporosis. Since the spongy part of a bone is more prone to bone loss, this research focuses on the propagation of acoustic waves in a cancellous bone-like material. The specific organization of this chapter is as follows. The first section will address the mathematical development of transient wave propagation in a cancellous bone-like material saturated with a viscous fluid based on the Biot-JKD theory. As mentioned earlier, due to the viscous interaction between the solid skeleton and fluid, the damping effect has a fractional relation with the frequency. Thereby, the fractional derivative is used in this formulation to describe the damping in the time domain. Two eigenvalues of Biot's equation are selected as the fast and slow waves propagating in the cancellous bone-like material. Furthermore, the reflection and transmission scattering operators are derived in the Laplace domain. Then, they are transferred to the time domain using the frequent run of Durbin's numerical inversion. The validity of the analytical results has been checked by comparing with the experimental model found in the literature. Hence, the effect of mechanical properties on the stress and reflected and transmitted pressures in a bone-like material is investigated through a case study. Next, the closing remarks are listed. Finally, the appendices relevant to the mathematical development are presented.

3.2 Mathematical Developments

In this section, a general configuration of the problem is defined first. Then, conventions and common assumptions are given. The governing equations for the wave propagation in a fully saturated bone-like porous material is presented. Furthermore, the effect of fractional derivative is introduced. Then, the explicit forms for fast and slow fractional propagation

waves are derived. The reflection and transmission coefficients in both Laplace and time domains are obtained. Finally, the explicit forms for the stress in the solid skeleton and fluid pressures are presented.

3.2.1 Problem Definition

A general schematic of the problem is illustrated in Figure 3.1. The domain is composed of an elastic solid skeleton filled with a viscous fluid. Different types of material properties can be assigned to each phase. An incident wave hits the left side of the medium, which will propagate longitudinally through the medium. The constitutive equations are described next.
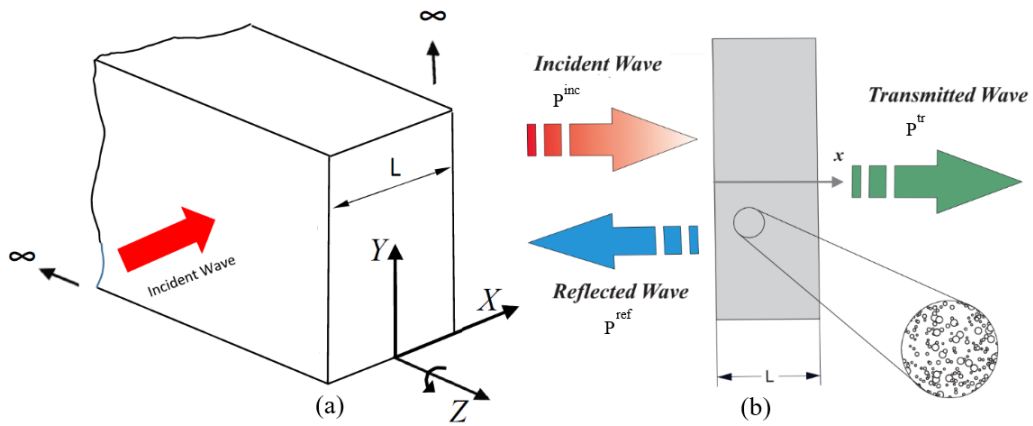
FIGURE 3.1: A schematic of the problem's geometry

3.2.2 Conventions and Common Assumptions

In this study, the state variables are the displacement of the solid skeleton, u_i, and the absolute displacement of the pore fluid, U_i. The derived governing equations are based on the following assumptions and conventions:

- The bone-like porous medium consists of the superposition of a continuum body consisting of a deformable skeleton, s, and a porous space filled with a fluid, f.
- The poroelastic medium of the skeleton is homogeneous, isotropic and linear.
- The deformation gradient of the solid skeleton $\mathbf{F}$ is defined by $\mathbf{F} = \mathbf{I} + \nabla\mathbf{u}$, in which $\mathbf{I}$ is the second-order isotropic tensor with component δ_{ij}, where δ_{ij} is the Kronecker delta. The symbol $\nabla = (\partial/\partial\mathbf{x})$ always stands for the gradient operation with respect to $\mathbf{x} = \mathbf{x}(\mathbf{X}, t)$, which is the Eulerian position vector at time t in a Cartesian coordinate frame of orthonormal basis. Also, $\mathbf{u}$ is the displacement vector of the skeleton whose initial and current positions are $\mathbf{X}$ and $\mathbf{x}$ ($\mathbf{u}=\mathbf{x}\text{-}\mathbf{X}$).

- The linearized form of Green-Lagrange strain tensor, ε, for infinitesimal deforamtion is $\varepsilon = \frac{1}{2}\left(\partial \mathbf{u}^t + \partial \mathbf{u}\right)$. The skeleton's volume dilatation ε_{ii} is required to match the variations of connected pore spaces (or porosity) ϕ because of the incompressibility of solid particles.

3.2.3 Field Equations

The field equations describing wave propagation in a bone-like porous medium can be derived for the state variables of the solid skeleton displacement, u_i, and absolute fluid displacement, U_i, as follows (Biot, 1956d).

$$\rho_{11}\frac{\partial^2 \mathbf{u}}{\partial t^2} + \rho_{12}\frac{\partial^2 \mathbf{U}}{\partial t^2} = P\nabla(\nabla.\mathbf{u}) + Q\nabla(\nabla.\mathbf{U}) - N\nabla \times (\nabla \times \mathbf{u}), \tag{3.1a}$$

$$\rho_{12}\frac{\partial^2 \mathbf{u}}{\partial t^2} + \rho_{22}\frac{\partial^2 \mathbf{U}}{\partial t^2} = Q\nabla(\nabla.\mathbf{u}) + R\nabla(\nabla.\mathbf{U}). \tag{3.1b}$$

in which the generalized elastic constants P, Q, and R are defined as follows.

$$P = \frac{K_s\left(K_b\left((\phi-1)K_f + \phi K_s\right) + (\phi-1)^2 K_f K_s\right)}{K_s\left(\phi K_s - (\phi-1)K_f\right) - K_b K_f} + \frac{4N}{3}, \tag{3.2a}$$

$$Q = \frac{\phi K_s\left(-\frac{K_b}{K_s} - \phi + 1\right)}{-\frac{K_b}{K_s} + \frac{\phi K_s}{K_f} - \phi + 1}, \tag{3.2b}$$

$$R = \frac{\phi^2 K_s}{-\frac{K_b}{K_s} + \frac{\phi K_s}{K_f} - \phi + 1}. \tag{3.2c}$$

where ϕ, K_f, K_s, and K_b are the porosity, bulk modulus of fluid, bulk modulus of solid particles, and bulk modulus of porous skeleton, respectively. Additionally, N stands for the shear modulus of the solid skeleton. The relationships between the above-mentioned mechanical properties and the elastic constants are given as follows.

$$K_s = \frac{E_s}{3 - 6v_s}, \quad K_b = \frac{E_b}{3 - 6v_b}, \quad N = \frac{E_b}{2v_b + 2}. \tag{3.3}$$

in which E_s, v_s, E_b, and v_b are the Young modulus and Poisson ratio of the solid and skeletal frame, respectively.

The mass coefficients in Eq. 3.1, ρ_{mn}, are expressed in terms of densities of solid particles ρ_s and pore fluid ρ_f by

$$\rho_{11} + \rho_{12} = (1 - \phi)\rho_s, \quad \rho_{12} + \rho_{22} = \phi\rho_f \tag{3.4}$$

Also the mass coupling between the fluid and solid skeleton is represented by ρ_{12} given by

$$\rho_{12} = -\phi \rho_f (\alpha_\infty - 1), \tag{3.5}$$

in which α_∞ stands for the tortuosity of the porous medium.

3.2.4 Fractional Derivative Effect

The interaction between the solid skeleton and pore fluid has an imperative role in damping of acoustic waves in a porous medium. This effect is considered in a Complex parameter called the dynamic tortuosity, $\tilde{\alpha}(\omega)$, which is expressed as a fractional exponent of frequency, ω, as follows (Johnson, Koplik, and Dashen, 1987).

$$\tilde{\alpha}(\omega) = \alpha_\infty \left(1 + \frac{2}{\Lambda_f} \left(\frac{\eta}{\omega j \rho_f} \right)^{\frac{1}{2}} \right) \tag{3.6}$$

in which Λ_f is the length of viscous characteristic, indicating the pore size distribution, η is the fluid viscosity, and j is the imaginary unit in the complex notation.

Applying the inverse Laplace transform to $\tilde{\alpha}(\omega)$ in high frequency domain (i.e., ultra-sonic applications) results in (Fellah and Depollier, 2000; Fellah et al., 2003)

$$\alpha(t) = \alpha_\infty \left(\delta(t) + \frac{2 \, t^{\frac{-1}{2}}}{\Lambda_f} \left(\frac{\eta}{\pi \rho_f} \right)^{\frac{1}{2}} \right), \tag{3.7}$$

where $\delta(t)$ is the Dirac function.

By substituting $\alpha(t)$ in Equation 3.5 and then Equation 3.5 in Equation 3.4 and inserting the obtained temporal mass coefficients in Equation 3.1a and Equation 3.1b, we obtain

$$\left((1-\phi)\rho_s + \phi \rho_f (at^{\frac{-1}{2}} - 1) \right) * \frac{\partial^2 \mathbf{u(t)}}{\partial t^2} - \phi \rho_f (at^{\frac{-1}{2}} - 1) * \frac{\partial^2 \mathbf{U(t)}}{\partial t^2} = \tag{3.8a}$$

$$P\nabla(\nabla.\mathbf{u(t)}) + Q\nabla(\nabla.\mathbf{U(t)}) - N\nabla \times (\nabla \times \mathbf{u(t)}),$$

$$-\phi \rho_f (at^{\frac{-1}{2}} - 1) * \frac{\partial^2 \mathbf{u(t)}}{\partial t^2} + \phi \rho_f at^{\frac{-1}{2}} * \frac{\partial^2 \mathbf{U(t)}}{\partial t^2} = \tag{3.8b}$$

$$Q\nabla(\nabla.\mathbf{u(t)}) + R\nabla(\nabla.\mathbf{U(t)}),$$

in which $*$ stands for the convolution integral for two functions such as $f(t)$ and $g(t)$, which is described as

$$(f * g)(x,t) = \int_0^t f(\tau)g(t-\tau)d\tau, \tag{3.9}$$

and

$$a = \alpha_\infty \left(\delta(t) + \frac{2}{\Lambda_f} \left(\frac{\eta}{\pi \rho_f} \right)^{\frac{1}{2}} \right)$$

As it can be seen in Equation 3.8, it results in a convolution of $t^{\frac{-1}{2}}$ with a temporal function. Thereby, this necessitates the application of fractional derivative of order n. There are several definitions for fractional derivative including (Oldham and Spanier, 1974; Miller and Ross, 1993; Butzer and Westphal, 2000; Yang, Ragulskis, and Taha, 2019; Yang, 2019; Yang et al., 2017; Ostoja-Starzewski and Zhang, 2018; Yang, Feng, and Hong-Wen, 2019; Li and Ostoja-Starzewski, 2019; YANG, 2018). In this paper, we formulate the problem using (Gorenflo and Mainardi, 2008) which is defined by

$$D^n[f(t)] = \frac{d^n f}{dt^n} = \frac{1}{\Gamma(m-n)} \int_0^t \frac{f^m(u)}{(t-u)^{n+1-m}} du. \tag{3.10}$$

in which f^m stands for $d^m f/dt^m$, and $\Gamma(m-n)$ represents the Gamma function; therefore, we use an encyclopedic treatment of fractional calculus presented by (Samko, Kilbas, and Marichev, 1993) given

$$D^n[f(x)] = \frac{1}{\Gamma(-n)} \int_0^t (t-u)^{-n-1} f(u) du, \tag{3.11}$$

in which $0 \leq n < 1$ and $f(u)$ is a derivative of u with respect to time. Note that the fractional derivative acts as a convolution integral operator in this model.

Subsequently, the tortuosity function in the field equations can be treated by using the fractional derivative in the time domain as follows.

$$\rho_{11}(t) * \frac{\partial^2 \mathbf{u(t)}}{\partial t^2} + \rho_{12}(t) * \frac{\partial^2 \mathbf{U(t)}}{\partial t^2} = \tag{3.12a}$$

$$P\nabla(\nabla.\mathbf{u(t)}) + Q\nabla(\nabla.\mathbf{U(t)}) - N\nabla \times (\nabla \times \mathbf{u(t)}),$$

$$\rho_{12}(t) * \frac{\partial^2 \mathbf{u(t)}}{\partial t^2} + \rho_{22}(t) * \frac{\partial^2 \mathbf{U(t)}}{\partial t^2} = \tag{3.12b}$$

$$Q\nabla(\nabla.\mathbf{u(t)}) + R\nabla(\nabla.\mathbf{U(t)})$$

where

$$\rho_{11}(t) = \phi\left(\alpha(t) - 1\right)\rho_f - (\phi - 1)\rho_s, \tag{3.13}$$

$$\rho_{12}(t) = -\phi\left(\alpha(t) - 1\right)\rho_f,$$

$$\rho_{22}(t) = \phi\,\alpha(t)\rho_f.$$

3.2.5 Compressional Displacement Potentials

The wave propagates in an elastic solid in two longitudinal and rotational forms. In this study, we only consider the compressional (longitudinal) wave propagating through a bone-like porous material, so ϕ_s and ϕ_f are taken as the scalar compressional displacement potentials for solid skeleton and fluid, respectively. Hence, the solid skeleton and fluid displacement fields, $\mathbf{u}(t)$ and $\mathbf{U}(t)$, can be written as

$$\mathbf{u}(t) = \nabla\phi_s(t), \quad \mathbf{U}(t) = \nabla\phi_f(t), \tag{3.14}$$

By substituting Equation 3.14 into Equation 3.12, we obtain

$$\begin{pmatrix} \rho_{11} & \rho_{12} \\ \rho_{21} & \rho_{22} \end{pmatrix} \frac{\partial^2}{\partial t^2} \begin{pmatrix} \phi_s(t) \\ \phi_f(t) \end{pmatrix} + \varpi \begin{pmatrix} 1 & -1 \\ -1 & 1 \end{pmatrix} \frac{\partial^{\frac{3}{2}}}{\partial t^{\frac{3}{2}}} \begin{pmatrix} \phi_s(t) \\ \phi_f(t) \end{pmatrix} = \tag{3.15}$$
$$\begin{pmatrix} P & Q \\ Q & R \end{pmatrix} \nabla^2 \begin{pmatrix} \phi_s(t) \\ \phi_f(t) \end{pmatrix},$$

in which $\varpi = \frac{1}{\Lambda_f} 2\phi\rho_f\alpha_\infty \sqrt{\frac{\eta}{\rho_f}}$.

The two eigenvalues for Equation 3.15, $\phi_1(t)$ and $\phi_2(t)$, which describe the fast and slow compressional wave modes, can be derived by solving the following equation

$$\begin{pmatrix} \rho_{11}\frac{\partial^2}{\partial t^2} + \varpi\frac{\partial^{\frac{3}{2}}}{\partial t^{\frac{3}{2}}} & \rho_{12}\frac{\partial^2}{\partial t^2} - \varpi\frac{\partial^{\frac{3}{2}}}{\partial t^{\frac{3}{2}}} \\ \rho_{12}\frac{\partial^2}{\partial t^2} - \varpi\frac{\partial^{\frac{3}{2}}}{\partial t^{\frac{3}{2}}} & \rho_{22}\frac{\partial^2}{\partial t^2} + \varpi\frac{\partial^{\frac{3}{2}}}{\partial t^{\frac{3}{2}}} \end{pmatrix} \begin{pmatrix} \phi_s(t) \\ \phi_f(t) \end{pmatrix} \tag{3.16}$$
$$-\nabla^2 \begin{pmatrix} P & Q \\ Q & R \end{pmatrix} \begin{pmatrix} \phi_s(t) \\ \phi_f(t) \end{pmatrix} = 0.$$

By writing Equation 3.16 in the from of an eigenvalue matrix, we obtain

$$\nabla^2 \begin{pmatrix} \phi_1(t) \\ \phi_2(t) \end{pmatrix} = \begin{pmatrix} \lambda_1(t) & 0 \\ 0 & \lambda_2(t) \end{pmatrix} \begin{pmatrix} \phi_1(t) \\ \phi_2(t) \end{pmatrix} \tag{3.17}$$

in which

$$\lambda_i(t) = C_i \frac{\partial^2 \phi_i(t)}{\partial t^2} + D_i \frac{\partial^{\frac{3}{2}} \phi_i(t)}{\partial t^{\frac{3}{2}}} + G_i \frac{\partial \phi_i(t)}{\partial t}, \quad i = 1, 2. \tag{3.18}$$

The eigenvectors corresponding to these eigenvalues are

$$\chi_i(t) = A_i + \frac{B_i}{\sqrt{\pi t}}, \quad i = 1, 2. \tag{3.19}$$

where A_i, B_i, C_i, D_i, and G_i are as follows.

$$A_i = \frac{\rho_1 - 2\rho_5 + (-1)^i \sqrt{\rho_1^2 - 4\rho_3}}{2\rho_7}, \tag{3.20}$$

$$B_i = \frac{2\rho_7 \left(\frac{(-1)^i (\rho_1 \rho_2 - 2\rho_4)}{\sqrt{\rho_1^2 - 4\rho_3}} + \rho_2 - 2\rho_6 \right) - 2 \left(\sqrt{\rho_1^2 - 4\rho_3} - \rho_1 + 2\rho_5 \right) \rho_6}{4\rho_7^2}$$

$$C_i = \frac{1}{2} \left((-1)^i \sqrt{\rho_1^2 - 4\rho_3} + \rho_1 \right),$$

$$D_i = \frac{1}{2} \left(\frac{(-1)^i (\rho_1 \rho_2 - 2\rho_4)}{\sqrt{\rho_1^2 - 4\rho_3}} + \rho_2 \right),$$

$$G_i = \frac{(-1)^i \left(\left(\rho_1^2 - 8\rho_3 \right) \rho_2^2 + 4\rho_1 \rho_4 \rho_2 - 4\rho_4^2 \right)}{8 \left(\rho_1^2 - 4\rho_3 \right)^{3/2}},$$

where ρ_i are in terms of acoustical and mechanical properties of porous media described as follows.

$$\rho_1 = \frac{P\rho_{22} - 2\rho_{12}Q + \rho_{11}R}{PR - Q^2}, \quad \rho_2 = \frac{\varpi(P + 2Q + R)}{PR - Q^2}, \quad \rho_3 = \frac{\rho_{12}^2 - \rho_{11}\rho_{22}}{Q^2 - PR},$$

$$\rho_4 = \frac{\varpi(\rho_{11} - 2\rho_{12} + \rho_{22})}{PR - Q^2}, \quad \rho_5 = \frac{\rho_{12}Q - \rho_{11}R}{Q^2 - PR}, \quad \rho_6 = \frac{\varpi(Q + R)}{PR - Q^2}, \tag{3.21}$$

$$\rho_7 = \frac{\rho_{22}Q - \rho_{12}R}{Q^2 - PR},$$

A complete expansion of Equation 3.20 is described in Appendix A by inserting ρ_i from Equation 3.21 to Equation 3.20.

Accordingly, the eigenvalues for Equation 3.17 in a three-dimensional coordinate system can be obtained by inserting Equation 3.18 to Equation 3.17 as follows.

$$\frac{\partial^2 \phi_i(t)}{\partial x^2} + \frac{\partial^2 \phi_i(t)}{\partial y^2} + \frac{\partial^2 \phi_i(t)}{\partial z^2} \tag{3.22}$$

$$-C_i \frac{\partial^2 \phi_i(t)}{\partial t^2} - D_i \frac{\partial^{\frac{3}{2}} \phi_i(t)}{\partial t^{\frac{3}{2}}} - G_i \frac{\partial \phi_i(t)}{\partial t} = 0, \quad i = 1, 2.$$

Since we deal with one-dimensional wave propagation in a bone-like material in this study, Equation 3.22 can be reduced to

$$\frac{\partial^2 \phi_i(t)}{\partial x^2} - C_i \frac{\partial^2 \phi_i(t)}{\partial t^2} - D_i \frac{\partial^{\frac{3}{2}} \phi_i(t)}{\partial t^{\frac{3}{2}}} - G_i \frac{\partial \phi_i(t)}{\partial t} = 0, \quad i = 1, 2. \tag{3.23}$$

The first two terms in Equation 3.23, $\frac{\partial^2 \phi_i(t)}{\partial x^2} - C_i \frac{\partial^2 \phi_i(t)}{\partial t^2}$, represent the propagation of both fast and slow waves by neglecting the effect of tortuosity. The third term, $D_i \frac{\partial^{3/2} \phi_i(t)}{\partial t^{3/2}}$, contains a fractional derivative term with order of $3/2$. This represents the viscous interaction between the solid skeleton and fluid, which leads to an acoustic attenuation in a bone-like porous medium. The last term in Equation 3.23 describes the acoustic attenuation due to viscosity between fluid and solid by neglecting the effect of tortuosity. It is worth mentioning that the signals containing high frequencies are mostly sensitive to the third term in Equation 3.23 because of the fractional derivative (Fellah et al., 2013). In addition, the last term also has an influence on the acoustic attenuation and shall be considered for those transient signals containing low frequency components (Fellah et al., 2004a).

The eigenvalues for Equation 3.17, $\phi_1(t)$ and $\phi_2(t)$, which correspond to the fast and slow compressional waves, can be related to the scalar compressional potentials for solid skeleton and fluid, $\phi_s(x,t)$ and $\phi_f(x,t)$, using the following matrix form (Fellah et al., 2013),

$$\begin{pmatrix} \phi_s(x,t) \\ \phi_f(x,t) \end{pmatrix} = \begin{pmatrix} I & I \\ \chi_1(t) & \chi_2(t) \end{pmatrix} * \begin{pmatrix} \phi_1(t) \\ \phi_2(t) \end{pmatrix}. \tag{3.24}$$

The eigenvalues corresponding to the fast and slow fractional waves propagating through a bone-like porous medium can be derived by $\phi_1(x,t) = G_1(x,t)$ and $\phi_2(x,t) = G_2(x,t)$. The expressions for $G_1(x,t)$ and $G_2(x,t)$ are provided in Appendix B. Thus, the expressions for $\phi_s(x,t)$ and $\phi_f(x,t)$ can be deduced as follows.

$$\phi_s(x,t) = I * G_1(x,t) + I * G_2(x,t) = G_1(x,t) + G_2(x,t) \tag{3.25a}$$

$$\phi_f(x,t) = \chi_1(t) * G_1(x,t) + \chi_2(t) * G_2(x,t) \tag{3.25b}$$

As mentioned above, the displacements of solid skeleton u_i and fluid U_i can be obtained by $\nabla \phi_s(x,t)$ and $\nabla \phi_f(x,t)$, respectively.

Additionally, the stress tensors for the solid skeleton, σ^s, and fluid, σ^f, can be derived as follows.

$$\sigma^s = ((P-2N)\nabla\mathbf{u}(t) + Q\nabla\mathbf{U}(t)) + N(\nabla\mathbf{u} + \nabla\mathbf{u}^T), \tag{3.26a}$$

$$\sigma^f = -\phi p_f = (R\nabla\mathbf{U}(t) + \nabla\mathbf{u}(t)), \tag{3.26b}$$

where p_f is the fluid pressure. Note that the pressure field and normal stress are continuous in boundaries.

The stress tensors for the solid skeleton and fluid phase in the Laplace domain can be written as

$$\tilde{\sigma}^s(x,s) = (P-2N)\frac{\partial^2 \tilde{\phi}_s(x,s)}{\partial x^2} + Q\frac{\partial^2 \tilde{\phi}_f(x,s)}{\partial x^2} + 2N\frac{\partial^2 \tilde{\phi}_s(x,s)}{\partial x^2},$$
$$\tilde{\sigma}^f(x,s) = R\frac{\partial^2 \tilde{\phi}_f(x,s)}{\partial x^2} + Q\frac{\partial^2 \tilde{\phi}_s(x,s)}{\partial x^2}, \tag{3.27}$$

Also, the strain tensor for the solid skeleton can be obtained for infinitesimal deformation as $\varepsilon = \frac{1}{2}(\nabla u + \nabla u^T)$. A complete extension of strains are brought in Appendix C.

In the next section, the reflection and transmission of incident waves propagating through a bone-like porous medium along with the boundary conditions are derived.

3.2.6 Reflection and Transmission Coefficients

When a normal sound wave in the fluid impinges on a porous medium, one part of the incident wave is reflected back to the fluid while another part of the incident wave is transmitted into the porous medium. Since only the reflection and transmission induced by the normal incident wave are investigated, there will be no shear effect in the medium. Also, the amplitude of the reflection and transmitted waves can be determined based on the boundary conditions.

Figure 3.1 depicts the schematic of the problem's geometry. Three propagating waves such as incident wave, reflected wave, and transmitted waves are shown. In addition, a homogeneous and isotropic elastic porous medium is considered between the span $0 \leq x \leq L$.

By impinging a wave pulse on the left side of the medium, the solid and fluid displacements, u_i and U_i, will be generated, respectively, in the porous medium according to Equation 3.12. As shown in Figure 3.1, the total pressure field at the left side of the medium $x \leq 0$ is the summation of the incident and reflected wave pressures given by

$$P^{left}(x,t) = P^{inc}\left(t - \frac{x}{c_0}\right) + P^{ref}\left(t + \frac{x}{c_0}\right), \tag{3.28}$$

in which P^{inc}, P^{ref}, and P^{left} are the incident wave, reflected wave, and total wave pressures in the left side of the medium $x \leq 0$, respectively. Likewise, the transmitted wave pressure at the right side of the medium is given by

$$P^{right}(x,t) = P^{tr}\left(t - \frac{x-L}{c_0}\right),$$ (3.29)

where P^{tr} stands for the transmitted wave in the right side of the medium $x \geq L$.

The incident and scattered waves can be related to each other by the reflection, $\mathfrak{R}(\tau)$, and transmission, $\mathscr{T}(\tau)$ kernel operators. In fact, the reflected and transmitted waves can be obtained using the integration of the product of the incident wave pressure with their operators represented by

$$P^{ref}(x,t) = \int_0^t \mathfrak{R}(\tau)P^{inc}\left(t - \tau + \frac{x}{c_0}\right)d\tau,$$ (3.30a)

$$P^{tr}(x,t) = \int_0^t \mathscr{T}(\tau)P^{inc}\left(t - \tau - \frac{L}{c} - \frac{x-L}{c_0}\right)d\tau,$$ (3.30b)

The kernel operators depend only on the material properties of the medium and are independent of the input incident wave pressures. The integration in Equation 3.30 is taken over the interval $[0 \quad t]$. The lower limit starts from 0 meaning the incident wave hits the medium at $t = 0$.

In order to solve Equation 3.30, the kernel operators, $\mathfrak{R}(\tau)$ and $\mathscr{T}(\tau)$, must be obtained first. In the next section, these kernels are derived in the Laplace domain and then inverted to the time domain using the inverse Laplace transform.

3.2.7 Reflection and Transmission Coefficients in Laplace Domain

In the left side of the medium, $x \leq 0$, where the incident wave hits the medium, the pressure field can be written

$$P_1(x,t) = \left(\delta\left(t - \frac{x}{c_0}\right) + \mathfrak{R}(t) * \delta\left(t + \frac{x}{c_0}\right)\right) * P^{inc}(t),$$ (3.31)

also, the pressure field in the right side of the medium, $x \geq L$ is given

$$P_3(x,t) = \left(\mathscr{T}(t) * \delta\left(t - \frac{L}{c} - \frac{x-L}{c_0}\right)\right) * P^{inc}(t).$$ (3.32)

The pressure fields can be expressed in the Laplace domain by applying the Laplace transform operator to $P_1(x,t)$ and $P_3(x,t)$. So,

$$\tilde{P}_1(x,s) = \mathscr{L}[P_1(x,t)] = \left(exp\left(-s\frac{x}{c_0}\right) + \tilde{R}(s)exp\left(s\frac{x}{c_0}\right) \right)\tilde{\phi}(s), \tag{3.33a}$$

$$\tilde{P}_3(x,s) = \mathscr{L}[P_3(x,t)] = \tilde{T}(s)exp\left(-\left(\frac{L}{c}+\frac{x-L}{c_0}\right)s\right)\tilde{\phi}(s), \tag{3.33b}$$

in which $\tilde{R}(s)$, $\tilde{T}(s)$ and $\tilde{\phi}(s)$ are the Laplace transform of $\mathfrak{R}(t)$, $\mathscr{T}(t)$ and $P^{inc}(t)$, respectively.

Note that the pressure field and normal stresses at the boundaries of the medium (Wu, Xue, and Adler, 1990) are continuous, so at $x=0$ and $x=L$, we have

$$\sigma^f(0^+,t) = -\phi P_1(0^-,t), \quad \sigma^s(0^+,t) = -(1-\phi)P_1(0^-,t)$$

$$\sigma^f(L^-,t) = -\phi P_3(L^+,t), \quad \sigma^s(L^-,t) = -(1-\phi)P_3(L^+,t) \tag{3.34}$$

Additionally, two more equations are needed to derive the scattering coefficients. There is also a relationship between the acoustic velocities inside and outside of the medium as

$$V_1(0^-,t) = (1-\phi)V_s(0^+,t) + \phi V_f(0^+,t),$$

$$V_3(L^+,t) = (1-\phi)V_s(L^-,t) + \phi V_f(0^+,t), \tag{3.35}$$

where V_1 and V_3 are acoustic velocity fields in $x \le 0$ and $x \ge L$, respectively. They are obtained using the Euler equation and field pressure around the medium given

$$\frac{\partial P_i(x,s)}{\partial x} = \rho_f s V_i(x,s) \quad i=1,3 \tag{3.36}$$

The acoustic velocities in fluid, V_f, and solid, V_s, are obtained by

$$\mathbf{u}(t) = \nabla\phi_s(t) \rightarrow \quad V_s(x,s) = s\left(\frac{\partial\tilde{\phi}_s(s)}{\partial x}\right),$$

$$\mathbf{U}(t) = \nabla\phi_f(t) \rightarrow \quad V_f(x,s) = s\left(\frac{\partial\tilde{\phi}_f(s)}{\partial x}\right). \tag{3.37}$$

Finally, using Equation 3.23 and Equation 3.24 along with the boundary conditions (Equation 3.34 − Equation 3.37), the reflection and transmission coefficients in Laplace domain

can be obtained as follows

$$\tilde{R}(s) = \frac{s^2(\beth_4^2(s) - \beth_3^2(s)) + 1}{(s\beth_3(s) - 1)^2 - s^2\beth_4^2(s)}$$

$$\tilde{T}(s) = \frac{2s(\beth_4(s))}{s^2\beth_4^2(s) - (s\beth_3(s) - 1)^2} \tag{3.38}$$

The expressions for $\beth_4(s)$ and $\beth_3(s)$ along with their temporal expressions of $\beth_4(s)$ and $\beth_3(s)$ are derived next.

3.2.8 Temporal Reflection and Transmission Operators

The expressions for $\tilde{R}(s)$ and $\tilde{T}(s)$ in Equation 3.38 can be decomposed to a simpler form,

$$\tilde{R}(s) = \frac{1}{1 - s\beth_3(s) + s\beth_4(s)} + \frac{1}{1 - s(\beth_3(s) + \beth_4(s))} - 1$$

$$\tilde{T}(s) = -\frac{2s\beth_4(s)}{(s\beth_3(s) - 1)^2 - s^2\beth_4^2(s)} \tag{3.39}$$

in which

$$\beth_3(s) = \beth_1(s)\cosh\left(l\sqrt{\tilde{\lambda}_1(s)}\right) + \beth_2(s)\cosh\left(l\sqrt{\tilde{\lambda}_2(s)}\right) \tag{3.40}$$

$$\beth_4(s) = \beth_1(s) + \beth_2(s)$$

$$\beth_i(s) = (1 + \phi(\tilde{\chi}_i(s) - 1))\left(\sqrt{\tilde{\lambda}_i(s)}\frac{2\rho_f c_0 \tilde{\Psi}_i(s)}{\sinh\left(l\sqrt{\tilde{\lambda}_i(s)}\right)\tilde{\Psi}(s)}\right) \quad i = 1, 2$$

$$\tilde{\chi}_i(s) = A_i + \frac{B_i}{\sqrt{s}} \quad i = 1, 2$$

$$\tilde{\lambda}_i(s) = C_i s^2 + D_i s\sqrt{s} + G_i s \quad i = 1, 2$$

$$\tag{3.41}$$

It is worth mentioning that $\tilde{\chi}_i(s)$ and $\tilde{\lambda}_i(s)$ are in the Laplace transform domain. The expressions for $\tilde{\Psi}_i$ mentioned in Equation 3.41 for $i = 1, 2$ are given by

$$\tilde{\Psi}_1(s) = \phi\tilde{Z}_2(s) - (1 - \phi)\tilde{Z}_4(s)$$

$$\tilde{\Psi}_2(s) = -\phi\tilde{Z}_1(s) + (1 - \phi)\tilde{Z}_3(s)$$

$$\tilde{\Psi}(s) = 2\left(\tilde{Z}_1(s)\tilde{Z}_4(s) - \tilde{Z}_2(s)\tilde{Z}_3(s)\right) \tag{3.42}$$

in which $\tilde{Z}_1(s)$ to $\tilde{Z}_4(s)$ are written

$$\tilde{Z}_1(s) = (P + Q\tilde{\chi}_1(s))\tilde{\lambda}_1(s)$$

$$\tilde{Z}_2(s) = (P + Q\tilde{\chi}_2(s))\tilde{\lambda}_2(s)$$

$$\tilde{Z}_3(s) = (P + R\tilde{\chi}_1(s))\tilde{\lambda}_1(s)$$

$$\tilde{Z}_4(s) = (P + R\tilde{\chi}_2(s))\tilde{\lambda}_2(s) \tag{3.43}$$

Substituting Equation 3.41 to Equation 3.43, the expressions for the reflection and transmission coefficients in the Laplace transform domain can be obtained,

$$\tilde{R}(s) = -\frac{2\tilde{X}(s)\left(\tilde{Y}(s) - 2e^{-2l\sqrt{\tilde{\lambda}_1(s)}}\right) - 4\tilde{Y}(s)e^{-2l\sqrt{\tilde{\lambda}_2(s)}} + \tilde{X}(s)^2 + \tilde{Y}(s)^2 - 1}{\left(\tilde{X}(s) + \tilde{Y}(s) - 1\right)^2},$$

$$\tilde{T}(s) = -\frac{4e^{-l\left(\sqrt{\tilde{\lambda}_1(s)} + \sqrt{\tilde{\lambda}_2(s)}\right)}\left(\tilde{X}(s)e^{l\sqrt{\tilde{\lambda}_2(s)}} + \tilde{Y}(s)e^{l\sqrt{\tilde{\lambda}_1(s)}}\right)}{\left(\tilde{X}(s) + \tilde{Y}(s) - 1\right)^2}, \tag{3.44}$$

where

$$\tilde{X}(s) = \frac{\tilde{\Psi}_1(s)}{\tilde{\Psi}(s)}2sc_0\rho_f\sqrt{\tilde{\lambda}_1(s)}\left(\phi\left(\tilde{\chi}_1(s) - 1\right) + 1\right),$$

$$\tilde{Y}(s) = \frac{\tilde{\Psi}_2(s)}{\tilde{\Psi}(s)}2sc_0\rho_f\sqrt{\tilde{\lambda}_2(s)}\left(\phi\left(\tilde{\chi}_2(s) - 1\right) + 1\right) \tag{3.45}$$

in which the expressions for $\frac{\tilde{\Psi}_1(s)}{\tilde{\Psi}(s)}$ and $\frac{\tilde{\Psi}_2(s)}{\tilde{\Psi}(s)}$ are

$$\frac{\tilde{\Psi}_1(s)}{\tilde{\Psi}(s)} = \frac{\phi(P+Q) + \tilde{\chi}_2(s)\left(\phi(Q+R) - R\right) - Q}{\tilde{\lambda}_1(s)\,2\left(Q^2 - PR\right)\left(\tilde{\chi}_1(s) - \tilde{\chi}_2(s)\right)},$$

$$\frac{\tilde{\Psi}_2(s)}{\tilde{\Psi}(s)} = \frac{\phi(P+Q) + \tilde{\chi}_1(s)(\phi(Q+R) - R) - Q}{\tilde{\lambda}_2(s)\,2\left(Q^2 - PR\right)\left(\tilde{\chi}_2(s) - \tilde{\chi}_1(s)\right)}, \tag{3.46}$$

The explicit forms for $\tilde{X}(s)$ and $\tilde{Y}(s)$ are provided in Appendix C.

The Durbin method for the numerical inversion of Laplace transform is applied to derive the transmission and reflection coefficients in the time domain (Durbin, 1974; Fan, Li, and Yu, 2005) for the time span of $[0, 2T_0]$ (Hasheminejad and Mousavi-Akbarzadeh, 2013), as

follows.

$$\Lambda(t) = \frac{2e^{\mu t}}{T_0} \left[\frac{1}{2} Re(\bar{\Lambda}(\mu)) + \sum_{k=1}^{\hat{N}} Re(\bar{\Lambda}(\mu + ik\frac{2\pi}{T_0})) \right.$$
$$\left. \cos\left(kt\frac{2\pi}{T_0}\right) - Im(\bar{\Lambda}(\mu + ik\frac{2\pi}{T_0})) \sin\left(kt\frac{2\pi}{T_0}\right) \right], \tag{3.47}$$

in which μ is a real number and is greater than all of the singularities of $\bar{\Lambda}(s)$. One may choose $\hat{N} = 4000$, $\mu T_0 = 7$ and $T_0 = 2t_{max} = 1$, when t_{max} is the maximum calculation time (Hasheminejad and Alaei-Varnosfaderani, 2012).

The computations were performed using a desktop computer including Intel(R) Xeon(R) with *CPU E*5-2630 at frequency 2.4*GHz*. Using a general MATLAB code, the numerical solutions were obtained in a trial error manner. In fact, the number of modes increased and looked for the stability in the numerical values of the computed solutions. In addition, the computing was accelerated due to MATLAB parallel Toolbox and multicore processors.

3.3 Validation

To show the robustness and validity of the analytical development, the theoretical results are compared with the experimental data provided by (Fellah et al., 2013). The first step is to find an analytical time domain function that matches the time history of the experimental incident signal. For this purpose, MATLAB$^{\circledR}$ Curve Fitting Toolbox$^{\text{TM}}$ 3.5.5 has been used to perform a curve fitting on the experimental incident signal. In order to increase the accuracy of the fitted function, a piecewise function was implemented. A fitted function can be given in a sequence of intervals as

$$f(t) = \begin{cases} 0 & 0 \leq t < t_1 \\ g(t) & t_1 \leq t < t_2 \\ h(t) & t_2 \leq t < t_3 \\ 0 & t_2 \leq t < t_3 \end{cases} \tag{3.48}$$

in which $t_1 = 93.00\,\mu s$, $t_2 = 97.21\,\mu s$ and $t_3 = 103.85\,\mu s$. Furthermore, the functions $g(t)$ and $h(t)$ can be written as

$$g(t) = \sum_{i=1}^{8} a_i \sin(b_i t + c_i) \tag{3.49a}$$

Coeff.	1	2	3	4	5	6	7	8
a	0.143	0.521	0.065	0.907	0.679	-0.830	0.099	0.103
b	4713386	5894250	154833	12257416	7345705	12255557	9117472	14119574
c	-11.727	15.178	60.377	-10.953	21.685	-155.249	-2.269	-43.706

TABLE 3.1: Coefficients in the fitted function $f(t)$.

Coefficient	1	2	3	4
d	0.114	0.695	0.606	0.017
e	6068996	6389826	6459584	292003
f	-133.011	-68.279	15.720	19.111

TABLE 3.2: Coefficients in the fitted function $g(t)$.

$$h(t) = \sum_{i=1}^{4} d_i \, sin \left(e_i t + f_i \right) \tag{3.49b}$$

where the coefficients of function $g(t)$ such as $a_i, b_i, c_i,$ and $h(t)$ including d_i, e_i and f_i are provided in Table 3.1 and Table 3.2, respectively. Figure 3.2 illustrates the comparison between the experimental signal and the analytical incident signals $f(t)$.
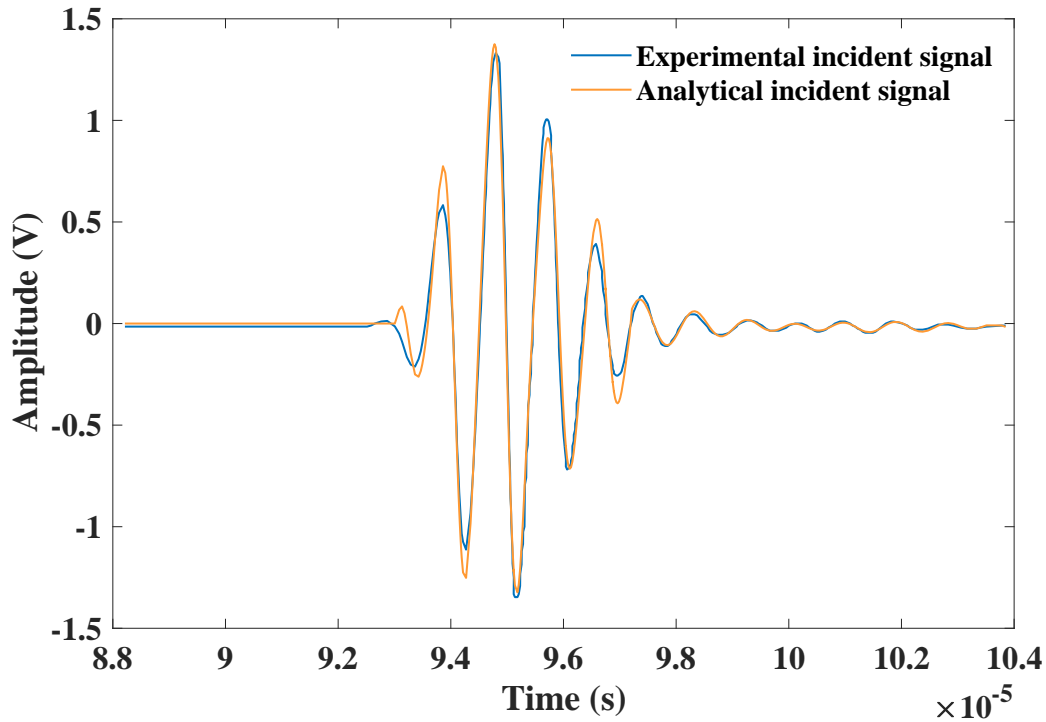
FIGURE 3.2: Comparison between the analytical and experimental incident plane wave signals.

Equation 3.30 can be written in the convolution form ($*$) as follows.

$$P^{tr}(x,t) = \mathcal{T}(\tau) * P^{inc}(t) * \delta \left(t - \frac{L}{c} - \frac{(x-L)}{c_0} \right) \tag{3.50}$$

By taking the Laplace transform, Equation 3.50 can be written

$$\tilde{P}^{tr}(x,s) = \tilde{T}(s)exp\left(-\left(\frac{L}{c} + \frac{x-L}{c_0}\right)s\right)\tilde{P}^{inc}(s) \tag{3.51}$$

in which $\tilde{P}^{inc}(s)$ can be replaced by $\mathscr{L}[f(t)] = \tilde{F}(s)$. So,

$$\tilde{F}(s) = \mathscr{L}[f(t)] \equiv \int_{t_1}^{t_2} g(t)e^{-st}\,dt + \int_{t_2}^{t_3} h(t)e^{-st}\,dt \rightarrow$$

$$\tilde{F}(s) \equiv \sum_{i=1}^{8}\left\{-\left.\frac{a_ie^{-st}\left(s\sin\left(tb_i+c_i\right)+b_i\cos\left(tb_i+c_i\right)\right)}{b_i^2+s^2}\right|_{t=t_1}^{t=t_2}\right\}+$$

$$\sum_{i=1}^{4}\left\{-\left.\frac{d_ie^{-st}\left(s\sin\left(te_i+f_i\right)+e_i\cos\left(te_i+f_i\right)\right)}{e_i^2+s^2}\right|_{t=t_1}^{t=t_2}\right\} \tag{3.52}$$

Finally, $\tilde{P}^{tr}(x,s)$ is derived as a function of x and s. Similarly, $P^{tr}(x,t)$ will be found using Durbin's numerical inversion. Figure 3.3 illustrates a comparison between $P^{tr}(x,t)$ derived in this study and experimental incident signal provided by (Fellah et al., 2013).
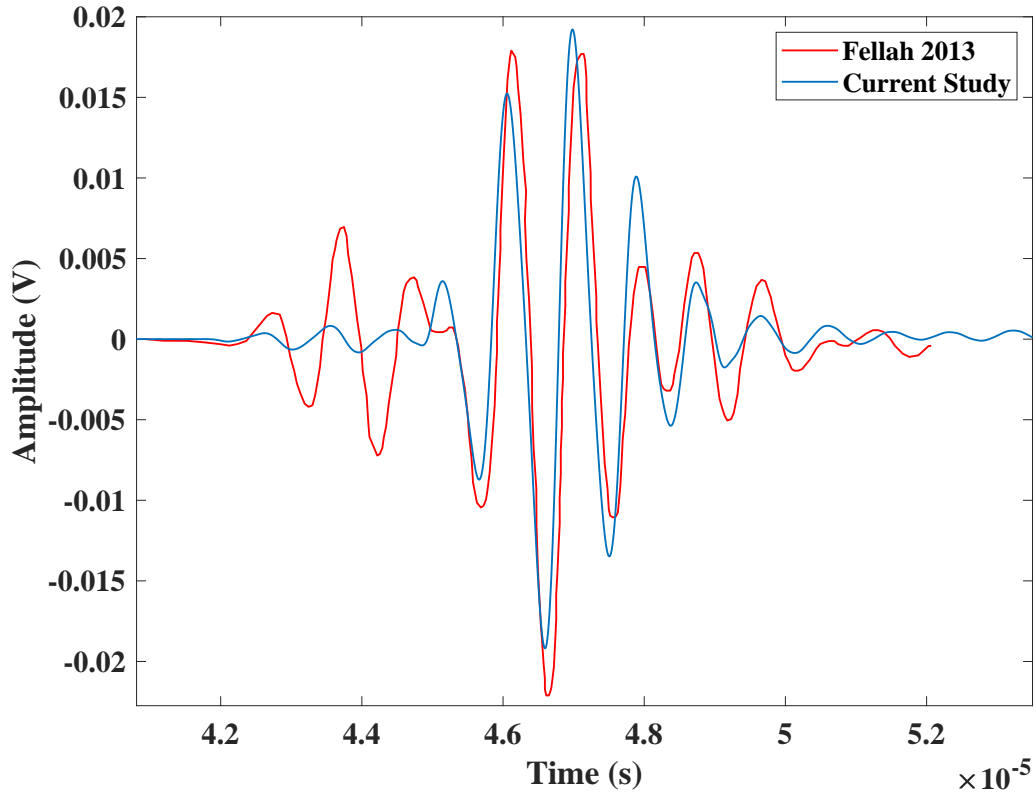
FIGURE 3.3: Comparison between the current study and the experimental transmitted signal provided by (Fellah et al., 2013)

3.4   Results and Discussion

In this section, the effect of viscosity and porosity on the stress, and reflected and transmitted pressures in bone-like porous materials is investigated. The stresses and acoustic pressures at the center of the medium $x = \frac{L}{2}$ are measured for air and bone marrow as pore fluids, which have distinct acoustical properties. In this research, the following characteristics are used for the bone specimen. The thickness $0.7cm$, dynamic tortuosity $\alpha_\infty = 1.06$, viscous characteristic length $\lambda = 240.8 \times 10^{-6}$ μm, solid density $\rho_s = 1960\frac{kg}{m^3}$, bulk modulus of pore fluid $k_f = 2.28GPa$, bulk modulus of elastic solid $k_s = 20GPa$, bulk modulus of the bone skeletal frame $k_b = 3.3$ GPa, shear modulus of the frame $N = 2.6GPa$, fluid viscosity for air $\eta = 1.81 \times 10^{-5}$, air density $\rho_f = 1.225\frac{kg}{m^3}$, air bulk modulus, $K_f = 101000$, bone marrow density $\rho_f = 1.225$, bone marrow viscosity $\eta = 0.0018$, bone marrow modulus $K_f = 2.28 \times 10^9$ GPa, Poisson ratio of the bone skeletal frame $\nu_b = 0.2$, Poisson ratio of the elastic solid $\nu_s = 0.37$. All information regarding the bone specimen are taken from (Fellah et al., 2013; Buchanan and Gilbert, 2007).

Figure 3.4 shows the time history of the stress induced in a bone-like porous material filled with air subjected to the incident signal $f(t)$ for $\phi = 0.6$ and $\phi = 0.9$. As shown, by increasing the porosity, the stress amplitude in a porous medium filled with air increases. This can be due to a decreased surface area when the porosity increases in a representative elementary volume. Because of a very low viscosity of air, no attenuation of wave can be seen in the bone's response in Figure 3.4.
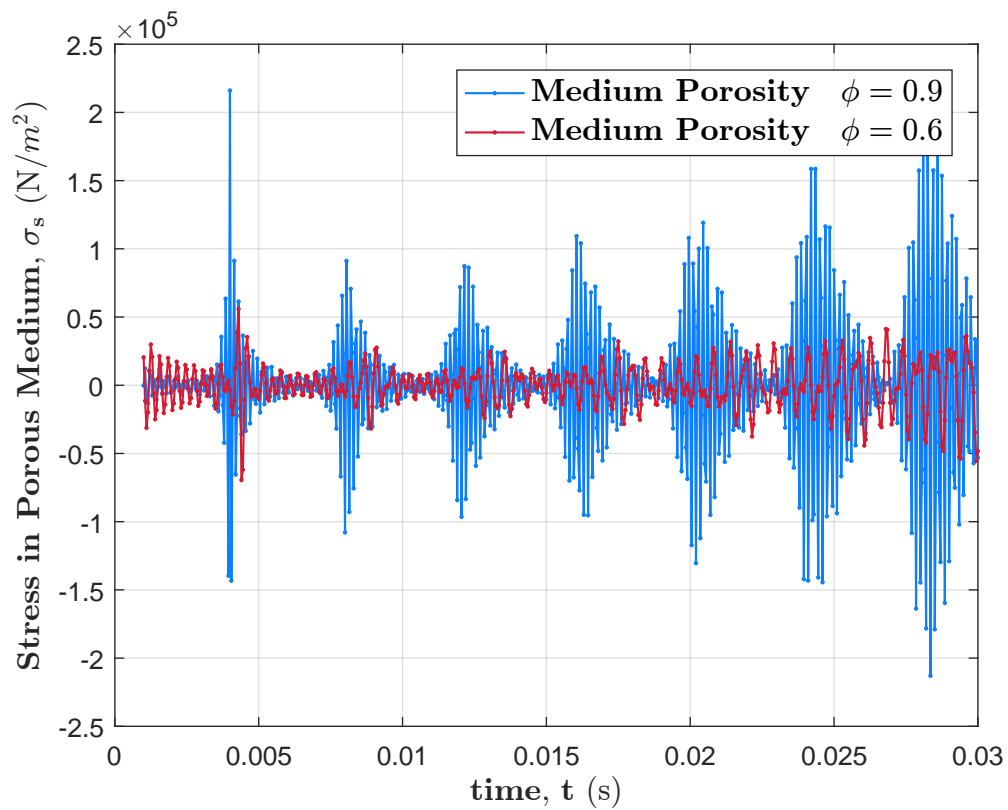
FIGURE 3.4: The effect of porosity on the stress in a bone-like porous medium filled with air

To study the effect of fluid viscosity on the wave attenuation, it is assumed that the bone-like porous medium is filled with bone marrow. The stress amplitude with respect to time for the porosities of 0.1, 0.7, and 0.9 is illustrated in Figure 3.5. As shown, by increasing the porosity the stress amplitude decreases. It can be concluded that even though an increase in porosity reduces the effective surface area and consequently increases the stress amplitude, the wave attenuation due to the fluid viscosity decreases the stress amplitude in a bone-like porous medium filled with bone marrow.
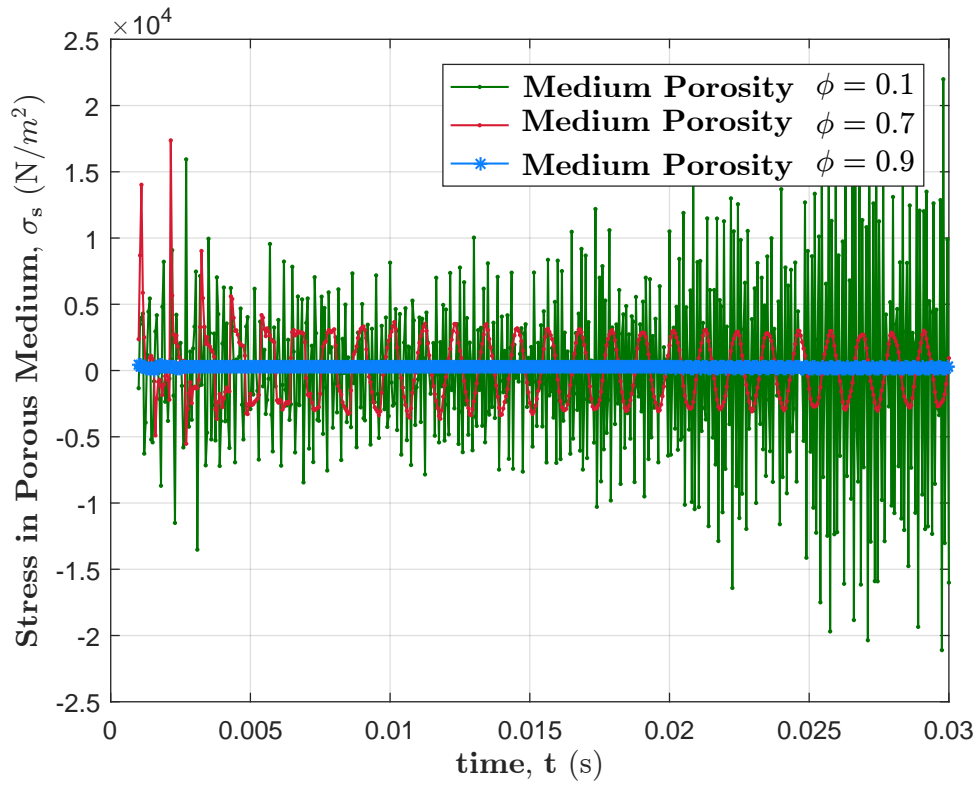
FIGURE 3.5: The effect of porosity on the stress in a bone-like porous medium filled with bone marrow

Figure 3.6 illustrates the time history of the transmitted acoustical pressure at the center of the medium subjected to an incident signal for $\phi = 0.3$, 0.6, and 0.9. As depicted, the transmitted pressure amplitude reduces by increasing the porosity. In fact, the bulk of solid, which is an important means to transfer the wave, is much more when the porosity is lower. In the other words, for a constant volume, an increase in porosity reduces the bulk of the solid part which can lead to a less transmission. Namely, it can be described that the speed of transmitted waves decreases by an increase in porosity leading to a decrease in transmission.
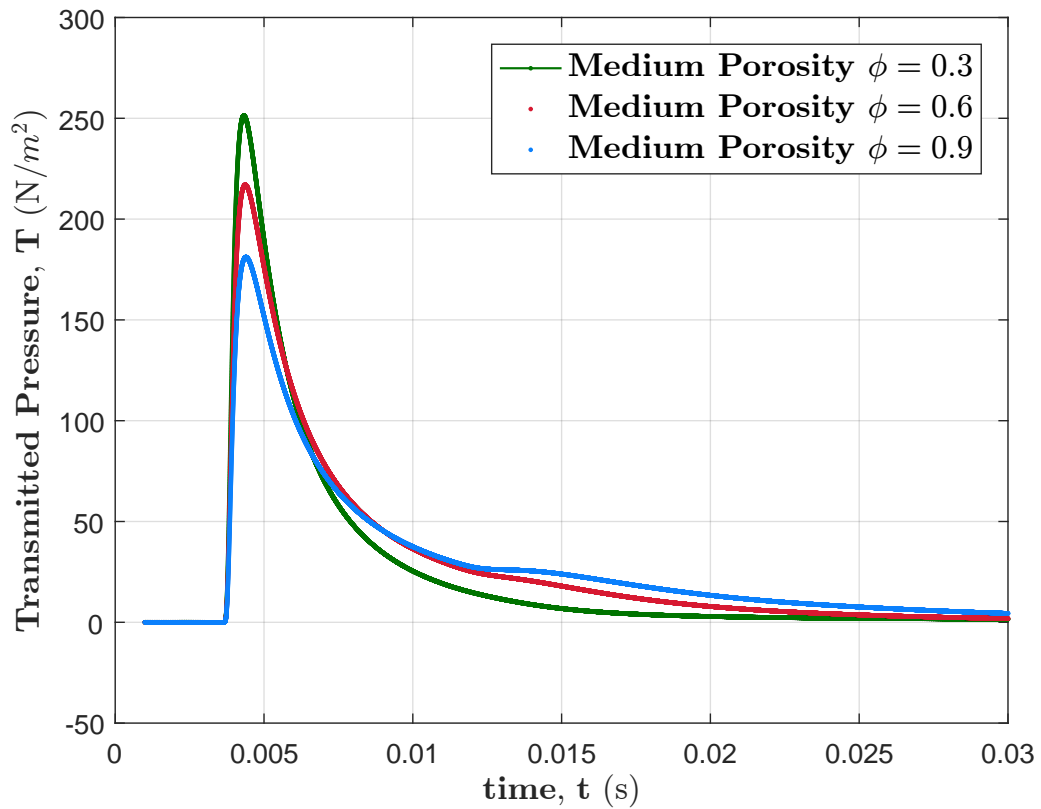
FIGURE 3.6: Transmitted pressure at the center of a bone-like porous medium filled with air

The reflected pressure is also influenced by the porosity of the medium. Figure 3.7 depicts the time history of the reflected pressure at the center of the porous medium filled with air for $\phi = 0.3$, 0.6, and 0.9. As illustrated, the amplitude of the reflected pressure increases by increasing the porosity when the medium is filled with air. In fact, the solid part of the medium decreases by increasing the porosity, so the transmission decreases and reflection increases. Bear in mind that the pore fluid in Figure 3.7 is air with a negligible attenuation effect on wave propagation.
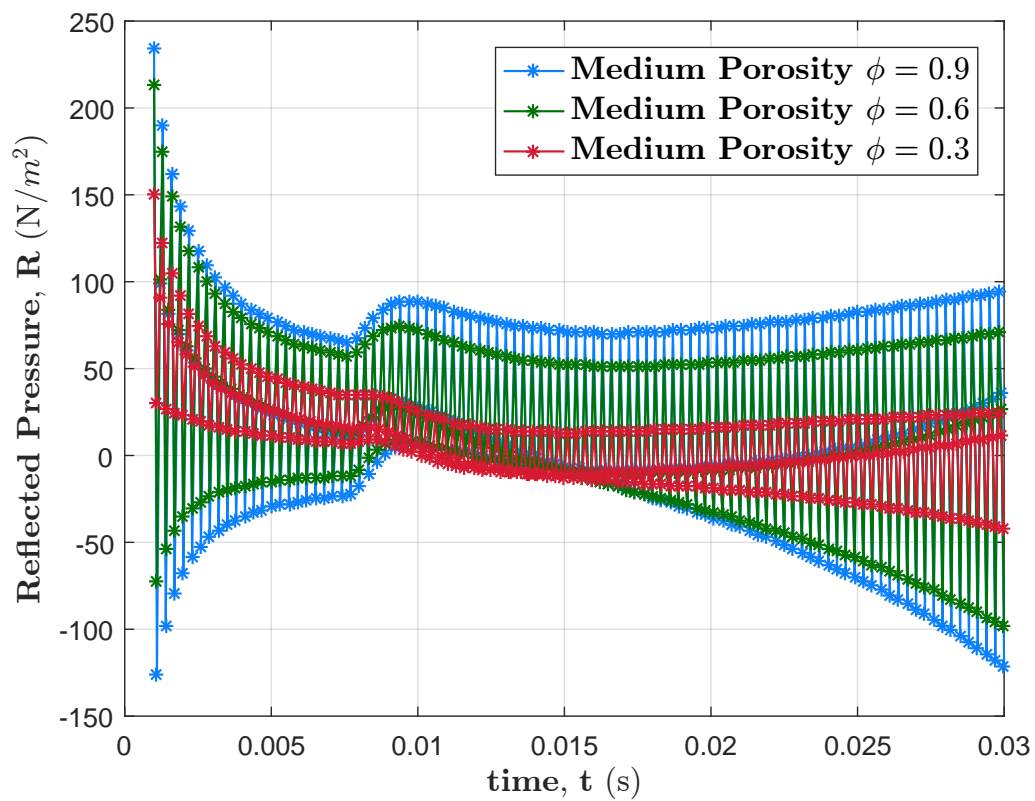
FIGURE 3.7: Reflected pressure at the center of the porous medium filled
with air

To study the effect of pore fluid viscosity on reflected and transmitted pressures, it is assumed that the bone-like porous medium is filled with bone marrow. Figure 3.8 shows the transmitted pressure in a porous medium filled with bone marrow for $\phi = 0.3$, 0.6, and 0.9. As illustrated, the transmitted pressure amplitude decreases by increasing the porosity. As mentioned above, by increasing the porosity in a representative elementary volume less solid medium will be available for the transmitted wave propagation.
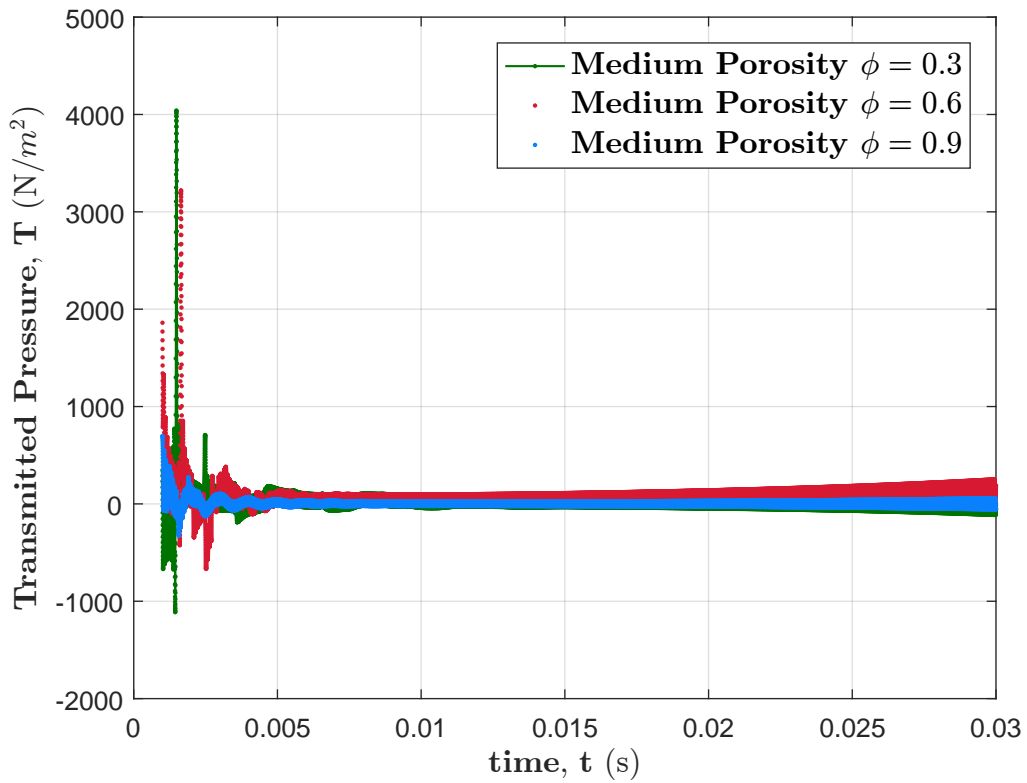
FIGURE 3.8: Transmitted pressure at the center of a bone-like porous medium filled with bone marrow

To study the effect of pore fluid viscosity, in addition to the effect of porosity on the transmitted pressure, it is assumed that the porous space in the medium is filled with bone marrow having a higher viscosity in comparison to air (Figure 3.9).

Regarding Figure 3.8 and Figure 3.6, The behaviour of transmitted pressure for the medium filled with bone marrow is almost identical to that of filled with air. That means by increasing the porosity the transmitted pressure decreases. But the attenuation of transmitted pressure in air is less than that of bone marrow. Additionally, Figure 3.7 and Figure 3.9 express that the reflected pressure for the medium filled with bone marrow decreases by increasing porosity. It is because a part of the wave is damped due to the higher viscosity of bone marrow with respect to air.

3.5 Conclusions

The transient wave propagation in bone-like porous media with an elastic structure is presented based on the Biot-JKD theory. The fractional derivatives are used to describe the viscous behavior of solid and fluid interaction. Two fast and one slow waves as a solution of Biot's equations are derived. The reflected and transmitted scattering operators in the time
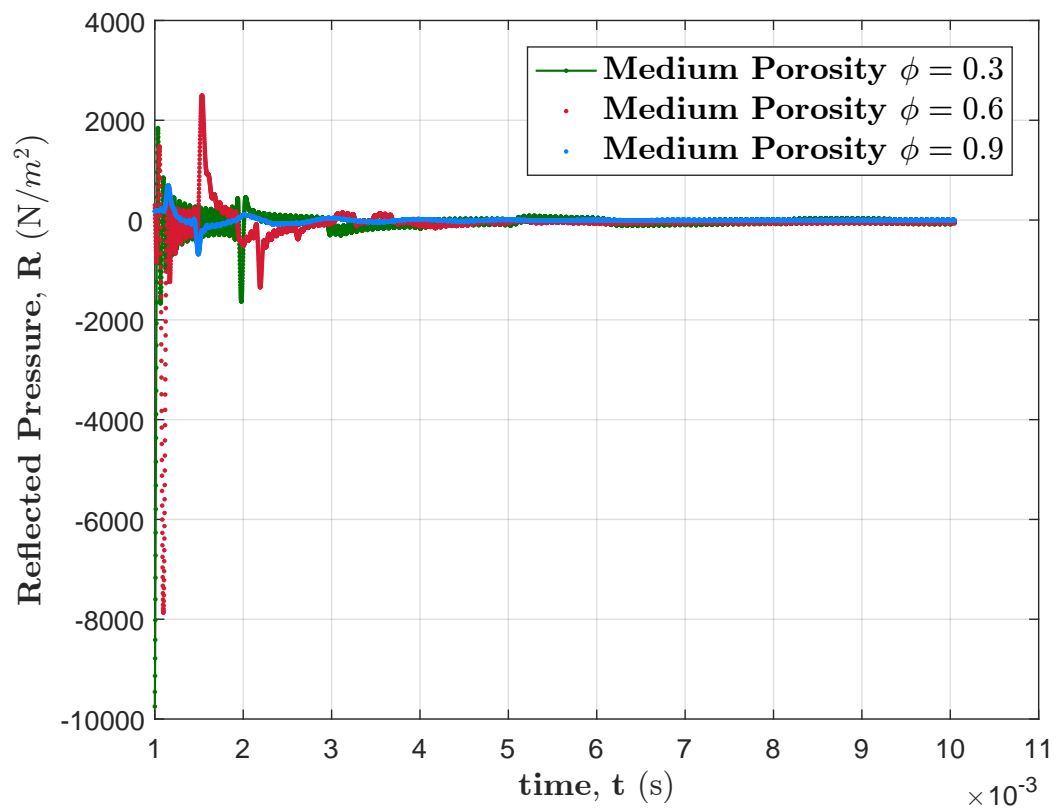
FIGURE 3.9: Reflected pressure at the center of a porous medium filled with bone marrow

domain are derived using Durbin's numerical inversion for porous materials. The theoretical solution is in good agreement compared with experimental results for waves propagating through a bone-like porous medium. It is shown that the stress in a cancellous bone is sensitive to the porosity of the medium as well as the viscosity of the pore fluid. A higher porosity makes more stresses in the medium due to a decrease in the surface area while the viscosity of the pore fluid decreases stresses due to the attenuation of wave propagation. That means that the response of an incident wave hitting a porous medium filled with air is different from that filled with bone marrow. Similarly, the reflected and transmitted pressures in the porous medium are influenced by porosity and viscosity. For a medium filled with a viscous fluid, the transmitted pressure decreases by increasing the porosity. Also the reflected pressure decreases for low viscous fluid while it increases when the pores are filled with a fluid having a higher viscosity.

Chapter 4

An Overview of the Acoustic Studies of Bone-like Porous Materials, and the Effect of Transverse Acoustic Waves

Abstract

The effects of transverse acoustic waves in characterizing a bone-like, porous medium filled with a viscous fluid are analyzed for the first time. Scattering operators along with stress fields are derived by using the standard Biot-JKD model. A short duration acoustical pulse is applied to one side of a bone-like, porous medium so that both longitudinal and transverse waves travel through the intermediate medium which is filled with a viscous fluid. The reflection and transmission operators along with stresses in the medium are expressed in terms of these waves. The numerical implementation is validated for the longitudinal wave by comparison with the numerical simulation performed by (Fellah et al., 2004a). The effects of the transverse waves on the reflection and transmission coefficients as well as the stress field are studied by considering different viscosities and porosities. It is shown that when the fluid viscosity in the medium is relatively high (such as bone marrow), the effect of the transverse wave dominates. However, this effect is negligible when the medium is filled with a relatively low viscous fluid (such as air). Furthermore, it is shown that the role of transverse waves in characterizing bone structures and bone loss is imperative since the acoustical response of such media at specific frequencies can be triggered only by considering the effects of transverse waves.

4.1 Introduction

Osteoporosis is recognized as a *silent epidemic* that reduces a bone's tissue and mass which increases its fragility (Osterhoff et al., 2016). Several studies contend that the fragility and

risk of a fracture in bone increases two or three times by decreasing the bone mineral density (Stegman et al., 1992; Hui, Slemenda, and Johnston, 1989; Cummings et al., 1993). While there is extensive relationship between bone mass and fracture, some other factors can participate in fracture risk such as age and past fractures which are independent of bone mass (Smith, Khairi, and Johnston, 1975; Krolner and Nielsen, 1982; Bohr and Schaadt, 1983). With regards to the dependent and independent factors contributing to fracture risks in bones, bone quality is defined as a property of bone which reflects a bone structure (Ross et al., 1991; Hui, Slemenda, and Johnston, 1988).

The structure of the bone is porous and spongy. It consists of a solid skeleton and pores which are filled with a viscous bone marrow. More precisely, the main formation of the bone structure is composed of a compact layer, which is a dense bone tissue found on the outside of a bone, and a spongy layer (cancellous bone) inside the bone structure, which is filled with marrow. This particular property of bone including dense part, spongy part, and fluid part makes it a unique tissue. One of the most important quantities in characterizing the bone structure in a diagnosis of osteoporosis is its porosity, which varies between 5 to 95 percent. Bone porosity varies not only in different bones, but also in the same bone. Consequently, any realistic model must consider the variation in porous properties of bone structure for reliable assessment of bone fracture risk under normal conditions.

There is an increasing need to improve the osteoporosis diagnosis and management. In fact, early stage diagnosis is essential if important preventive measures are to be taken. Among the many early osteoporosis detection methods available, Quantitative Ultrasound (QUS) may have many advantages over other electromagnetic methods such as dual X-ray. It can be small, which makes a portable unit a viable option. Further, it is relatively cheap compared to a similar electromagnetic wave-based tools, is a non-invasive technique, and does not employ harmful ionizing radiation.

Using ultrasound to image solid objects like bone, typically results in the generation of two types of waves that can be measured and represent the raw imaging data. Longitudinal waves are those that follow the contours of the object's surface, while transverse waves travel through a solid object. The mechanical properties of bone such as modulus of elasticity, density, porosity, and the viscosity of fluid inside the bone would be important in osteoporosis detection using ultrasound techniques since such factors affect the acoustic wave propagation in the medium.

Several studies have been conducted in the literature to measure the elastic characteristics of cancellous and trabecular bones (Ashman, Corin, and Turner, 1987; Ashman and Rho,

1988; Yousefian et al., 2018; Langton, Palmer, and Porter, 1984). It is worth mentioning that the study of wave propagation in a cancellous bone is a very complex task due to the inhomogeneous nature of its structure.

One of the most prominent theories to study the wave propagation in porous materials saturated with a fluid is the theory of Biot originally developed in the 1950s-1960s (Biot, 1956d; Biot, 1941; Biot, 1955; Biot, 1956b; Biot, 1962b). According to the theory of Biot, two longitudinal waves appear in a porous medium subjected to an external solicitation. The first longitudinal wave, called *fast* wave, is relevant to in-phase motion of solid skeleton while the second longitudinal wave, called *slow* wave, is related to the out-phase motions of solid skeleton and pore fluid.

This theory has been widely used in oil and gas applications and geo-science testings. The Biot's theory has been also applied to model the bone structure in several studies. For example, (Lauriks et al., 1994) investigated the ultrasonic transmission pulses in bovine trabecular bones using Biot's theory. In this study, they measured the different parameters involved in the Biot theory and made several simplified assumptions in their model. They observed a satisfactory agreement between the theory and their experimental data obtained on water-filled bone samples. (McKelvie and Palmer, 1991) explained the ultrasonic attenuation frequency dependence of cancellous bones using Biot's theory. Similarly, they made several assumptions and insufficiently defined the Biot parameters for cancellous bone to allow a complete test of the model. They concluded that even though the qualitative trend between the theory and measurements is in good agreement, the quantitative results are significantly deviant due to imprecise parameters used in the model.

The wave propagation in human and bovine bones has been experimentally studied, which validate the presence of the second longitudinal wave in such media. For instance, (Lakes, Yoon, and Katz, 1983) studied the ultrasonic wave propagation in wet human and bovine cortical bones and observed a new longitudinal waves. The speed of new longitudinal waves was lower than ordinary longitudinal waves. They mentioned that the slow wave is associated with the fluid motion in the bone pores. Furthermore, these two waves were determined independently in bovine cancellous bone (Hosokawa and Otani, 1997; Hosokawa and Otani, 1998). (Cardoso et al., 2003) studied the wave propagation in cancellous bone for material characterization. They demonstrated a correlation between velocities of fast and slow waves with the porosity. They also mentioned that the presence of two waves is mandatory to obtain the accurate results and failure in accounting any of them may lead to inaccurate qualification of bone properties.

In these studies, two important phenomena when a wave propagates through the porous media were neglected: first, the effect of transverse waves were not considered; second, the viscous exchange between the pore fluid and solid skeletal frame is ignored.

Considering the complex bone structure, the interaction between marrow and solid skeleton of a bone subjected to an acoustic incident can lead to a complex solution. In fact, to model accurately the wave propagation in a porous medium filled with a viscous fluid, such considerations are of paramount importance.

The original Biot's theory was modified by (Johnson, Koplik, and Dashen, 1987) in the late 1980s to address one of the limitations of Biot's theory related to the viscous dissipation in porous media filled with viscous fluids. This is of significant importance when it is aimed to model the energy dissipation in the medium at different frequency ranges. The modified theory, called Biot-JKD, introduces the concept of dynamic tortuosity, viscous characteristic length, and dynamic permeability to describe the viscous dissipation occurring in the pores. The wave propagation in trabecular and cancellous bones, as a porous medium saturated with a viscous fluid, using the Biot-JKD theory has been studied in the literature (for example, see (Fellah et al., 2004a; Hughes et al., 2007; Marutyan, Holland, and Miller, 2006; Sebaa et al., 2006b; Pakula et al., 2008; Mizuno et al., 2009)). These studies focus mainly on the effect of bone anisartopy, tortuasity, as well as viscous exchange between pore fluid and soid skeletal frame on wave propagation in bones. However, the effect of transverse waves was not considered in the above-mentioned studies.

It is worth mentioning that in original Biot's theory, the wavelength is assumed to be larger than the macroscopic geometry of medium to neglect the scattering effect. But when the dimensions of pores in a cancellous bone is close to wavelength, the scattering effect should be taken into account (Wear, 1999; Chaffaı et al., 2000; Luppé, Conoir, and Franklin, 2002). Considering the scattering effect is of paramount importance since it is assumed that any change in bone characteristic due to bone loss or osteoporosis can be determined by the speed of wave and its attenuation. For example, (Bennamane and Boutkedjirt, 2017) proposed a theoretical approach combining both absorption and scattering to study ultrasonic attenuation in bovine cancellous bone samples filled with water based on Biot's analytical model. They concluded that the predominant mechanism for attenuation in trabecular bone is scattering. (Buchanan, Gilbert, and Ou, 2012) insonified the cancellous bone immersed in water by an acoustic pulse and studied the reflection and transmission of both fast and slow waves. Furthermore, they proposed a series of transfer functions for the reflection and transmission of fast and slow waves propagating in poro-elastic medium filled with a fluid

based on the Biot-JKD model.

Several studies concerning the reflection and transmission of acoustic waves in both time and frequency domain have been performed for different media (Caviglia and Morro, 2004; Szabo, 1994; Norton and Novarini, 2003; Waters et al., 2000). (Fellah et al., 2004a) studied the effect of ultrasonic waves on reflection and transmission coefficients in human cancellous bone at high frequency ranges based on the Biot-JKD theoery. They used a slab immersed in water to model a bone. Similar to previous works, they only investigated the effect of longitudinal wave propagating in porous media and neglected the effect of transverse waves in their model . They considered the effect of porosity, density, shear modulus and viscosity on their scattering coefficients, describing the importance of these parameters in the fast and slow waves. (Fellah et al., 2013) developed a temporal model to describe wave propagation in porous media saturated with fluid using the Biot-JKD theory by applying dynamic tortuosity and fractional calculus to describe the viscous exchange between pore fluid and solid skeletal frame. They also did not apply the effect of transverse wave in their model and only investigated the effect of longitudinal waves in solid and fluid phases. They used Green's function for fast and slow waves and compared them with their experimental work. Their theoretical results showed a good agreement with experimental results. (Hodaei, Rabbani, and Maghoul, 2020) presented an analytical transient acoustical model using JKD-Biot's theory for a bone-like porous medium saturated with viscous fluid. The fractional calculus is used to describe the viscous exchange between the solid and fluid interaction. Their analytical model showed a good agreement with the experimental data. They considered the effect of porosity and viscosity on scattering operators along with stresses. Their results expressed that the stresses in the porous medium is so sensitive to the medium's porosity and pore fluid's viscosity. In addition, the porosity and viscosity have a significant influence on the scattering operators.

Briefly, in above-mentioned studies to consider scattering effects, either the effect of transverse wave was neglected or the dynamic tortuosity was assumed constant. Additionally, for those studies in time domain, which assume the dynamic tortuosity as a function of frequency, it is needed to use the fractional calculus leading to higher computational efforts. Consequently, it is preferred to solve the scattering equations using the Biot-JKD theory in frequency domain to reduce calculation time and computational effort.

In this chapter, we aim to study the effect of transverse acoustic waves, in addition to longitudinal waves, on the response of a bone-like porous material filled with a viscous fluid. The reflection and transmission operators as well as stresses are expressed, for the first time, by including the effect of transverse acoustic waves for different porosity and viscosity in

frequency domain. The problem is solved in frequency domain because considering the effect of both transverse acoustic waves and dynamic tortuosity as a function of frequency needs a lower computational effort. This inclusion may be of great importance in predicting any change in bone structure due to osteoporosis or bone loss.

The structure of this chapter is outlined as follows. The first section is related to mathematical formulations of wave propagation in a bone-like material saturated with a viscous fluid in frequency domain based on the Biot-JKD theory of poroelasticity (Johnson, Koplik, and Dashen, 1987). Then, the eigenvalues for governing equations are derived. These eigenvalues are selected as fast and slow waves in the bone-like material. The boundary conditions at both sides of the medium, at $x = 0$ and $x = L$ respectively, are described by pressure field, acoustic velocity field, fluid and solid stresses. The analytical results are then verified in comparison with the experimental data found in the literature. Next, the conclusion is drawn. Finally, the appendices relevant to the mathematical formulation are presented.

4.2 Mathematical Developments

In this section, a general configuration of the problem is defined first. Then, conventions and common assumptions are given. The governing equations for both longitudinal and transverse waves propagating in a bone-like porous material saturated with a viscous fluid are presented. The effect of transverse waves on the scattering operators in frequency domain is considered. Then, the fast waves and slow waves are explicitly described. Finally, the explicit forms for the stress fields in the medium are presented.

4.2.1 Problem Definition

A segment of a bone-like material representing a human femoral bone, as illustrated in Figure 4.1, is analytically studied. The domain is composed of poroelastic medium filled with a viscous fluid. Different types of material properties are assigned to each phase. It is assumed that the two dimensions of the geometry in Y and Z directions have an infinite length. This isotropic-homogeneous porous medium is located in the region of $0 \leq x \leq L$. The wave propagates in the XZ plane and along the X-axis. The incident wave as well as its scatterings are shown in Figure 4.1.

An incident wave hits perpendicularly the left limit of the medium. This causes the propagation of waves through the medium. While it is expected to have only longitudinal wave in the medium due to the normal direction of the incident wave, the transverse wave also

appears due to the viscous interaction between the pore fluid and solid within the medium. The constitutive equations are described next.
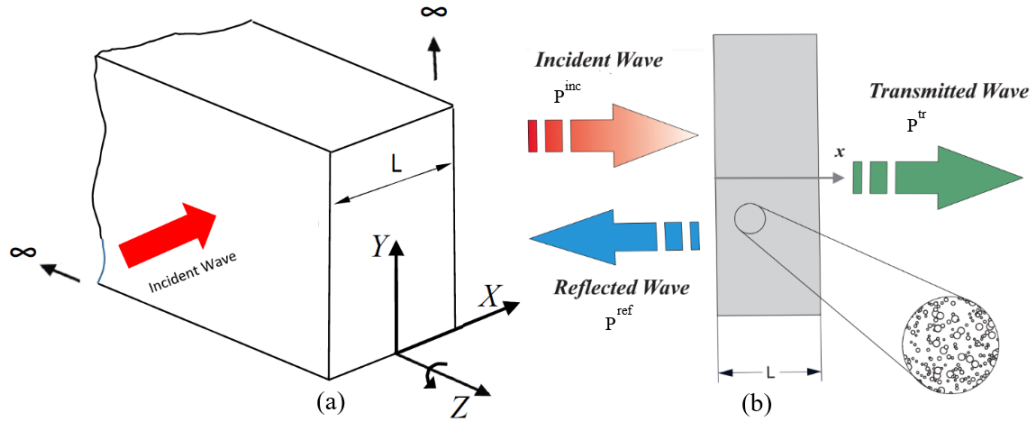
FIGURE 4.1: Showing (a) schematic of the problem's geometry, and (b) the cancellous part of the bone

4.2.2 Conventions and Common Assumptions

In this study, the current state variables are the average macroscopic displacement of the solid skeletal frame, u_i, and the pore fluid, U_i. Number of assumptions and conventions are used as follows.

- The bone-like porous medium consists of the superposition of a continuum body consisting of a deformable skeleton, s, and a porous space filled with a fluid, f.

- The poroelastic medium of the skeleton is homogeneous, isotropic and linear.

- The deformation gradient of the solid skeleton $\mathbf{F}$ is defined by $\mathbf{F} = \mathbf{I} + \nabla \mathbf{u}$, in which $\mathbf{I}$ is the second-order isotropic tensor with component δ_{ij}, where δ_{ij} is the Kronecker delta. The symbol $\nabla = (\partial/\partial \mathbf{x})$ always stands for gradients with respect to $\mathbf{x} = \mathbf{x}(\mathbf{X}, t)$, which is the Eulerian position vector at time t in a Cartesian coordinate frame of an orthonormal basis. Also, $\mathbf{u}$ is the displacement vector of the skeleton whose initial and current positions are $\mathbf{X}$ and $\mathbf{x}$ ($\mathbf{u} = \mathbf{x} - \mathbf{X}$).

- The linearized form of the Green-Lagrange strain tensor, ε, for infinitesimal deformation is $\varepsilon = \frac{1}{2}\left(\partial \mathbf{u}^T + \partial \mathbf{u}\right)$. The skeleton's volume dilatation ε_{ii} is required to match the variations of connected pore spaces (or porosity) ϕ because of the incompressibility of solid particles.

4.3 Modified Biot's Theory

Field equations for the propagation of waves in a bone-like porous medium are derived respectively for the state variables of the displacements of the solid skeleton, $\mathbf{u}$, and the absolute displacements of the pore fluid, $\mathbf{U}$, as (Biot, 1956d).

$$\rho_{11}\frac{\partial^2 \mathbf{u}}{\partial t^2} + \rho_{12}\frac{\partial^2 \mathbf{U}}{\partial t^2} + b_0 \frac{\partial(\mathbf{u\text{-}U})}{\partial t} = P\nabla(\nabla\mathbf{.u}) + Q\nabla(\nabla\mathbf{.U}) - N\nabla\times(\nabla\times\mathbf{u}), \tag{4.1a}$$

$$\rho_{12}\frac{\partial^2 \mathbf{u}}{\partial t^2} + \rho_{22}\frac{\partial^2 \mathbf{U}}{\partial t^2} - b_0 \frac{\partial(\mathbf{u\text{-}U})}{\partial t} = Q\nabla(\nabla\mathbf{.u}) + R\nabla(\nabla\mathbf{.U}). \tag{4.1b}$$

The $\nabla\times$ is the Curl operator, and the term $b_0\frac{\partial(\mathbf{u\text{-}U})}{\partial t}$ is related to the friction force per unit volume of the bulk material in the *x* direction. In fact, this force is exerted on the solid part by the fluid in the direction of the wave motion. In the term $b_0\frac{\partial(\mathbf{u\text{-}U})}{\partial t}$, b_0 is the drag coefficient which is related to the fluid's viscosity,η, and the permeability of the porous medium, k_0. In addition, the relative displacement of the pore fluid, $u - U$, with respect to the solid skeleton follows the Poiseuille type. So the validity of this term is limited to low frequency range where the assumption of Poiseuille flow is valid and it will be neglected in high frequency where the Poiseuille 's law breaks down. In fact, in high frequencies, the fluid flow in porous media follows the Navier-Stokes linearization by neglecting the effect of viscosity while the effect of viscosity is more dominant in low frequency with respect to acceleration.

In high frequencies, the thickness of the viscous layer $\delta = \sqrt{\frac{2\eta}{\omega\rho_0}}$ is very thin with respect to the low frequency due to the negligible effect of viscous exchange and the pore fluid does not follow a potential flow pattern. Generally speaking, in low frequency ranges the effect of viscosity is dominant, while the acceleration effect dominates in high frequency ranges (Biot, 1956a; Biot, 1956e). Subsequently, by removing the term $b_0\partial(\mathbf{u\text{-}U})/\partial t$ for the applications in high frequency ranges, Equation 4.1a and Equation 4.1b are reduced to

$$\rho_{11}\frac{\partial^2 \mathbf{u}}{\partial t^2} + \rho_{12}\frac{\partial^2 \mathbf{U}}{\partial t^2} + = P\nabla(\nabla\mathbf{.u}) + Q\nabla(\nabla\mathbf{.U}) - \tag{4.2a}$$
$$N\nabla\times(\nabla\times\mathbf{u}),$$

and

$$\rho_{12}\frac{\partial^2 \mathbf{u}}{\partial t^2} + \rho_{22}\frac{\partial^2 \mathbf{U}}{\partial t^2} = Q\nabla(\nabla\mathbf{.u}) + R\nabla(\nabla\mathbf{.U}). \tag{4.2b}$$

It is possible to write Equation 4.2a and Equation 4.2b in frequency domain by applying the Fourier transform function,

$$\tilde{F}(\omega) = \mathscr{L}[F(t)] = \int_{-\infty}^{\infty} \exp(-j\omega t)F(t)dt \tag{4.3}$$

then, Equation 4.2a and Equation 4.2b can be written in the frequency domain as

$$\tilde{\rho}_{11}(\omega)(-\omega^2)\mathbf{u}(X,t) + \tilde{\rho}_{12}(\omega)(-\omega^2)\mathbf{U}(X,t) = \tag{4.4a}$$
$$P\nabla(\nabla.\mathbf{u}(X,\omega)) +$$
$$Q\nabla(\nabla.\mathbf{U}(X,\omega)) - N\nabla \times (\nabla \times \mathbf{u}(X,\omega)),$$

$$\tag{4.4b}$$

$$\tilde{\rho}_{12}(\omega)(-\omega^2)\mathbf{u}(X,t) + \tilde{\rho}_{22}(\omega)(-\omega^2)\mathbf{U}(X,t) =$$
$$Q\nabla(\nabla.\mathbf{u}(X,\omega)) +$$
$$R\nabla(\nabla.\mathbf{U}(X,\omega)).$$

respectively.

The P, Q, and R in the above equations are generalized elastic constants. They are related to measurable quantities such as porosity, bulk modulus of fluid, bulk modulus of solid, and bulk modulus of porous skeletal frame given by K_f, K_s, and K_b, respectively. Furthermore, N is the shear modulus of the skeletal frame. The explicit relation of the generalized elastic constants and the measurable quantities can be expressed as (Bourbie et al., 1987),

$$P = \frac{K_s\left(K_b\left((\phi-1)K_f+\phi K_s\right)+(\phi-1)^2K_fK_s\right)}{K_s\left(\phi K_s-(\phi-1)K_f\right)-K_bK_f} + \frac{4N}{3}, \tag{4.5a}$$

$$Q = \frac{\phi K_s\left(-\frac{K_b}{K_s}-\phi+1\right)}{-\frac{K_b}{K_s}+\frac{\phi K_s}{K_f}-\phi+1}, \tag{4.5b}$$

$$R = \frac{\phi^2 K_s}{-\frac{K_b}{K_s}+\frac{\phi K_s}{K_f}-\phi+1}. \tag{4.5c}$$

The porosity is defined by $\phi = \frac{V_f}{V_b}$ for an elastic porous matrix and a medium filled with a compressible-viscous fluid having a statistical distribution for the interconnected pores. Moreover, V_f and V_b are the respective volumes of the pores and bulk.

The mechanical properties of the solid and porous skeletal frame are given by

$$K_s = \frac{E_s}{3 - 6v_s}, \quad K_b = \frac{E_b}{3 - 6v_b}, \quad N = \frac{E_b}{2v_b + 2}. \tag{4.6}$$

in which E_s, v_s and E_b, v_b are the elastic modulus and Poisson's ratio of the solid and and bulk, respectively. The relationship between the mass coefficients, ρ_{mn}, and the densities of solid matrix, ρ_s, and the density of the pore fluid, ρ_f, are given by

$$\rho_{11} + \rho_{12} = (1 - \phi)\rho_s, \quad \rho_{12} + \rho_{22} = \phi\rho_f \tag{4.7}$$

where $\rho_{11}, \rho_{12}, \rho_{22}$ are time independent, effective densities (Allard and Daigle, 1994). In addition, ρ_{12} represents the mass coupling between the fluid and solid which is given by

$$\rho_{12} = -\phi\rho_f(\alpha_\infty - 1) \tag{4.8}$$

in which α_∞ is the tortuosity of the porous medium. The α_∞ relates the macroscopic flow through the medium to the microscopic flow inside the pores. By using a homogenization averaging technique (Smeulders, 1992) for high frequencies, α_∞ is written as

$$\alpha_\infty = \frac{< \mid v_p \mid^2 >}{\mid v_0 \mid^2} \tag{4.9}$$

in which $<>$ represents the averaging operator, v_0 is the macroscopic velocity of the pore fluid, and v_p is the corresponding microscopic velocity. If the macroscopic and microscopic velocities are identical $\alpha_\infty = 1$ and there is no mass coupling factor, ρ_{12}, between the fluid and solid.

The acoustical behaviour of porous materials is related to the materials' dynamic permeability and tortuosity. These factors depend on the pore fluid and they are completely independent of the solid skeletal frame's characteristics. The dynamic tortuosity depends greatly on the frequency range of 0-6 MHz and its theoretical formulation is given by (Johnson, Koplik, and Dashen, 1987; Allard and Atalla, 1993; Lafarge et al., 1997).

$$\tilde{\alpha}(\omega) = \alpha_\infty \left(1 + \frac{\eta\phi}{j\omega\alpha_\infty\rho_f k_0} \sqrt{(1 - j\frac{4k_0^2\rho_f\omega\alpha_\infty^2}{\eta\Lambda^2\phi^2})} \right), \tag{4.10}$$

where $j^2 = -1$, k_0 is the permeability, η is the viscosity of the pore fluid, and Λ is the length of the viscous characteristic defining the distribution of the size of pores in which viscous exchanges occur. This parameter controls the effect of the pore fluid's viscosity in

the medium and it is related to the size of interconnections between pores as illustrated in Figure 4.2 (Johnson, Koplik, and Dashen, 1987).
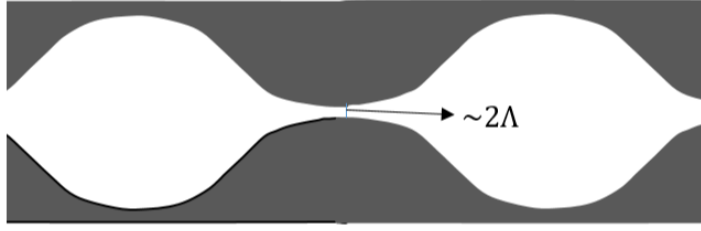
FIGURE 4.2: A schematic of viscous characteristic length in porous media

The flow regime of the pore fluid in a porous medium subjected to high frequencies can be determined by the transient or critical frequency defined by

$$f_c = \frac{\eta \phi}{2\pi a k_0 \rho_f} \tag{4.11}$$

in which a is the characteristic of the size of a pore and its geometry. The flow inside the pore for the frequencies less than f_c follows Poiseuille's law in which the viscosity of the fluid is proportional to the relative velocity of motion between the solid skeleton and the pore fluid (Biot, 1956c). The viscous layer for the frequencies greater than f_c is not large in comparison with the diameter of pores as Poiseuille's law is not applicable and modeling the viscous dissipation in this case becomes a complex task. It should be noted that the application of Biot's theory for pore geometries is limited to parallel walls and circular ducts for 2D and 3D, respectively (Biot, 1956e) while considering the dissipation in the case of random pores is proposed by (Johnson, Koplik, and Dashen, 1987) which led to the widely-used Biot-JKD model. The breaking down of Poiseuille's law for pores of flat and circular shapes happens beyond the critical frequency (Biot, 1956e). This research is implemented for high frequencies and exceeding the range of critical frequency, so that Equation 4.10 which was initially developed by (Johnson, Koplik, and Dashen, 1987) is rewritten as

$$\tilde{\alpha}(\omega) = \alpha_\infty \left(1 + \frac{2}{\Lambda} (\frac{\eta}{\omega j \rho_f})^{\frac{1}{2}} \right), \tag{4.12}$$

It is worth mentioning that $\tilde{\alpha}(\omega)$ has a critical role in the attenuation of acoustic waves in a porous medium because it describes the viscous exchanges between the solid structure and fluid (Johnson, Koplik, and Dashen, 1987). Consequently, the relationships for the mass

coefficients in the frequency domain, $\rho_{mn}(\omega)$, of Equation 4.4 are

$$\tilde{\rho}_{11}(\omega) = \rho_{11} + \tilde{\Xi}(\omega) \tag{4.13a}$$

$$\tilde{\rho}_{12}(\omega) = \rho_{12} - \tilde{\Xi}(\omega) \tag{4.13b}$$

$$\tilde{\rho}_{22}(\omega) = \rho_{22} + \tilde{\Xi}(\omega) \tag{4.13c}$$

$$\tilde{\Xi}(\omega) = \frac{2\phi \ \alpha_\infty}{\Lambda} \left(\frac{\rho_f \eta}{j\omega} \right)^{\frac{1}{2}}$$

4.4 Ultrasonic Waveforms

Waves can propagate in an elastic medium in longitudinal and transverse forms which are defined by scalar and vector displacement potentials. According to the Helmholtz decomposition, both **u** and **U** in Equation 4.4, can be presented as

$$\mathbf{u}(X,t) = \nabla \phi_s(X,t) + \nabla \times \Psi_s(X,t), \quad \mathbf{U}(X,t) = \nabla \phi_f(X,t) + \nabla \times \Psi_f(X,t) \tag{4.14}$$

The vector **x** can be written as $\mathbf{x} = \mathbf{x}(\mathbf{X},t)$ where $\vec{X} = x\hat{i}$.

By substituting Equation 4.14 and Equation 4.13 in to Equation 4.4, then

$$(-\omega^2) \left(\tilde{\rho}_{11}(\omega)(\tilde{\phi}_s(x,\omega) + \tilde{\Psi}_s(x,\omega)) + \tilde{\rho}_{12}(\omega)(\tilde{\phi}_f(x,\omega) + \tilde{\Psi}_f(x,\omega)) \right) =$$
$$P\nabla \left(\nabla \cdot \left[\nabla \tilde{\phi}_s(x,\omega) + \nabla \times \tilde{\Psi}_f(x,\omega) \right] \right) + Q\nabla \left(\nabla \cdot \left[\nabla \tilde{\phi}_s(x,\omega) + \nabla \times \tilde{\Psi}_f(x,\omega) \right] \right)$$
$$- N\nabla \times \nabla \times \left(\nabla \tilde{\phi}_f(x,\omega) + \nabla \times \tilde{\Psi}_f(x,\omega) \right), \tag{4.15a}$$

$$(-\omega^2) \left(\tilde{\rho}_{12}(\omega)(\nabla \phi_s(x,t) + \nabla \times \Psi_s(x,t)) + \tilde{\rho}_{22}(\omega)(\nabla \phi_f(x,t) + \nabla \times \Psi_f(x,t)) \right) =$$
$$Q\nabla \left(\nabla \cdot [\nabla \phi_s(x,t) + \nabla \times \Psi_f(x,t)] \right) + R\nabla \left(\nabla \cdot [\nabla \phi_f(x,t) + \nabla \times \Psi_f(x,t)] \right) \tag{4.15b}$$

Equation 4.15a and Equation 4.15b are equations of motion for the solid frame and pore fluid, respectively, which include the scalar and vector displacement potentials. Due to the statistical isotropy of medium, longitudinal and transverse waves can be decoupled by applying the divergence and curl operators in Equation 4.15. This procedure leads to the following

independent equations in the frequency domain.

$$-\omega^2\left(\tilde{\rho}_{11}(\omega)\tilde{\phi}_s(x,\omega)+\tilde{\rho}_{12}(\omega)\tilde{\phi}_f(x,\omega)\right)=\nabla^2\left(P\tilde{\phi}_s(x,\omega)+Q\tilde{\phi}_f(x,\omega)\right) \tag{4.16a}$$

and

$$-\omega^2\left(\tilde{\rho}_{12}(\omega)\tilde{\phi}_s(x,\omega)+\tilde{\rho}_{22}(\omega)\tilde{\phi}_f(x,\omega)\right)=\nabla^2\left(Q\tilde{\phi}_s(x,\omega)+R\tilde{\phi}_f(x,\omega)\right) \tag{4.16b}$$

and

$$-\omega^2\left(\tilde{\rho}_{11}(\omega)\tilde{\Psi}_s(x,\omega)+\tilde{\rho}_{12}(\omega)\tilde{\Psi}_f(x,\omega)\right)=-N\nabla\times\nabla\times\left(\tilde{\Psi}_s(x,\omega)\right) \tag{4.16c}$$

with

$$-\tilde{\rho}_{12}(\omega)\tilde{\Psi}_s(x,\omega)=\tilde{\rho}_{22}(\omega)\tilde{\Psi}_f(x,\omega) \tag{4.16d}$$

A close inspection of Equation 4.16 shows that the longitudinal and transverse waves are decoupled. Rewriting Equation 4.16a and Equation 4.16b in the linear form using matrix form, $\tilde{\phi}_s(x,\omega)$ and $\tilde{\phi}_f(x,\omega)$ can be derived. Similarly, $\tilde{\Psi}_s(x,\omega)$ and $\tilde{\Psi}_f(x,\omega)$ can be obtained by solving Equation 4.16c and Equation 4.16d. The matrix forms of Equation 4.16a and Equation 4.16b are

$$\begin{pmatrix} -\rho_{11}\omega^2+A(j\omega)^{\frac{3}{2}}-P\nabla^2 & -\rho_{12}\omega^2-A(j\omega)^{\frac{3}{2}}-Q\nabla^2 \\ -\rho_{12}\omega^2-A(j\omega)^{\frac{3}{2}}-Q\nabla^2 & -\rho_{22}\omega^2+A(j\omega)^{\frac{3}{2}}-R\nabla^2 \end{pmatrix}\begin{pmatrix} \tilde{\phi}_s(x,\omega) \\ \tilde{\phi}_f(x,\omega) \end{pmatrix}=0. \tag{4.17}$$

in which $A=\frac{1}{\Lambda_f}2\phi\rho_f\alpha_\infty\sqrt{\frac{\eta}{\rho_f}}$. Or, more simply,

$$\nabla^2\begin{pmatrix} \tilde{\phi}_s(x,\omega) \\ \tilde{\phi}_f(x,\omega) \end{pmatrix}=H\begin{pmatrix} \tilde{\phi}_s(x,\omega) \\ \tilde{\phi}_f(x,\omega) \end{pmatrix} \tag{4.18}$$

Details of H are given more conveniently in Appendix D. The interaction between the solid skeleton and pore viscous fluid leads to the appearance of a second longitudinal wave in a porous medium, which is called a slow wave. To obtain explicit forms of both the fast and

slow longitudinal waves, Equation 4.18 is rewritten first in the matrix form

$$\nabla^2 \begin{pmatrix} \tilde{\phi}_1(x,\omega) \\ \tilde{\phi}_2(x,\omega) \end{pmatrix} = \begin{pmatrix} \tilde{\lambda}_1(\omega) & 0 \\ 0 & \tilde{\lambda}_2(\omega) \end{pmatrix} \begin{pmatrix} \tilde{\phi}_1(x,\omega) \\ \tilde{\phi}_2(x,\omega) \end{pmatrix} \tag{4.19}$$

in which $\tilde{\lambda}_1(\omega)$ and $\tilde{\lambda}_2(\omega)$ are the eigenvalues of matrix H. Details are given in Appendix D. As the incident wave travels in the medium along the X-axis, the $\tilde{\phi}_1$ and $\tilde{\phi}_2$ of the last equation have the forms:

$$\tilde{\phi}_1(x,\omega) = \tilde{\Phi}_{11}(\omega)\exp\left[-x\sqrt{\tilde{\lambda}_1(\omega)}\right] + \tilde{\Phi}_{12}(\omega)\exp\left[x\sqrt{\tilde{\lambda}_1(\omega)}\right] \tag{4.20a}$$

$$\tilde{\phi}_2(x,\omega) = \tilde{\Phi}_{21}(\omega)\exp\left[-x\sqrt{\tilde{\lambda}_2(\omega)}\right] + \tilde{\Phi}_{22}(\omega)\exp\left[x\sqrt{\tilde{\lambda}_2(\omega)}\right] \tag{4.20b}$$

It is clear that both fluid and solid potentials, $\tilde{\phi}_f(x,\omega)$ and $\tilde{\phi}_s(x,\omega)$, can be linked to the slow and fast wave potentials, $\tilde{\phi}_1(x,\omega)$ and $\tilde{\phi}_2(x,\omega)$, using the eigenvectors of $\tilde{\lambda}_1(\omega)$ and $\tilde{\lambda}_2(\omega)$ through the following matrix form

$$\begin{pmatrix} \tilde{\phi}_s(x,\omega) \\ \tilde{\phi}_f(x,\omega) \end{pmatrix} = \begin{pmatrix} 1 & 1 \\ \tilde{V}_1(\omega) & \tilde{V}_2(\omega) \end{pmatrix} \begin{pmatrix} \tilde{\phi}_1(x,\omega) \\ \tilde{\phi}_2(x,\omega) \end{pmatrix} \tag{4.21}$$

where $\tilde{V}_1(\omega)$ and $\tilde{V}_2(\omega)$ are the eigenvectors of the matrix H. Subsequently, the solution for $\tilde{\phi}_s(x,\omega)$ and $\tilde{\phi}_f(x,\omega)$ will be

$$\tilde{\phi}_s(x,\omega) = \tilde{\phi}_1(x,\omega) + \tilde{\phi}_2(x,\omega) \tag{4.22a}$$

$$\tilde{\phi}_f(x,\omega) = \tilde{V}_1(\omega)\tilde{\phi}_1(x,\omega) + \tilde{V}_2(\omega)\tilde{\phi}_2(x,\omega) \tag{4.22b}$$

Similarly, the solution for rotational waves can be derived as.

$$\tilde{\Psi}_s(x,\omega) = \tilde{\psi}_1(\omega)\exp\left[-jx\sqrt{\tilde{\chi}(\omega)}\right] + \tilde{\psi}_2(\omega)\exp\left[xj\sqrt{\tilde{\chi}(\omega)}\right] \tag{4.23}$$

A complete description of $\tilde{\phi}_{11}(\omega)$, $\tilde{\phi}_{12}(\omega)$, $\tilde{\phi}_{21}(\omega)$, $\tilde{\phi}_{22}(\omega)$, $\tilde{\psi}_1(\omega)$, $\tilde{\psi}_2(\omega)$, and $\tilde{\chi}(\omega)$ is given more conveniently in Appendix E. The reflection and transmission coefficients are derived next.

4.5 Reflection and Transmission Coefficients

When an incident wave travels through a fluid surrounding the medium and impinges upon a porous medium filled with a viscous fluid, one part of the wave is reflected back into the fluid and another part is transmitted into the porous medium. The transmitted wave is composed of fast and slow longitudinal waves in addition to a transverse wave caused by the viscous exchange between the solid skeleton and fluid in a porous medium subjected to a high frequency incident wave. The amplitudes of reflected and transmitted waves will depends upon travel direction.

As shown in Figure 4.1, an incident short acoustic pulse (in time domain) impinges upon the left side of the fluid medium. The short pulse is a practical representation of Dirac Delta function illustrated in Figure 4.3. This study is implemented in the frequency domain because calculating dynamic tortuosity in time domain may necessitate using complicated fractional calculus. As a matter of fact, all manipulations are performed much more easier in frequency domain using the operational calculus mainly Fourier transform. Thereby, input short pulse in time domain is transferred to the frequency domain using Fourier transform depicted in Figure 4.4.
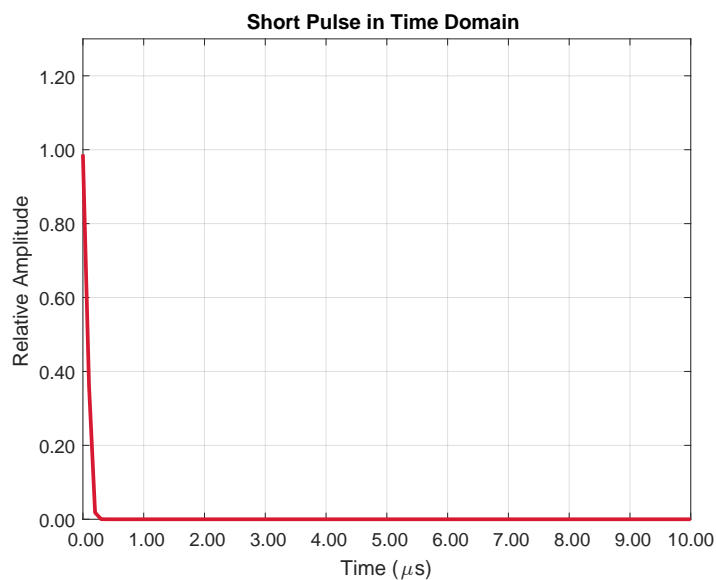
FIGURE 4.3: The Input signal as a short pulse in the time domain
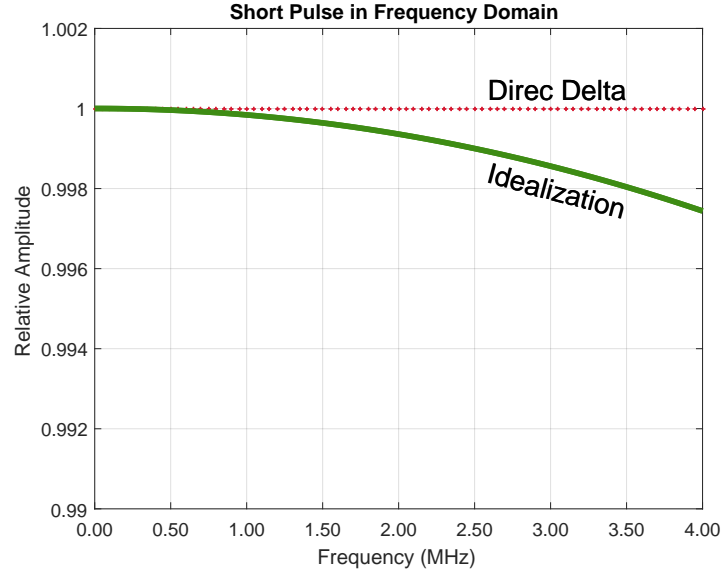
FIGURE 4.4: The Input signal as a short pulse in the frequency domain

The pressure fields for both sides of the medium are derived as follows. At the left side of the medium, in the region of $x \leq 0$, the pressure field is the sum of the pressures induced by incident and reflected waves as

$$P_{left}(x,t) = P^{inc}\left(t - \frac{x}{c_0}\right) + P^{ref}\left(t + \frac{x}{c_0}\right), \qquad (4.24)$$

where $P_{left}(x,t)$ stands for the total pressure field at the left side of the medium, i.e. $x \leq 0$. P^{inc} is the pressure field induced by the incident wave. P^{ref} is the pressure field induced by the reflected wave.

Similarly, the pressure field at the right side of the medium, i.e. $L \leq x$, induced by the transmitted wave can be obtained,

$$P_{right}(x,t) = P^{tr}\left(t - \frac{x-L}{c_0}\right) \qquad (4.25)$$

in which P^{tr} represents the transmitted wave's pressure at the right side of the medium.

With regards to ultrasonic standards for any material under an incident wave, the reflected and transmitted pressures can be derived by integrating the product of reflection $R(\tau)$ and transmission $T(\tau)$ operators by incident wave. So, The reflected and transmitted pressure

filed are written

$$P^{ref}(x,t) = \int_0^t R(\tau) P^{inc}\left(t - \tau + \frac{x}{c_0}\right) d\tau \tag{4.26a}$$

$$= R(t) * P^{inc}(t) * \delta\left(t + \frac{x}{c_0}\right)$$

$$P^{tr}(x,t) = \int_0^t T(\tau) P^{inc}\left(t - \tau - \frac{L}{c} - \frac{x-L}{c_0}\right) d\tau \tag{4.26b}$$

$$= T(t) * P^{inc}(t) * \delta\left(t - \frac{x-L}{c_0}\right)$$

Note that the kernel operators depend on the material properties of the medium. The lower limit of the integration in Equation 4.26 is zero, which means that at $\tau = 0$ the wave impinges upon the medium. So $P_{left}(x,t)$ and $P_{right}(x,t)$ are expressed by the following equations

$$P_{left}(x,t) = \left(\delta\left(t - \frac{x}{c_0}\right) + R(t) * \delta\left(t + \frac{x}{c_0}\right)\right) * P^{inc}(t) \tag{4.27a}$$

$$P_{right}(x,t) = P^{tr}\left(t - \frac{x-L}{c_0}\right). \tag{4.27b}$$

By taking the Fourier transform of Equation 4.27, the pressure fields at both sides of the medium can be obtained in frequency domain, so

$$\tilde{P}_{left}(x,\omega) = \mathscr{F}[P_{left}(x,t)] = \left(exp\left(-j\omega\frac{x}{c_0}\right) + \tilde{R}(\omega)exp\left(j\omega\frac{x}{c_0}\right)\right)\tilde{\varphi}(\omega), \tag{4.28a}$$

$$\tilde{P}_{right}(x,\omega) = \mathscr{F}[P_{right}(x,t)] = \tilde{T}(\omega)exp\left(-j\omega\frac{x-L}{c_0}\right)\tilde{\varphi}(\omega) \tag{4.28b}$$

in which $\tilde{P}_{left}(x,\omega)$ and $\tilde{P}_{right}(x,\omega)$ are the Fourier transform of $P_{left}(x,t)$ and $P_{right}(x,t)$, respectively. Also, $\tilde{\varphi}(\omega)$ is the Fourier transform of $P^{inc}(t)$.

Now, by applying these pressure fields, as boundary conditions, to left and right sides of the medium, we will be able to find the reflection and transmission coefficients as explained in the next section.

4.5.1 Stress Fields

The σ_{ij}^s and σ_{ij}^f are the normal stresses in the solid skeleton and fluid, respectively, and τ_{ij} is the shear stress in the solid skeleton. These stresses can be written as

$$\sigma_{ij}^s = \Big((P-2N)u_{i,j} + QU_{i,j}\Big)\delta_{ij} + N(u_{i,j}+u_{j,i}), \tag{4.29a}$$

$$\sigma_{ij}^f = -\phi p_f \delta_{ij} = (RU_{i,j} + Qu_{i,j})\delta_{ij}, \tag{4.29b}$$

$$\tau_{ij} = N(u_{i,j}+u_{j,i}) \tag{4.29c}$$

in which p_f represents the fluid pressure.

The stress amplitude in frequency domain can be written as follows.

$$|\tilde{\sigma}^s(x,\omega)| = P\tilde{\phi}_{si,i}(x,\omega) + Q\tilde{\phi}_{fi,i}(x,\omega),$$

$$|\tilde{\sigma}^f(x,\omega)| = R\tilde{\phi}_{fi,i}(x,\omega) + Q\tilde{\phi}_{si,i}(x,\omega),$$

$$|\tilde{\tau}(x,\omega)| = 2N\tilde{\phi}_{si,i}(x,\omega) \tag{4.30}$$

By substituting Equation 4.22 and Equation 4.23 into Equation 4.30 and taking derivatives with respect to x, the stress fields can be derived as

$$\tilde{\sigma}^s(x,\omega) = P\Big[\tilde{\lambda}_1(\omega)\tilde{\Phi}_{11}(\omega)e^{-\sqrt{\tilde{\lambda}_1(\omega)}x} + \tilde{\lambda}_1(\omega)\tilde{\Phi}_{12}(\omega)e^{\sqrt{\tilde{\lambda}_1(\omega)}x} + \tag{4.31a}$$

$$\tilde{\lambda}_2(\omega)\tilde{\Phi}_{21}(\omega)e^{-\sqrt{\tilde{\lambda}_2(\omega)}x} + \tilde{\lambda}_2(\omega)\tilde{\Phi}_{22}(\omega)e^{\sqrt{\tilde{\lambda}_2(\omega)}x}\Big] +$$

$$Q\Big[\tilde{\lambda}_1(\omega)\tilde{\Phi}_{11}(\omega)\tilde{V}_1(\omega)e^{-\sqrt{\tilde{\lambda}_1(\omega)}x} + \tilde{\lambda}_1(\omega)\tilde{\Phi}_{12}(\omega)\tilde{V}_1(\omega)e^{\sqrt{\tilde{\lambda}_1(\omega)}x} +$$

$$\tilde{\lambda}_2(\omega)\tilde{\Phi}_{21}(\omega)\tilde{V}_2(\omega)e^{-\sqrt{\tilde{\lambda}_2(\omega)}x} + \tilde{\lambda}_2(\omega)\tilde{\Phi}_{22}(\omega)\tilde{V}_2(\omega)e^{\sqrt{\tilde{\lambda}_2(\omega)}x}\Big]$$

$$\tilde{\sigma}^f(x,\omega) = Q\Big[\tilde{\lambda}_1(\omega)\tilde{\Phi}_{11}(\omega)e^{-\sqrt{\tilde{\lambda}_1(\omega)}x} + \tilde{\lambda}_1(\omega)\tilde{\Phi}_{12}(\omega)e^{\sqrt{\tilde{\lambda}_1(\omega)}x} + \tag{4.31b}$$

$$\tilde{\lambda}_2(\omega)\tilde{\Phi}_{21}(\omega)e^{-\sqrt{\tilde{\lambda}_2(\omega)}x} + \tilde{\lambda}_2(\omega)\tilde{\Phi}_{22}(\omega)e^{\sqrt{\tilde{\lambda}_2(\omega)}x}\Big] +$$

$$R\Big[\tilde{\lambda}_1(\omega)\tilde{\Phi}_{11}(\omega)\tilde{V}_1(\omega)e^{-\sqrt{\tilde{\lambda}_1(\omega)}x} + \tilde{\lambda}_1(\omega)\tilde{\Phi}_{12}(\omega)\tilde{V}_1(\omega)e^{\sqrt{\tilde{\lambda}_1(\omega)}x} +$$

$$\tilde{\lambda}_2(\omega)\tilde{\Phi}_{21}(\omega)\tilde{V}_2(\omega)e^{-\sqrt{\tilde{\lambda}_2(\omega)}x} + \tilde{\lambda}_2(\omega)\tilde{\Phi}_{22}(\omega)\tilde{V}_2(\omega)e^{\sqrt{\tilde{\lambda}_2(\omega)}x}\Big]$$

$$\tilde{\tau}(x,\omega) = 2N\Big[\tilde{\lambda}_1(\omega)\check{\Phi}_{11}(\omega)e^{-x\sqrt{\tilde{\lambda}_1(\omega)}} + \tilde{\lambda}_1(\omega)\check{\Phi}_{12}(\omega)e^{x\sqrt{\tilde{\lambda}_1(\omega)}} + \quad\quad (4.31c)$$

$$\tilde{\lambda}_2(\omega)\check{\Phi}_{21}(\omega)e^{-x\sqrt{\tilde{\lambda}_2(\omega)}} + \tilde{\lambda}_2(\omega)\check{\Phi}_{22}(\omega)e^{x\sqrt{\tilde{\lambda}_2(\omega)}} -$$

$$\tilde{\chi}(\omega)e^{-jx\sqrt{\tilde{\chi}(\omega)}}\left(\check{\psi}_1(\omega) + \check{\psi}_2(\omega)e^{2jx\sqrt{\tilde{\chi}(\omega)}}\right)\Big]$$

As the pressure and stress fields at the boundaries of the medium are continuous (Wu, Xue, and Adler, 1990), the relation between the pressure field and stresses at $x = 0$ and $x = L$ can be written as

$$\tilde{\sigma}^f(0^+,\omega) = -\phi\tilde{P}_{left}(0^-,\omega), \quad\quad (4.32)$$

$$\tilde{\sigma}^s(0^+,\omega) = -(1-\phi)\tilde{P}_{left}(0^-,\omega),$$

$$\tilde{\sigma}^f(L^-,\omega) = -\phi\tilde{P}_{right}(L^+,\omega),$$

$$\tilde{\sigma}^s(L^-,\omega) = -(1-\phi)\tilde{P}_{right}(L^+,\omega),$$

$$\tilde{\tau}(0^+,\omega) = 0,$$

$$\tilde{\tau}(L^-,\omega) = 0$$

By using Equation 4.31 and Equation 4.32, it is possible to obtain the 6 unknown variables $\check{\Phi}_1(x,\omega)$, $\check{\Phi}_{11}(x,\omega)$, $\check{\Phi}_2(x,\omega)$, $\check{\Phi}_{22}(x,\omega)$, $\check{\psi}_1(x,\omega)$, and $\check{\psi}_2(x,\omega)$. Hence, the displacement potentials for the solid skeleton and pore fluid can be obtained. In addition, in order to obtain the scattering operators, $\tilde{R}(\omega)$ and $\tilde{T}(\omega)$, two more equations are still needed. This can be achieved by considering the relation between the solid and fluid velocity fields and the acoustic velocity field at the boundaries of the medium at $x = 0$ and $x = L$ as follows.

$$\tilde{V}_1(0^-,\omega) = (1-\phi)\tilde{V}_s(0^+,\omega) + \phi\tilde{V}_f(0^+,\omega),$$

$$\tilde{V}_3(L^+,\omega) = (1-\phi)\tilde{V}_s(L^-,\omega) + \phi\tilde{V}_f(0^+,\omega), \quad\quad (4.33)$$

where $\tilde{V}_1$ and $\tilde{V}_3$ are the acoustic velocity fields at $x = 0$ and $x = L$, respectively. In fact, Equation 4.33 explains that if the porosity, ϕ, approaches zero, the acoustic velocity field will be equal to the velocity of solid and if there is no solid part, i.e. $\phi \to 1$, then the acoustical velocity field will be equal to the velocity of fluid. The acoustical velocity fields

is obtained by considering the surrounding fluid field pressure and the Euler equation as,

$$\nabla \tilde{P}_i(x,\omega) = \rho_f j\omega \tilde{V}_i(x,\omega) \quad i = left, right$$

$$V_1(x) = -\frac{\tilde{\varphi}(\omega)e^{-\frac{j\omega x}{c_0}}(-1 + \tilde{R}(\omega)e^{\frac{2j\omega x}{c_0}})}{c_0\rho_f}$$

$$V_3(x) = \frac{\tilde{T}(\omega)\tilde{\varphi}(\omega)e^{-\frac{j\omega(x-l)}{c_0}}}{c_0\rho_f} \tag{4.34}$$

Note that the fluid, V_f, and solid, V_s, velocity fields are derived using

$$\mathbf{u}(x,t) = \nabla \tilde{\phi}_s(t) + \nabla \times \tilde{\psi}_s(t) \rightarrow \quad \tilde{V}_s(x,\omega) = j\omega \left(\frac{\partial \tilde{\phi}_s(\omega)}{\partial x} + \frac{\partial \tilde{\psi}_s(\omega)}{\partial x}\right),$$

$$\mathbf{U}(x,t) = \nabla \tilde{\phi}_f(t) + \nabla \times \tilde{\psi}_f(t) \rightarrow \quad \tilde{V}_f(x,\omega) = j\omega \left(\frac{\partial \tilde{\phi}_f(\omega)}{\partial x} + \frac{\partial \tilde{\psi}_f(\omega)}{\partial x}\right) \tag{4.35}$$

By using the boundary conditions Equation 4.33, Equation 4.34 and the expressions for fluid and solid velocity fields, $\tilde{V}_s(x,\omega)$ and $\tilde{V}_f(x,\omega)$, the transmission and reflection coefficients, $\tilde{T}(\omega)$ and $\tilde{R}(\omega)$, are derived as.

$$\tilde{R}(\omega) = 1/\tilde{\varphi}(\omega)\left[jc_0\rho_f\left(\sqrt{\tilde{\lambda}_1(\omega)}\omega\tilde{\Phi}_{11}(\omega) - \sqrt{\tilde{\lambda}_1(\omega)}\omega\phi\tilde{\Phi}_{11}(\omega)\right.\right. \tag{4.36}$$
$$+ \sqrt{\tilde{\lambda}_1(\omega)}\omega\phi\tilde{V}_1(\omega)\tilde{\Phi}_{11}(\omega) - \sqrt{\tilde{\lambda}_1(\omega)}\omega\tilde{\Phi}_{12}(\omega)$$
$$+ \sqrt{\tilde{\lambda}_1(\omega)}\omega\phi\tilde{\Phi}_{12}(\omega) - \sqrt{\tilde{\lambda}_1(\omega)}\omega\phi\tilde{V}_1(\omega)\tilde{\Phi}_{12}(\omega) +$$
$$\sqrt{\tilde{\lambda}_2(\omega)}\omega\tilde{\Phi}_{21}(\omega) - \sqrt{\tilde{\lambda}_2(\omega)}\omega\phi\tilde{\Phi}_{21}(\omega) +$$
$$\sqrt{\tilde{\lambda}_2(\omega)}\omega\phi\tilde{V}_2(\omega)\tilde{\Phi}_{21}(\omega) - \sqrt{\tilde{\lambda}_2(\omega)}\omega\tilde{\Phi}_{22}(\omega) +$$
$$\sqrt{\tilde{\lambda}_2(\omega)}\omega\phi\tilde{\Phi}_{22}(\omega) - \sqrt{\tilde{\lambda}_2(\omega)}\omega\phi\tilde{V}_2(\omega)\tilde{\Phi}_{22}(\omega)\right) +$$
$$1/(\rho_{22})\left(\tilde{\varphi}(\omega)\rho_{22} + c_0\sqrt{\tilde{\chi}(\omega)}\omega\phi\rho_{12}\tilde{\Psi}_1(\omega) - c_0\sqrt{\tilde{\chi}(\omega)}\omega\rho_{22}\tilde{\Psi}_1(\omega) +\right.$$
$$c_0\sqrt{\tilde{\chi}(\omega)}\omega\phi\rho_{12}\tilde{\Psi}_2(\omega) + c_0\sqrt{\tilde{\chi}(\omega)}\omega\rho_{22}\tilde{\Psi}_2(\omega) -$$
$$\left.\left.c_0\sqrt{\tilde{\chi}(\omega)}\omega\phi\rho_{22}\tilde{\Psi}_2(\omega)\right)\right],$$

$$\tilde{T}(\omega) = \frac{1}{\tilde{\varphi}(\omega)}\left[\left(jc_0\omega\rho_f e^{-l\sqrt{\tilde{\lambda}_1(\omega)}-l\sqrt{\tilde{\lambda}_2(\omega)}}\right)\left[\sqrt{\tilde{\lambda}_1(\omega)}\phi\check{\Phi}_{11}(\omega)e^{l\sqrt{\tilde{\lambda}_2(\omega)}}-\right.\right. \qquad (4.37)$$

$$\sqrt{\tilde{\lambda}_1(\omega)}\phi\Phi_{12}(\tilde{\omega})e^{2l\sqrt{\tilde{\lambda}_1(\omega)}+l\sqrt{\tilde{\lambda}_2(\omega)}}+\sqrt{\tilde{\lambda}_2(\omega)}\phi\check{\Phi}_{21}(\omega)e^{l\sqrt{\tilde{\lambda}_1(\omega)}}-$$

$$\sqrt{\tilde{\lambda}_2(\omega)}\phi\check{\Phi}_{22}(\omega)e^{l\sqrt{\tilde{\lambda}_1(\omega)}+2l\sqrt{\tilde{\lambda}_2(\omega)}}-\sqrt{\tilde{\lambda}_1(\omega)}\phi\check{\Phi}_{11}(\omega)\tilde{V}_1(\omega)$$

$$e^{l\sqrt{\tilde{\lambda}_2(\omega)}}+\sqrt{\tilde{\lambda}_1(\omega)}\phi\check{\Phi}_{12}(\omega)\tilde{V}_1(\omega)e^{2l\sqrt{\tilde{\lambda}_1(\omega)}+l\sqrt{\tilde{\lambda}_2(\omega)}}-\sqrt{\tilde{\lambda}_2(\omega)}\phi$$

$$\check{\Phi}_{21}(\omega)\tilde{V}_2(\omega)e^{l\sqrt{\tilde{\lambda}_1(\omega)}}+$$

$$\sqrt{\tilde{\lambda}_2(\omega)}\phi\check{\Phi}_{22}(\omega)\tilde{V}_2(\omega)e^{l\sqrt{\tilde{\lambda}_1(\omega)}+2l\sqrt{\tilde{\lambda}_2(\omega)}}+\sqrt{\tilde{\lambda}_1(\omega)}\check{\Phi}_{11}(\omega)$$

$$\left(-\exp\left(l\sqrt{\tilde{\lambda}_2(\omega)}\right)\right)+$$

$$\sqrt{\tilde{\lambda}_1(\omega)}\check{\Phi}_{12}(\omega)e^{2l\sqrt{\tilde{\lambda}_1(\omega)}+l\sqrt{\tilde{\lambda}_2(\omega)}}-\sqrt{\tilde{\lambda}_2(\omega)}\check{\Phi}_{21}(\omega)e^{l\sqrt{\tilde{\lambda}_1(\omega)}}+$$

$$\left.\sqrt{\tilde{\lambda}_2(\omega)}\check{\Phi}_{22}(\omega)e^{l\sqrt{\tilde{\lambda}_1(\omega)}+2l\sqrt{\tilde{\lambda}_2(\omega)}}\right]+$$

$$c_0\sqrt{\tilde{\chi}(\omega)}\omega\rho_f\exp\left(-jl\sqrt{\tilde{\chi}(\omega)}\right)(\phi\rho_{12}+\phi\rho_{22}-\rho_{22})$$

$$\left.\left(-\tilde{\psi}_1(\omega)+\tilde{\psi}_2(\omega)\exp\left(2jl\sqrt{\tilde{\chi}(\omega)}\right)\rho_{22}\right)\right]$$

4.6 Computational Details

The governing equations were implemented in a MATLAB code. Computations were performed by using a desktop computer including Intel(R) Xeon(R) with CPU E5-2630 at 2.4 GHz. The computing effort was accelerated due to MATLAB parallel Toolbox and multicore processors (Sharma and Martin, 2009).

4.6.1 Validation

To validate the analytical solutions, terms related to the transverse wave alone are neglected. Consequently the transmission coefficient in the frequency domain which is based solely on longitudinal waves can be compared directly with that derived by (Fellah et al., 2004a) (Appendix G). Material properties used for the representation of a bone specimen are given in Table 4.1. As shown in Figure 4.5, the transmission coefficients agree perfectly with the results of (Fellah et al., 2004a).

4.7 Results and Discussion

The effects of the transverse acoustical waves on the response of bone-like porous materials is considered in this section. First, the transmission and reflection coefficients with and without terms related to the transverse acoustical waves are investigated and compared. Then

Porosity	$\phi = 0.83$
Bulk Modulus of Pore Fluid	$K_f = 2.28$ GPa
Length of a Porous Medium	L=0.007 m
Bulk Modulus of Solid	$K_s = 20$ GPa
Dynamic Turtuosity	$\alpha_\infty = 1.05$
Bulk Modulus of a Porous Skeletal Frame	$K_b = 3.3$ GPa
Characteristic Length of a Viscous Medium	$\Lambda = 5\ \mu m$
Density of Solid	$\rho_s = 1960$ kg/m^3
Shear Modulus of Frame	$N = 2.6$ GPa
Modulus of Elasticity of Solid Medium	$E_s = 15$ GPa
Modulus of Elasticity of Skeleton Medium	$E_b = 3.73 GPa$
Poisson's ratio of Solid Medium	$v_s = 0.37$
Poisson's ratio of Skeleton Medium	$v_b = 0.35$
Viscosity of a Fluid	$\eta = 0.001$ kgm/s
Density of Pore Fluid	$\rho_f = 1000$ kg/m^3

TABLE 4.1: Mechanical properties of the bone resulting in Figure 4.5

.
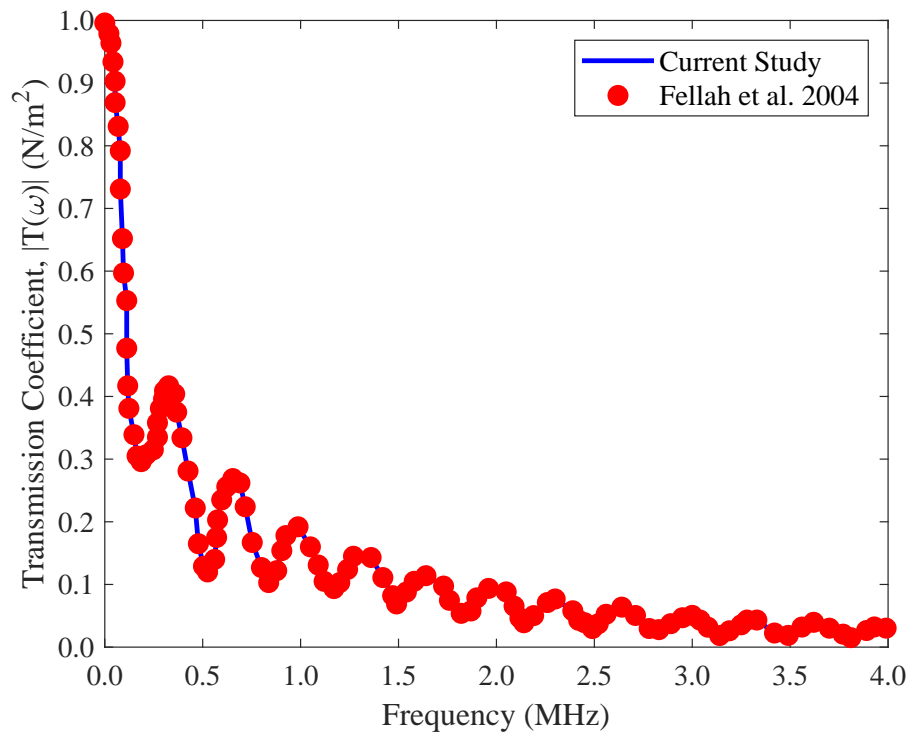
FIGURE 4.5: A comparison with the result of (Fellah et al., 2004a)

the effects of porosity and pore fluid's viscosity on the scattering operators are considered. Subsequently, the sensitivity of the shear and normal stresses in a bone-like porous medium are examined for different porosities and pore fluid's viscosity ranges.

4.7.1 Material Properties

To study the importance of porosity on the acoustical response of bone structures, different porosities ranging from 0.1 to 0.9 are considered. This indicates a range of bone conditions from a very stiff state to sever structural deterioration due to bone loss. Furthermore, to consider the effect of pore fluid's viscosity, two different fluids including a relatively low viscous (air) and high viscous (bone marrow) fluids are considered. The mechanical properties of the human bone specimen presented in Table 4.1 are obtained from (Fellah et al., 2013; Buchanan and Gilbert, 2007).

4.7.2 The Effect of Transverse Ultrasonic Waveform on Transmission Coefficient

The effect of transverse acoustical waves, generated in a bone-like medium subjected to an incident short acoustic pulse, on the transmission coefficient is considered. The responses of a bone specimen filled with a relatively high viscous material such as bone marrow are illustrated in Figure 4.6. The bone specimen has a porosity of $\phi = 0.83$ and is subjected to a short-period sound pulse impinging normally upon the left side of the medium. The short pulse causes an acoustical pressure and velocity within the material.

The transmission coefficient is calculated with and without the effects of the transverse waves. As shown in Figure 4.6, the effect of transverse acoustical wave along with longitudinal wave on the transmission coefficient is significant at 1.13, 2.38, and 3.51 MHz. These picks in acoustical response of the bone specimen cannot be captured by considering only the effect of longitudinal wave on the bone's response. These picks, related to the excitation of the system, appears due to including the effects of transverse waves. Thus, considering the effects of both longitudinal and transverse waves will provide a more complete set of information regarding the response of a bone structure at different frequency ranges.
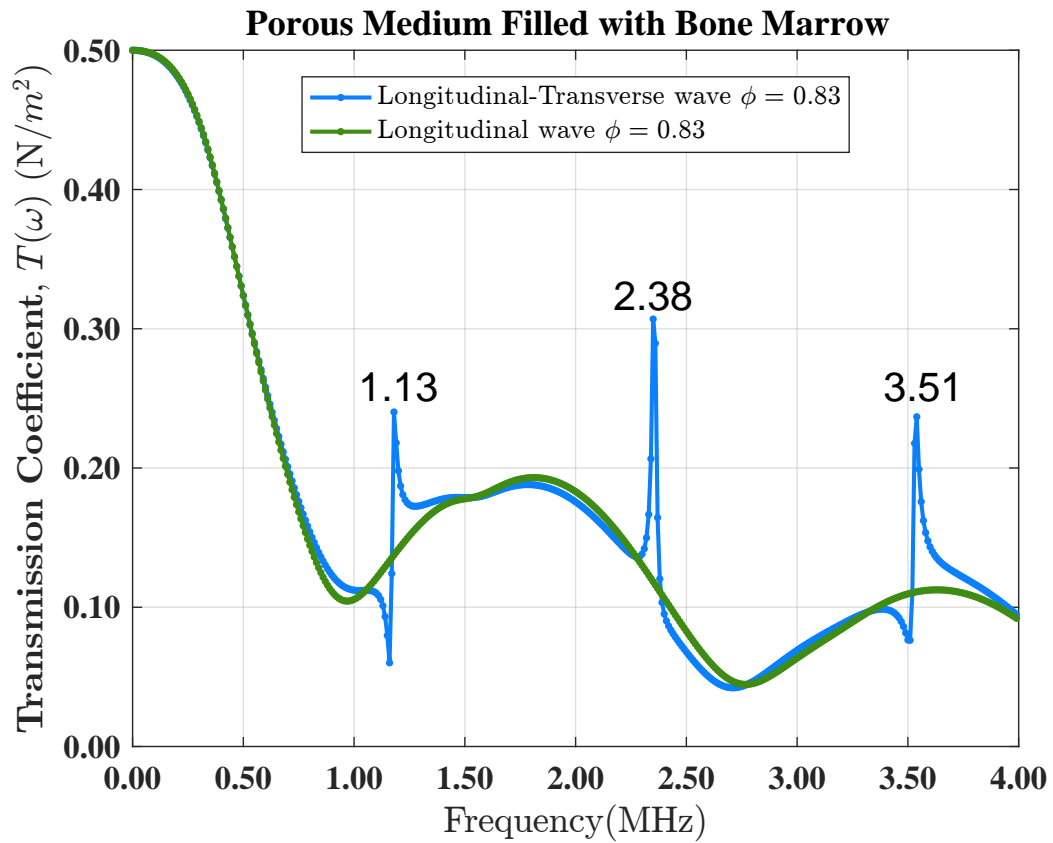
FIGURE 4.6: The effect of transverse waves on the transmission coefficient for a bone-like, porous medium filled with bone marrow

4.7.3 The Effect of Porosity on Acoustical Response of Bone-Like Materials Subjected to Ultrasonic Waveforms

The effect of porosity on the propagation of transverse acoustical waves in a bone-like medium filled with bone marrow is discussed in this section. As discussed before, the porosity range can describe the stage of bone loss and failure.

The variation of transmission coefficient by considering the effect of longitudinal wave and transverse wave alone with respect to frequency for the porosities of 0.3, 0.6, and 0.83 is illustrated in Figure 4.7 and Figure 4.8, respectively. Furthermore, the effects of both longitudinal wave and transverse waves on the acoustical response of the bone-like medium are illustrated in Figure 4.9.

Regardless of the type of wave, these Figures illustrate that by increasing the porosity from $\phi = 0.3$ to $\phi = 0.83$ for a medium filled with a relatively high viscous fluid (bone marrow), the transmission deceases. It is because by increasing the porosity in a Representative Elementary Volume, the volume of the viscous bone marrow inside the pores increases so that the transmitted wave inside the bone is attenuated noticeably due to an increase in damping
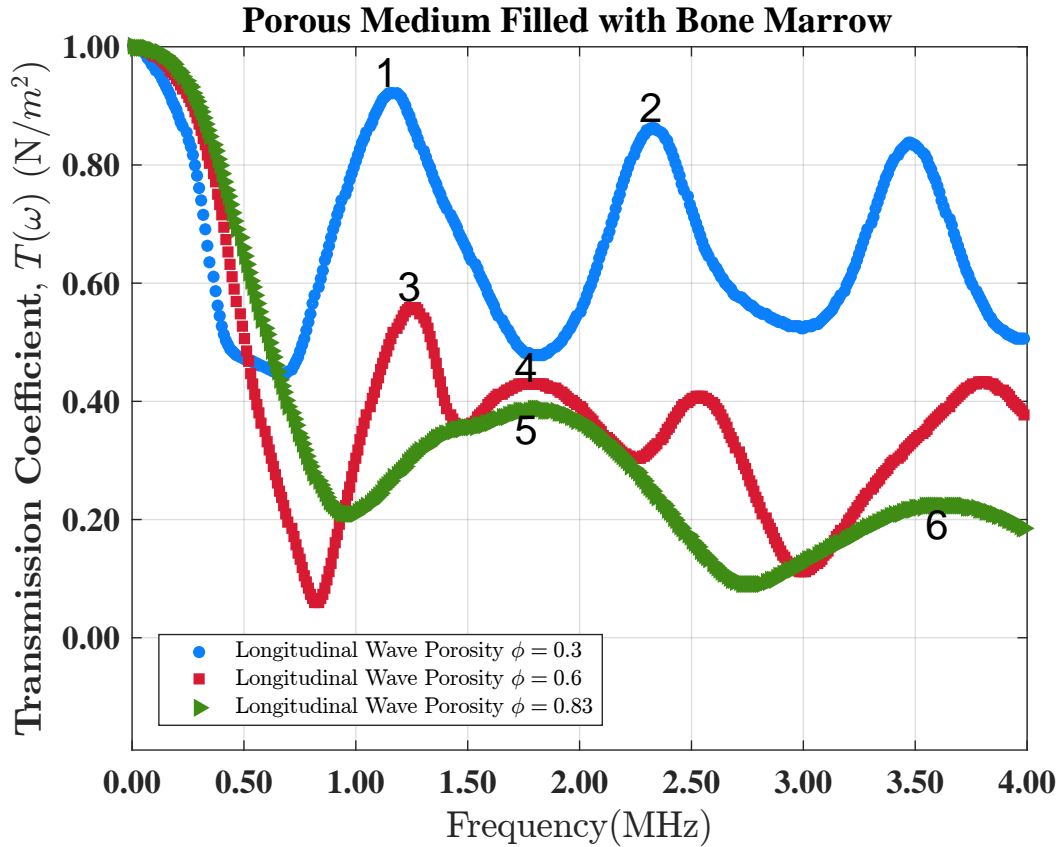
FIGURE 4.7: Transmission coefficients for different porosities of a bone-like medium filled with bone marrow. The effects of transverse waves are neglected.

ratio.

To calculate the effect of damping ratio on the wave's attenuation, as shown in Figure 4.7, the points 1 and 2 at two consecutive picks for the longitudinal wave when the porosity is $\phi = 0.3$ is selected. Similarly, the points 3 and 4 for $\phi = 0.6$ and points 5 and 6 for $\phi = 0.83$ are chosen. Then the amplitude for these picks are obtained. Subsequently the damping ratio is obtained by (Thomson, 2018):

$$\zeta = \frac{1}{2\pi} Ln \left(\frac{x_i}{x_{i+1}} \right). \tag{4.38}$$

in which x_i and x_{i+1} are the amplitudes of the first and second selected picks. For instance, the amplitude for points 1 and 2 are $x_1 = 0.9255$ and $x_2 = 0.8643$, respectively. Thereby, the damping ratio would be $\zeta_{0.3} = 0.019$. By repeating this scenario for $\phi = 0.6$ and $\phi = 0.83$, the damping ratio will be $\zeta_{0.6} = 0.0413$ and $\zeta_{0.83} = 0.08252$, respectively. Therefore, it can be concluded that in a medium filled with a relatively high viscous pore fluid the damping ratio increases by increasing the porosity which results in a wave attenuation.
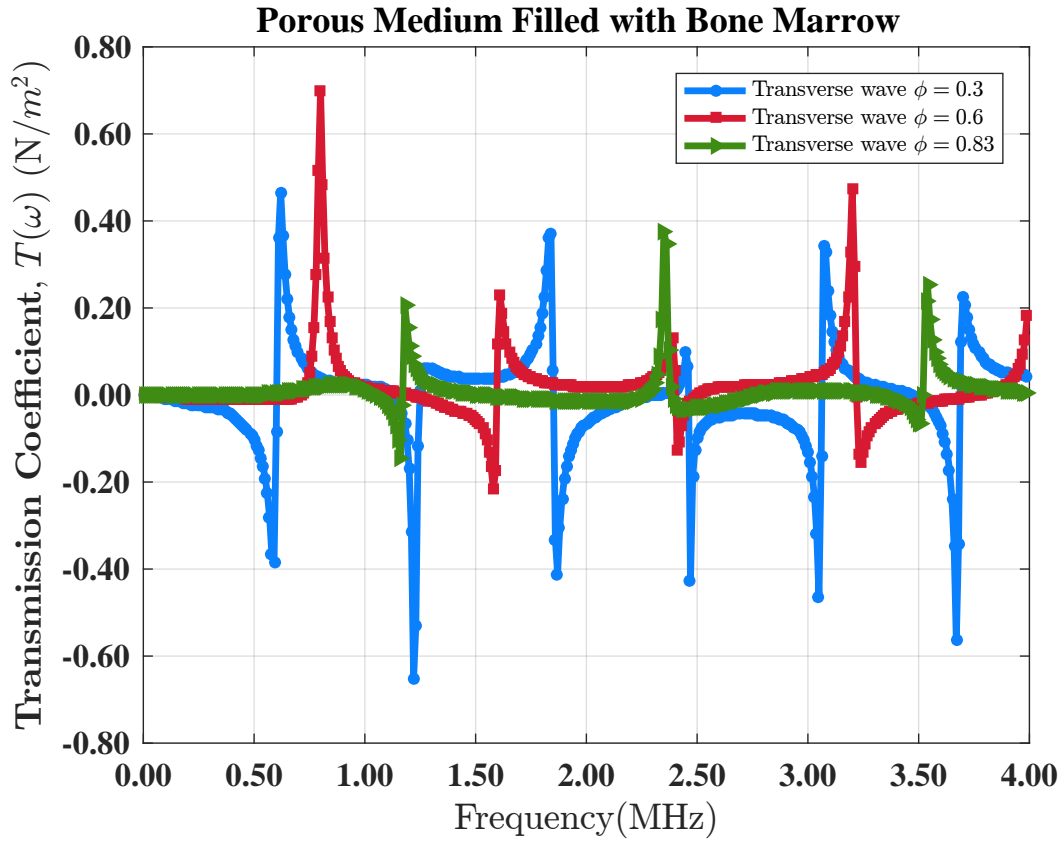
FIGURE 4.8: Transmission coefficients for different porosities of a bone-like medium filled with bone marrow by considering the effects of transverse wave alone.

To study the effect of porosity on the transmitted wave attenuation in a bone-like medium filled with air, the transmission coefficient versus frequency is presented in Figure 4.10 and Figure 4.11 by considering the effect of only longitudinal wave and both longitudinal and transverse waves, respectively.

As shown, there is no significant difference in transmission coefficient between two figures. Thereby, it can be resulted that regardless of the porosity of the medium the behaviour of the bone-like medium filled with a relatively low viscous fluid such as air is almost identical for transverse wave or longitudinal wave as one of these waveforms can provide sufficient information.

Additionally, a comparison between Figure 4.7 and Figure 4.9 with Figure 4.10 and Figure 4.11 explains that while the porosity increases, the transmission coefficient decreases but the rate of decreasing of transmission in a medium filled with bone marrow is lower than that of filled with the air. Subsequently, it can be concluded that not only the porosity but also the pore fluid's viscosity affect the transmitted wave propagation in a porous medium.
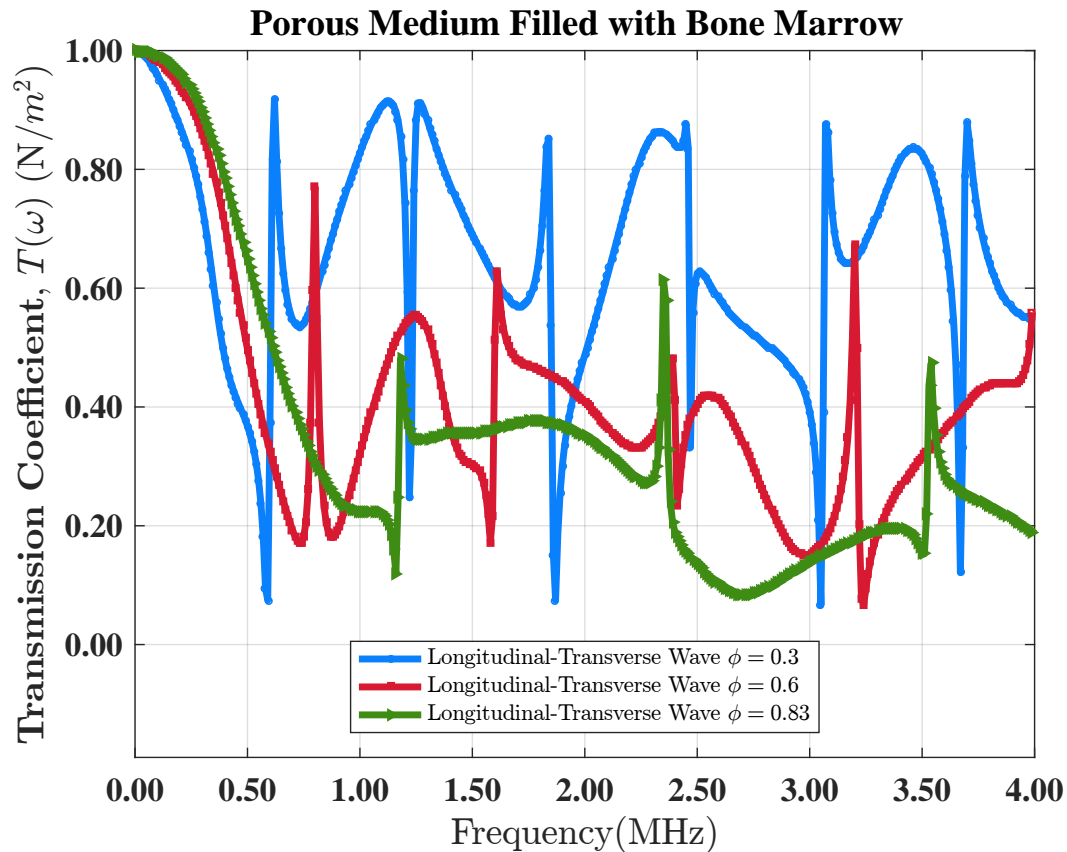
FIGURE 4.9: Transmission coefficients for different porosities in a bone-like medium filled with bone marrow by considering the effects of both longitudinal and transverse waves.

4.7.4 The Effect of Pore Fluid's Viscosity on Acoustical Response of Bone-Like Materials Subjected to Ultrasonic Waveforms

To study the influence of pore fluid's viscosity on the ultrasonic waveforms, the transmission coefficients for three different media composing a bone-like material including air, bone marrow and a stiff bone structure (SBS) are separately considered and compared. Figure 4.12 shows the transmission coefficients for three different media (air, bone marrow, and SBS) by considering the effect of longitudinal wave alone. It can be observed that the transmission coefficient in air is negligible and becomes zero at frequencies greater than 1 MHz due to the air's negligible stiffness. In fact, the main factor affecting the transmission of longitudinal waves is the stiffness of the medium. Since, the stiffness of the air is insignificant, the insignificant transmission occurs. Likewise, the transmission coefficient for a SBS is completely different due to its relatively high stiffness. Comparing the transmission coefficient between the SBS and bone marrow shows that the transmission attenuation in SBS is almost
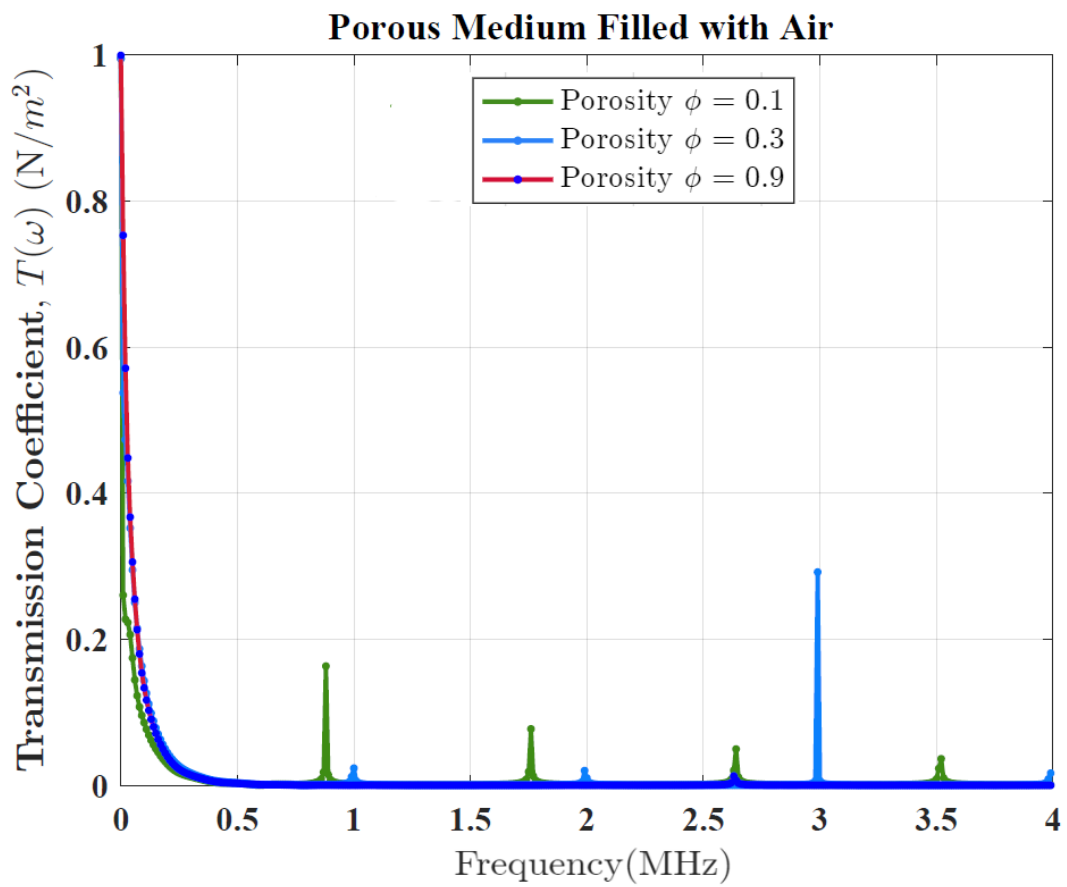
FIGURE 4.10: Transmission coefficients for different porosities in a bone-like porous medium filled with air by considering the effect of longitudinal wave alone.
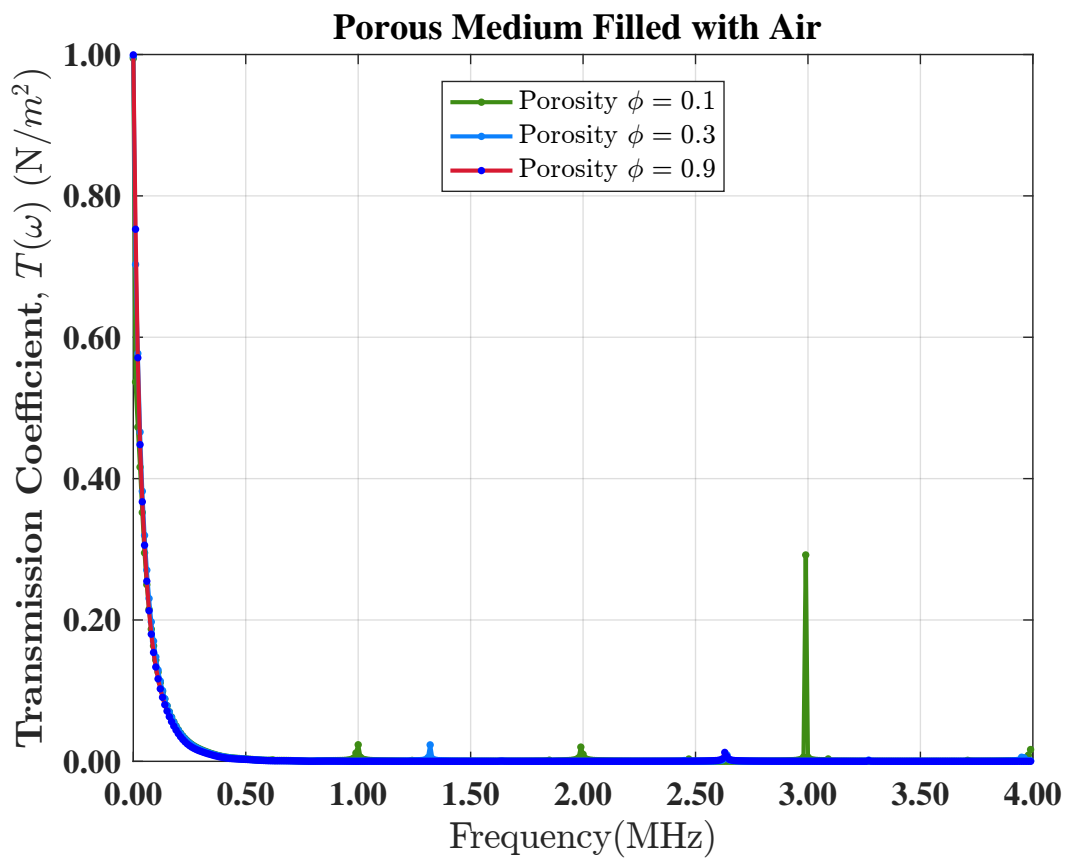
FIGURE 4.11: Transmission coefficients for different porosities in a bone-like porous medium filled with air by considering the effects of both longitudinal and transverse waves.
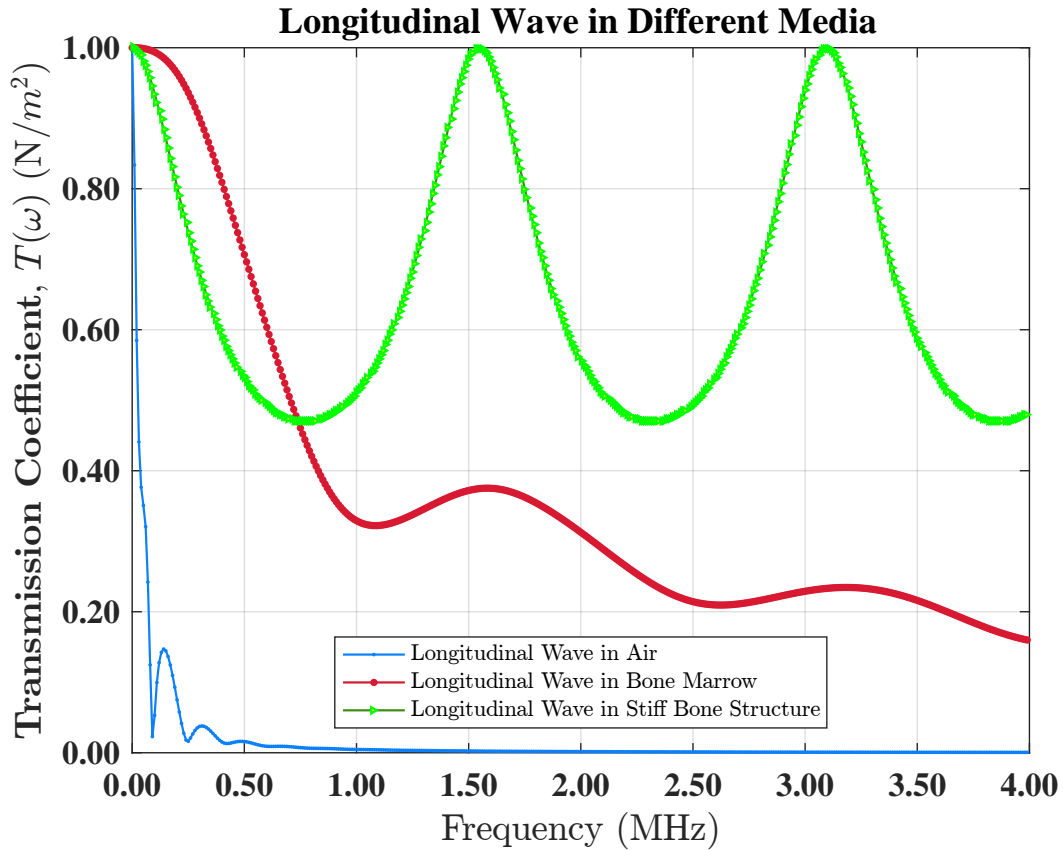
FIGURE 4.12: Transmission comparison in different media (air, bone marrow, and stiff bone structure) by considering the effects of longitudinal waves alone.

negligible, while it is significant in bone marrow. This attenuation in the transmission coefficient for bone marrow is due to its relatively high viscosity and damping characteristics.

Figure 4.13 investigates the transmission coefficients for three different media (air, bone marrow, and SBS) by considering the effect of transverse wave alone. Since the viscosity of the air is relatively low and its shear modulus is effectively zero, the effect of transverse wave in the air is negligible. The viscosity of the bone marrow with respect to the air is relatively high as the transmission induced by the transverse waves is striking. Figure 4.13 shows a pick at 3.1 MHz while this pick is not triggered by longitudinal wave as illustrated in Figure 4.12. Therefore, it can be resulted that in a relatively high viscous fluid the transverse wave is important and neglecting this wave can lead to miss some valuable information. By changing the medium phase from a fluid to a stiff bone structure, both longitudinal and transverse waves appeared because of its relatively high stiffness and shear strength.

Figure 4.14 illustrates the effects of both longitudinal and transverse waves on the transmission coefficient for three different media (air, bone marrow, and SBS). It can be seen that the transmission coefficient in air is governed by the longitudinal waves at low frequencies.
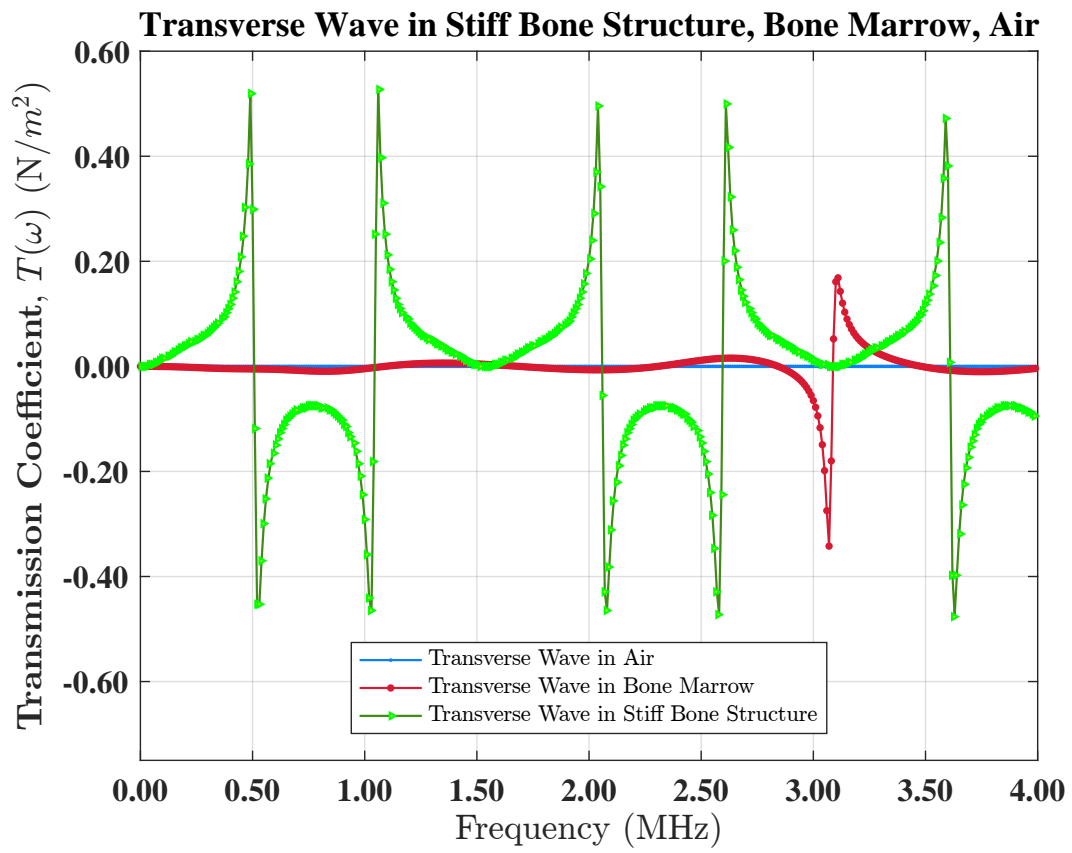
FIGURE 4.13: Transmission comparison in different media (air, bone mar-
row, and stiff bone structure) by considering the effects of transverse waves
alone.
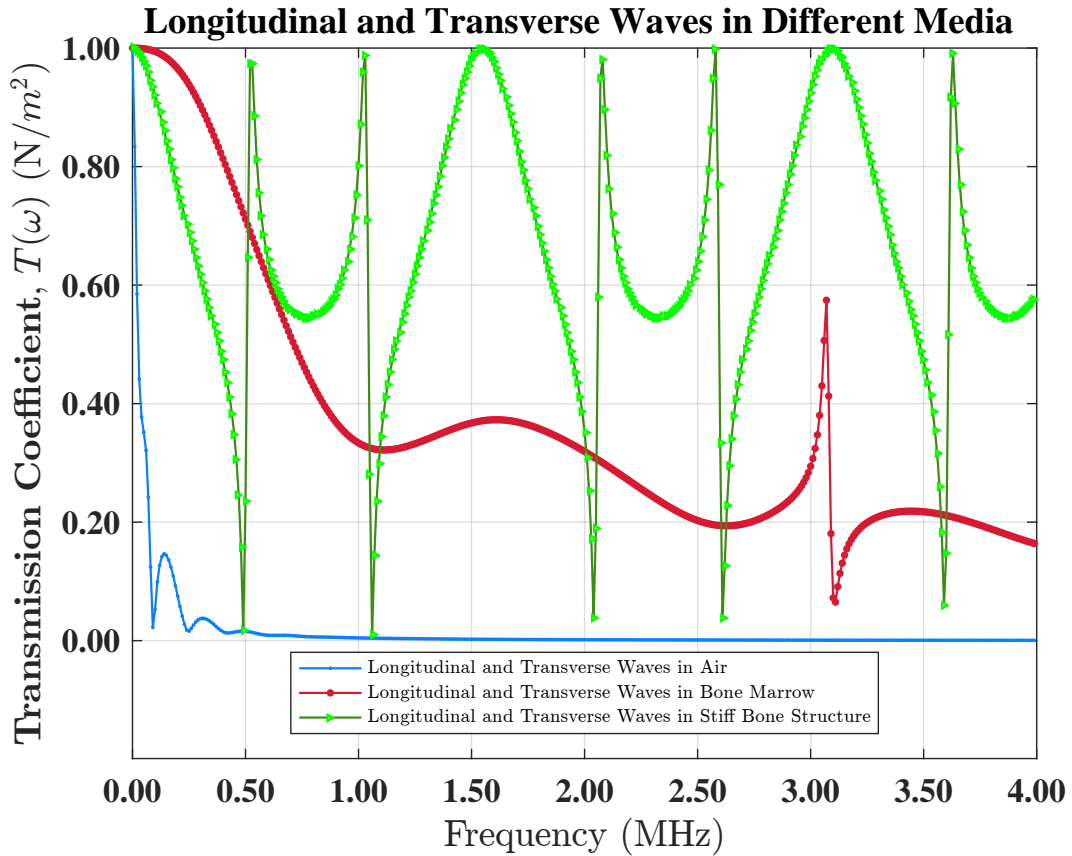
FIGURE 4.14: Transmission comparison in different media (air, bone marrow, and stiff bone structure) by considering the effects of both longitudinal and transverse waves.

For frequencies greater than 1 MHz, the transmission coefficient becomes negligible.

The transmission coefficient in bone marrow and SBS is governed by the superposition of both the longitudinal and transverse waves. It shows that the comprehensive study of the acoustical response of viscous, stiff materials necessitates the consideration of both the longitudinal and transverse waves.

To have a better insight into the effect of the pore fluid's viscosity on the propagation of transverse waves, the acoustical response of a bone-like medium filled with bone marrow (Figure 4.8) is compared with the one filled with air (Figure 4.15) for $\phi = 0.83$. It can be seen that the transmission of transverse waves are very sensitive to the viscosity of the pore fluid. The fluctuation trend in Figure 4.8 is very different from that of Figure 4.15 due to a relatively higher viscosity of the bone marrow with respect to the air.

Furthermore, to evaluate the effect of the viscosity of the pore fluid on the transmission coefficient, it is assumed that the bone-like porous medium is filled with air rather than bone marrow. The variation of transmission coefficient with respect to frequency for this case is plotted in Figure 4.16. As can be seen, the transmission coefficient in a medium filled
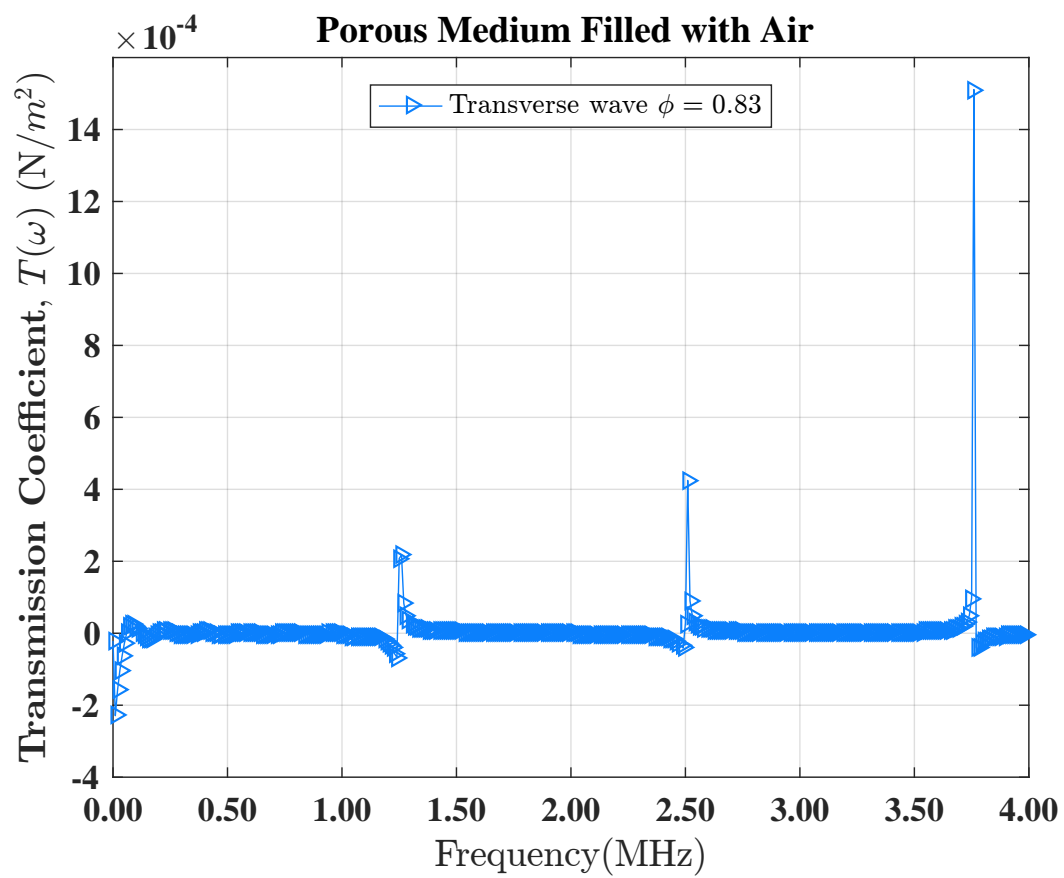
FIGURE 4.15: Transmission coefficients for porosity $\phi = 0.83$ for a bone-like medium filled with the air by considering the effects of transverse wave alone.

Porous Medium Filled with Air
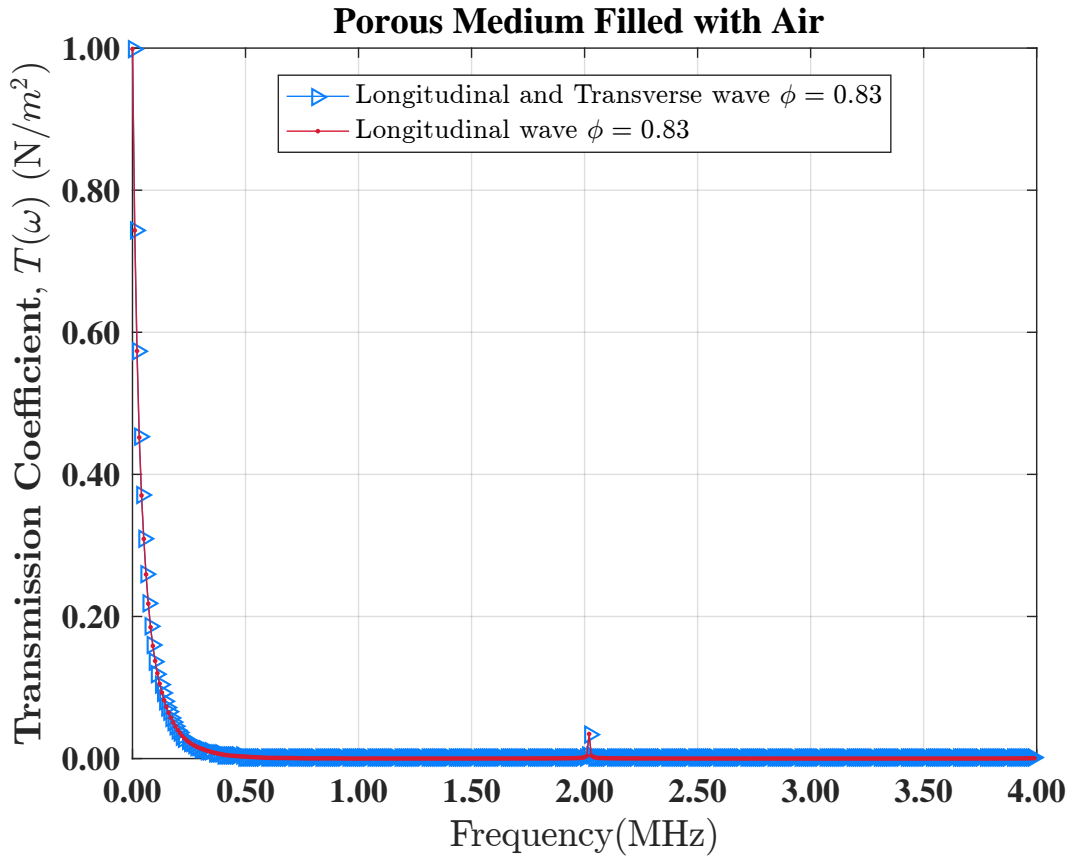
FIGURE 4.16: The effect of transverse acoustical waves on the transmission coefficients in a bone-like porous medium filled with air

with air by considering the effect of transverse wave alone and longitudinal-transverse waves follows almost the same path. It can be concluded that for a medium filled with a relatively low viscous fluid, considering the effect of transverse wave has no significant effect on the bone response. Also, the effect of transverse wave in characterizing the bone-like materials is highly sensitive to the viscosity of the pore fluid.

4.7.5 The Effect of Transverse Acoustical Waves on Reflection Coefficient

The effect of transverse and longitudinal waves on the reflection coefficient in a bone-like porous material filled with air is illustrated in Figure 4.17. The bone specimen has a porosity of $\phi = 0.9$. As illustrated, there is essentially no significant difference in the reflection coefficient between the longitudinal wave and that of both longitudinal and transverse waves. Figure 4.18 shows the effect of transverse wave on the reflection coefficient when the porosity is constant and the porous medium is filled with a higher viscous fluid such as bone marrow. In fact, By changing the pore fluid inside the medium from air to bone marrow, the response is completely different. Subsequently, it can be concluded that the effect of transverse wave
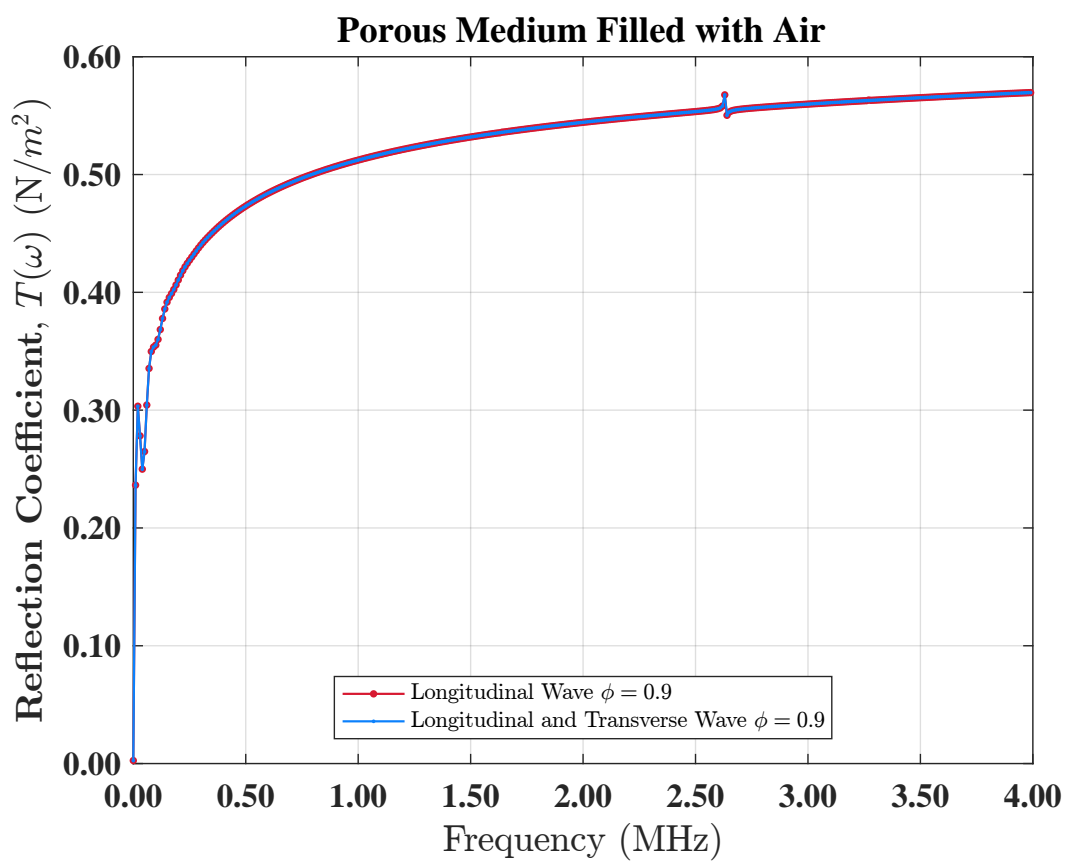
FIGURE 4.17: The effect of transverse wave on the reflection coefficient for
a porous medium filled with air
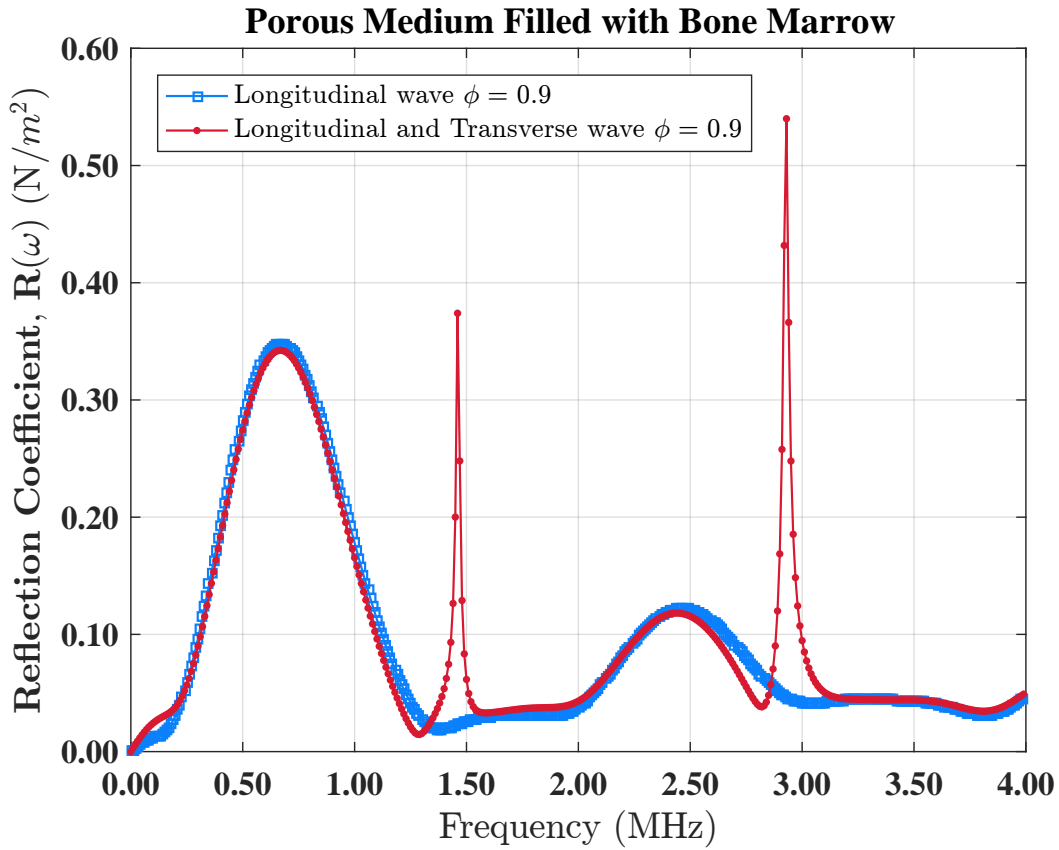
FIGURE 4.18: The effect of transverse wave on the reflection coefficient in comparison with longitudinal wave for a porous medium filled with bone marrow, $\phi = 0.9$

on the reflected wave front is significant when the porous medium is filled with a relatively high viscous fluid such as bone marrow. This result was also confirmed for the transmission coefficient.

Figure 4.19 illustrates the effect of transverse wave on the reflection coefficient when the bone-like material has a porosity of $\phi = 0.6$ and it is filled with bone marrow. By comparing Figure 4.18 and Figure 4.19, it can be shown that the reflection coefficients increases by decreasing the porosity which leads to more available solid medium for wave propagation. In addition, the number of picks reduces by increasing the porosity because the volume of bone marrow increases which leads to more damping and attenuation.

4.7.6   Stress Field in Bone-like Porous Media

This section shows the effect of different waves, porosity, as well as pore fluid's viscosity on the stress field in bone-like porous media. For this purpose, the stresses and acoustical pressures at the middle of the porous medium, $x = \frac{L}{2}$, are calculated for different porosities as well as pore fluids which have distinct acoustical properties.
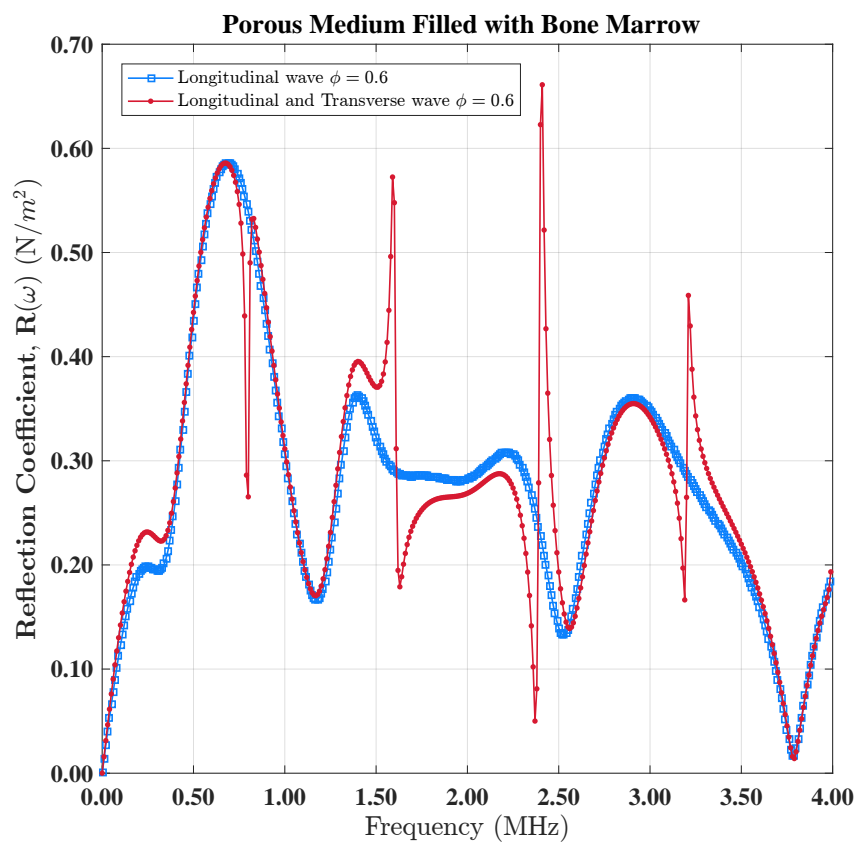
FIGURE 4.19: The effect of transverse wave on the reflection coefficient for
a porous medium filled with bone marrow, $\phi = 0.6$
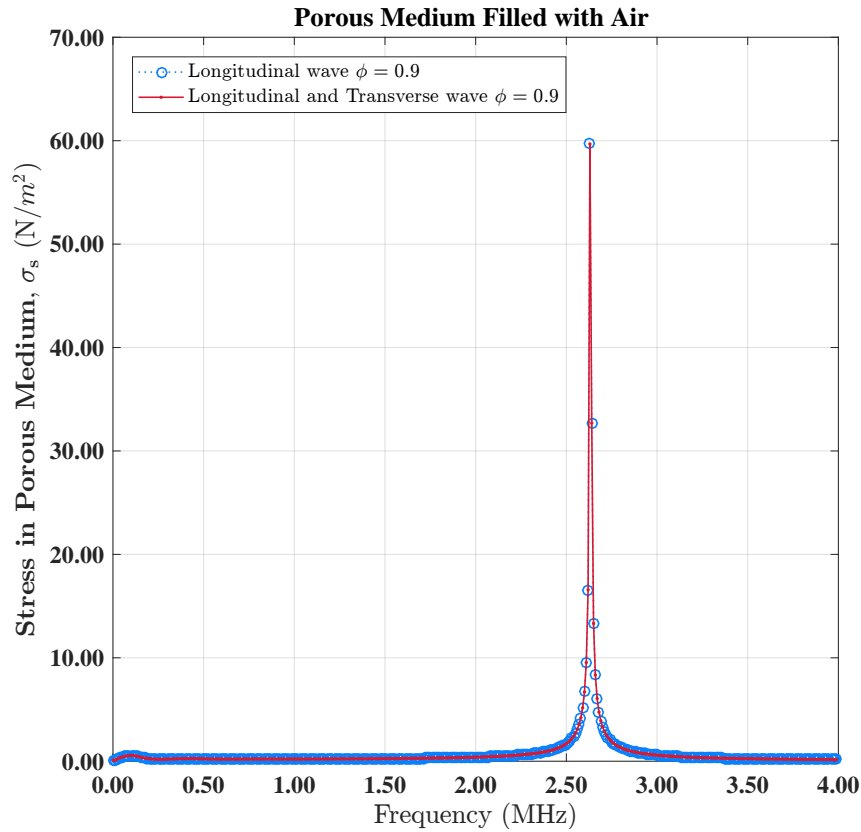
FIGURE 4.20: Normal stress created by differnt waves at the middle of a bone-like porous medium filled with air, $\phi = 0.9$

Figure 4.20 illustrates the normal stress in the middle of a bone-like, porous medium filled with air by considering longitudinal and transverse waves for porosity $\phi = 0.9$. It shows that due to a relatively low viscosity of pore air, the transverse wave does not provide an imperative effect on the stress field in the medium. In contrast, to consider the effect of viscosity, it is assumed that the bone-like medium is filled with bone marrow. The normal stress field is plotted for a porosity of $\phi = 0.3$ in Figure 4.21. As illustrated, the transverse wave has an influence on the normal stress field when the medium is filled with a relatively high viscous fluid. Furthermore, it is observed that the normal stress amplitude severely decreases in comparison with Figure 4.20. It is because the bone marrow causes more attenuation in acoustical waves which leads to less stress.

More specifically, Figure 4.21 shows the effect of different porosity $\phi = 0.3$ and $\phi = 0.9$ on the wave attenuation in a medium filled with bone marrow. Additionally, the effect of transverse wave on normal stress with respect to longitudinal wave is considered. By comparing the amplitude of normal stress in Figure 4.20 and Figure 4.21 it can be concluded that the viscosity of pore fluid has a significant effect on the amount of normal stress field in bone-like porous medium. When the porous medium is filled with a relatively high viscous
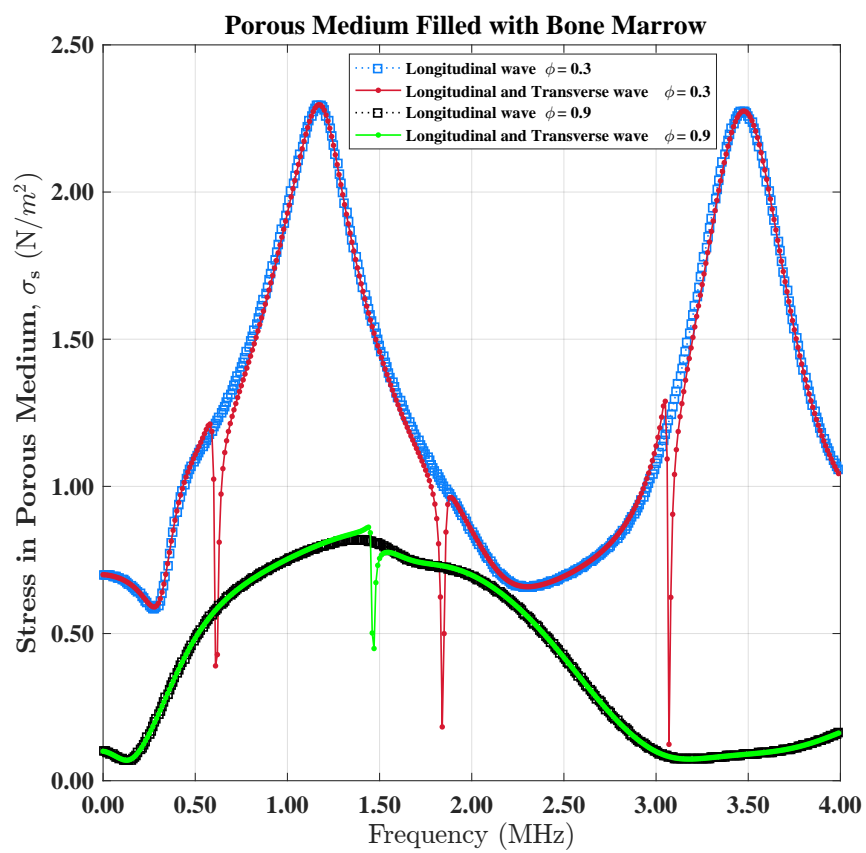
FIGURE 4.21: Normal stress created by different waves at the center of a bone-like porous medium filled with bone marrow for different porosities

fluid such as bone marrow, the porosity is very imperative in attenuating the stresses. In fact, a comparison between parts a and b of Figure 4.21 shows the effect of porosity on the amplitude of stress. The greater porosity makes more available viscous pore fluid which results in a lower stress.

4.8 Conclusions

The ultrasonic waves in porous media saturated with a viscus fluid is developed based on the Biot-JKD theory. Two types of longitudinal wave named fast and slow waves as well as transverse wave obtained in the frequency domain are derived to calculate the reflection and transmission coefficients along with stress fields. It is found that the scattering operators and stress fields in a bone-like, porous medium are sensitive to the porosity of the medium and the viscosity of the pore fluid. The effect of transverse wave on the stresses and scattering operators for different porosity and viscosity are investigated as well. The results describe that considering the transverse waves propagating in a bone-like porous medium filled with a relatively high viscous fluid has a significant effect on the scattering operators. In contrast, if the medium is filled with a lower viscous fluid such as air, no significant difference in bone response is observed between different types of ultrasonic waves. Additionally, the transmission and reflection coefficients are decreased severely by increasing the porosity in a bone-like porous medium filled with bone marrow while there is no predominant behavior when the medium is filled with air. Regarding the stress fields, the transverse wave has an imperative effect on the stress in a porous medium filled with bone marrow whereas this effect is virtually negligible when the pores are filled with air.

Chapter 5

Three-Dimensional Biomechanical Modeling of Cylindrical Bone-Like Porous Materials Subject to Acoustic Waves

Abstract

A three-dimensional (3D) analytical solution for the acoustic response of cancellous bone-like porous materials saturated with a viscous fluid. The effect of dynamic tortuosity, especially in clinically relevant ultrasound frequency ranges, is considered to investigate the effect of viscous interaction between the fluid and solid phases. The solution includes the effects of both fast and slow longitudinal waves as well as transverse waves propagating through the medium. The scattering operators and radial displacements are derived in terms of ultrasonic waveforms by applying the Helmholtz decomposition. The effect of different porosities, wall thickness ratios, and frequencies of incident waves on the radial displacement and scattering operators are investigated by considering various incident wave angles at forward and sideward directions. The results demonstrates that the incident wave angle has a significant effect on the radial displacement and scattering operators regardless of the porosity, wall thickness ratio, and viscosity of pore fluid. Furthermore, the distribution pattern of the radial displacement and scattering operators in relatively low frequency ranges is almost symmetric while asymmetric in relatively high frequency ranges. It is shown that the bone characterization using ultrasonic techniques is not only based on the mineral density, as used currently by electromagnetic wave-based tools, but also other biomechanical factors such as porosity, viscosity of pore fluid, and wall thickness ratio of a cancellous bone structure. Also, the pattern of the reflected pressure can be an indicator of the state of a cancellous bone (healthy versus osteoporosis).

5.1 Introduction

Osteoporosis is often called the *silent thief* because bone loss occurs without symptoms and can cause painful fractures, disability, and deformity Osterhoff et al., 2016. The risk of bone fracture raises two-fold to three-fold by decreasing bone mass-dependent factors such as bone mineral density Cummings et al., 1993; Stegman et al., 1992; Hui, Slemenda, and Johnston, 1989, or age and past fractures Hui, Slemenda, and Johnston, 1988; Ross et al., 1991. Although bones are constantly being renewed naturally, this process becomes less efficient with age and bone becomes very thin and weak over time. Factors related to bone structure and composition contributing to bone strength and fracture risks are defined as bone quality. Such factors are independent of bone mineral density Ross et al., 1991; Hui, Slemenda, and Johnston, 1988.

The main structure of this organ is made up of three main types of bone tissues: cortical (or compact) bone, cancellous (or spongy) bone, and bone marrow. Unlike cortical bone which is mostly solid and the hardest type of bone, the structure of the cancellous bone is spongy and is full of open sections called pores. The porous skeletal frame in the bone is filled with marrow, nerves, and blood vessels. The porosity of a bone is one of the main quantities used to characterize the strength of the bone structure. This may vary from 5% for a healthy bone to 95% when the cancellous bone structure is affected by bone loss diseases such as osteoporosis Fritsch and Hellmich, 2007.

Various approaches have been employed for osteoporosis detection Wear, Hoffmeister, and Laugier, 2018; Lin and Lane, 2004. Quantitative ultrasound (QUS) for osteoporosis detection has advantages over electromagnetic wave tools. For instance, QUS packages are smaller and potable relative to bulky MRI or X-ray techniques. Also, they are relatively cheap, do not utilize harmful radiations, and are recognized as a non-invasive technique. It should be noted that the lack of understanding of the mechanism of ultrasound wave propagation through a porous, complex bone structure is one of the reasons for the limitations of QUS techniques in diagnosing osteoporosis.

Several researchers have been involved in measuring the elastic characteristics of a cancellous bone using different experimental setups Ashman, Corin, and Turner, 1987; Ashman and Rho, 1988; Yousefian et al., 2018; Langton, Palmer, and Porter, 1984. In addition to experimental work, several theoretical studies regarding wave propagation in porous media saturated with different types of fluids (inviscid, viscous, co-existence of several fluids in pores) have been developed Maghoul, Gatmiri, and Duhamel, 2011a; Maghoul, Gatmiri, and

Duhamel, 2011b; Hughes et al., 1999; Roh, Lee, and Yoon, 2003; Lee, Roh, and Yoon, 2003; McKelvie and Palmer, 1991; Lauriks et al., 1994; Hosokawa and Otani, 1997. The most popular theory which considers the wave propagation in porous media filled with a viscous fluid is the poroelastic theory proposed by Biot (1956d), Biot (1941), Biot (1955), Biot (1956b), and Biot (1962b). Biot's theory predicts two longitudinal waves such as fast and slow waves. The fast wave is relevant to the in-phase motion of fluid (fluid in pores) and solid (bare structure) and the slow wave is related to the out-phase motion of these phases. The presence of slow and fast longitudinal waves, was shown by performing some experiments on human and bovine bone samples Lakes, Yoon, and Katz, 1983; Hosokawa and Otani, 1997; Hosokawa and Otani, 1998; Cardoso et al., 2003. Based on Biot's theory, wave propagation in cancellous bone structures filled with a viscous fluid has been studied in the literature. For example, the speeds of fast and slow longitudinal waves as well as their attenuation were investigated to predict the state of a bone Hosokawa and Otani, 1997; Hosokawa and Otani, 1998; Haire and Langton, 1999; Cardoso and Cowin, 2011; Fellah et al., 2004a; Sebaa et al., 2006b; Marutyan, Holland, and Miller, 2006; Hughes et al., 2007; Pakula et al., 2008; Anderson et al., 2008; Mizuno et al., 2009; Wear, 2010; Nelson et al., 2011; Langton, Palmer, and Porter, 1984.

Johnson, Koplik, and Dashen (1987) addressed the limitations of original Biot's theory regarding the energy dissipation in porous media filled with viscous fluids at different frequencies. The modified theory, called Biot-JKD, reconstructed original Biot's theory by introducing the dynamic tortuosity, viscous characteristic length, and dynamic permeability to consider the energy dissipation due to viscous exchanges between the pore fluid and solid skeletal frame. Based on the Biot-JKD theory, several studies have been performed on the wave propagation in cancellous bone structures filled with bone marrow by considering the effect of dynamic tortuosity as an indication of viscous exchange between the solid skeletal frame and the pore fluid (for example, see Fellah et al., 2004a; Hughes et al., 2007; Marutyan, Holland, and Miller, 2006; Sebaa et al., 2006b; Pakula et al., 2008; Mizuno et al., 2009). It is worth noting that the cancellous bone in the above-mentioned studies was analytically modeled using a medium whose two dimensions have infinite lengths. Also, the effect of the transverse wave was not investigated in these studies.

Any change in the speed or frequency content of acoustic waves in a cancellous bone can be an indicator of an abnormality or bone loss, so considering the scattering effects in osteoporosis detection is very important. Several studies have been performed to study the

back-scattering and transmission of acoustical waves in cancellous bones. For instance, Bennamane and Boutkedjirt (2017) studied the attenuation of ultrasonic waves in bovine bone using a theoretical approach including both scattering and dissipation. Their analytical approach was based on Biot's model. They used 12 bovine cancellous bone samples immersed in a water tank for the experiments, and measured ultrasonic attenuation at a frequency range between 0.1 and 1 MHz. The attenuation due to absorption has been studied by Biot's theory and experimental data. They showed that the wave scattering due to the porous nature of a cancellous bone is mainly responsible for ultrasonic attenuation. Buchanan, Gilbert, and Ou (2012) studied the wave propagation in a cancellous bone insonified by a short pulse immersed in the water. They derived the transmission and reflection coefficients of both slow and fast waves using modified Biot's theory.

Pakula, Padilla, and Laugier (2009) studied several human cancellous bone samples saturated with water, marrow, and alcohol to investigate the energy absorption, wave scattering and attenuation. They concluded that the pore fluid has no influence on the attenuation coefficient at ultrasonic frequency ranges between 0.35 and 1.2 MHz. Also, the ultrasonic attenuation is mainly important due to the viscoelastic absorption of the cancellous bone structure. In addition, the type of pore fluid determines the phase velocity. Gilbert et al. (2009) followed the model proposed by Buchanan et al. (2003) and calculated the porosity of a cancellous bone sample by the measured ultrasonic wave signals. They used a two-dimensional infinite length porous slab for a cancellous bone surrounded by the cortical bone and muscles phantoms. They performed their test in the water tank. Their results showed that the ultrasonic wave of a relatively high frequency can be used to determine accurately the porosity of a bone sample. Nguyen, Naili, and Sansalone (2010) proposed an analytical model to consider the transient wave propagation in a water-saturated cancellous bone. They used a two-dimensional infinite length slab to model a bone. A finite element model was employed to model an anisotropic porous medium saturated with water. The results showed that the transmission and reflection characteristics are strongly dependent on the anisotropy of cancellous bones. Gilbert, Guyenne, and Ou (2012) studied the effect of the viscosity of the pore fluid inside the cancellous bone on attenuation at ultrasound frequency ranges using the modified Biot theory. They used a one-dimensional model for cancellous bone immersed in the water tank. It was concluded that the ultrasonic attenuation is a linear function of frequency and significantly influenced by the viscosity of the interstitial fluid. Nguyen and Naili (2012) considered the wave propagation in anisotropic cortical long bones using Biot's theory and a hybrid analytical and finite element methods. They derived a finite element formulation in

the spectral domain for anisotropic structures of the cortical bone immersed in water. Their results showed that the proposed hybrid approach can fairly simulate the wave propagation in the poroelastic and anisotropic structure of cortical bones, especially in high frequencies. Also, it was concluded that the velocity of the fast arrival signal is significantly influenced by the porosity of the cortical bone.

Fellah et al. (2004a) studied ultrasonic wave propagation in cancellous bones. They used a two-dimension infinite length porous slab to model a cancellous bone. They also considered the effect of dynamic tortuosity for viscous exchange between the solid skeletal frame and pore fluid in high frequency ranges. The sensitivity of some parameters were investigated. It was shown that the bulk modulus of the pore fluid and the viscous characteristic length are sensitive to slow waves while the porosity, tortuosity, and bulk modulus of the solid skeletal frame are sensitive to both fast and slow waves. They derived the scattering operators for a cancellous bone-like sample for high frequency ranges by considering the dynamic tortuosity based on the Biot-JKD theory. Buchanan, Gilbert, and Miao-jung (2011) developed Fellah's model by considering a cortical bone and muscles around the cancellous bone. They modeled the cortical bone and muscles as elastic materials, and the cancellous bone as a poroelastic material. They assumed that the pores of the cancellous bone are filled with water. They did an analysis to determine which paths of reflection or transmission through the cancellous bone, cortical bone, and muscles have a significant sensitivity to the received waveform. This information is useful for estimating the material properties by employing an inverse algorithm. Grimes et al. (2012) used two types of longitudinal waves, fast and slow waves, as an effective tool for detecting osteoporosis. They conducted a test on a 4 mm thick cancellous bovine bone by generating an incident wave parallel to the cancellous bone alignment. Their numerical solution was in good agreement with the experimental results. Gilbert, Guyenne, and Li (2013a) proposed a visco-elastic model for wave propagation through a cancellous bone. They used the turning band method to provide a two-dimensional field for the distribution of pores in the medium. They used a second-order staggered-grid finite difference method to solve velocity-stress equations. They also studied the effect of porosity on some material properties such as Young's modulus, Poisson's ratio, and shear modulus. They obtained a good agreement between their proposed model and the homogenization technique. They concluded that the attenuation of ultrasonic waves depends not only on the viscous exchange in the pores but also heterogeneity of the medium. Gilbert, Guyenne, and Li (2013b) modeled a cancellous bone using the solid-fluid mixture theory. They showed that the amplitude of attenuation increases by an increase in

frequency which is in agreement with the experimental data and pertinent literature Jacobs, 2000; Ilic, Hackl, and Gilbert, 2010; Ilic, Hackl, and Gilbert, 2011. Gilbert, Guyenne, and Li (2014) numerically investigated ultrasonic attenuation through cancellous bone structures reconstructed from CT-scan and random realization. They proposed an ultrasonic theoretical expression for composite fluid-solid structures by a staggered-grid finite-difference scheme in the time domain. They investigated the ultrasound attenuation with respect to excitation frequency and structural porosity. Comparing results from these constructed bone structures showed the significant effect of bone micro-structure involving rods and plates on ultrasound attenuation. Sadouki et al. (2015) studied the wave propagation in cancellous bone using Biot-JKD's theory. They used a two-dimension infinite-length porous slab to model 1D wave propagation within a cancellous bone. They studied the effect of dynamic tortuosity due to viscous exchanges between the solid skeletal frame and pore fluid in high frequency ranges. In their model, they ignored the effect of transverse waves on the frequency response of the cancellous bone. They concluded that the sensitivity of the structural porosity and dynamic tortuosity of the cancellous bone with respect to the reflected waves strongly depends on the coupling between the fluid and solid phases of the cancellous bone. Chen, Gilbert, and Guyenne (2018) presented a numerical study to determine the mechanical parameters of a cancellous bone using acoustic waves. The cancellous bone was described as an isotropic and homogeneous medium. In the formulations, it was assumed that the cancellous bone sample is immersed in the water tank for the in-vitro experiments. Their model was able to derive accurately some parameters such as porosity using an inverse scheme. It should be noted that in the formulations, the dynamic tortuosity was assumed constant.

Hodaei, Rabbani, and Maghoul (2020) proposed an analytical model based on the Biot-JKD theory for acoustic wave propagation through bone-like porous media saturated with a viscous fluid. Similarly, they only considered the effect of longitudinal waves in their transient analytical solution. They also employed fractional calculus to describe the damping effect induced by the viscous exchange between the solid skeleton and pore fluid. Their transient analytical model was verified by complementary experimental data. Subsequently, they investigated the effect of structural porosity and pore fluid viscosity on solid and fluid stresses as well as scattering coefficients. As a result, they demonstrated that the porosity and pore fluid viscosity affect significantly the stress and scattering in a cancellous bone.

It is worth mentioning that in above-mentioned theoretical models, the cancellous bone-like materials have been modeled using a porous slab saturated with water whose two dimensions have an infinite length. It was also assumed that the ultrasonic waves propagate in

one direction via longitudinal waves. In other words, the effect of transverse waves on the ultrasonic response of a cancellous bone-like medium is neglected.

In a recent work, Hodaei, Maghoul, and Popplewell (2020) presented, for the first time, an analytical model using the Biot-JKD theory by considering the coupling effect of longitudinal and transverse waves on the reflected-transmitted pressure and stresses within a cancellous bone-like material. In this model, the bone-like porous material has an infinite length in two dimensions. It was shown that the effect of the transverse wave in characterizing a cancellous bone-like material filled with a relatively low viscous pore fluid, such as air, is negligible and the longitudinal wave can provide sufficient information. However, the effect of the transverse wave propagating through a bone-like porous medium filled with a relatively high viscous fluid, such as bone marrow, on reflected and transmitted pressures as well as stresses is significant and should not be ignored. Subsequently, considering the effect of the transverse wave in porous media interspersed with a relatively high viscous fluid provides some information which cannot be triggered by longitudinal waves alone. More precisely, their results showed that considering the effects of transverse waves is of paramount importance in characterizing the bone structures as the acoustical response related to some specific information of cancellous bone is created only by investigating such waves.

In the light of the above, this paper aims to explore, for the first time, the effect of both longitudinal and transverse acoustical waves on the response of a hollow cylindrical cancellous bone-like porous material saturated with a viscous fluid by presenting a three-dimensional (3D) biomechanical model. The analytical model is developed based on the Biot-JKD theory of viscoporoelasticty. In this model, the dynamic tortuosity is considered as a fractional exponent of frequency, so the analytical solution is found in the frequency domain due to lower computational costs and efforts. Consequently, the radial displacements, reflected pressures, and transmitted pressures for various porosities and wall thickness ratios, as an indicator of the bone condition (healthy versus osteoporosis), are described.

The structure of the paper is described as follows. First, after reviewing the literature, the mathematical developments of ultrasonic waves propagating through a fluid acoustic field and hollow cylindrical bone-like porous material saturated with a viscous fluid are presented in the frequency domain. The eigenvalues for governing equations which are defined as the squared complex wavenumbers are derived for longitudinal and transverse waves. Next, the general solutions in cylindrical coordinates are obtained. Then, the boundary conditions for inner and outer radii are described using the pressure field, fluid, and solid stresses and acoustic velocity field. The developed analytical model is then validated against the experimental

data found in the literature as well as the FEM numerical results for simplified limit cases. Finally, after discussing the results, the concluding remarks as well as appendices for the mathematical developments are provided.

5.2 Mathematical Developments

In this section, a general configuration of the problem is defined. Then, conventions and common assumptions are given. Next, the governing equations for acoustic waves propagating through a hollow cylindrical bone-like porous material saturated with a viscous fluid are described. Finally, the radial displacement and the reflected-transmitted pressure versus the wall thickness ratio and porosity for different frequencies are presented.

5.2.1 Problem Definition

Figure 5.1 illustrates a schematic of a hollow cylindrical cancellous bone-like porous material with an infinite length. This can represent a human femoral cancellous bone, which is the target of this study. The porous hollow cylinder is excited by a harmonic incident plane wave. The structure consists of a poroelastic medium saturated with a viscous fluid such as bone marrow while the hollow cavity is filled with air. The geometrical properties of the cylindrical bone are specified by the inner radius of b, the outer radius of a, and the wall thickness ratio of b/a. In this study, the cylindrical coordinate system (r, θ, z) is used in which, r, θ and z express the radial, circumferential, and axial directions, respectively; the (x,y,z) are the corresponding components of the Cartesian coordinate system.

The plane wave impinges upon the hollow cylindrical cancellous bone-like porous material with an incident angle of γ. Figure 5.1 represents the reflected and transmitted waves induced by the incident wave as well. Due to the incident wave impinging upon the medium, two types of ultrasonic waveforms including the longitudinal and transverse waves propagate through the cylindrical cancellous bone-like porous material. It should be noted that the cavity inside the cylindrical bone is assumed to be anechoic as the wave inside the cavity is an inward traveling wave. The inviscid acoustical media of outside and inside the hollow cylindrical bone are characterized by the speed and density of v_1, v_3 and ρ_1, ρ_3, respectively.
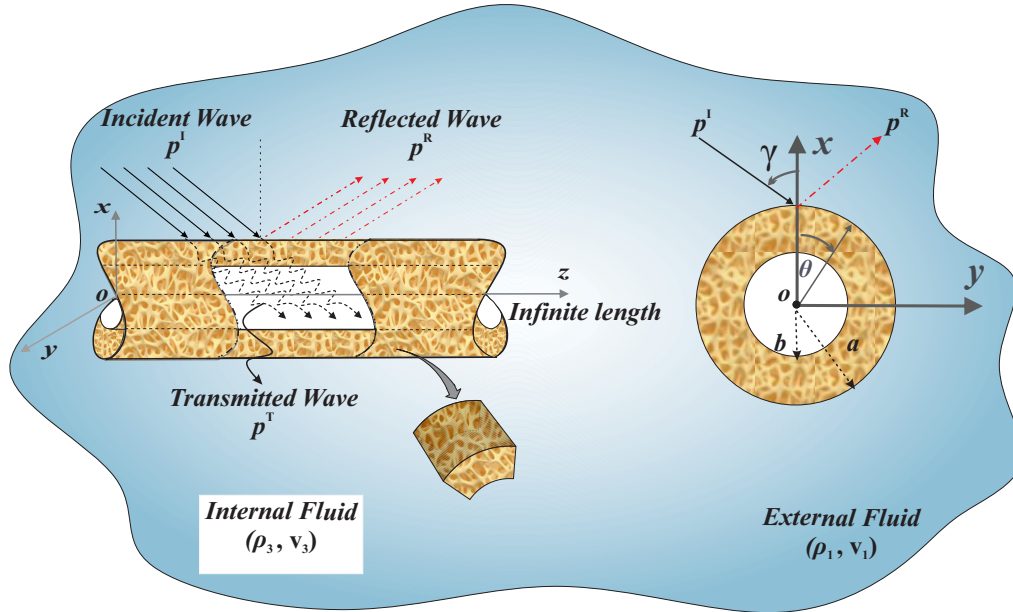
FIGURE 5.1: Left: Showing a 3D schematic of a cancellous bone-like medium along with its porosity distribution. The incident wave impinged upon the medium generates transmitted waves and reflected waves. Right: Showing the cross-section of the hollow cylindrical cancellous bone-like porous medium. γ designates the incident wave angle, and b and a are the medium outer and inner radii, respectively.

5.2.2 Assumptions and Conventions

In this problem, the macroscopic displacement vectors of the pore fluid, U_i, and the solid skeleton, u_i, are the state variables. The conventions and assumptions are as follows.

- The cylindrical cancellous bone-like porous medium, as a continuum body, is composed of a solid, deformable skeletal frame, s, filled with a viscous fluid, f.

- The poroelastic medium of the skeleton is isotropic, linear, and homogeneous.

- The deformation gradient of the solid skeletal frame, $\mathbf{F}$, is described as $\mathbf{F} = \mathbf{I} + \nabla \mathbf{u}$ in which $\mathbf{I}$ is the isotropic tensor of second-order with the Kronecker delta, δ_{ij}. The symbol $\nabla = (\partial/\partial \mathbf{r} + \frac{1}{r}\partial/\partial \theta + \partial/\partial \mathbf{z})$ is the gradient operator and $\mathbf{r} = \mathbf{r}(\mathbf{r}_0, t)$ is the Eulerian position vector at time t in a cylindrical coordinate system in an orthonormal basis. Also, $\mathbf{u}$ is the displacement vector of the solid skeletal frame which has the initial and current position vectors of $\mathbf{r}_0$ and $\mathbf{r}$ ($\mathbf{u}=\mathbf{r}-\mathbf{r}_0$), respectively.

- The linerized Green-Lagrange strain tensor, ε, is defined for infinitesimal deformation as $\varepsilon = \frac{1}{2}\left(\partial \mathbf{u}^T + \partial \mathbf{u}\right)$. Since the solid particles are incompressible, the volume dilatation of solid skeletal frame ε_{ii} is described to compensate the variations of interconnected pores (or porosity) ϕ.

5.2.3 Governing Equations

Fluid Acoustic Field

A harmonic incident plane wave with the acoustical pressure p_1^I travels through the surrounding fluid (external acoustical medium) and impinges on the bone-like porous material. The incident waves cause a reflected wave p_1^R from the cylindrical bone-like porous medium to the external fluid medium and a transmitted wave into the cavity p_3^T of the medium.

The acoustic wave equations for the inviscid fluid surrounding the bone-like cylinder (external acoustical medium) and filled the internal cavity can be written, respectively, as follows.

$$c_1^2 \nabla^2 \left(p_1^I + p_1^R \right) - \frac{\partial^2 \left(p_1^I + p_1^R \right)}{\partial t^2} = 0 \tag{5.1a}$$

$$c_3^2 \nabla^2 p_3^T - \frac{\partial^2 p_3^T}{\partial t^2} = 0 \tag{5.1b}$$

in which ∇^2 is Laplacian operator in the cylindrical coordinate system and p_1^R and p_3^T are the acoustical pressures of the reflected and transmitted waves, respectively. The mathematical descriptions for the incident waves, the reflected waves, and the transmitted waves are given in Appendix H.

Ultrasonic Waves in Cylindrical Cancellous Bone-Like Porous Medium

The Biot-JKD theory is employed to model acoustical wave propagation through a cancellous bone-like porous medium in high frequency ranges as follows:

$$\rho_{11} \frac{\partial^2 \mathbf{u}}{\partial t^2} + \rho_{12} \frac{\partial^2 \mathbf{U}}{\partial t^2} = P \nabla (\nabla . \mathbf{u}) + Q \nabla (\nabla . \mathbf{U}) - N \nabla \times (\nabla \times \mathbf{u}), \tag{5.2a}$$

$$\rho_{12} \frac{\partial^2 \mathbf{u}}{\partial t^2} + \rho_{22} \frac{\partial^2 \mathbf{U}}{\partial t^2} = Q \nabla (\nabla . \mathbf{u}) + R \nabla (\nabla . \mathbf{U}) \tag{5.2b}$$

in which $\mathbf{u}$ and $\mathbf{U}$ represent the state variables of solid and fluid displacement vectors in the cylindrical coordinate system defined as $\mathbf{u} = (u_r, u_\theta, u_z)$ and $\mathbf{U} = (U_r, U_\theta, U_z)$, respectively. The symbols ∇, $\nabla .$ and $\nabla \times$ are the gradient, divergence, and curl operators, respectively. N is defined as the shear modulus of the solid skeletal frame. Moreover, $\rho_{ij}(i, j = 1, 2)$ are the mass coefficients which relate the fluid and solid densities. P, Q, and R are poroelastic constants related to some measurable quantities which are thoroughly explained in Appendix J. Equation 5.2 can be written in the frequency domain by employing the Fourier transform function with respect to time (Hodaei, Rabbani, and Maghoul, 2020). Thus, Equation 5.2 in

the frequency domain will be

$$\tilde{\rho}_{11}(\omega)(-\omega^2)\mathbf{u}(\mathbf{r},\omega)+\tilde{\rho}_{12}(\omega)(-\omega^2)\mathbf{U}(\mathbf{r},\omega)=P\nabla(\nabla.\mathbf{u}(\mathbf{r},\omega))+ \tag{5.3a}$$

$$Q\nabla(\nabla.\mathbf{U}(\mathbf{r},\omega))-N\nabla\times(\nabla\times\mathbf{u}(\mathbf{r},\omega)),$$

$$\tilde{\rho}_{12}(\omega)(-\omega^2)\mathbf{u}(\mathbf{r},\omega)+\tilde{\rho}_{22}(\omega)(-\omega^2)\mathbf{U}(\mathbf{r},\omega)=Q\nabla(\nabla.\mathbf{u}(\mathbf{r},\omega))+$$

$$R\nabla(\nabla.\mathbf{U}(\mathbf{r},\omega)). \tag{5.3b}$$

in which $\tilde{\rho}_{ij}(\omega)$ includes the term of dynamic tortuosity indicating the damping characteristics of the medium given as,

$$\tilde{\alpha}(\omega)=\alpha_\infty\left(1+\frac{2}{\Lambda}\left(\frac{\eta}{\omega j\rho_f}\right)^{\frac{1}{2}}\right), \tag{5.4}$$

More explanations are provided in Appendix J.

5.2.4 Ultrasonic Waveforms

The ultrasonic waves propagate in poroelastic media with two longitudinal and transverse wave types described by scalar and vector displacement potentials, respectively. Employing the Helmholtz decomposition theorem, the displacement fields $\mathbf{u}$ and $\mathbf{U}$ in Equation 5.3, can be expressed as

$$\mathbf{u}=\nabla\phi^s(\mathbf{r},\omega)+\nabla\times\Psi^s(\mathbf{r},\omega),\quad\mathbf{U}=\nabla\phi^f(\mathbf{r},\omega)+\nabla\times\Psi^f(\mathbf{r},\omega) \tag{5.5}$$

in which $\phi^s(\mathbf{r},\omega)$ and $\phi^f(\mathbf{r},\omega)$ express the longitudinal wave scalar potentials for the solid skeletal frame and fluid, respectively, and $\Psi^s(\mathbf{r},\omega)$ and $\Psi^f(\mathbf{r},\omega)$ are the transverse wave vector potentials for the solid skeletal frame and fluid, respectively. Note that $\Psi^s(\mathbf{r},\omega)=(\psi_r^s,\psi_\theta^s,\psi_z^s)$ and $\Psi^f(\mathbf{r},\omega)=(\psi_r^f,\psi_\theta^f,\psi_z^f)$ with the condition $\nabla.\Psi(\mathbf{r},\omega)=0$. By substituting Equation 5.5 into Equation 5.3, one obtains

$$(-\omega^2)\Big[\tilde{\rho}_{11}(\omega)(\tilde{\phi}^s(\mathbf{r},\omega)+\tilde{\Psi}^s(\mathbf{r},\omega))+ \tag{5.6a}$$

$$\tilde{\rho}_{12}(\omega)(\tilde{\phi}^f(\mathbf{r},\omega)+\tilde{\Psi}^f(\mathbf{r},\omega))\Big]=$$

$$P\nabla\Big(\nabla.\big[\nabla\tilde{\phi}^s(\mathbf{r},\omega)+\nabla\times\tilde{\Psi}^f(\mathbf{r},\omega)\big]\Big)+$$

$$Q\nabla\Big(\nabla.\big[\nabla\tilde{\phi}^s(\mathbf{r},\omega)+\nabla\times\tilde{\Psi}^f(\mathbf{r},\omega)\big]\Big)-$$

$$N\nabla\times\nabla\times\big(\nabla\tilde{\phi}^f(\mathbf{r},\omega)+\nabla\times\tilde{\Psi}^f(\mathbf{r},\omega)\big),$$

$$(-\omega^2)\Big[\tilde{\rho}_{12}(\omega)(\nabla\phi^s(\mathbf{r},\omega)+\nabla\times\Psi^s(\mathbf{r},\omega))\tag{5.6b}$$

$$+\tilde{\rho}_{22}(\omega)(\nabla\phi^f(\mathbf{r},\omega)+\nabla\times\Psi^f(\mathbf{r},\omega))\Big]=$$

$$Q\nabla\Big(\nabla.[\nabla\phi^s(\mathbf{r},\omega)+\nabla\times\Psi^f(\mathbf{r},\omega)]\Big)+$$

$$R\nabla\Big(\nabla.[\nabla\phi^f(\mathbf{r},\omega)+\nabla\times\Psi^f(\mathbf{r},\omega)]\Big).$$

Equation 5.6 is defined as the equation of motion for the solid skeletal frame and fluid including the scalar and vector displacement potentials. Since the medium is isotropic, the longitudinal and transverse wave potentials can be decoupled by applying the divergence and curl operators to both Equation 5.6a and Equation 5.6b. Then,

$$-\omega^2\Big(\tilde{\rho}_{11}(\omega)\tilde{\phi}^s(\mathbf{r},\omega)+\tilde{\rho}_{12}(\omega)\tilde{\phi}^f(\mathbf{r},\omega)\Big)=\nabla^2\Big(P\tilde{\phi}^s(\mathbf{r},\omega)+Q\tilde{\phi}^f(\mathbf{r},\omega)\Big)\tag{5.7a}$$

and

$$-\omega^2\Big(\tilde{\rho}_{12}(\omega)\tilde{\phi}^s(\mathbf{r},\omega)+\tilde{\rho}_{22}(\omega)\tilde{\phi}^f(\mathbf{r},\omega)\Big)=\nabla^2\Big(Q\tilde{\phi}^s(\mathbf{r},\omega)+R\tilde{\phi}^f(\mathbf{r},\omega)\Big)\tag{5.7b}$$

and

$$-\omega^2\Big(\tilde{\rho}_{11}(\omega)\tilde{\Psi}^s(\mathbf{r},\omega)+\tilde{\rho}_{12}(\omega)\tilde{\Psi}^f(\mathbf{r},\omega)\Big)=-N\nabla\times\nabla\times\Big(\tilde{\Psi}^s(\mathbf{r},\omega)\Big)\tag{5.7c}$$

with

$$-\tilde{\rho}_{12}(\omega)\tilde{\Psi}^s(\mathbf{r},\omega)=\tilde{\rho}_{22}(\omega)\tilde{\Psi}^f(\mathbf{r},\omega)\tag{5.7d}$$

The scalar potentials $\tilde{\phi}^s(\mathbf{r},\omega)$ and $\tilde{\phi}^f(\mathbf{r},\omega)$ can be derived by rewriting Equation 5.7a and Equation 5.7b in the linear matrix form as follows.

$$\begin{pmatrix}-\rho_{11}\omega^2+A(j\omega)^{\frac{3}{2}}-P\nabla^2 & -\rho_{12}\omega^2-A(j\omega)^{\frac{3}{2}}-Q\nabla^2 \\ -\rho_{12}\omega^2-A(j\omega)^{\frac{3}{2}}-Q\nabla^2 & -\rho_{22}\omega^2+A(j\omega)^{\frac{3}{2}}-R\nabla^2\end{pmatrix}\begin{pmatrix}\tilde{\phi}^s(\mathbf{r},\omega) \\ \tilde{\phi}^f(\mathbf{r},\omega)\end{pmatrix}=0.\tag{5.8}$$

in which $A=\frac{1}{\Lambda_f}2\phi\rho_f\alpha_\infty\sqrt{\frac{\eta}{\rho_f}}$. Equation 5.8 can be rewritten in a more compact form,

$$\nabla^2\begin{pmatrix}\tilde{\phi}^s(\mathbf{r},\omega) \\ \tilde{\phi}^f(\mathbf{r},\omega)\end{pmatrix}=M\begin{pmatrix}\tilde{\phi}^s(\mathbf{r},\omega) \\ \tilde{\phi}^f(\mathbf{r},\omega)\end{pmatrix}\tag{5.9}$$

where the components of matrix M are given in Appendix I. Using the corresponding eigenvalue problem, the explicit form of two longitudinal waves propagating through a porous medium, fast and slow waves, can be derived. Hence, Equation 5.9 can be reformulated as

$$\nabla^2 \begin{pmatrix} \tilde{\phi}_1(\mathbf{r},\omega) \\ \tilde{\phi}_2(\mathbf{r},\omega) \end{pmatrix} = \begin{pmatrix} \tilde{\delta}_1^2(\omega) & 0 \\ 0 & \tilde{\delta}_2^2(\omega) \end{pmatrix} \begin{pmatrix} \tilde{\phi}_1(\mathbf{r},\omega) \\ \tilde{\phi}_2(\mathbf{r},\omega) \end{pmatrix} \tag{5.10}$$

or,

$$\nabla^2 \tilde{\phi}_{1,2}(\mathbf{r},\omega) + \tilde{\delta}_{1,2}^2(\omega) = 0 \tag{5.11}$$

in which $\tilde{\delta}_1^2(\omega)$ and $\tilde{\delta}_2^2(\omega)$ are the eigenvalues of matrix M and defined as the squared complex wavenumbers for two fast and slow dilatational waves given in Appendix K.

The scalar potentials related to the fast and slow waves, $\tilde{\phi}_1(\mathbf{r},\omega)$ and $\tilde{\phi}_2(\mathbf{r},\omega)$, can be associated with the scalar potentials related to the solid skeletal frame and fluid, $\tilde{\phi}^s(\mathbf{r},\omega)$ and $\tilde{\phi}^f(\mathbf{r},\omega)$, respectively. After some algebraic manipulations in Equation 5.7a, Equation 5.7b and Equation 5.11, we deduce the following matrix form

$$\begin{pmatrix} \tilde{\phi}^s(\mathbf{r},\omega) \\ \tilde{\phi}^f(\mathbf{r},\omega) \end{pmatrix} = \begin{pmatrix} 1 & 1 \\ \tilde{\mu}_1(\omega) & \tilde{\mu}_2(\omega) \end{pmatrix} \begin{pmatrix} \tilde{\phi}_1(\mathbf{r},\omega) \\ \tilde{\phi}_2(\mathbf{r},\omega) \end{pmatrix}. \tag{5.12}$$

Therefore, the scalar potentials related to the solid skeletal frame and fluid, $\tilde{\phi}^s(\mathbf{r},\omega)$ and $\tilde{\phi}^f(\mathbf{r},\omega)$, can be, respectively, written as,

$$\tilde{\phi}^s(\mathbf{r},\omega) = \tilde{\phi}_1(\mathbf{r},\omega) + \tilde{\phi}_2(\mathbf{r},\omega) \tag{5.13a}$$

$$\tilde{\phi}^f(\mathbf{r},\omega) = \tilde{\mu}_1(\omega)\tilde{\phi}_1(\mathbf{r},\omega) + \tilde{\mu}_2(\omega)\tilde{\phi}_2(\mathbf{r},\omega) \tag{5.13b}$$

where

$$\tilde{\mu}_i(\omega) = \frac{P\tilde{\delta}_i^2(\omega) - \omega^2\rho_{11}}{\omega^2\rho_{12} - Q\tilde{\delta}_i^2(\omega)} = \frac{Q\tilde{\delta}_i^2(\omega) - \omega^2\rho_{12}}{\omega^2\rho_{22} - R\tilde{\delta}_i^2(\omega)}, \quad i = 1,2. \tag{5.14}$$

The vector potential functions for the solid skeletal frame and fluid, $\tilde{\Psi}^s(\mathbf{r},\omega)$ and $\tilde{\Psi}^f(\mathbf{r},\omega)$, can be derived similarly. In this case, following Equation 5.7c and Equation 5.7d, the equation of motion for the transverse wave propagating through the cancellous bone-like porous medium will be as,

$$\nabla^2 \tilde{\Psi}^s(\mathbf{r},\omega) + \tilde{\delta}_3^2(\omega)\tilde{\Psi}^s(\mathbf{r},\omega) = 0 \tag{5.15}$$

in which $\tilde{\delta}_3^2(\omega)$ is the squared wave number for the transverse wave given by

$$\tilde{\delta}_3^2(\omega) = \frac{\omega^2}{N}\left(\frac{\tilde{\rho}_{11}\tilde{\rho}_{22} - \tilde{\rho}_{12}^2}{\tilde{\rho}_{22}}\right). \tag{5.16}$$

Furthermore, the ratio between the transverse wave vector potentials for the solid skeletal frame and fluid can be written as,

$$\mu_3 = \frac{\tilde{\Psi}^s(\mathbf{r},\omega)}{\tilde{\Psi}^f(\mathbf{r},\omega)} = -\frac{\rho_{22}}{\rho_{12}} \tag{5.17}$$

The general solutions for Equation 5.11 and Equation 5.15 in the cylindrical coordinate system are given in Appendix L (Allard and Atalla, 2009).

Furthermore, the displacement field induced by an acoustic wave in a cylindrical cancellous bone-like porous medium in the cylindrical coordinate is written

$$u_r(r,\theta,z,t) = \sum_{n=0}^{\infty} u_r^n(r)\cos(n\theta)e^{j(\omega t - K_z z)} \tag{5.18a}$$

$$U_r(r,\theta,z,t) = \sum_{n=0}^{\infty} U_r^n(r)\cos(n\theta)e^{j(\omega t - K_z z)} \tag{5.18b}$$

$$u_\theta(r,\theta,z,t) = \sum_{n=0}^{\infty} u_\theta^n(r)\sin(n\theta)e^{j(\omega t - K_z z)} \tag{5.18c}$$

$$U_\theta(r,\theta,z,t) = \sum_{n=0}^{\infty} U_\theta^n(r)\sin(n\theta)e^{j(\omega t - K_z z)} \tag{5.18d}$$

$$u_z(r,\theta,z,t) = \sum_{n=0}^{\infty} u_z^n(r)\cos(n\theta)e^{j(\omega t - K_z z)} \tag{5.18e}$$

$$U_z(r,\theta,z,t) = \sum_{n=0}^{\infty} U_z^n(r)\cos(n\theta)e^{j(\omega t - K_z z)} \tag{5.18f}$$

The components of the displacement vectors, $u_r^n(r)$, $U_r^n(r)$, $u_\theta^n(r)$, $U_\theta^n(r)$, $u_z^n(r)$ and $U_z^n(r)$, are more conveniently expanded in Appendix M. Accordingly, the components of the strain

tensor in terms of displacement in the cylindrical coordinate system can be derived as,

$$\varepsilon_{rr}(r,\theta,z,t) = \frac{\partial u_r(r,\theta,z,t)}{\partial r} \tag{5.19a}$$

$$\varepsilon_{rz}(r,\theta,z,t) = \frac{1}{2}\left(\frac{\partial u_r(r,\theta,z,t)}{\partial z} + \frac{\partial u_z(r,\theta,z,t)}{\partial r}\right) \tag{5.19b}$$

$$\varepsilon_{r\theta}(r,\theta,z,t) = \frac{1}{2}\left(\frac{\partial u_r(r,\theta,z,t)}{\partial \theta} + \frac{\partial u_\theta(r,\theta,z,t)}{\partial r} - \frac{u_\theta(r,\theta,z,t)}{r}\right) \tag{5.19c}$$

$$\varepsilon_{zz}(r,\theta,z,t) = \frac{\partial u_z(r,\theta,z,t)}{\partial z} \tag{5.19d}$$

$$\varepsilon_{\theta\theta}(r,\theta,z,t) = \frac{1}{r}\left(\frac{\partial u_\theta(r,\theta,z,t)}{\partial \theta} + u_r(r,\theta,z,t)\right) \tag{5.19e}$$

$$\varepsilon_{z\theta}(r,\theta,z,t) = \frac{1}{2}\left(\frac{\partial u_\theta(r,\theta,z,t)}{\partial z} + \frac{1}{r}\frac{\partial u_z(r,\theta,z,t)}{\partial \theta}\right). \tag{5.19f}$$

The solid stress, σ_{ij}^s, and fluid stress, σ_{ij}^f, for a porous medium saturated with a viscous fluid are obtained by (Fellah et al., 2004a)

$$\sigma_{ij}^s = (2N)\varepsilon_{ij} + \left((P-N)\nabla.u_{ij} + Q\nabla.U_{ij}\right)\delta_{ij}, \quad (i,j=r,\theta,z) \tag{5.20a}$$

$$\sigma_{ij}^f = -\phi p_f \delta_{ij} = (R\nabla.U_{ij} + Q\nabla.u_{ij})\delta_{ij}, \tag{5.20b}$$

in which δ_{ij} and p_f stand for the Kronecker delta function and the fluid pressure, respectively. The stress field for the solid skeletal frame and fluid can be derived by substituting the displacement vector components (Equation 5.18) and the strain tensor components (Equation 5.19) into Equation 5.20. Thus, the components of the stress tensor, after some algebraic manipulations, are written as

$$\sigma_{rr}(r,\theta,z,t) = \sum_{n=0}^{\infty} \sigma_{rr}^n(\mathbf{r})\cos(n\theta)e^{j(\omega t - k_z z)} \tag{5.21a}$$

$$\sigma_{r\theta}(r,\theta,z,t) = \sum_{n=0}^{\infty} \sigma_{r\theta}^n(\mathbf{r})\sin(n\theta)e^{j(\omega t - k_z z)} \tag{5.21b}$$

$$\sigma_{rz}(r,\theta,z,t) = \sum_{n=0}^{\infty} \sigma_{rz}^n(\mathbf{r})\cos(n\theta)e^{j(\omega t - k_z z)} \tag{5.21c}$$

$$\sigma^f(r,\theta,z,t) = \sum_{n=0}^{\infty} S^n(\mathbf{r})\cos(n\theta)e^{j(\omega t - k_z z)} \tag{5.21d}$$

where $S^n(\mathbf{r})$ is the pore fluid pressure and $\sigma_{rr}^n(\mathbf{r})$, $\sigma_{r\theta}^n(\mathbf{r})$, $\sigma_{rz}^n(\mathbf{r})$ express the stress in the radial, circumferential, and axial directions, respectively. A detailed expansion of these components are provided in Appendix N.

A close look at Equation 5.21 and Equation 5.18 reveals that the stress and displacement fields can be related to each other using the following matrix form described as

$$\{\sigma\}_{8\times1} = \{\Upsilon\}_{8\times8}\{C\}_{8\times1} \tag{5.22a}$$

$$\{u\}_{8\times1} = \{\Gamma\}_{8\times8}\{C\}_{8\times1} \tag{5.22b}$$

in which

$$C = \begin{bmatrix} A_1 & A_3 & B_1 & B_3 & C_1 & C_2 & C_3 & C_4 \end{bmatrix} \tag{5.23}$$

$$\sigma = \begin{bmatrix} \sigma_{rr}r=a & \sigma_{r\theta}r=a & \sigma_{rz}r=a & \sigma^f r=a & \sigma_{rr}r=b & \sigma_{r\theta}r=b & \sigma_{rz}r=b & \sigma^f r=b \end{bmatrix} \tag{5.24}$$

$$\mathbf{u} = \begin{bmatrix} u_r r=a & u_\theta r=a & u_z r=a & U_r r=a & u_r r=b & u_\theta r=b & u_z r=b & U_r r=b \end{bmatrix} \tag{5.25}$$

where $r = a$ and $r = b$ are the outer and inner boundary radii of the cylindrical bone-like porous medium. The vector C is obtained from Equation 5.22a and substituted into Equation 5.22b. Therefore, the relationship between the stress tensor and displacement vector fields will be as,

$$\{u\}_{8\times1} = [Q]_{8\times8}\{\sigma\}_{8\times1} \tag{5.26}$$

in which $[Q]_{8\times8} = [\Gamma]_{8\times1}[\Upsilon]_{8\times1}^{-1}$. The matrices Υ and Γ are composed of the components of the displacement vector and stress tensor fields. It should be noted that the displacement field $\{u\}_{8\times1}$ can be derived by substituting the stress field $\{\sigma\}_{8\times1}$, Equation 5.21, into Equation 5.26 along with employing the boundary conditions. The explicit expansions of Q_{ij}, Γ_{ij} and Υ_{ij}^{-1} are provided in Appendix O. The boundary conditions are derived next.

5.2.5   Acoustical Boundary Conditions

On the shared boundaries of the hollow cylindrical cancellous bone-like porous medium, the relationship between the radial displacement and pore fluid pressure at $r = a$ and $r = b$ can be written, respectively, as (Lee and Kim, 2002)

$$\frac{\partial\left(p_1^I(r,\theta,z,t)+p_1^R(r,\theta,z,t)\right)}{\partial r} = -\rho_1\frac{\partial^2 v_a^p(r,\theta,z,t)}{\partial t^2}, \quad r = a \tag{5.27a}$$

$$\frac{\partial p_3^T(r,\theta,z,t)}{\partial r} = -\rho_3\frac{\partial^2 v_b^p(r,\theta,z,t)}{\partial t^2}, \quad r = b$$

in which v_a^p and v_b^p are defined as the acoustic radial displacement fields at $r = a$ and $r = b$ given by

$$v_a^p(a,\theta,z,t) = (1-\phi)u_r(a,\theta,z,t) + \phi U_r(a,\theta,z,t) \tag{5.28a}$$

$$= \sum_{n=0}^{\infty} V_a^{pn}(a,\theta,z,t)\cos(n\theta)e^{j(\omega t - k_z z)}$$

$$v_b^p(b,\theta,z,t) = (1-\phi)u_r(b,\theta,z,t) + \phi U_r(b,\theta,z,t) \tag{5.28b}$$

$$= \sum_{n=0}^{\infty} V_b^{pn}(b,\theta,z,t)\cos(n\theta)e^{j(\omega t - k_z z)}$$

where V_a^{pn} and V_b^{pn} are the acoustic displacement coefficients at $r = a$ and $r = b$, respectively. Additionally, the stresses at the boundaries of a hollow cylindrical cancellous bone like porous medium where $r = a$ and $r = b$ can be defined as,

$$\sigma_{rr}(a,\theta,z,t) = -(1-\phi)\left(p_1^I(a,\theta,z,t) + p_1^R(a,\theta,z,t)\right) \tag{5.29a}$$

$$\sigma_{r\theta}(a,\theta,z,t) = 0 \tag{5.29b}$$

$$\sigma_{rz}(a,\theta,z,t) = 0 \tag{5.29c}$$

$$\sigma^f(a,\theta,z,t) = -\phi\left(p_1^I(a,\theta,z,t) + p_1^R(a,\theta,z,t)\right) \tag{5.29d}$$

$$\sigma_{rr}(b,\theta,z,t) = -(1-\phi)p_3^T(b,\theta,z,t) \tag{5.29e}$$

$$\sigma_{r\theta}(b,\theta,z,t) = 0 \tag{5.29f}$$

$$\sigma_{rz}(b,\theta,z,t) = 0 \tag{5.29g}$$

$$\sigma^f(b,\theta,z,t) = -\phi p_3^T(b,\theta,z,t)$$

By substituting Equation 5.29 into Equation 5.26 and simplifying the equations, we can derive the following matrix system given by

$$
\begin{bmatrix}
u_r(r=a) \\
u_\theta(r=a) \\
u_z(r=a) \\
U_r(r=a) \\
u_r(r=b) \\
u_\theta(r=b) \\
u_z(r=b) \\
U_r(r=b)
\end{bmatrix}
=
\begin{bmatrix}
Q_{11} & Q_{12} & Q_{13} & Q_{14} & Q_{15} & Q_{16} & Q_{17} & Q_{18} \\
Q_{21} & Q_{22} & Q_{23} & Q_{24} & Q_{25} & Q_{26} & Q_{27} & Q_{28} \\
Q_{31} & Q_{32} & Q_{33} & Q_{34} & Q_{35} & Q_{36} & Q_{37} & Q_{38} \\
Q_{41} & Q_{42} & Q_{43} & Q_{44} & Q_{45} & Q_{46} & Q_{47} & Q_{48} \\
Q_{51} & Q_{52} & Q_{53} & Q_{54} & Q_{55} & Q_{56} & Q_{57} & Q_{58} \\
Q_{61} & Q_{62} & Q_{63} & Q_{64} & Q_{65} & Q_{66} & Q_{67} & Q_{68} \\
Q_{71} & Q_{72} & Q_{73} & Q_{74} & Q_{75} & Q_{76} & Q_{77} & Q_{78} \\
Q_{81} & Q_{82} & Q_{83} & Q_{84} & Q_{85} & Q_{86} & Q_{87} & Q_{88}
\end{bmatrix}
\begin{bmatrix}
\sigma_{rr}(r=a) \\
\sigma_{r\theta}(r=a) \\
\sigma_{rz}(r=a) \\
\sigma^f(r=a) \\
\sigma_{rr}(r=b) \\
\sigma_{r\theta}(r=b) \\
\sigma_{rz}(r=b) \\
\sigma^f(r=b)
\end{bmatrix}
\tag{5.30}
$$

Four unknown coefficients, $u_r(r=a)$, $u_r(r=b)$, $U_r(r=a)$ and $U_r(r=b)$, in Equation 5.30 can be simultaneously obtained in terms of transmission and reflection coefficients denoted by p_{3n}^T and p_{1n}^R, respectively. In fact, by isolating the radial displacement components along with their corresponding stress boundary conditions in Equation 5.30, the following simplified matrix equation is obtained,

$$
\begin{bmatrix} u_r(r=a) \\ U_r(r=a) \\ u_r(r=b) \\ U_r(r=b) \end{bmatrix} = \begin{bmatrix} Q_{11} & Q_{14} & Q_{15} & Q_{18} \\ Q_{41} & Q_{44} & Q_{45} & Q_{48} \\ Q_{51} & Q_{54} & Q_{55} & Q_{58} \\ Q_{81} & Q_{84} & Q_{85} & Q_{88} \end{bmatrix} \begin{bmatrix} -(1-\phi)p_3^T(r=a) \\ -\phi p_3^T(r=a) \\ -(1-\phi)(p_1^R+p_1^I)(r=b) \\ -\phi(p_1^R+p_1^I)(r=b) \end{bmatrix}.
\tag{5.31}
$$

Therefore, the radial displacements at the inner and outer boundaries of a cylindrical bone-like porous medium are obtained in terms of p_{3n}^T and p_{1n}^R as follows.

$$u_r(b,\theta,z,t) = (\phi-1)Q_{15}(p_1^I(a)+p_1^R(a))- \tag{5.32a}$$

$$\phi Q_{18}(p_1^I(a)+p_1^R(a))+(\phi-1)Q_{11}p_3^T(b)-\phi Q_{14}p_3^T(b)$$

$$u_r(a,\theta,z,t) = (-1+\phi)Q_{55}(p_1^I(a)+p_1^R(a))- \tag{5.32b}$$

$$\phi Q_{58}(p_1^I(a)+p_1^R(a))+(-1+\phi)Q_{51}p_3^T(b)-\phi Q_{54}p_3^T(b)$$

$$U_r(b,\theta,z,t) = (\phi-1)Q_{45}(p_1^I(a))+p_1^R(a))- \tag{5.32c}$$

$$\phi Q_{48}(p_1^I(a))+p_1^R(a))+(\phi-1)Q_{41}p_3^T(b)-\phi Q_{44}p_3^T(b)$$

$$U_r(a,\theta,z,t) = (\phi-1)Q_{85}(p_1^I(a))+p_1^R(a))- \tag{5.32d}$$

$$\phi Q_{88}(p_1^I(a))+p_1^R(a))+(\phi-1)Q_{81}p_3^T(b)-\phi Q_{84}p_3^T(b)$$

Moreover, $u_r(r=a)$ and $u_r(r=b)$ have a relationship with p_{3n}^T, p_{1n}^R by considering Equation 5.27 and Equation 5.28. Subsequently, it is possible to find p_{3n}^T, p_{1n}^R along with $u_r(r=a)$, $u_r(r=b)$, $U_r(r=a)$ and $U_r(r=b)$. More precisely, the acoustic radial displacement fields v_a^p and v_b^p can be derived by substituting Equation 5.32 into Equation 5.28. Then, by replacing v_a^p and v_b^p into Equation 5.27 the following matrix equation for p_{3n}^T, p_{1n}^R is obtained

$$
\begin{bmatrix} p_{1n}^R \\ p_{3n}^T \end{bmatrix} = \begin{bmatrix} H_{11} & H_{12} \\ H_{21} & H_{22} \end{bmatrix}^{-1} \begin{bmatrix} \chi_{11} \\ \chi_{12} \end{bmatrix}.
\tag{5.33}
$$

Consequently, the amplitude of p_3^T and p_1^R are calculated as,

$$p_{3n}^T = \frac{\chi_{12}H_{11} - \chi_{11}H_{21}}{H_{11}H_{22} - H_{12}H_{21}} \tag{5.34a}$$

$$p_{1n}^R = \frac{\chi_{11}H_{22} - \chi_{12}H_{12}}{H_{11}H_{12} - H_{12}H_{21}}. \tag{5.34b}$$

The expansions of H_{11}, H_{12}, H_{21}, H_{22}, χ_{11}, χ_{12} are provided in Appendix P.

5.2.6 Computational Implementation

The governing equations presented above were implemented in a computational code. The computations were performed on a desktop computer powered by an Intel(R) Xeon(R) CPU E5-2630 @ 2.4 GHz. The parallel computing toolbox and multicore processors were used to speed up the computing effort (Sharma and Martin, 2009).

5.2.7 Validation

The analytical solutions for a bone-like porous material subjected to an acoustical wavefront presented in this study were compared against simplified limit cases found in the literature (Lee and Kim, 2003; Daneshjou et al., 2010; Talebitooti, Daneshjou, and Kornokar, 2016). The first limit case presented in (Lee and Kim, 2003) studied sound transmission through the cylindrical wall of a circular cylindrical cavity enclosed by a thin solid elastic shell subjected to a plane incident wave. The second limit case presented in (Daneshjou et al., 2010) dealt with acoustic transmission through an infinitely long and relatively thick FGM cylindrical shell composed of metal and ceramic (solid materials) with a power-law distribution of volume fraction through the thickness. The shell was immersed in a fluid with an external airflow and an oblique plane wave impinges on the external sidewall of the shell. The third study presented in (Talebitooti, Daneshjou, and Kornokar, 2016) investigated sound transmission through a poroelastic cylindrical shell in the presence of subsonic flow. To compare our analytical solutions developed in this study for hollow cylindrical cancellous bone-like porous materials subjected to an acoustical wavefront with the above-mentioned limit cases (Lee and Kim, 2003; Daneshjou et al., 2010), the fluid components in the solutions are neglected and the solutions are derived by approaching the porosity to zero. It is also worth noting that in these studies, the transmission loss coefficient was derived in the frequency domain for solid materials given as

$$TL = 10\,log_{10}\left(\frac{\Pi_I}{\Pi_T}\right) \tag{5.35}$$

where Π_I and Π_T are the incident and transmitted acoustic powers, respectively. More explanation of Π_I and Π_T are provided in Appendix Q. Figure 5.2 illustrates an excellent agreement for the transmission loss derived by the analytical solution presented in this study and that of the literature. The dynamic tortuosity defined in our solution is a function of frequency, so the transmission loss can be calculated even in the clinically relevant ultrasound frequency range which has not been addressed before. The pertinent literature (Talebitooti, Daneshjou, and Kornokar, 2016) used a constant dynamic tortuosity limiting the transmission loss to relatively low frequency ranges. The material properties used for these validations are given in Table 5.1.
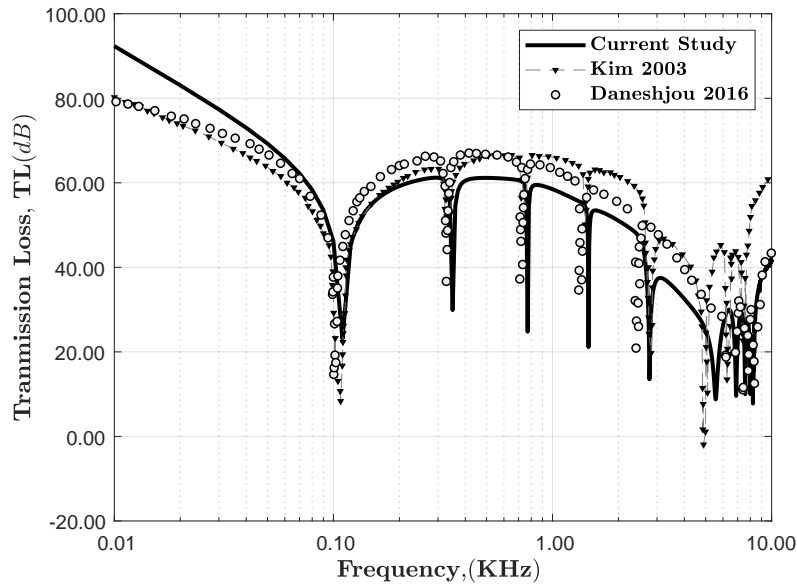
FIGURE 5.2: Comparison of the transmission loss calculated by the analytical solution presented in this study with the simplified limit cases found in the literature for isotropic shell made of steel (Lee and Kim, 2003; Daneshjou, Talebitooti, and Tarkashvand, 2017; Talebitooti, Daneshjou, and Kornokar, 2016). The validation shown by this study and the previous literature evaluates the robustness of the proposed analytical expression.

	Body	**external acoustical medium**	**Cavity**
Material	Steel	Air	Air
Density (kg/m^3)	7750	1.21	0.9389
Young's Modulus (GPa)	190	-	-
Poisson's ratio	0.30	-	-
Radius (m)	0.10	-	-
Thickness (mm)	1.00	-	-
Sound Speed (m/s)	-	388	343
Incident Angle (degree)	45	-	-

TABLE 5.1: Mechanical properties used in Figure 5.2.

In addition, the radial displacements and transmitted pressure obtained in this study are

compared with a FEM analysis for a simplified limit case. For this purpose, COMSOL Multiphysics software (Multiphysics, 1998) was employed to model wave propagation in an elastic medium in the frequency domain. The elastic medium is a solid hollow cylinder with no pores which has the same geometry and material properties of the model proposed in the analytical expression, Table 5.1. It should be noted that since the solid hollow cylinder modeled in COMSOL does not have any pores filled with viscous fluid, all the terms related to the viscous fluid removed from the proposed analytical solution derived in this study and let the porosity approach zero $\phi \to 0$. Then, the radial displacement and transmitted pressure obtained from COMSOL and the proposed analytical expression are compared. Figure 5.3 shows the radial displacements of a solid hollow cylinder modeled by COMSOL Multiphysics as well as a hollow cylindrical bone-like porous medium derived by the analytical solution presented in this study by neglecting the porosity and other terms related to the pore fluid. Figure 5.3a describes the radial displacement at the point where the incident wave impinges upon the cylinder ($\theta = 0$) and Figure 5.3b shows the radial displacement at the sideward direction, a right (90 degrees) angle with respect to the point of the incident wave ($\theta = 90°$). As can be seen, there is a good agreement between the current study and FEM results. Figure 5.4 illustrates the transmitted pressure inside the medium derived by the current study and COMSOL Multiphysics software in the frequency domain. The results show a good agreement between the transmitted pressure calculated in this study and FEM numerical solution. It is worth mentioning that the same as other FEM software, COMSOL has disadvantages such as difficulty in modeling infinitely large domains, running-time cost and the numerical instability in high frequencies. Likewise, the module of dynamic tortuosity defined in COMSOL is not a function of frequency, which means it is not able to compute radial displacement and transmitted pressure in high frequency ranges.

(A)

(B)
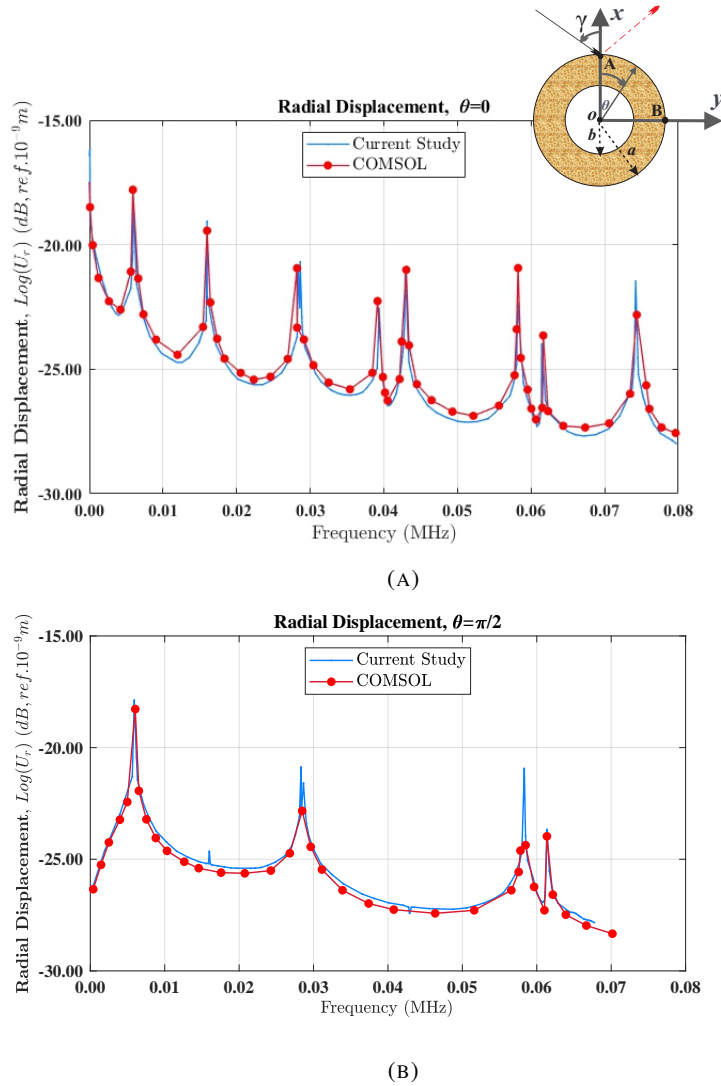
FIGURE 5.3: Figure (a) shows the radial displacement between the current study and FEM numerical results at the point where the incident wave impinges upon the cylinder $\theta = 0$. Figure (b) shows the radial displacement between the current study and FEM numerical results at the sideward direction $\theta = \pi/2$. A hollow cylinder modeled by COMSOL is solid (not porous). Hence for comparison, porosity approaches zero and the terms related to pore fluid in the proposed analytical solution presented in this study are removed.

Figure 5.5 and Figure 5.6 show the robustness of the proposed analytical solution by considering the effect of porosity and dynamic tortuosity. Figure 5.5 compares the transmission coefficients of a cancellous bone-like porous material filled with water for a two-dimensional porous slab with an infinite length, as presented by Fellah et al. Fellah et al., 2004a. In this case, the radius of the hollow cylinder in our model is assumed large enough to disregard the curvatures. The differences between the transmission coefficients obtained in this study and the one proposed by Fellah et al., 2004a can be attributed to the geometrical simplifications made in our study to simulate wave propagation in a 2D porous slab with an infinite
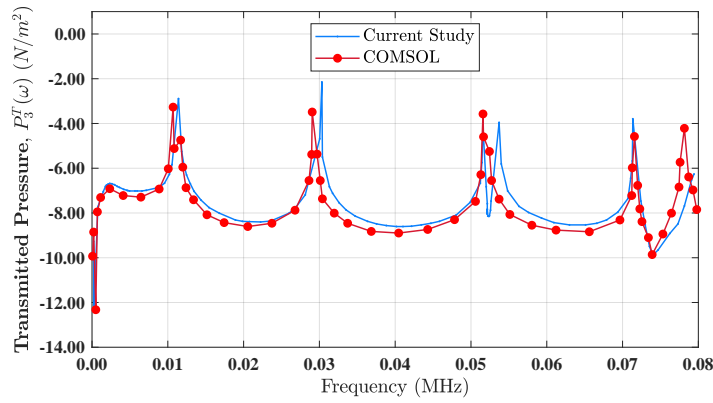
FIGURE 5.4: Comparison of the transmitted pressure obtained by the current study and FEM numerical results for a simplified limit case. In this verification, in the analytical solution derived in this study for a cylindrical bone-like porous medium the porosity approaches zero $\phi \to 0$ and all the terms related to pore fluid are removed. A hollow cylinder modeled in COMSOL is solid.

Material properties used for validation	Fellah et al. (2004a)	Bolton, Shiau, and Kang (1996)
Porosity	$\phi = 0.83$	$\phi = 0.9$
Bulk modulus of pore fluid (GPa)	$K_f = 2.28$	$K_f = 101 \times 10^{-6}$
Thickness (m)	0.007	0.00127
Dynamic tortuosity	1.05	α_∞ 1.05
Bulk modulus of porous skeletal frame (GPa)	$K_b = 3.3$	$K_b = 3.83$
Bulk modulus solid (GPa)	$K_s = 20$	$K_s = 4.6$
Viscous characteristic length (μm)	$\Lambda = 5$	$\Lambda = 5$
Density of solid (kg/m^3)	$\rho_s = 1960$	$\rho_s = 30$
Shear modulus of porous skeletal frame (GPa)	$N = 2.6$	$N = 0.92$
Bulk Young's modulus (GPa)	$E_s = 15$	$E_s = 2.76$
Bulk Poisson's ratio	$\nu = 0.37$	$\nu = 0.4$
Viscosity of pore fluid (kgm/s)	$\eta = 0.001$	$\eta = 1.81 \times 10^{-6}$
Density of pore fluid (kg/m^3)	$\rho_f = 1000$	$\rho_f = 1.225$

TABLE 5.2: Mechanical properties used for validation with Fellah et al. (2004a) and Bolton, Shiau, and Kang (1996).

length. In addition, in the solutions proposed by Fellah et al. Fellah et al., 2004a for a 2D porous slab with an infinite length, the effect of transverse waves was neglected. In spite of the differences in these two models, the comparison between the two transmission coefficients shows that they follow the same trend in broadband frequencies. Similarly, Figure 5.6 compares the transmission loss obtained in this study with the ones presented by Bolton et al. Bolton, Shiau, and Kang, 1996. Although the results are not exactly the same, however, a good agreement between the results exists. Material properties used for both validation are presented in Table 5.2 .
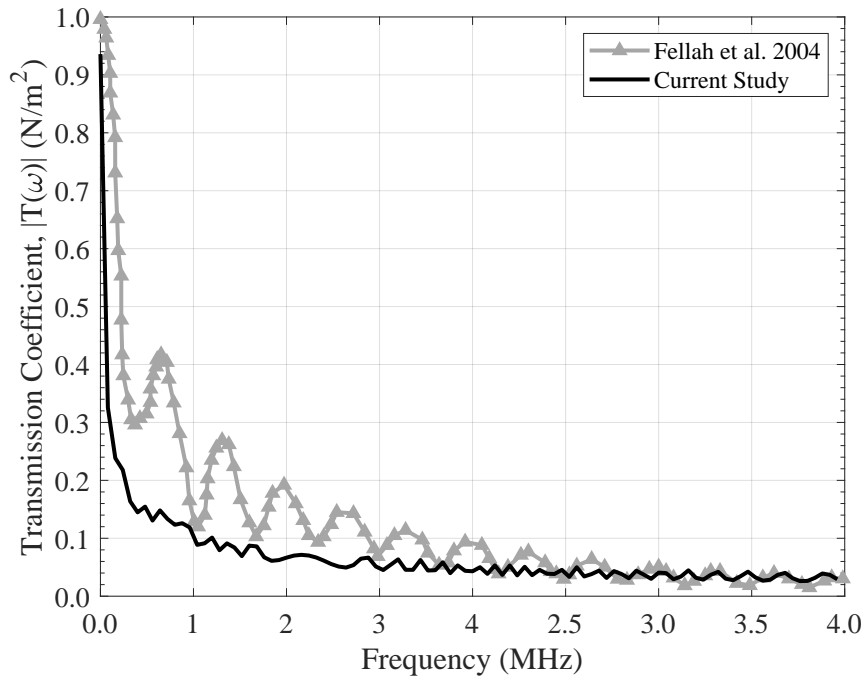
FIGURE 5.5: Comparison of the transmission coefficient obtained in the current study with the one presented by Fellah et al., 2004a for a 2D porous slab with an infinite length and a porosity of $\phi = 0.83$.
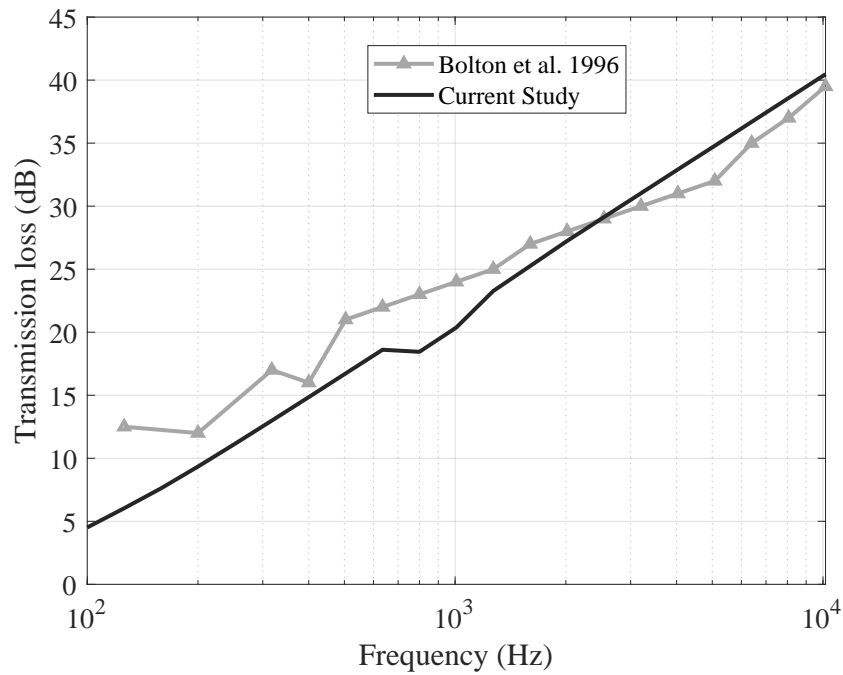
FIGURE 5.6: Comparison of the transmission loss obtained in the current study with the one presented by Bolton, Shiau, and Kang, 1996 for a panel structure lined with elastic porous material and a porosity of $\phi = 0.9$.

Bulk modulus of pore fluid	$K_f = 2$ **GPa**
Inner and outer radii for cylinder medium	a=0.015m, b=0.025 m
Bulk modulus of solid	$K_s = 20$ **GPa**
Dynamic tortuosity	α_∞ **=7.05**
Bulk modulus of porous skeletal frame	$K_b = 3.3$ **GPa**
Viscous characteristic length	$\Lambda = 5 \ \mu m$
Density of solid	$\rho_s = 1960$ kg/m^3
Shear modulus of porous skeletal frame	$N = 2.6$ **GPa**
Modulus of elasticity of solid	$E_s = 15$ **GPa**
Modulus of elasticity of porous skeletal frame	$E_b = 3.73$**GPa**
Poisson's ratio of solid	$v_s = 0.37$
Poisson's ratio of porous skeletal frame	$v_b = 0.35$
Viscosity of pore fluid	$\eta = 1.5$ kgm/s
Density of pore fluid	$\rho_f = 930$ kg/m^3

TABLE 5.3: Mechanical properties of the bone-like porous material used in this study.

5.3 Results and Discussion

The biomechanical model presented in this study is used to investigate the acoustical response of a hollow cylindrical bone-like porous medium saturated with a viscous fluid. As mentioned previously, it can be considered as a human femoral cancellous bone. An oblique plane wave impinges upon the poroelastic cylinder with the incident angle of γ with respect to the *x*-axis as shown in Figure 5.1. In this section, the radial displacements and transmitted-reflected pressures are calculated first at different locations of the hollow cylindrical medium. Then, the effect of porosity and wall thickness ratio as the indicators of bone conditions and bone loss are considered. Accordingly, the acoustical response of a cancellous bone-like porous structure with different porosities ranging from 0.0001 to 0.9 along with different selected wall thickness ratios ($b/a = 0.5, 0.75, 0.9$) is investigated. The mechanical properties of the hollow cylindrical cancellous bone-like porous material used in this study are similar to those presented by (Fellah et al., 2013; Buchanan and Gilbert, 2007) and shown in Table 5.3.

5.3.1 Effect of wall thickness ratio and incident wave angle on radial displacement response

The effect of wall thickness ratio on the radial displacement of a hollow cylindrical cancellous bone-like porous medium saturated with bone marrow subject to acoustical waves is investigated in this section. The porosity is assumed constant, $\phi = 0.0001$, while the wall

thickness ratio changes from 0.5 to 0.9. The effect of the wall thickness ratio on the radial displacement is studied for different incident wave angles: $\gamma = 0$, $\gamma = \pi/4$ and $\gamma = \pi/3$.

Figure 5.7 displays the radial displacements versus a relatively low frequency narrow-band which varies from 0 to 200 Hz. Figure 5.7a and Figure 5.7c illustrate the radial displacements induced by an acoustical wave for the wall thickness ratio of $b/a = 0.5$ at two different points located on the outer surface of the cylindrical bone-like material $\theta = 0$ and at sideward direction along $\theta = \pi/2$, respectively. By comparing these figures, it can be seen that the amplitude of the radial displacement of the cylindrical bone-like medium at sideward direction along $\theta = \pi/2$ is lower than that of forward direction $\theta = 0$ regardless of the angle of incident waves and wall thickness ratio. Increasing the wall thickness ratio decreases the number of resonance peaks of the system for a given excitation frequency range, (see Figure 5.7a to Figure 5.7b). In addition, the effect of γ is more significant by an increase in the wall thickness ratio at $\theta = 0$ while almost negligible at sideward direction along $\theta = \pi/2$. Therefore, it can be inferred that an increase in the incident wave angle from $\gamma = 0$ to $\gamma = \pi/3$ at a relatively low frequency narrowband is important at $\theta = 0$ and has no significant influence on radial displacements at $= \pi/2$ regardless of the wall thickness ratio.

We consider the effect of frequency-dependent dynamic tortuosity,Equation 5.4, for the first time, to consider the viscous exchange between the solid skeletal frame and pore fluid in high frequency ranges, which has a significant effect on wave attenuation. We increase the range of frequency and consider the effect of wall thickness ratio and the incident wave angles on the radial displacement at forward direction $\theta = 0$ and sideward direction along $\theta = \pi/2$. Figure 5.8 displays the radial displacements versus a relatively high frequency range for both forward and sideward directions. It should be noted that the range of frequency for both forward and sideward directions is selected in such a way to visibly distinguish the radial displacements induced by different incident wave angles. As can be seen, at frequencies around 200 kHz, the radial displacements at forward, $\theta = 0$, and sideward, $\theta = \pi/2$, directions are visibly distinguished for different angles of incident waves regardless of the wall thickness ratio. A close look at Figure 5.8a to Figure 5.8b illustrates that by increasing the incident wave angle from $\gamma = 0$ to $\gamma = \pi/3$, the radial displacements decrease regardless of the wall thickness ratio. In addition, an increase in the wall thickness ratio leads to a decrease in the number of resonance peaks of the system. The same trend can be observed in the other subfigures in Figure 5.8.

Figure 5.7 and Figure 5.8 show that the frequency response of radial displacement decreases by increasing the wall thickness ratio. Also, the wall thickness ratio can be considered as an indicator of the bone condition (healthy versus osteoporosis). The lower the wall thickness ratio, the healthier a bone is. Thus, one can conclude that the wall thickness ratio, regardless of the incident wave angle, affects the frequency response of the cylindrical bone-like porous medium. Generally speaking, by increasing the wall thickness ratio, for example, from 0.5 to 0.9, the number of resonance peaks of the system at $\theta = 0$ and range of frequency 200.1-200.18 kHz decreases from 11 to 3 picks, and furthermore, the difference between the resonant frequencies will be greater. Also, the incident wave angle has a more significant effect on the radial displacement of the crown (point $\theta = 0$) by increasing the wall thickness ratio.
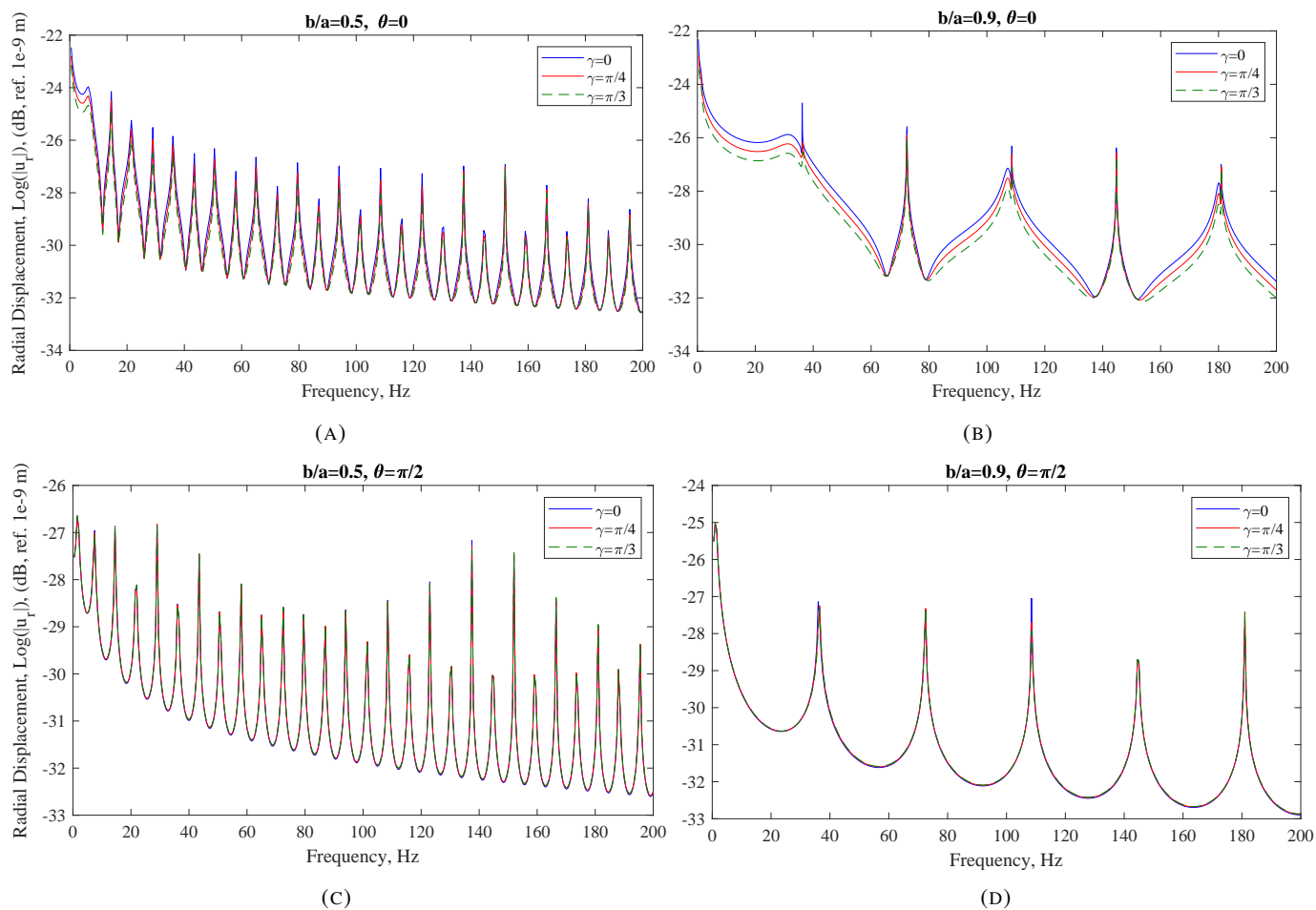
FIGURE 5.7: Figures (a) and (b) show the radial displacements versus frequency at a relatively low narrowband for the wall thickness ratio of $b/a = 0.5$ and $b/a = 0.9$, respectively, where the wave impinges upon the forward direction, $\theta = 0$, at the outer location of the bone structure. Figures (c) and (d) show the radial displacements versus frequency at a relatively low narrowband for the wall thickness ratio of $b/a = 0.5$ and $b/a = 0.9$, respectively, where the wave impinges upon sideward direction, $\theta = \pi/2$, at the outer location of the bone structure. In these figures, the medium with a porosity of $\phi = 0.0001$ is subject to different incident wave angles: $\gamma = 0$, $\pi/4$ and $\pi/3$ shown in blue, red, and green lines, respectively.
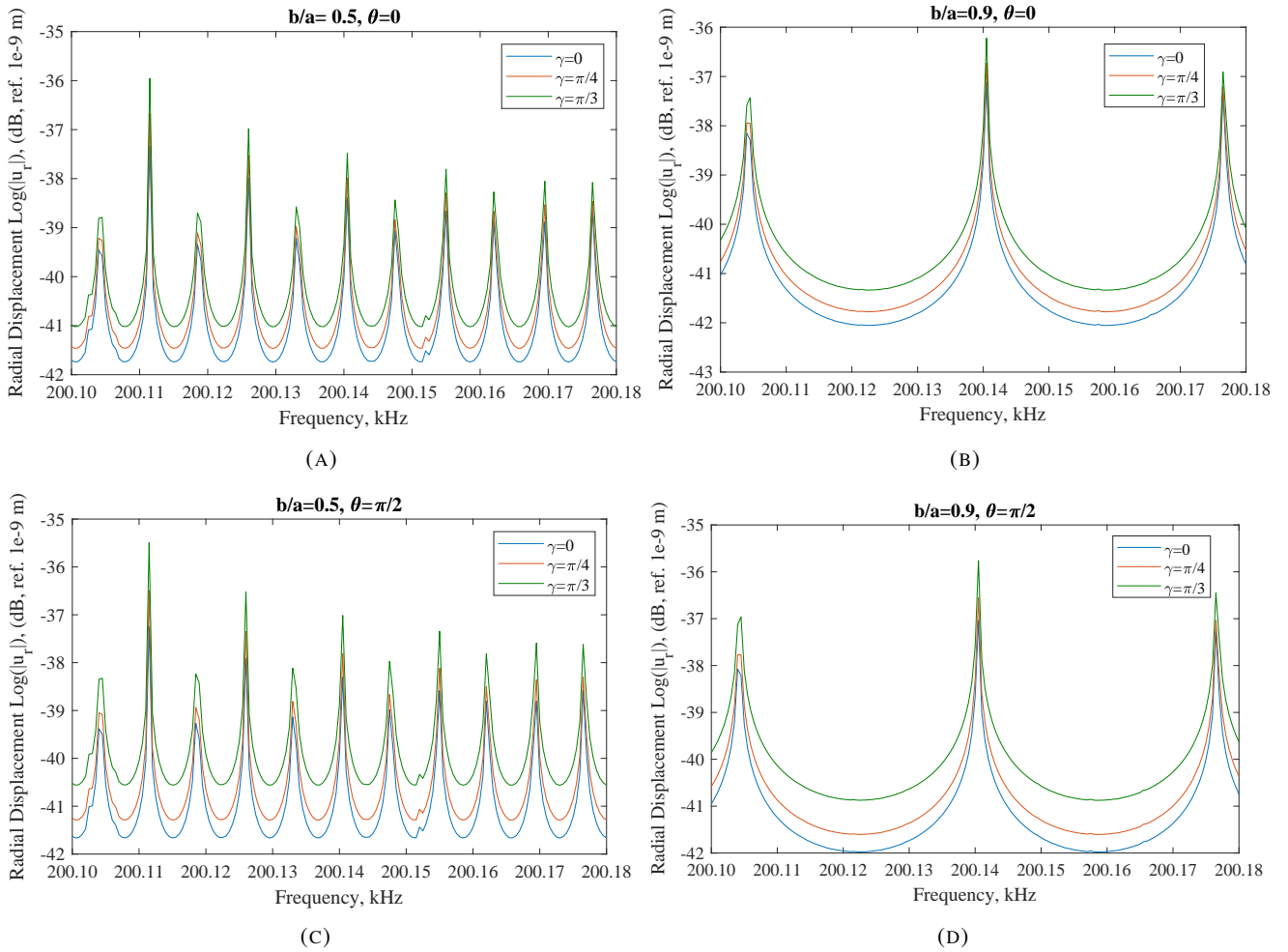
FIGURE 5.8: Figures (a) and (b) show the radial displacements versus frequency at a relatively high narrowband for the wall thickness ratio of $b/a = 0.5$ and $b/a = 0.9$, respectively, where the wave impinges upon forward direction, $\theta = 0$, at the outer location of the bone structure. Figures (c) and (d) show the radial displacements versus frequency at a relatively high narrowband for the wall thickness ratio of $b/a = 0.5$ and $b/a = 0.9$, respectively, where the wave impinges upon sideward direction, $\theta = \pi/2$, at the outer location of the bone structure. In these figures, the medium with a porosity of $\phi = 0.0001$ is subject to different incident wave angles: $\gamma = 0$, $\pi/4$, and $\pi/3$ shown in blue, red, and green lines, respectively.

5.3.2 Effect of porosity on radial displacement response

Figure 5.9 displays the radial displacements of a hollow cylindrical cancellous bone-like porous medium subjected to an incident acoustical wave with an incident angle of $\gamma = 0$. The results are presented for the point located at the crown of the hollow cylinder ($\theta = 0$) for the wall thickness ratios of 0.75 and 0.9 and the porosities of 0.0001, 0.001, and 0.01.

As can be seen, by increasing the porosity of the cancellous bone-like porous medium saturated with a relatively high viscous fluid (bone marrow) from $\phi = 0.0001$ to $\phi = 0.01$, the amplitude of the radial displacement decreases regardless of the wall thickness ratio. As a matter of fact, by increasing the porosity the stiffness of a porous structure decreases sharply. This can affect the frequency response of the medium

subjected to an ultrasonic waveform in terms of radial displacement. Also, increasing the porosity will provide more space for a viscous exchange between the viscous pore fluid (bone marrow) and the porous skeletal frame, which results in more attenuation. However, it is worth noting that, considering the porosity range studied in this section, the volume of the viscous pore fluid in comparison to the bulk volume is negligible. Hence, the effect of porosity on the stiffness of the porous structure is more significant with respect to the effect of viscous attenuation in the frequency response of the medium.

By comparing Figure 5.9a with Figure 5.9c as well as Figure 5.9b with Figure 5.9d, it can be concluded that for the same porosity, for instance $\phi = 0.0001$, the wall thickness ratio has a significant effect on the frequency response of the cancellous bone-like material in terms of radial displacement. Subsequently, the radial displacement of a cancellous bone-like material depends on not only the porosity but also the wall thickness ratio. These two factors are among the most important parameters in determining the bone conditions (healthy versus osteoporosis) as well. In the next section, the effective frequency range (low vs high frequency ranges) along with other associated circumstances will be investigated.

(A) Incident wave, b/a=0.75.

(B) Incident wave, b/a=0.75

(C) Incident wave, b/a=0.9

(D) Incident wave, b/a=0.9
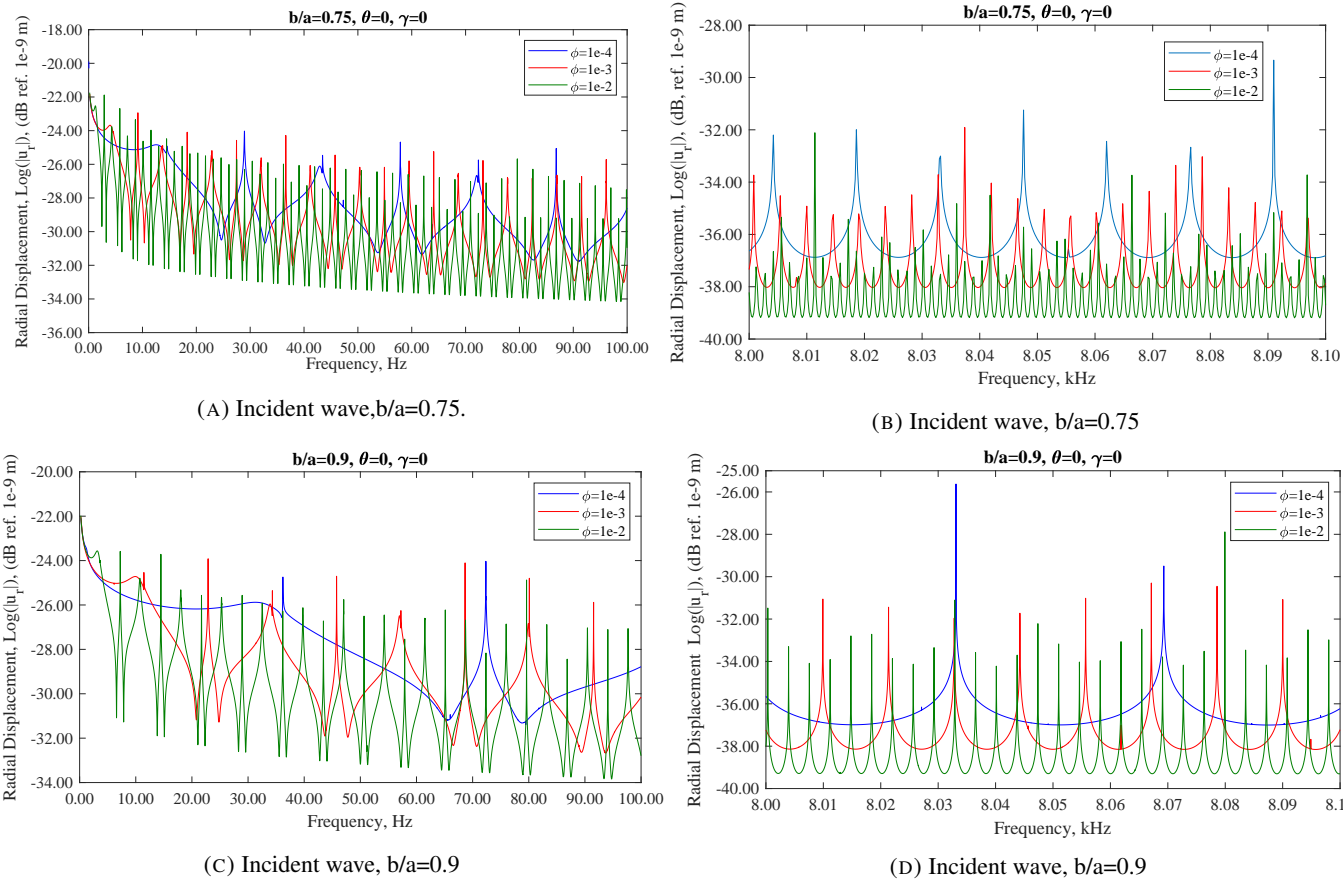
FIGURE 5.9: Figure (a) and (b) show the radial displacements for low and high frequency ranges, respectively. The wall thickness ratio of the bone structure is 0.75 and the incident wave impinges upon the bone normally, $\gamma = 0$, at the forward direction at the outer location of bone, $\theta = 0$. Figures (c) and (d) show the radial displacements for low and high frequency ranges, respectively. The wall thickness ratio of the bone structure is 0.9 and the incident wave impinges upon the bone normally, $\gamma = 0$, at the forward direction at the outer location of bone, $\theta = 0$. In these figures, the radial displacements for the porosities of $\phi = 0.0001$, $\phi = 0.001$, and $\phi = 0.01$ are shown in blue, red, and green lines, respectively.

5.3.3 Effect of excitation frequency on angular radial displacement

In this section, the effect of excitation frequencies at 800 Hz, 8 kHz, and 200 kHz on the angular radial displacement is investigated. Then, the effect of wall thickness ratios of 0.75, and 0.9 at different excitation frequencies is studied. Next, the effect of different porosities of 0.1, 0.5, and 0.9 on the angular radial displacement at different excitation frequencies is considered.

The effect of different excitation frequencies on the angular radial displacement for different porosities and wall thickness ratio is illustrated in Figure 5.10. It shows that the amplitude of the radial displacement in relatively low frequencies is higher than that of relatively high frequencies regardless of the wall thickness ratio. In addition, the pattern of angular radial displacement in relatively low frequency is almost symmetric while it is asymmetric in relatively high frequency.

Next, let consider the effect of porosity on the angular radial displacement. A comparison between Figure 5.10a and Figure 5.10b shows the effect of different porosities for the wall thickness ratio of $b/a = 0.75$ on the angular radial displacements. As can be seen, by increasing the porosity from $\phi = 0.1$ to $\phi = 0.9$, the radial displacement in each figure increases, but the rate of this increase for a higher frequency, 8 kHz, is more significant than that of a lower frequency, 800 Hz. In fact, by increasing the porosity the stiffness of the porous structure decreases, and subsequently the displacement increases. Note that the patterns are mainly distributed uniformly along with the forward and backward directions. Considering a relatively higher excitation frequency (f=200 kHz) as shown in Figure 5.10c, the radial displacement patterns are not distributed uniformly. It is shown that there is a forward and backward direction regarding the porosity. For example, for the porosity of $\phi = 0.1$ and $\phi = 0.5$, the pattern is mainly distributed along the backward direction (i.e., along $\theta = 0$ for an incident wave angle of $\gamma = 0$). However, it is distributed in forward and backward direction for porosity $\phi = 0.9$. In addition, the radial displacement decreases by increasing porosity from 0.1 to 0.5 which causes more marrow inside the pores leading more attenuation. However, the radial displacement increases by an increase in porosity from 0.5 to 0.9 due to a decrease in the stiffness of the medium causing more displacement. It is worth noting that changing the porosity from 0.5 to 0.9 increases the amount of bone marrow inside the pores which can lead to more attenuation, but it has much more influence on reducing the stiffness of medium.

The effect of wall thickness ratio is discussed next. Figure 5.10c and Figure 5.10f show the radial displacements versus angular locations for the excitation frequency of f=200 kHz and the incident wave angle of $\gamma = 0$ for the wall thickness ratios of $b/a = 0.75$ and $b/a = 0.9$. It can be seen that the radial displacement pattern at the same excitation frequency and the same porosity but with different wall thickness ratio is completely different. In fact, the stiffness of the bone structure is affected by a change in the wall thickness ratio. Quantifying the bone condition requires that different parameters such as excitation

frequency, wall thickness ratio, porosity, as well as the incident wave angle be considered. In other words, the response of a bone-like porous material to a waveform depends on the combination of these factors.

(A) Incident wave,b/a=0.75.

(B) Incident wave, b/a=0.75

(C) Incident wave, $b/a = 0.75$

(D) Incident wave, $b/a = 0.9$

(E) Incident wave, $b/a = 0.9$

(F) Incident wave, $b/a = 0.9$
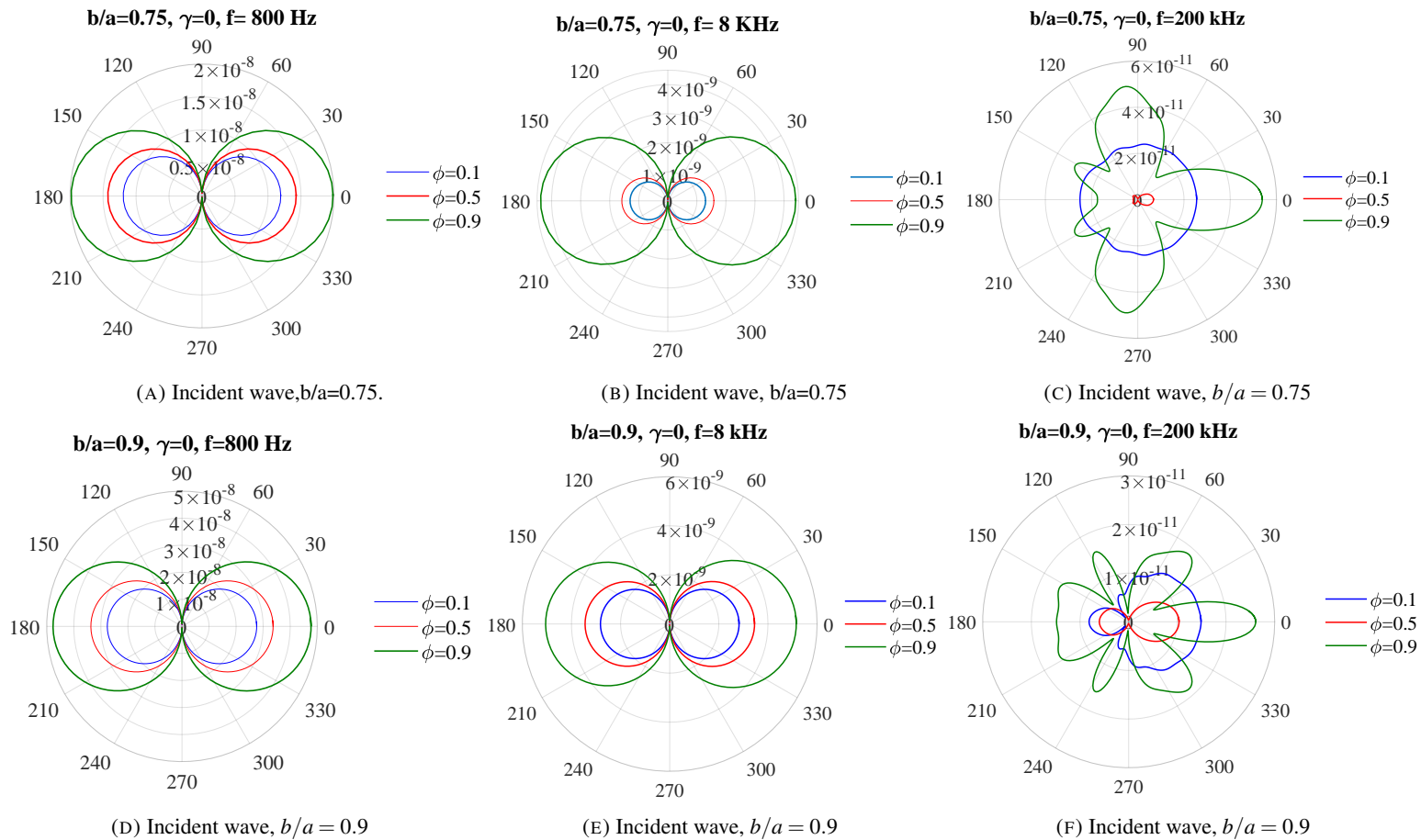
FIGURE 5.10: Figures (a), (b), and (c) show the angular displacements at the frequencies of 800 Hz, 8 kHz, and 200 kHz, respectively, for the wall thickness ratio of 0.75. Figures (d), (e) and (f) show the angular displacements at the frequencies of 800 Hz, 8 kHz, and 200 kHz, respectively, for the wall thickness ratio of 0.9. In these figures, the incident wave impinges upon the bone structure normally, $\gamma = 0$ and the radial displacements for the porosities of $\phi = 0.1$, $\phi = 0.5$, and $\phi = 0.9$ are shown in blue, red, and green lines, respectively.

5.3.4   Effect of porosity and wall thickness ratio on the transmitted and reflected pressures

In this section, the transmitted and reflected pressures at relatively low frequency, 800 Hz, and high frequency, 0.8 MHz, are studied. Then, the effect of wall thickness ratio of 0.5, 0.75, and 0.9 on the excitation frequencies is studied. Next, the effect of different porosities of 0.1, 0.5, and 0.9 at different excitation frequencies on the transmitted and reflected pressures is investigated.

Figure 5.11 and Figure 5.12 consider the transmitted and reflected pressures, respectively, with respect to different excitation frequencies. It is shown that the magnitude of transmitted pressures at relatively high frequencies is greater than that at a relatively low frequency range. Also, the magnitude of the reflected pressures increases by an increase in the excitation frequency regardless of the porosity and wall thickness ratio. In addition, the pattern of reflected and transmitted pressures are uniformly distributed at a relatively low frequency range and it changes to the forward and backward directions or distributed directionally in a relatively high frequency range.

To study the effect of porosity and wall thickness ratio on the transmitted and reflected pressures, a close look at Figure 5.11 shows that the magnitude of the transmitted wave at the frequency of 800 Hz increases by an increase in porosity regardless of the wall thickness ratio. It can be concluded that by increasing the porosity the stiffness of the medium decreases which leads to an increase in the magnitude of transmitted pressures. By the further increase in the excitation frequency to 0.8 MHz, it is observed that for the wall thickness ratio of $b/a = 0.5$, Figure 5.11d, the growth of porosity increases the magnitude of transmitted pressures, which is due to a decrease in the stiffness of the medium. However, the magnitude of transmitted pressures for a medium with a wall thickness ratio of $b/a = 0.75$, Figure 5.11e, increases by increasing the porosity from $\phi = 0.1$ to $\phi = 0.5$ and decreases when the porosity reaches to $\phi = 0.9$. As a matter of fact, increasing the porosity to $\phi = 0.5$ causes a decrease in the stiffness of the medium leading to an increase in the magnitude of the transmitted pressures. However, the growth of porosity from $\phi = 0.5$ to $\phi = 0.9$ increases the space for viscous exchange between the pore fluid (bone marrow) and the porous skeletal frame which results in more attenuation and decreasing the magnitude of transmitted pressures. In addition, for the wall thickness ratio of $b/a = 0.9$ as shown in Figure 5.11f, the stiffness of the medium severely decreases by increasing the porosity which causes the magnitude of the transmitted pressure to increase.

Regarding the reflected pressures, it can be seen that at a relatively low frequency, 800 Hz, the pattern is symmetric regardless of the wall thickness and porosity. In fact, the wall thickness ratio and the porosity have no significant influence on the reflected pressures at the low frequency of 800 Hz. By increasing the excitation frequency from 800 Hz to 0.8 MHz, the effect of wall thickness ratio as well as porosity is striking. As can be seen, for the wall thickness ratios from $b/a = 0.5$ to $b/a = 0.9$, Figure 5.12d-Figure 5.12f, the magnitude of reflected pressures decreases by increasing porosity from $\phi = 0.1$ to $\phi = 0.5$. In fact, the effect

of damping increases when the viscous exchange between the pore fluid and skeletal frame increases in the medium. The damping effect also increases by an increase in porosity from $\phi = 0.5$ to $\phi = 0.9$, however, the rate of decrease in the stiffness of the medium is more than that of increasing the damping effect, so the magnitude of reflected pressures decreases.
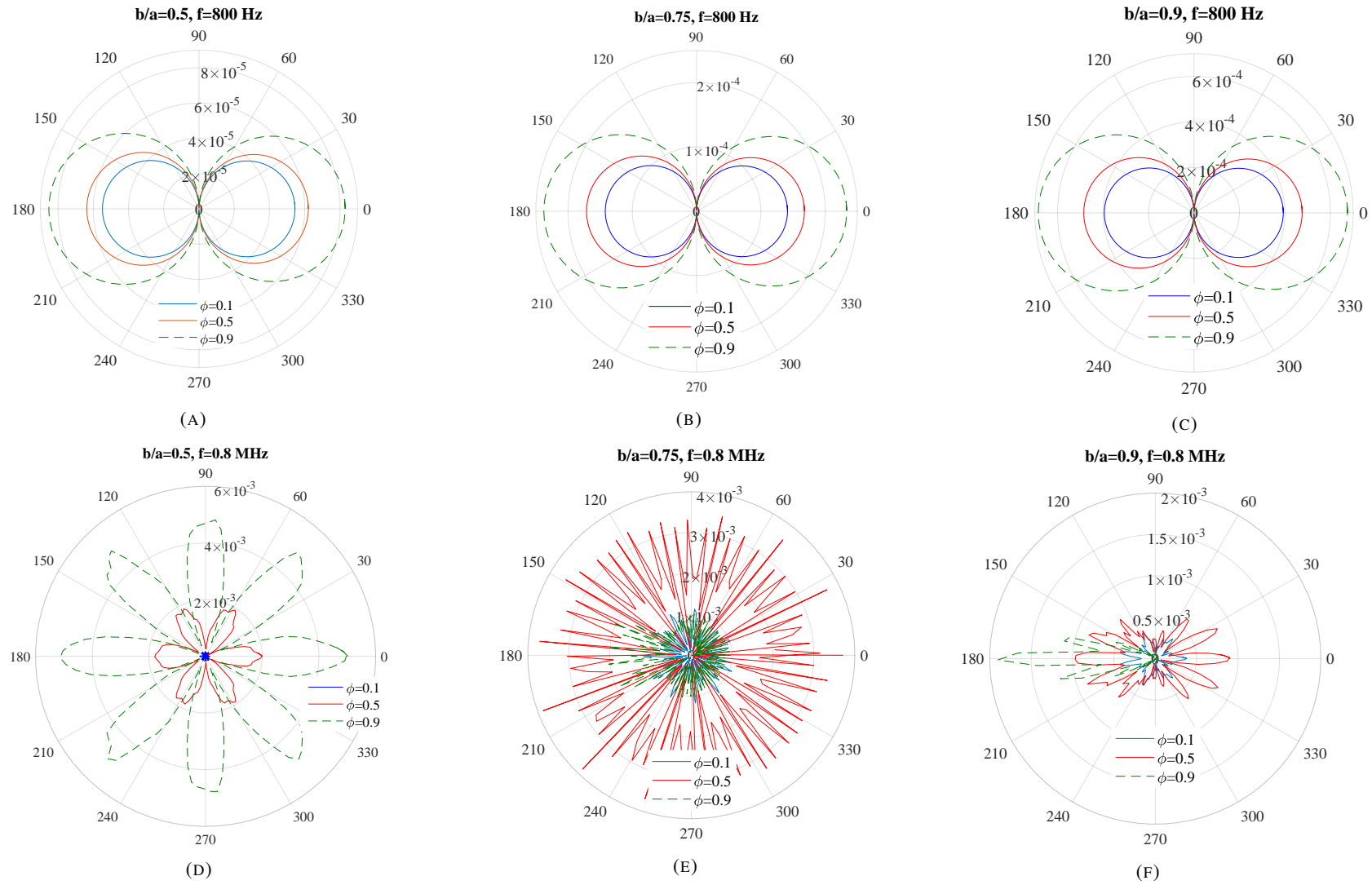
FIGURE 5.11: Figures (a), (b), and (c) show the angular transmitted pressure at a relatively low frequency of 800 Hz for the wall thickness ratios of 0.5, 0.75, and 0.9, respectively. Figures (d),(e), and (f) show the angular transmitted pressure at a relatively high frequency of 0.8 MHz for the wall thickness ratios of 0.5, 0.75, and 0.9, respectively. The incident wave impinges upon the bone structure normally, $\gamma = 0$. In these figures, the angular transmitted pressure for the porosities of $\phi = 0.1$, $\phi = 0.5$, and $\phi = 0.9$ are shown in blue, red, and green lines, respectively.
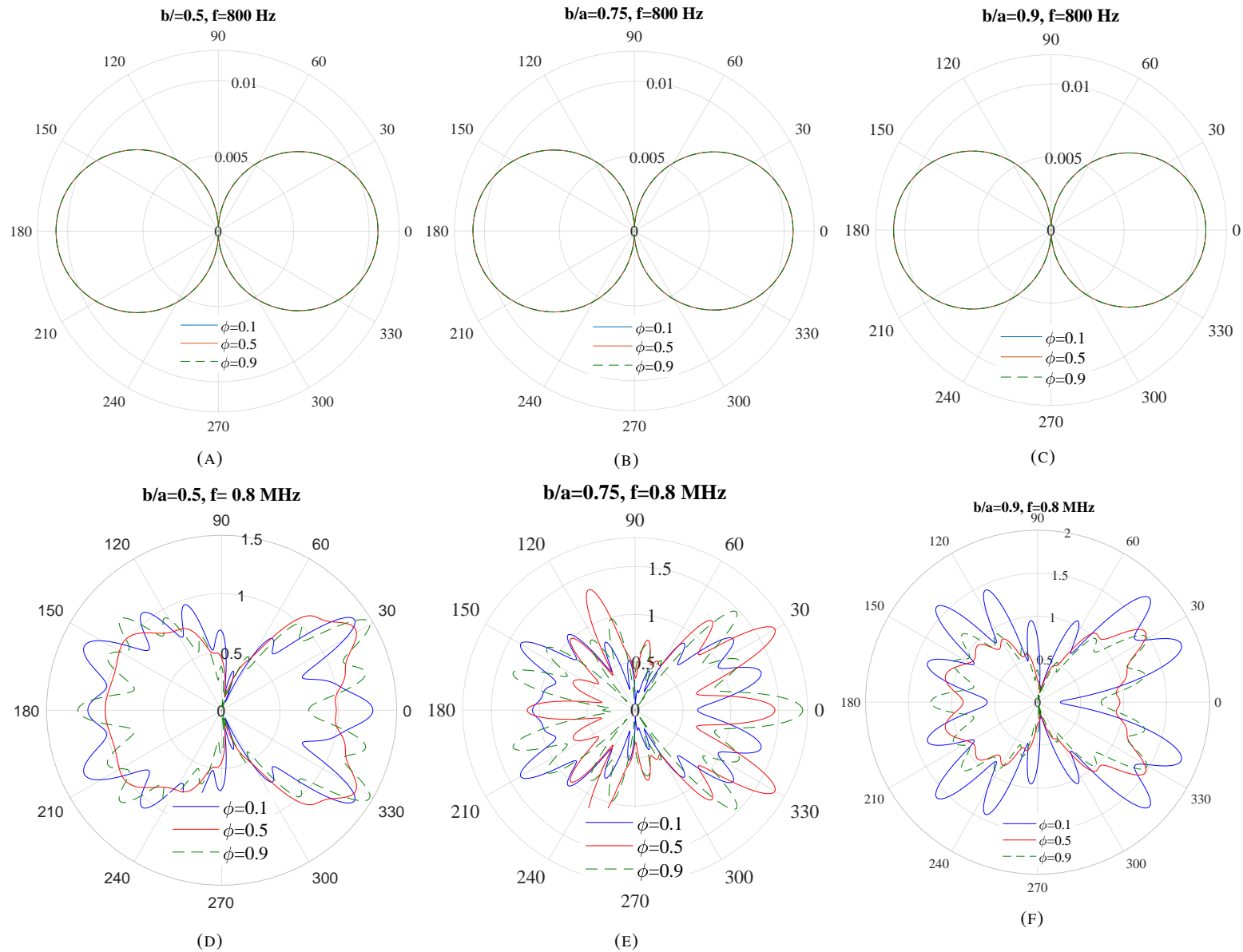
FIGURE 5.12: Figures (a), (b), and (c) show the angular transmitted pressure at a relatively low frequency of 800 Hz for the wall thickness ratios of 0.5, 0.75, and 0.9, respectively. Figures (d), (e), and (f) show the angular transmitted pressure at a relatively high frequency of 0.8 MHz for the wall thickness ratio of 0.5, 0.75, and 0.9, respectively. The incident wave impinges upon the bone structure normally, $\gamma = 0$. In these figures, the angular reflected pressure for the porosities of $\phi = 0.1$, $\phi = 0.5$, and $\phi = 0.9$ are shown in blue, red, and green lines, respectively.

5.4   Concluding Remarks

The analytical modeling of a hollow cylindrical cancellous bone-like porous media saturated with a viscous fluid and subjected to acoustic waves is developed based on the Biot-JKD theory. The radial displacements and scattering operators are obtained using the well-known Helmholtz decomposition. The effect of porosity, wall thickness ratio, incident wave angle, and excitation on the radial displacements and scattering operators at different frequencies for forward $\theta = 0$ and sideward $\theta = \pi/2$ locations at the outer surface of the hollow cylinder are investigated.

It is concluded that the radial displacement decreases by increasing the wall thickness ratio for low porosities, and the radial displacement for the sideward direction is smaller than that of the forward direction regardless of the thickness ratio and incident wave angle. In addition, by increasing the porosity the radial displacement decreases because increasing the porosity results in an increase in viscous exchanges between the pore fluid and solid skeletal frame leading to higher attenuations. Moreover, the effect of incident wave angle on the radial displacement in relatively high frequencies is more significant than that in relatively low frequencies regardless of the porosity. Also, the effect of the incident wave angle in the forward direction is more significant than in the sideward direction regardless of the excitation frequencies.

In a relatively high frequency range, the angular radial displacement at lower wall thickness ratios raises by increasing the porosity to $\phi = 0.5$ and decreases for porosities higher than this threshold. However, for higher wall thickness ratios, the angular radial displacement reduces by increasing the porosity to $\phi = 0.5$ and increases for porosities higher than this threshold. It is worth noting that the pattern distribution of the angular displacement in relatively low frequency ranges is symmetric while it is asymmetric in relatively high frequencies regardless of the incident wave angle and wall thickness ratio.

It can be concluded that bone characterization using quantitative ultrasound techniques is not only based on the mineral density, as used currently by electromagnetic wave-based tools, but also other biomechanical factors such as the porosity, viscosity of pore fluid, and wall thickness ratio of a cancellous bone structure. Moreover, the pattern distribution of the reflected pressure can be an indicator of the bone condition (healthy versus osteoporosis or osteopenia) of a cancellous bone. The pattern distribution of the reflected-transmitted pressure is symmetric for relatively low frequencies while it is directional for relatively high frequencies regardless of the porosity and wall thickness ratio.

To investigate the bone condition (healthy versus osteoporosis), it is essential to consider different biomechanical parameters such as porosity, wall thickness ratio, and the range of excitation frequency

(low or high); the radial displacement and scattering operators of a bone specimen should be measured at a relatively high frequency. Any asymmetric pattern distribution of radial displacements or asymmetric or directional pattern distribution of both transmitted and reflected signals may be a sign of bone loss.

Chapter 6

Conclusion and Future Work

In this research, the wave propagation in bone like-porous materials saturated with a viscous fluid is studied in the time and frequency domains. The analytical solutions derived in this research are based on the Biot-JKD theory. Accordingly, the effect of viscous exchange between the solid skeletal frame and pore fluid has been considered.

In summary, the major contributions made in this research are as follows: (*i*) considering the effect of transverse waves, in addition to longitudinal waves, in characterizing a porous bone-like material filled with a relatively low (e.g. air) or high viscous fluid (e.g. bone marrow); (*ii*) developing a 3-D acoustical model using the Biot-JKD theory to model coupled longitudinal and transverse wave propagation in porous bone-like media. The effect of tortuosity in high frequency is also considered.

The limitation of this research are as follow: (*i*) considering the effect of cortical bone is ignored;(*ii*) inside and outside the bone is filled with air and the effect of soft tissues such as skins, muscles,and blood vessels are neglected; (*iii*) the shape and section of a three dimensional model to mimic a bone in this study are limited to a cylinder and circle respectively; (*iv*) it is assumed that the bone is isotropic and ultrasonic waves can be decoupled using Helmholtz's decomposition.

6.1 Recommendations for Future Work

The experimental acoustical tests, which was the last part of this PhD research, have been interrupted due to the COVID-19 pandemic. Acoustical testing should be performed to experimentally investigate the effect of transverse waves on the response of a porous bone-like material subject to acoustical waves, measure the transmitted and reflected waves, and thoroughly validate the 2-D and 3-D computational solvers developed in this study.

The recommendations for future work are as follows:

- Developing an analytical expression for cortical bone in addition to cancellous bone and then comparing with in-vitro experimental results. The significance of considering

cortical bone would be minimizing the systematic error in estimating bone characteristics using inverse techniques.

- Developing an analytical expression for cortical-cancellous bone by considering the soft tissue inside and outside a bone such as muscles, blood vessels, red-yellow bone marrow and skin. The estimated parameters at this section can be compared with those of obtained from ex-vivo experimental results.

- Developing an analytical expression for cortical-cancellous bone using canonical shape with elliptical cross-section to mimic a real bone sample along with soft tissues.

- Finally, a wave field inversion algorithm should be developed for the processing of in-vitro and in-vivo measurements and bone characterization using the computational solvers.

Appendix A

Coefficients in Eigenvalue and Eigenvector Expressions used in Chapter 3

The mathematical expressions for the coefficients used in the expressions of eigenvalues and eigenvectors (Equation 3.20):

$$\rho_1 = \frac{A1 + B1}{C1 + D1} \tag{A.1}$$

$$A1 = K_s \left[\frac{E_b K_f \left(-2\rho_{12}\phi - \rho_{22}(\phi - 1) \right)}{E_b K_f + 3(2v_b - 1)K_s \left(-\phi K_f + K_f + \phi K_s \right)} + \frac{\rho_{11}\phi^2}{-\frac{E_b}{3K_s - 6v_b K_s} + \frac{\phi K_s}{K_f} - \phi + 1} \right],$$

$$B1 = \frac{K_s^2 \left(3(\phi - 1)(2v_b - 1)K_f \left(2\rho_{12}\phi + \rho_{22}(\phi - 1) \right) - \rho_{22}\phi E_b \right)}{E_b K_f + 3(2v_b - 1)K_s \left(-\phi K_f + K_f + \phi K_s \right)} + \frac{2\rho_{22} E_b}{3(v_b + 1)},$$

$$C1 = \phi^2 K_s \left(\frac{\frac{K_s \left(E_b \left((\phi - 1)K_f + \phi K_s \right) - 3(\phi - 1)^2 (2v_b - 1)K_f K_s \right)}{3(1 - 2v_b)K_s \left(\phi K_s - (\phi - 1)K_f \right) - E_b K_f} + \frac{2E_b}{3(v_b + 1)}}{-\frac{E_b}{3K_s - 6v_b K_s} + \frac{\phi K_s}{K_f} - \phi + 1} \right),$$

$$D1 = \phi^2 K_s \left(\frac{K_f^2 K_s \left(E_b - 3(\phi - 1)(2v_b - 1)K_s \right)^2}{\left(E_b K_f + 3(2v_b - 1)K_s \left(\phi K_s - (\phi - 1)K_f \right) \right)^2} \right).$$

$$\rho_2 = \frac{A2 + B2}{C2 + D2}, \tag{A.2}$$

$$A2 = -2\eta\,\alpha_\infty \left(\frac{2\phi K_f K_s \left(3(\phi - 1)(2v_b - 1)K_s - E_b \right)}{E_b K_f + 3(2v_b - 1)K_s \left(\phi K_s - (\phi - 1)K_f \right)} \right),$$

$$B2 = 2\eta\,\alpha_\infty \left[\frac{K_s \left(\mathrm{E}_b \left((\phi-1)K_f + \phi K_s\right) - 3(\phi-1)^2\,(2v_b-1)\,K_f K_s\right)}{3\,(1-2v_b)\,K_s\,(\phi K_s - (\phi-1)K_f) - \mathrm{E}_b K_f} \right.$$
$$\left. + \frac{\phi^2 K_s}{-\frac{\mathrm{E}_b}{3K_s - 6v_b K_s} + \frac{\phi K_s}{K_f} - \phi + 1} + \frac{2\mathrm{E}_b}{3\,(v_b+1)} \right],$$

$$C2 = \Lambda \phi K_s \sqrt{\frac{\eta}{\rho_f}} \left[\frac{\frac{K_s \left(\mathrm{E}_b \left((\phi-1)K_f + \phi K_s\right) - 3(\phi-1)^2 (2v_b-1) K_f K_s\right)}{3(1-2v_b)K_s\left(\phi K_s - (\phi-1)K_f\right) - \mathrm{E}_b K_f} + \frac{2\mathrm{E}_b}{3(v_b+1)}}{-\frac{\mathrm{E}_b}{3K_s - 6v_b K_s} + \frac{\phi K_s}{K_f} - \phi + 1} \right],$$

$$D2 = -\Lambda \phi K_s \sqrt{\frac{\eta}{\rho_f}} \left[\frac{K_f^2 K_s \left(\mathrm{E}_b - 3(\phi-1)\,(2v_b-1)\,K_s\right)^2}{\left(\mathrm{E}_b K_f + 3\,(2v_b-1)\,K_s\,(\phi K_s - (\phi-1)K_f)\right)^2} \right].$$

$$\rho_3 = \frac{A3}{B3 - C3}, \tag{A.3}$$

$$A3 = (\rho_{12}^2 - \rho_{11}\rho_{22})/(\phi^2 K_s),$$

$$B3 = \frac{K_f^2 K_s \left(\mathrm{E}_b - 3(\phi-1)\,(2v_b-1)\,K_s\right)^2}{\left(\mathrm{E}_b K_f + 3\,(2v_b-1)\,K_s\,(\phi K_s - (\phi-1)K_f)\right)^2},$$

$$C3 = \frac{\frac{K_s \left(\mathrm{E}_b \left((\phi-1)K_f + \phi K_s\right) - 3(\phi-1)^2 (2v_b-1) K_f K_s\right)}{3(2v_b-1)K_s\left((\phi-1)K_f - \phi K_s\right) - \mathrm{E}_b K_f} + \frac{2\mathrm{E}_b}{3(v_b+1)}}{-\frac{\mathrm{E}_b}{3K_s - 6v_b K_s} + \frac{\phi K_s}{K_f} - \phi + 1}.$$

$$\rho_4 = \frac{A4}{B4 - C4}, \tag{A.4}$$

$$A4 = -(2\eta\,(\rho_{11} - 2\rho_{12} + \rho_{22})\,\alpha_\infty)/(\Lambda \phi K_s \sqrt{\frac{\eta}{\rho_f}}),$$

$$B4 = \frac{K_f^2 K_s \left(\mathrm{E}_b - 3(\phi-1)\,(2v_b-1)\,K_s\right)^2}{\left(\mathrm{E}_b K_f + 3\,(2v_b-1)\,K_s\,(\phi K_s - (\phi-1)K_f)\right)^2},$$

$$C4 = \frac{\frac{K_s \left(\mathrm{E}_b \left((\phi-1)K_f + \phi K_s\right) - 3(\phi-1)^2 (2v_b-1) K_f K_s\right)}{3(2v_b-1)K_s\left((\phi-1)K_f - \phi K_s\right) - \mathrm{E}_b K_f} + \frac{2\mathrm{E}_b}{3(v_b+1)}}{-\frac{\mathrm{E}_b}{3K_s - 6v_b K_s} + \frac{\phi K_s}{K_f} - \phi + 1}.$$

$$\rho_5 = \frac{A5}{B5 + C5}, \tag{A.5}$$

$$A5 = \frac{\rho_{11}\phi}{-\frac{E_b}{3K_s - 6v_b K_s} + \frac{\phi K_s}{K_f} - \phi + 1} -$$

$$\frac{\rho_{12}K_f\left(E_b - 3\left(\phi - 1\right)\left(2v_b - 1\right)K_s\right)}{E_b K_f + 3\left(2v_b - 1\right)K_s\left(-\phi K_f + K_f + \phi K_s\right)},$$

$$B5 = \phi\left(\frac{\frac{K_s\left(E_b\left((\phi-1)K_f + \phi K_s\right) - 3(\phi-1)^2(2v_b-1)K_f K_s\right)}{3(1-2v_b)K_s\left(\phi K_s - (\phi-1)K_f\right) - E_b K_f} + \frac{2E_b}{3(v_b+1)}}{-\frac{E_b}{3K_s - 6v_b K_s} + \frac{\phi K_s}{K_f} - \phi + 1}\right),$$

$$C5 = -\frac{K_f^2 K_s\left(E_b - 3\left(\phi - 1\right)\left(2v_b - 1\right)K_s\right)^2}{\left(E_b K_f + 3\left(2v_b - 1\right)K_s\left(\phi K_s - (\phi - 1)K_f\right)\right)^2}.$$

$$\rho_6 = \frac{A6}{B6 + C6}, \tag{A.6}$$

$$A6 = 2\eta\,\alpha_\infty\left[\frac{K_f\left(E_b - 3\left(\phi - 1\right)\left(2v_b - 1\right)K_s\right)}{E_b K_f + 3\left(2v_b - 1\right)K_s\left(\phi K_s - (\phi - 1)K_f\right)}\right.$$

$$\left. + \frac{\phi}{-\frac{E_b}{3K_s - 6v_b K_s} + \frac{\phi K_s}{K_f} - \phi + 1}\right],$$

$$B6 = \Lambda\sqrt{\frac{\eta}{\rho_f}}\left(\frac{\frac{K_s\left(E_b\left((\phi-1)K_f + \phi K_s\right) - 3(\phi-1)^2(2v_b-1)K_f K_s\right)}{3(1-2v_b)K_s\left(\phi K_s - (\phi-1)K_f\right) - E_b K_f} + \frac{2E_b}{3(v_b+1)}}{-\frac{E_b}{3K_s - 6v_b K_s} + \frac{\phi K_s}{K_f} - \phi + 1}\right),$$

$$C6 = -\Lambda\sqrt{\frac{\eta}{\rho_f}}\left(\frac{K_f^2 K_s\left(E_b - 3\left(\phi - 1\right)\left(2v_b - 1\right)K_s\right)^2}{\left(E_b K_f + 3\left(2v_b - 1\right)K_s\left(\phi K_s - (\phi - 1)K_f\right)\right)^2}\right).$$

$$\rho_7 = \frac{A7}{B7 + C7}, \tag{A.7}$$

$$A7 = \frac{\rho_{12}\phi}{-\frac{E_b}{3K_s - 6v_b K_s} + \frac{\phi K_s}{K_f} - \phi + 1} - \frac{\rho_{22}K_f\left(E_b - 3\left(\phi - 1\right)\left(2v_b - 1\right)K_s\right)}{E_b K_f + 3\left(2v_b - 1\right)K_s\left(-\phi K_f + K_f + \phi K_s\right)},$$

$$B7 = \phi\left(\frac{\frac{K_s\left(E_b\left((\phi-1)K_f + \phi K_s\right) - 3(\phi-1)^2(2v_b-1)K_f K_s\right)}{3(2v_b-1)K_s\left((\phi-1)K_f - \phi K_s\right) - E_b K_f} + \frac{2E_b}{3(v_b+1)}}{-\frac{E_b}{3K_s - 6v_b K_s} + \frac{\phi K_s}{K_f} - \phi + 1}\right),$$

$$C7 = -\phi\left(\frac{K_f^2 K_s\left(E_b - 3\left(\phi - 1\right)\left(2v_b - 1\right)K_s\right)^2}{\left(E_b K_f + 3\left(2v_b - 1\right)K_s\left(\phi K_s - (\phi - 1)K_f\right)\right)^2}\right).$$

Appendix B

Wave Functions used in Chapter 3

$$\tilde{G}_1(x,s) = \check{\Phi}_1(s)e^{-x\sqrt{\tilde{\lambda}_1(s)}} + \check{\Phi}_{11}(s)e^{x\sqrt{\tilde{\lambda}_1(s)}}$$

$$\tilde{G}_2(x,s) = \check{\Phi}_2(s)e^{-x\sqrt{\tilde{\lambda}_2(s)}} + \check{\Phi}_{22}(s)e^{-x\sqrt{\tilde{\lambda}_2(s)}}$$

$$\check{\Phi}_1(s) = \tilde{\varphi}(s)\frac{\tilde{\Psi}_1(s)}{\tilde{\Psi}(s)}\left[(1+\tilde{R}(s))\left(1+\frac{\cosh\left(l\sqrt{\tilde{\lambda}_1(s)}\right)}{\sinh\left(l\sqrt{\tilde{\lambda}_1(s)}\right)}\right) - \frac{\tilde{\mathscr{T}}(s)}{\sinh\left(l\sqrt{\tilde{\lambda}_1(s)}\right)}\right],$$

$$\check{\Phi}_{11}(s) = \tilde{\varphi}(s)\frac{\tilde{\Psi}_1(s)}{\tilde{\Psi}(s)}\left[(1+\tilde{R}(s))\left(1-\frac{\cosh\left(l\sqrt{\tilde{\lambda}_1(s)}\right)}{\sinh\left(l\sqrt{\tilde{\lambda}_1(s)}\right)}\right) + \frac{\tilde{\mathscr{T}}(s)}{\sinh\left(l\sqrt{\tilde{\lambda}_1(s)}\right)}\right],$$

$$\check{\Phi}_2(s) = \tilde{\varphi}(s)\frac{\tilde{\Psi}_2(s)}{\tilde{\Psi}(s)}\left[(1+\tilde{R}(s))\left(1+\frac{\cosh\left(l\sqrt{\tilde{\lambda}_2(s)}\right)}{\sinh\left(l\sqrt{\tilde{\lambda}_2(s)}\right)}\right) - \frac{\tilde{\mathscr{T}}(s)}{\sinh\left(l\sqrt{\tilde{\lambda}_2(s)}\right)}\right],$$

$$\check{\Phi}_{22}(s) = \tilde{\varphi}(s)\frac{\tilde{\Psi}_2(s)}{\tilde{\Psi}(s)}\left[(1+\tilde{R}(s))\left(1+\frac{\cosh\left(l\sqrt{\tilde{\lambda}_2(s)}\right)}{\sinh\left(l\sqrt{\tilde{\lambda}_2(s)}\right)}\right) + \frac{\tilde{\mathscr{T}}(s)}{\sinh\left(l\sqrt{\tilde{\lambda}_2(s)}\right)}\right],$$

$$\tilde{\lambda}_1(s) = \frac{1}{2}\left[-\rho_1 s^2 + \rho_2 s^{\frac{3}{2}} - \sqrt{(\rho_1^2 - 4\rho_3)s^4 + 2(\rho_1\rho_2 - 2\rho_4)s^{\frac{7}{2}} + \rho_2^2 s^3}\right],$$

$$\tilde{\lambda}_2(s) = \frac{1}{2}\left[-\rho_1 s^2 + \rho_2 s^{\frac{3}{2}} + \sqrt{(\rho_1^2 - 4\rho_3)s^4 + 2(\rho_1\rho_2 - 2\rho_4)s^{\frac{7}{2}} + \rho_2^2 s^3}\right],$$

$$\tilde{\chi}_1(s) = \frac{\rho_1 - 2\rho_5 - \sqrt{\rho_1^2 - 4\rho_3}}{2\rho_7} +$$

$$\frac{(\rho_2 - 2\rho_6 - \frac{\rho_1\rho_2 - 2\rho_4}{\sqrt{\rho_1^2 - 4\rho_3}})2\rho_7 + (\rho_1 - 2\rho_5 - \sqrt{\rho_1^2 - 4\rho_3})2\rho_6}{4\rho_7^2\sqrt{s}},$$

$$\tilde{\chi}_2(s) = \frac{\rho_1 - 2\rho_5 - \sqrt{\rho_1^2 - 4\rho_3}}{2\rho_7} +$$

$$\frac{(\rho_2 - 2\rho_6 + \frac{\rho_1\rho_2 - 2\rho_4}{\sqrt{\rho_1^2 - 4\rho_3}})2\rho_7 + (\rho_1 - 2\rho_5 - \sqrt{\rho_1^2 - 4\rho_3})2\rho_6}{4\rho_7^2\sqrt{s}},$$

in which $\tilde{\Psi}_1(s)$ and $\tilde{\Psi}_2(s)$ and $\tilde{\Psi}(s)$ are given in Equation 3.42 and Equation 3.43.

Appendix C

Transmission and Reflection Coefficients used in Chapter 3

$$\tilde{X}(s) = x_0 \frac{\sqrt{\tilde{\lambda}_1(s)}\Big(-(1\tilde{\lambda}_2(s))(x_1 + \phi\tilde{\lambda}_2(s)x_2)\Big)}{(\tilde{\lambda}_1(s)\tilde{\lambda}_2(s)(x_3x_4 - x_5x_6))}$$

$$x_0 = 2sc_0\rho_f\sqrt{\tilde{\lambda}_1(s)}(\phi(\tilde{\chi}_1(s) - 1) + 1)$$

$$x_1 = \frac{E_s\phi^2\_2(s)}{3(1 - 2v_s)\left(-\frac{E_b(1 - 2v_s)}{E_s(1 - 2v_b)} + \frac{E_s\phi}{3K_f(1 - 2v_s)} - \phi + 1\right)} +$$

$$\frac{E_s\phi\left(-\frac{E_b(1 - 2v_s)}{E_s(1 - 2v_b)} - \phi + 1\right)}{3(1 - 2v_s)\left(-\frac{E_b(1 - 2v_s)}{E_s(1 - 2v_b)} + \frac{E_s\phi}{3K_f(1 - 2v_s)} - \phi + 1\right)}$$

$$x_2 = \frac{E_s\phi\tilde{\chi}_2(s)\left(-\frac{E_b(1 - 2v_s)E_s(1 - 2v_b)}{\phi} + 1\right)}{3(1 - 2v_s)\left(-\frac{E_b(1 - 2v_s)}{E_s(1 - 2v_b)} + \frac{E_s\phi}{3K_f(1 - 2v_s)} - \phi + 1\right)} +$$

$$\frac{\frac{E_bE_s\phi}{9K_f(1 - 2v_b)(1 - 2v_s)} + \frac{E_s(1 - \phi)\left(-\frac{E_b(1 - 2v_s)}{E_s(1 - 2v_b)} - \phi + 1\right)}{3(1 - 2v_s)}}{-\frac{E_b(1 - 2v_s)}{E_s(1 - 2v_b)} + \frac{E_s\phi}{3K_f(1 - 2v_s)} - \phi + 1} + \frac{2E_b}{3(v_b + 1)}$$

$$x_3 = \frac{E_s\phi\tilde{\chi}_1(s)\left(-\frac{E_b(1 - 2v_s)}{E_s(1 - 2v_b)} - \phi + 1\right)}{3(1 - 2v_s)\left(-\frac{E_b(1 - 2v_s)}{E_s(1 - 2v_b)} + \frac{E_s\phi}{3K_f(1 - 2v_s)} - \phi + 1\right)} +$$

$$\frac{\frac{E_bE_s\phi}{9K_f(1 - 2v_b)(1 - 2v_s)} + \frac{E_s(1 - \phi)\left(-\frac{E_b(1 - 2v_s)}{E_s(1 - 2v_b)} - \phi + 1\right)}{3(1 - 2v_s)}}{-\frac{E_b(1 - 2v_s)}{E_s(1 - 2v_b)} + \frac{E_s\phi}{3K_f(1 - 2v_s)} - \phi + 1} + \frac{2E_b}{3(v_b + 1)}$$

$$x_4 = \frac{E_s \phi^2 \tilde{\chi}_2(s)}{3(1-2v_s)\left(-\frac{E_b(1-2v_s)}{E_s(1-2v_b)} + \frac{E_s\phi}{3K_f(1-2v_s)} - \phi + 1\right)} +$$

$$\frac{E_s\phi\left(-\frac{E_b(1-2v_s)}{E_s(1-2v_b)} - \phi + 1\right)}{3(1-2v_s)\left(-\frac{E_b(1-2v_s)}{E_s(1-2v_b)} + \frac{E_s\phi}{3K_f(1-2v_s)} - \phi + 1\right)}$$

$$x_5 = \frac{E_s \phi^2 \tilde{\chi}_1(s)}{3(1-2v_s)\left(-\frac{E_b(1-2v_s)}{E_s(1-2v_b)} + \frac{E_s\phi}{3K_f(1-2v_s)} - \phi + 1\right)} +$$

$$\frac{E_s\phi\left(-\frac{E_b(1-2v_s)}{E_s(1-2v_b)} - \phi + 1\right)}{3(1-2v_s)\left(-\frac{E_b(1-2v_s)}{E_s(1-2v_b)} + \frac{E_s\phi}{3K_f(1-2v_s)} - \phi + 1\right)}$$

$$x_6 = \frac{E_s \phi \tilde{\chi}_2(s)\left(-\frac{E_b(1-2v_s)}{E_s(1-2v_b)} - \phi + 1\right)}{3(1-2v_s)\left(-\frac{E_b(1-2v_s)}{E_s(1-2v_b)} + \frac{E_s\phi}{3K_f(1-2v_s)} - \phi + 1\right)} +$$

$$\frac{\frac{E_b E_s \phi}{9K_f(1-2v_b)(1-2v_s)} + \frac{E_s(1-\phi)\left(-\frac{E_b(1-2v_s)}{E_s(1-2v_b)} - \phi + 1\right)}{3(1-2v_s)}}{-\frac{E_b(1-2v_s)}{E_s(1-2v_b)} + \frac{E_s\phi}{3K_f(1-2v_s)} - \phi + 1} + \frac{2E_b}{3(v_b + 1)}$$

$$\tilde{Y}(s) = y_0 \frac{\sqrt{\tilde{\lambda}_2(s)}\left(-(1-\phi)\tilde{\lambda}_1(s)\right)\left(y_1 + \phi\tilde{\lambda}_1(s)y_2\right)}{\left(\tilde{\lambda}_1(s)\tilde{\lambda}_2(s)(y_3 y_4 - y_5 y_6)\right)}$$

$$y_0 = 2sc_0\rho_f\sqrt{\tilde{\lambda}_2(s)}\left(\phi(\tilde{\chi}_2(s) - 1) + 1\right)$$

$$y_1 = \frac{E_s \phi^2 \tilde{\chi}_1(s)}{3(1-2v_s)\left(-\frac{E_b(1-2v_s)}{E_s(1-2v_b)} + \frac{E_s\phi}{3K_f(1-2v_s)} - \phi + 1\right)} +$$

$$\frac{E_s\phi\left(-\frac{E_b(1-2v_s)}{E_s(1-2v_b)} - \phi + 1\right)}{3(1-2v_s)\left(-\frac{E_b(1-2v_s)}{E_s(1-2v_b)} + \frac{E_s\phi}{3K_f(1-2v_s)} - \phi + 1\right)}$$

$$y_2 = \frac{E_s \phi \tilde{\chi}_1(s)\left(-\frac{E_b(1-2v_s)E_s(1-2v_b)}{\phi} + 1\right)}{3(1-2v_s)\left(-\frac{E_b(1-2v_s)}{E_s(1-2v_b)} + \frac{E_s\phi}{3K_f(1-2v_s)} - \phi + 1\right)} +$$

$$\frac{\frac{E_b E_s \phi}{9K_f(1-2v_b)(1-2v_s)} + \frac{E_s(1-\phi)\left(-\frac{E_b(1-2v_s)}{E_s(1-2v_b)} - \phi + 1\right)}{3(1-2v_s)}}{-\frac{E_b(1-2v_s)}{E_s(1-2v_b)} + \frac{E_s\phi}{3K_f(1-2v_s)} - \phi + 1} + \frac{2E_b}{3(v_b + 1)}$$

$$y_3 = \frac{E_s \phi \tilde{\chi}_1(\mathrm{s}) \left(-\frac{E_b(1-2v_s)}{E_s(1-2v_b)} - \phi + 1 \right)}{3(1-2v_s) \left(-\frac{E_b(1-2v_s)}{E_s(1-2v_b)} + \frac{E_s \phi}{3K_f(1-2v_s)} - \phi + 1 \right)} +$$

$$\frac{\frac{E_b E_s \phi}{9K_f(1-2v_b)(1-2v_s)} + \frac{E_s(1-\phi)\left(-\frac{E_b(1-2v_s)}{E_s(1-2v_b)} - \phi + 1 \right)}{3(1-2v_s)}}{-\frac{E_b(1-2v_s)}{E_s(1-2v_b)} + \frac{E_s \phi}{3K_f(1-2v_s)} - \phi + 1} + \frac{2E_b}{3(v_b+1)}$$

$$y_4 = \frac{E_s \phi^2 \tilde{\chi}_2(\mathrm{s})}{3(1-2v_s) \left(-\frac{E_b(1-2v_s)}{E_s(1-2v_b)} + \frac{E_s \phi}{3K_f(1-2v_s)} - \phi + 1 \right)} +$$

$$\frac{E_s \phi \left(-\frac{E_b(1-2v_s)}{E_s(1-2v_b)} - \phi + 1 \right)}{3(1-2v_s) \left(-\frac{E_b(1-2v_s)}{E_s(1-2v_b)} + \frac{E_s \phi}{3K_f(1-2v_s)} - \phi + 1 \right)}$$

$$y_5 = \frac{E_s \phi^2 \tilde{\chi}_1(\mathrm{s})}{3(1-2v_s) \left(-\frac{E_b(1-2v_s)}{E_s(1-2v_b)} + \frac{E_s \phi}{3K_f(1-2v_s)} - \phi + 1 \right)} +$$

$$\frac{E_s \phi \left(-\frac{E_b(1-2v_s)}{E_s(1-2v_b)} - \phi + 1 \right)}{3(1-2v_s) \left(-\frac{E_b(1-2v_s)}{E_s(1-2v_b)} + \frac{E_s \phi}{3K_f(1-2v_s)} - \phi + 1 \right)}$$

$$y_6 = \frac{E_s \phi \tilde{\chi}_2(\mathrm{s}) \left(-\frac{E_b(1-2v_s)}{E_s(1-2v_b)} - \phi + 1 \right)}{3(1-2v_s) \left(-\frac{E_b(1-2v_s)}{E_s(1-2v_b)} + \frac{E_s \phi}{3K_f(1-2v_s)} - \phi + 1 \right)} +$$

$$\frac{\frac{E_b E_s \phi}{9K_f(1-2v_b)(1-2v_s)} + \frac{E_s(1-\phi)\left(-\frac{E_b(1-2v_s)}{E_s(1-2v_b)} - \phi + 1 \right)}{3(1-2v_s)}}{-\frac{E_b(1-2v_s)}{E_s(1-2v_b)} + \frac{E_s \phi}{3K_f(1-2v_s)} - \phi + 1} + \frac{2E_b}{3(v_b+1)}$$

$$\tilde{e}(x,s) = \frac{\partial^2 \tilde{\phi}_s(x,s)}{\partial x^2} = \frac{\partial^2 \left(\check{\Phi}_1(x,s) + \check{\Phi}_2(x,s) \right)}{\partial x^2},$$

$$\tilde{e}(x,s) = \frac{(a_1 a_2 + a_3 a_4 + a_5 a_6 - a_7 a_8)\tilde{\varphi}(s)}{a},$$

$$a_1 = e^{x\sqrt{s(C_1 s + D_1\sqrt{s} + G_1)}} \left(\left[-s(1-\phi)\left(C_1 s + D_1\sqrt{s} + G_1\right)\left(A_1 Q + \frac{B_1 Q}{\sqrt{s}} + P\right) \right] \right.$$
$$\left. + \left[s\phi\left(C_2 s + D_2\sqrt{s} + G_2\right)\left(A_2 Q + \frac{B_2 Q}{\sqrt{s}} + P\right) \right] \right),$$

$$a_2 = \left[\tilde{\mathscr{T}}(s)\text{csch}\left(l\sqrt{s\left(C_1 s + D_1\sqrt{s} + G_1\right)} \right) \right.$$
$$\left. - (\tilde{\mathfrak{R}}(s) + 1)\left(\coth\left(l\sqrt{s\left(C_1 s + D_1\sqrt{s} + G_1\right)} \right) - 1 \right) \right],$$

$$a_3 = e^{-x\sqrt{s(C_1 s + D_1\sqrt{s} + G_1)}} \left[s\phi\left(C_2 s + D_2\sqrt{s} + G_2\right)\left(A_2 Q + \frac{B_2 Q}{\sqrt{s}} + P\right) \right.$$
$$\left. - s(1-\phi)\left(C_1 s + D_1\sqrt{s} + G_1\right)\left(A_1 Q + \frac{B_1 Q}{\sqrt{s}} + P\right) \right],$$

$$a_4 = \left[(\tilde{\mathfrak{R}}(s) + 1)\left(\coth\left(l\sqrt{s\left(C_1 s + D_1\sqrt{s} + G_1\right)} \right) + 1 \right) \right.$$
$$\left. - \tilde{\mathscr{T}}(s)\text{csch}\left(l\sqrt{s\left(C_1 s + D_1\sqrt{s} + G_1\right)} \right) \right],$$

$$a_5 = e^{x\sqrt{s(C_2 s + D_2\sqrt{s} + G_2)}} \left[s\left(C_2 s + D_2\sqrt{s} + G_2\right)\left(A_1(R - \phi(Q+R))\right) \right.$$
$$\left. + \frac{B_1(R - \phi(Q+R))}{\sqrt{s}} - 2P\phi + P \right],$$

$$a_6 = \tilde{\mathscr{T}}(s)\text{csch}\left(l\sqrt{s\left(C_2 s + D_2\sqrt{s} + G_2\right)}\right)$$
$$-(\tilde{\mathfrak{R}}(s)+1)\left(\coth\left(l\sqrt{s\left(C_2 s + D_2\sqrt{s} + G_2\right)}\right)-1\right),$$

$$a_7 = e^{-x\sqrt{s(C_2 s + D_2\sqrt{s}+G_2)}}\left[\sqrt{s\left(C_2 s + D_2\sqrt{s}+G_2\right)}\left(A_1\sqrt{s}+B_1\right)(Q\phi + R(\phi-1))\right.$$
$$\left.+P\sqrt{s}(2\phi-1)\right],$$

$$a_8 = (\tilde{\mathfrak{R}}(s)+1)\left(\coth\left(l\sqrt{s\left(C_2 s + D_2\sqrt{s}+G_2\right)}\right)+1\right)$$
$$-\tilde{\mathscr{T}}(s)\text{csch}\left(l\sqrt{s\left(C_2 s + D_2\sqrt{s}+G_2\right)}\right),$$

$$a = 2s\left(C_1 s + D_1\sqrt{s}+G_1\right)\left(A_1 Q + \frac{B_1 Q}{\sqrt{s}} + P\right)^2$$
$$-2s\left(C_2 s + D_2\sqrt{s}+G_2\right)\left(A_2 Q + \frac{B_2 Q}{\sqrt{s}} + P\right)\left(A_1 R + \frac{B_1 R}{\sqrt{s}} + P\right),$$

$$\tilde{\varepsilon}(x,s) = \frac{\partial^2 \tilde{\phi}_f(x,s)}{\partial x^2} = \frac{\partial^2\left(\tilde{\chi}_1(x,s)\tilde{\Phi}_1(x,s)+\tilde{\chi}_2(x,s)\tilde{\Phi}_2(x,s)\right)}{\partial x^2},$$

$$\tilde{\varepsilon}(x,s) = \tilde{\varphi}(s)\tilde{\lambda}_1(s)\tilde{\chi}_1(x,s)\frac{(b_1+b_2)(b_3+b_4+b_5+b_6)}{b_7+b_8}$$
$$+\tilde{\varphi}(s)\tilde{\chi}_2(x,s)\tilde{\lambda}_2(s)\frac{(c_1+c_2)(c_3+c_4+c_5+c_6)}{c_7+c_8},$$

$$b_1 = -\,(1-\phi)\left(C_1 s^2 + D_1 s^{3/2} + G_1 s\right)\left(Q\left(A_1 + \frac{B_1}{\sqrt{s}}\right)+P\right),$$

$$b_2 = \phi\left(C_2 s^2 + D_2 s^{3/2} + G_2 s\right)\left(Q\left(A_2 + \frac{B_2}{\sqrt{s}}\right)+P\right),$$

$$b_3 = \tilde{\mathscr{T}}(s)\left(-\text{csch}\left(l\sqrt{C_1 s^2 + D_1 s^{3/2} + G_1 s}\right)\right),$$

$$b_4 = (\tilde{\mathfrak{R}}(s)+1)\left(\coth\left(l\sqrt{C_1 s^2 + D_1 s^{3/2} + G_1 s}\right)+1\right),$$

$$b_5 = \tilde{\mathscr{T}}(s)\text{csch}\left(l\sqrt{C_1 s^2 + D_1 s^{3/2} + G_1 s}\right),$$

$$b_6 = (\tilde{\mathfrak{R}}(s)+1)\left(1-\coth\left(l\sqrt{C_1 s^2 + D_1 s^{3/2} + G_1 s}\right)\right),$$

$$b_7 = 2\left(C_1 s^2 + D_1 s^{3/2} + G_1 s\right)^2\left(Q\left(A_1 + \frac{B_1}{\sqrt{s}}\right)+P\right)^2,$$

$$b_8 = \left(C_1 s^2 + D_1 s^{3/2} + G_1 s\right)\left(C_2 s^2 + D_2 s^{3/2} + G_2 s\right)$$
$$\left(Q\left(A_2 + \frac{B_2}{\sqrt{s}}\right)+P\right)\left(-\left(R\left(A_1 + \frac{B_1}{\sqrt{s}}\right)+P\right)\right),$$

$$c_1 = -\phi \left(C_1 s^2 + D_1 s^{3/2} + G_1 s \right) \left(Q \left(A_1 + \frac{B_1}{\sqrt{s}} \right) + P \right),$$

$$c_2 = (1 - \phi) \left(C_1 s^2 + D_1 s^{3/2} + G_1 s \right) \left(R \left(A_1 + \frac{B_1}{\sqrt{s}} \right) + P \right),$$

$$c_3 = \tilde{\mathscr{T}}(s) \left(-\mathrm{csch} \left(l \sqrt{C_2 s^2 + D_2 s^{3/2} + G_2 s} \right) \right),$$

$$c_4 = (\tilde{\mathfrak{R}}(s) + 1) \left(\coth \left(l \sqrt{C_2 s^2 + D_2 s^{3/2} + G_2 s} \right) + 1 \right),$$

$$c_5 = \tilde{\mathscr{T}}(s) \mathrm{csch} \left(l \sqrt{C_2 s^2 + D_2 s^{3/2} + G_2 s} \right),$$

$$c_6 = (\tilde{\mathfrak{R}}(s) + 1) \left(1 - \coth \left(l \sqrt{C_2 s^2 + D_2 s^{3/2} + G_2 s} \right) \right),$$

$$c_7 = \left(C_1 s^2 + D_1 s^{3/2} + G_1 s \right)^2 \left(Q \left(A_1 + \frac{B_1}{\sqrt{s}} \right) + P \right)^2,$$

$$c_8 = \left(C_1 s^2 + D_1 s^{3/2} + G_1 s \right) \left(C_2 s^2 + D_2 s^{3/2} + G_2 s \right)$$
$$\left(Q \left(A_2 + \frac{B_2}{\sqrt{s}} \right) + P \right) \left(- \left(R \left(A_1 + \frac{B_1}{\sqrt{s}} \right) + P \right) \right),$$

in which P, Q, R are mentioned in Equation 3.2. The coefficients A_1, B_1, C_1, D_1, and G_1 are used in Equation 3.20. φ is the Laplace transform of the incident wave P^{inc}. $\tilde{\mathfrak{R}}(s)$ and $\tilde{\mathscr{T}}(s)$ are the reflection and transmission operators in Laplace domain given in Equation 3.38 and $\tilde{\lambda}_1(s)$, $\tilde{\lambda}_2(s)$, $\tilde{\chi}_i(s)$, $\tilde{\chi}_2(s)$ are eigenvalues and eigenvectors of Biot's equations explicated in details in Laplace domain in Appendix B.

Appendix D

Eigenvalues and Eigenvectors Coefficients used in Chapter 4

To solve Equation 4.17, it is preferred to separate variables and parameters by defining matrix H illustrated in Equation 4.18. To derive the fast and slow longitudinal wave which propagate in one direction in porous media, Equation 4.18 is written in the form of Equation 4.19.

$$H = \begin{pmatrix} H_{11} & H_{12} \\ H_{21} & H_{22} \end{pmatrix},$$

in which a complete extension of arrays of Matrix H is explained as

$$H_{11} = \omega^2 \mathrm{Qq} \left(\rho_{12} - \frac{a}{\sqrt{j\omega}} \right) - \omega^2 Rr \left(\rho_{11} + \frac{a}{\sqrt{j\omega}} \right),$$

$$H_{12} = \omega^2 \mathrm{Qq} \left(\rho_{22} + \frac{a}{\sqrt{j\omega}} \right) - \omega^2 \mathrm{Rr} \left(\rho_{12} - \frac{a}{\sqrt{j\omega}} \right),$$

$$H_{21} = \omega^2 \mathrm{Qq} \left(\rho_{11} + \frac{a}{\sqrt{j\omega}} \right) - \omega^2 \mathrm{Pp} \left(\rho_{12} - \frac{a}{\sqrt{j\omega}} \right),$$

$$H_{22} = \omega^2 \mathrm{Qq} \left(\rho_{12} - \frac{a}{\sqrt{j\omega}} \right) - \omega^2 \mathrm{Pp} \left(\rho_{22} + \frac{a}{\sqrt{j\omega}} \right).$$

In addition, the extension of $\tilde{\lambda}_1(\omega)$ and $\tilde{\lambda}_2(\omega)$ mentioned in Equation 4.19 are written as

$$\tilde{\lambda}_1(\omega) = \rho_{11} + \frac{1}{2}\sqrt{\rho_{12}},$$

$$\tilde{\lambda}_2(\omega) = \rho_{11} - \frac{1}{2}\sqrt{\rho_{12}},$$

$$\tilde{V}_1(\omega) = \frac{a\omega^2(-\mathrm{Pp} + \mathrm{Rr})}{\rho_{15}} + $$
$$\frac{\left[\sqrt{j\omega}(\omega^2(\rho_{11}\mathrm{Rr} - \mathrm{Pp}\rho_{22}) + \sqrt{-j\omega^2(\rho_{13} + \rho_{14})}) \right]}{\rho_{15}},$$

$$\tilde{V}_2(\omega) = \frac{a\omega^2(-\mathrm{Pp} + \mathrm{Rr})}{\rho_{15}} - $$
$$\frac{\left[\sqrt{j\omega}(\omega^2(-\rho_{11}\mathrm{Rr} + \mathrm{Pp}\rho_{22}) + \sqrt{-j\omega^2(\rho_{13} + \rho_{14})}) \right]}{\rho_{15}},$$

It should be noted that $\tilde{V}_1(\omega)$ and $\tilde{V}_2(\omega)$ describe the relation between the potentials of fast and slow waves with that of solid and fluid shown in Equation 4.21.

$$\rho_{11} = \frac{1}{2}a\mathrm{Pp}(j\omega)^{3/2} + a\mathrm{Qq}(j\omega)^{3/2} + \frac{1}{2}a\mathrm{Rr}(j\omega)^{3/2} - \frac{1}{2}\omega^2\mathrm{Pp}\rho_{22} + \omega^2\mathrm{Qq}\rho_{12} - \frac{1}{2}\omega^2\rho_{11}\mathrm{Rr},$$

$$\begin{aligned}\rho_{12} = &- j\omega^3\Big[a^2(\mathrm{Pp} + 2\mathrm{Qq} + \mathrm{Rr})^2 + \\ &j\omega(\mathrm{Pp}^2\rho_{22}^2 - 4\mathrm{Qq}\rho_{12}(\mathrm{Pp}\rho_{22} + \rho_{11}\mathrm{Rr}) - \\ &2\mathrm{Pp}\rho_{11}\rho_{22}\mathrm{Rr} + 4\mathrm{Pp}\rho_{12}^2\mathrm{Rr} + 4\mathrm{Qq}^2\rho_{11}\rho_{22} + \rho_{11}^2\mathrm{Rr}^2) + \\ &2a\sqrt{j\omega}(\mathrm{Pp}^2\rho_{22} + 2\mathrm{Qq}(-\mathrm{Pp}\rho_{12} + \mathrm{Pp}\rho_{22} + \rho_{11}\mathrm{Rr} - \rho_{12}\mathrm{Rr}) - \\ &\mathrm{Pp}\mathrm{Rr}(\rho_{11} + 4\rho_{12} + \rho_{22}) + 2\mathrm{Qq}^2(\rho_{11} + \rho_{22}) + \rho_{11}\mathrm{Rr}^2)\Big],\end{aligned}$$

$$\begin{aligned}\rho_{13} = &a^2(\mathrm{Pp} + 2\mathrm{Qq} + \mathrm{Rr})^2 + j\omega(\mathrm{Pp}^2\rho_{22}^2 - 4\mathrm{Qq}\rho_{12}(\mathrm{Pp}\rho_{22} + \rho_{11}\mathrm{Rr}) - \\ &2\mathrm{Pp}\rho_{11}\rho_{22}\mathrm{Rr} + 4\mathrm{Pp}\rho_{12}^2\mathrm{Rr} + 4\mathrm{Qq}^2\rho_{11}\rho_{22} + \rho_{11}^2\mathrm{Rr}^2),\end{aligned}$$

$$\begin{aligned}\rho_{14} = &2a\sqrt{j\omega}(\mathrm{Pp}^2\rho_{22} + 2\mathrm{Qq}(-\mathrm{Pp}\rho_{12} + \mathrm{Pp}\rho_{22} + \rho_{11}\mathrm{Rr} - \rho_{12}\mathrm{Rr}) - \\ &\mathrm{Pp}\mathrm{Rr}(\rho_{11} + 4\rho_{12} + \rho_{22}) + 2\mathrm{Qq}^2(\rho_{11} + \rho_{22}) + \rho_{11}\mathrm{Rr}^2),\end{aligned}$$

$$\rho_{15} = 2\omega^2\left(a(\mathrm{Qq} + \mathrm{Rr}) + \sqrt{j\omega}(\mathrm{Qq}\rho_{22} - \rho_{12}\mathrm{Rr})\right)$$

In addition, the expressions Pp and Qq and Rr are written as,

$$Pp = \frac{P}{PQ - R^2}$$

and

$$Qq = \frac{Q}{PQ - R^2}$$

and

$$Rr = \frac{R}{PQ - R^2}.$$

Appendix E

Stresses, Transmission and Reflection Coefficients used in Chapter 4

The extension of the coefficients used for solid, fluid, and shear stresses in a porous medium based on both longitudinal and transverse waves.

$$
\begin{pmatrix}
\tilde{\Phi}_{11}(\omega) \\
\tilde{\Phi}_{12}(\omega) \\
\tilde{\Phi}_{21}(\omega) \\
\tilde{\Phi}_{22}(\omega) \\
\tilde{\psi}_{1}(\omega) \\
\tilde{\psi}_{2}(\omega) \\
\tilde{T}(\omega) \\
\tilde{R}(\omega)
\end{pmatrix}
=
\begin{pmatrix}
A_{11} & A_{12} & . & . & . & A_{18} \\
A_{21} & . & . & . & . & . \\
. & . & . & . & . & . \\
. & . & . & . & . & . \\
. & . & . & . & . & . \\
A_{81} & . & . & . & . & A_{88}
\end{pmatrix}^{-1}
\begin{pmatrix}
(1-\phi)\tilde{\varphi}(\omega) \\
-\phi\tilde{\varphi}(\omega) \\
0 \\
0 \\
\frac{\tilde{\varphi}(\omega)}{c_0\rho_f} \\
0 \\
0 \\
0
\end{pmatrix}
$$

$$
A_{11} = \tilde{\lambda}_1(\omega)P + \tilde{\lambda}_1(\omega)Q\tilde{V}_1(\omega), \quad A_{12} = \tilde{\lambda}_1(\omega)Q + \tilde{\lambda}_1(\omega)R\tilde{V}_1(\omega),
$$

$$
A_{13} = \tilde{\lambda}_2(\omega)P + \tilde{\lambda}_2(\omega)Q\tilde{V}_2(\omega), \quad A_{14} = \tilde{\lambda}_2(\omega)P\tilde{\lambda}_2(\omega)Q\tilde{V}_2(\omega),
$$

$$
A_{15} = \tilde{\varphi}(\omega)(1-\phi), \quad A_{16} = 0, \quad A_{17} = 0, \quad A_{18} = 0,
$$

$$
A_{21} = \tilde{\lambda}_1(\omega)Q + \tilde{\lambda}_1(\omega)R\tilde{V}_1(\omega), \quad A_{22} = \tilde{\lambda}_1(\omega)Q + \tilde{\lambda}_1(\omega)R\tilde{V}_1(\omega),
$$

$$
A_{23} = \tilde{\lambda}_2(\omega)Q + \tilde{\lambda}_2(\omega)R\tilde{V}_2(\omega), \quad A_{24} = \tilde{\lambda}_2(\omega)Q + \tilde{\lambda}_2(\omega)R\tilde{V}_2(\omega),
$$

$$
A_{25} = \phi\tilde{\varphi}(\omega), \quad A_{26} = 0, \quad A_{27} = 0, \quad A_{28} = 0,
$$

$$
A_{31} = \tilde{\lambda}_1(\omega)e^{-l\sqrt{\tilde{\lambda}_1(\omega)}}(P + Q\tilde{V}_1(\omega)), \quad A_{32} = \tilde{\lambda}_1(\omega)e^{l\sqrt{\tilde{\lambda}_1(\omega)}} + (P + Q\tilde{V}_1(\omega)),
$$

$$
A_{33} = \tilde{\lambda}_2(\omega)e^{-l\sqrt{\tilde{\lambda}_2(\omega)}}(P + Q\tilde{V}_2(\omega)), \quad A_{34} = \tilde{\lambda}_2(\omega)e^{l\sqrt{\tilde{\lambda}_2(\omega)}} + (P + Q\tilde{V}_2(\omega)),
$$

$$A_{35} = 0, \quad A_{36} = (1-\phi)\tilde{\varphi}(\omega), \quad A_{37} = 0, \quad A_{38} = 0,$$

$$A_{41} = \tilde{\lambda}_1(\omega)e^{-l\sqrt{\tilde{\lambda}_1(\omega)}}(Q + R\tilde{V}_1(\omega)), \quad A_{42} = \tilde{\lambda}_1(\omega)e^{l\sqrt{\tilde{\lambda}_1(\omega)}} + (Q + R\tilde{V}_1(\omega)),$$

$$A_{43} = \tilde{\lambda}_2(\omega)e^{-l\sqrt{\tilde{\lambda}_2(\omega)}}(Q + R\tilde{V}_2(\omega)), \quad A_{44} = \tilde{\lambda}_2(\omega)e^{l\sqrt{\tilde{\lambda}_2(\omega)}} + (Q + R\tilde{V}_2(\omega)),$$

$$A_{45} = 0, \quad A_{46} = \phi\tilde{\varphi}(\omega), \quad A_{47} = 0, \quad A_{48} = 0,$$

$$A_{51} = j\sqrt{\tilde{\lambda}_1(\omega)}(\omega\phi\tilde{V}_1(\omega) - \omega\phi + \omega), \quad A_{52} = j\sqrt{\tilde{\lambda}_1(\omega)}(-\omega\phi\tilde{V}_1(\omega) + \omega\phi - \omega),$$

$$A_{53} = j\sqrt{\tilde{\lambda}_2(\omega)}(\omega\phi\tilde{V}_2(\omega) - \omega\phi + \omega), \quad A_{54} = j\sqrt{\tilde{\lambda}_2(\omega)}(-\omega\phi\tilde{V}_2(\omega) + \omega\phi - \omega),$$

$$A_{55} = -\frac{\tilde{\varphi}(\omega)}{c_0}\rho_f, \quad A_{56} = 0,$$

$$A_{57} = \sqrt{\tilde{\chi}(\omega)}(\frac{\omega\phi\rho_{12}}{\rho_{22}}\omega\phi - \omega), \quad A_{58} = \sqrt{\tilde{\chi}(\omega)}(-\frac{\omega\phi\rho_{12}}{\rho_{22}} - \omega\phi + \omega),$$

$$A_{61} = \sqrt{\tilde{\lambda}_1(\omega)}j\omega e^{-l\sqrt{\tilde{\lambda}_1(\omega)}}(\phi\tilde{V}_1(\omega) - \phi + 1),$$

$$A_{62} = \sqrt{\tilde{\lambda}_1(\omega)}j\omega e^{-l\sqrt{\tilde{\lambda}_1(\omega)}}(-\phi\tilde{V}_1(\omega) + \phi - 1),$$

$$A_{63} = \sqrt{\tilde{\lambda}_2(\omega)}j\omega e^{-l\sqrt{\tilde{\lambda}_2(\omega)}}(\phi\tilde{V}_2(\omega) - \phi + 1),$$

$$A_{64} = \sqrt{\tilde{\lambda}_2(\omega)}j\omega e^{-l\sqrt{\tilde{\lambda}_2(\omega)}}(-\phi\tilde{V}_2(\omega) + \phi - 1),$$

$$A_{65} = 0, \quad A_{66} = \frac{\tilde{\varphi}(\omega)}{c_0\rho_f},$$

$$A_{67} = e^{-jl\sqrt{\tilde{\chi}(\omega)}}\omega\sqrt{\tilde{\chi}(\omega)}(\frac{\phi\rho_{12}}{\rho_{22}} + \omega\phi - 1),$$
$$A_{68} = e^{jl\sqrt{\tilde{\chi}(\omega)}}\omega\sqrt{\tilde{\chi}(\omega)}(\frac{-\phi\rho_{12}}{\rho_{22}} - \omega\phi + 1),$$

$$A_{71} = 2N\tilde{\lambda}_1(\omega), \quad A_{72} = 2N\tilde{\lambda}_1(\omega), \quad A_{73} = 2N\tilde{\lambda}_2(\omega), \quad A_{74} = 2N\tilde{\lambda}_2(\omega),$$

$$A_{75} = 0, \quad A_{76} = 0, \quad A_{77} = -2N\tilde{\chi}(\omega), \quad A_{78} = -2N\tilde{\chi}(\omega),$$

$$A_{81} = 2N\tilde{\lambda}_1(\omega)e^{-l\sqrt{\tilde{\lambda}_1(\omega)}}, \quad A_{82} = 2N\tilde{\lambda}_1(\omega)e^{l\sqrt{\tilde{\lambda}_1(\omega)}},$$

$$A_{83} = 2N\tilde{\lambda}_2(\omega)e^{-l\sqrt{\tilde{\lambda}_2(\omega)}}, \quad A_{84} = 2N\tilde{\lambda}_2(\omega)e^{l\sqrt{\tilde{\lambda}_2(\omega)}},$$

$$A_{85} = 0, \quad A_{86} = 0,$$

$$A_{87} = -2N\tilde{\chi}(\omega)e^{-jl\sqrt{\tilde{\chi}(\omega)}},$$
$$A_{88} = -2N\tilde{\chi}(\omega)e^{jl\sqrt{\tilde{\chi}(\omega)}},$$

Note that $\chi(\omega)$ is written as

$$\chi(\omega) = \frac{\omega^2}{N}\left(\tilde{\rho}_{11}(\omega) - \frac{\tilde{\rho}_{11}(\omega)^2}{\tilde{\rho}_{22}(\omega)}\right).$$

Appendix F

Transmission and Reflection Coefficients used in Chapter 4

The extension of the coefficients used for the bone structure, fluid, and shear stresses in a porous medium based on both compression and shear waves.

$$
\begin{pmatrix}
\tilde{\Phi}_{11}(\omega) \\
\tilde{\Phi}_{12}(\omega) \\
\tilde{\Phi}_{21}(\omega) \\
\tilde{\Phi}_{22}(\omega) \\
\tilde{\psi}_1(\omega) \\
\tilde{\psi}_2(\omega) \\
\tilde{T}(\omega) \\
\tilde{R}(\omega)
\end{pmatrix}
=
\begin{pmatrix}
A_{11} & A_{12} & . & . & . & A_{18} \\
A_{21} & . & . & . & . & . \\
. & . & . & . & . & . \\
. & . & . & . & . & . \\
. & . & . & . & . & . \\
. & . & . & . & . & . \\
A_{71}. & . & . & . & A_{78} \\
A_{81}. & . & . & . & A_{88}
\end{pmatrix}^{-1}
\begin{pmatrix}
(1-\phi)\tilde{\varphi}(\omega) \\
-\phi\tilde{\varphi}(\omega) \\
0 \\
0 \\
\frac{\tilde{\varphi}(\omega)}{c_0\rho_f} \\
0 \\
0 \\
0
\end{pmatrix}
$$

$$A_{11} = \tilde{\lambda}_1(\omega)P + \tilde{\lambda}_1(\omega)Q\tilde{V}_1(\omega), \quad A_{12} = \tilde{\lambda}_1(\omega)Q + \tilde{\lambda}_1(\omega)R\tilde{V}_1(\omega),$$

$$A_{13} = \tilde{\lambda}_2(\omega)P + \tilde{\lambda}_2(\omega)Q\tilde{V}_2(\omega), \quad A_{14} = \tilde{\lambda}_2(\omega)P\tilde{\lambda}_2(\omega)Q\tilde{V}_2(\omega),$$

$$A_{15} = \tilde{\varphi}(\omega)(1-\phi), \quad A_{16} = 0, \quad A_{17} = 0, \quad A_{18} = 0,$$

$$A_{21} = \tilde{\lambda}_1(\omega)Q + \tilde{\lambda}_1(\omega)R\tilde{V}_1(\omega), \quad A_{22} = \tilde{\lambda}_1(\omega)Q + \tilde{\lambda}_1(\omega)R\tilde{V}_1(\omega),$$

$$A_{23} = \tilde{\lambda}_2(\omega)Q + \tilde{\lambda}_2(\omega)R\tilde{V}_2(\omega), \quad A_{24} = \tilde{\lambda}_2(\omega)Q + \tilde{\lambda}_2(\omega)R\tilde{V}_2(\omega),$$

$$A_{25} = \phi\tilde{\varphi}(\omega), \quad A_{26} = 0, \quad A_{27} = 0, \quad A_{28} = 0,$$

$$A_{31} = \tilde{\lambda}_1(\omega)e^{-l\sqrt{\tilde{\lambda}_1(\omega)}}(P + Q\tilde{V}_1(\omega)), \quad A_{32} = \tilde{\lambda}_1(\omega)e^{l\sqrt{\tilde{\lambda}_1(\omega)}} + (P + Q\tilde{V}_1(\omega)),$$

$$A_{33} = \tilde{\lambda}_2(\omega)e^{-l\sqrt{\tilde{\lambda}_2(\omega)}}(P + Q\tilde{V}_2(\omega)), \quad A_{34} = \tilde{\lambda}_2(\omega)e^{l\sqrt{\tilde{\lambda}_2(\omega)}} + (P + Q\tilde{V}_2(\omega)),$$

$$A_{35} = 0, \quad A_{36} = (1 - \phi)\tilde{\varphi}(\omega), \quad A_{37} = 0, \quad A_{38} = 0,$$

$$A_{41} = \tilde{\lambda}_1(\omega)e^{-l\sqrt{\tilde{\lambda}_1(\omega)}}(Q + R\tilde{V}_1(\omega)), \quad A_{42} = \tilde{\lambda}_1(\omega)e^{l\sqrt{\tilde{\lambda}_1(\omega)}} + (Q + R\tilde{V}_1(\omega)),$$

$$A_{43} = \tilde{\lambda}_2(\omega)e^{-l\sqrt{\tilde{\lambda}_2(\omega)}}(Q + R\tilde{V}_2(\omega)), \quad A_{44} = \tilde{\lambda}_2(\omega)e^{l\sqrt{\tilde{\lambda}_2(\omega)}} + (Q + R\tilde{V}_2(\omega)),$$

$$A_{45} = 0, \quad A_{46} = \phi\tilde{\varphi}(\omega), \quad A_{47} = 0, \quad A_{48} = 0,$$

$$A_{51} = j\sqrt{\tilde{\lambda}_1(\omega)}(\omega\phi\tilde{V}_1(\omega) - \omega\phi + \omega), \quad A_{52} = j\sqrt{\tilde{\lambda}_1(\omega)}(-\omega\phi\tilde{V}_1(\omega) + \omega\phi - \omega),$$

$$A_{53} = j\sqrt{\tilde{\lambda}_2(\omega)}(\omega\phi\tilde{V}_2(\omega) - \omega\phi + \omega), \quad A_{54} = j\sqrt{\tilde{\lambda}_2(\omega)}(-\omega\phi\tilde{V}_2(\omega) + \omega\phi - \omega),$$

$$A_{55} = -\frac{\tilde{\varphi}(\omega)}{c_0}\rho_f, \quad A_{56} = 0,$$

$$A_{57} = \sqrt{\tilde{\chi}(\omega)}(\frac{\omega\phi\rho_{12}}{\rho_{22}}\omega\phi - \omega), \quad A_{58} = \sqrt{\tilde{\chi}(\omega)}(-\frac{\omega\phi\rho_{12}}{\rho_{22}} - \omega\phi + \omega),$$

$$A_{61} = \sqrt{\tilde{\lambda}_1(\omega)}j\omega e^{-l\sqrt{\tilde{\lambda}_1(\omega)}}(\phi\tilde{V}_1(\omega) - \phi + 1),$$

$$A_{62} = \sqrt{\tilde{\lambda}_1(\omega)}j\omega e^{-l\sqrt{\tilde{\lambda}_1(\omega)}}(-\phi\tilde{V}_1(\omega) + \phi - 1),$$

$$A_{63} = \sqrt{\tilde{\lambda}_2(\omega)}j\omega e^{-l\sqrt{\tilde{\lambda}_2(\omega)}}(\phi\tilde{V}_2(\omega) - \phi + 1),$$

$$A_{64} = \sqrt{\tilde{\lambda}_2(\omega)}j\omega e^{-l\sqrt{\tilde{\lambda}_2(\omega)}}(-\phi\tilde{V}_2(\omega) + \phi - 1),$$

$$A_{65} = 0, \quad A_{66} = \frac{\tilde{\varphi}(\omega)}{c_0\rho_f},$$

$$A_{67} = e^{-jl\sqrt{\tilde{\chi}(\omega)}}\omega\sqrt{\tilde{\chi}(\omega)}(\frac{\phi\rho_{12}}{\rho_{22}} + \omega\phi - 1),$$

$$A_{68} = e^{jl\sqrt{\tilde{\chi}(\omega)}}\omega\sqrt{\tilde{\chi}(\omega)}(\frac{-\phi\rho_{12}}{\rho_{22}} - \omega\phi + 1),$$

$$A_{71} = 2N\tilde{\lambda}_1(\omega), \quad A_{72} = 2N\tilde{\lambda}_1(\omega), \quad A_{73} = 2N\tilde{\lambda}_2(\omega), \quad A_{74} = 2N\tilde{\lambda}_2(\omega),$$

$$A_{75} = 0, \quad A_{76} = 0, \quad A_{77} = -2N\tilde{\chi}(\omega), \quad A_{78} = -2N\tilde{\chi}(\omega),$$

$$A_{81} = 2N\tilde{\lambda}_1(\omega)e^{-l\sqrt{\tilde{\lambda}_1(\omega)}}, \quad A_{82} = 2N\tilde{\lambda}_1(\omega)e^{l\sqrt{\tilde{\lambda}_1(\omega)}},$$

$$A_{83} = 2N\tilde{\lambda}_2(\omega)e^{-l\sqrt{\tilde{\lambda}_2(\omega)}}, \quad A_{84} = 2N\tilde{\lambda}_2(\omega)e^{l\sqrt{\tilde{\lambda}_2(\omega)}},$$

$$A_{85} = 0, \quad A_{86} = 0,$$

$$A_{87} = -2N\tilde{\chi}(\omega)e^{-jl\sqrt{\tilde{\chi}(\omega)}},$$
$$A_{88} = -2N\tilde{\chi}(\omega)e^{jl\sqrt{\tilde{\chi}(\omega)}},$$

Note that $\chi(\omega)$ is written as

$$\chi(\omega) = \frac{\omega^2}{N}\left(\tilde{\rho}_{11}(\omega) - \frac{\tilde{\rho}_{11}(\omega)^2}{\tilde{\rho}_{22}(\omega)}\right).$$

The transmission and reflection coefficients are given respectively by

$$
\begin{aligned}
\tilde{T}(\omega) ={} & \frac{1}{\tilde{\varphi}(\omega)} \Bigg[\left(jc_0 \omega \rho_f e^{-l\sqrt{\tilde{\lambda}_1(\omega)} - l\sqrt{\tilde{\lambda}_2(\omega)}} \right) \left[\sqrt{\tilde{\lambda}_1(\omega)} \phi \tilde{\Phi}_{11}(\omega) e^{l\sqrt{\tilde{\lambda}_2(\omega)}} \right. \\
& - \sqrt{\tilde{\lambda}_1(\omega)} \phi \Phi_{12}(\tilde{\omega}) e^{2l\sqrt{\tilde{\lambda}_1(\omega)} + l\sqrt{\tilde{\lambda}_2(\omega)}} + \sqrt{\tilde{\lambda}_2(\omega)} \phi \tilde{\Phi}_{21}(\omega) e^{l\sqrt{\tilde{\lambda}_1(\omega)}} \\
& - \sqrt{\tilde{\lambda}_2(\omega)} \phi \tilde{\Phi}_{22}(\omega) e^{l\sqrt{\tilde{\lambda}_1(\omega)} + 2l\sqrt{\tilde{\lambda}_2(\omega)}} - \sqrt{\tilde{\lambda}_1(\omega)} \phi \tilde{\Phi}_{11}(\omega) \tilde{V}_1(\omega) e^{l\sqrt{\tilde{\lambda}_2(\omega)}} \\
& + \sqrt{\tilde{\lambda}_1(\omega)} \phi \tilde{\Phi}_{12}(\omega) \tilde{V}_1(\omega) e^{2l\sqrt{\tilde{\lambda}_1(\omega)} + l\sqrt{\tilde{\lambda}_2(\omega)}} \\
& - \sqrt{\tilde{\lambda}_2(\omega)} \phi \tilde{\Phi}_{21}(\omega) \tilde{V}_2(\omega) e^{l\sqrt{\tilde{\lambda}_1(\omega)}} \\
& + \sqrt{\tilde{\lambda}_2(\omega)} \phi \tilde{\Phi}_{22}(\omega) \tilde{V}_2(\omega) e^{l\sqrt{\tilde{\lambda}_1(\omega)} + 2l\sqrt{\tilde{\lambda}_2(\omega)}} \\
& + \sqrt{\tilde{\lambda}_1(\omega)} \tilde{\Phi}_{11}(\omega) \left(-\exp\left(l\sqrt{\tilde{\lambda}_2(\omega)} \right) \right) \\
& + \sqrt{\tilde{\lambda}_1(\omega)} \tilde{\Phi}_{12}(\omega) e^{2l\sqrt{\tilde{\lambda}_1(\omega)} + l\sqrt{\tilde{\lambda}_2(\omega)}} - \sqrt{\tilde{\lambda}_2(\omega)} \tilde{\Phi}_{21}(\omega) e^{l\sqrt{\tilde{\lambda}_1(\omega)}} \\
& \left. + \sqrt{\tilde{\lambda}_2(\omega)} \tilde{\Phi}_{22}(\omega) e^{l\sqrt{\tilde{\lambda}_1(\omega)} + 2l\sqrt{\tilde{\lambda}_2(\omega)}} \right] \\
& + c_0 \sqrt{\tilde{\chi}(\omega)} \omega \rho_f \exp\left(-jl\sqrt{\tilde{\chi}(\omega)} \right) (\phi \rho_{12} + \phi \rho_{22} - \rho_{22}) \\
& \left(-\tilde{\psi}_1(\omega) + \tilde{\psi}_2(\omega) \exp\left(2jl\sqrt{\tilde{\chi}(\omega)} \right) \rho_{22} \right) \Bigg],
\end{aligned}
$$

and

$$
\begin{aligned}
\tilde{R}(\omega) ={} & 1/\tilde{\varphi}(\omega) \Bigg[jc_0 \rho_f \left(\sqrt{\tilde{\lambda}_1(\omega)} \omega \tilde{\Phi}_{11}(\omega) - \sqrt{\tilde{\lambda}_1(\omega)} \omega \phi \tilde{\Phi}_{11}(\omega) \right. \\
& + \sqrt{\tilde{\lambda}_1(\omega)} \omega \phi \tilde{V}_1(\omega) \tilde{\Phi}_{11}(\omega) - \sqrt{\tilde{\lambda}_1(\omega)} \omega \tilde{\Phi}_{12}(\omega) \\
& + \sqrt{\tilde{\lambda}_1(\omega)} \omega \phi \tilde{\Phi}_{12}(\omega) 1 - \sqrt{\tilde{\lambda}_1(\omega)} \omega \phi \tilde{V}_1(\omega) \tilde{\Phi}_{12}(\omega) 1 \\
& + \sqrt{\tilde{\lambda}_2(\omega)} \omega \tilde{\Phi}_{21}(\omega) - \sqrt{\tilde{\lambda}_2(\omega)} \omega \phi \tilde{\Phi}_{21}(\omega) \\
& + \sqrt{\tilde{\lambda}_2(\omega)} \omega \phi \tilde{V}_2(\omega) \tilde{\Phi}_{21}(\omega) - \sqrt{\tilde{\lambda}_2(\omega)} \omega \tilde{\Phi}_{22}(\omega) \\
& \left. + \sqrt{\tilde{\lambda}_2(\omega)} \omega \phi \tilde{\Phi}_{22}(\omega) - \sqrt{\tilde{\lambda}_2(\omega)} \omega \phi \tilde{V}_2(\omega) \tilde{\Phi}_{22}(\omega) \right) \\
& + 1/(\rho_{22}) \left(\tilde{\varphi}(\omega) \rho_{22} + c_0 \sqrt{\tilde{\chi}(\omega)} \omega \phi \rho_{12} \tilde{\Psi}_1(\omega) - c_0 \sqrt{\tilde{\chi}(\omega)} \omega \rho_{22} \tilde{\Psi}_1(\omega) \right. \\
& + c_0 \sqrt{\tilde{\chi}(\omega)} \omega \phi \rho_{12} \tilde{\Psi}_2(\omega) + c_0 \sqrt{\tilde{\chi}(\omega)} \omega \rho_{22} \tilde{\Psi}_2(\omega) \\
& \left. - c_0 \sqrt{\tilde{\chi}(\omega)} \omega \phi \rho_{22} \tilde{\Psi}_2(\omega) \right) \Bigg].
\end{aligned}
$$

Appendix G

Equations presented by (Fellah et al., 2004a) as used in Chapter 4

The equations used by (Fellah et al., 2004a) are implemented to obtain the transmission coefficient versus frequency by considering the longitudinal wave only. Figure 4.5 illustrates their result.

$$\tilde{T}(\omega) = \frac{2j\omega\rho_f c_0 \tilde{F}_4(\omega)}{(j\omega\rho_f c_0 \tilde{F}_4(\omega))^2 - (j\omega\tilde{F}_3(\omega) - 1)^2},$$

in which

$$\tilde{F}_i(\omega) = \left((1 + \phi(\tilde{\jmath}_i(\omega) - 1))\sqrt{\tilde{\lambda}_i(\omega)}\right)\frac{2\tilde{\Psi}_i(\omega)}{sinh(\sqrt{\tilde{\lambda}_i(\omega)})}\frac{1}{\tilde{\Psi}(\omega)} \quad i = 1, 2,$$

$$\tilde{F}_3(\omega) = \rho_f c_0 \left(\tilde{F}_1(\omega)cosh(l\sqrt{\tilde{\lambda}_1(\omega)}) + \tilde{F}_2(\omega)cosh(l\sqrt{\tilde{\lambda}_2(\omega)})\right)$$

$$\tilde{F}_4(\omega) = \tilde{F}_1(\omega) + \tilde{F}_2(\omega),$$

The expressions $\tilde{\Psi}_i(\omega)$ are written as

$$\tilde{\Psi}_1(\omega) = \phi\tilde{Z}_2(\omega) - (1 - \phi)\tilde{Z}_4(\omega),$$

$$\tilde{\Psi}_2(\omega) = (1 - \phi)\tilde{Z}_3(\omega) - \phi\tilde{Z}_1(\omega),$$

$$\tilde{\Psi}(\omega) = 2(\tilde{Z}_1(\omega)\tilde{Z}_4(\omega) - \tilde{Z}_2(\omega)\tilde{Z}_3(\omega))$$

where $\tilde{Z}_i(\omega)$ is written as

$$\tilde{Z}_1(\omega) = (P + Q\tilde{\jmath}_1(\omega))\tilde{\lambda}_1(\omega),$$

$$\tilde{Z}_2(\omega) = (P + Q\tilde{\jmath}_2(\omega))\tilde{\lambda}_2(\omega),$$

$$\tilde{Z}_3(\omega) = (Q + R\tilde{\jmath}_1(\omega))\tilde{\lambda}_1(\omega),$$

$$\tilde{Z}_4(\omega) = (Q + R\tilde{\jmath}_2(\omega))\tilde{\lambda}_2(\omega)$$

P, Q, R mentioned in Equation 4.5 are generalized elastic constants which are related to measurable quantities such as porosity, bulk modulus of fluid, bulk modulus of solid, and bulk modulus of porous skeletal frame. The terms of $\tilde{\lambda}_1(\omega)$, $\tilde{\lambda}_2(\omega)$, $\tilde{\jmath}_1(\omega)$, $\tilde{\jmath}_2(\omega)$ are eigenvalues and eigenvectors of Biot's matrix mentioned in the paper of (Fellah et al., 2004a) given by

$$\tilde{\lambda}_1(\omega) = \frac{\tau_2(j\omega)^{3/2} - \omega^2(\tau_1)}{2} +$$
$$\frac{1}{2}\left(-\sqrt{2(j\omega)^{7/2}(\tau_1\tau_2 - 2\tau_4) + \tau_2^2(j\omega)^3 + \omega^4\left(\tau_1^2 - 4\tau_3\right)}\right)$$

$$\tilde{\lambda}_2(\omega) = \frac{\tau_2(j\omega)^{3/2} - \omega^2(\tau_1)}{2} +$$
$$\frac{1}{2}\left(+\sqrt{2(j\omega)^{7/2}(\tau_1\tau_2 - 2\tau_4) + \tau_2^2(j\omega)^3 + \omega^4\left(\tau_1^2 - 4\tau_3\right)}\right)$$

$$\tilde{\jmath}_1(\omega) = \frac{-\sqrt{\tau_1^2 - 4\tau_3} + \tau_1 - 2\tau_5}{2\tau_7} - \frac{2\tau_7\left(\frac{\tau_1\tau_2 - 2\tau_4}{\sqrt{\tau_1^2 - 4\tau_3}} - \tau_2 + 2\tau_6\right)}{4\tau_7^2\sqrt{j\omega}} +$$
$$\frac{2\tau_6\left(-\sqrt{\tau_1^2 - 4\tau_3} + \tau_1 - 2\tau_5\right)}{4\tau_7^2\sqrt{j\omega}},$$

$$\tilde{\jmath}_1(\omega) = \frac{-\sqrt{\tau_1^2 - 4\tau_3} + \tau_1 - 2\tau_5}{2\tau_7} + \frac{2\tau_7\left(\frac{\tau_1\tau_2 - 2\tau_4}{\sqrt{\tau_1^2 - 4\tau_3}} + \tau_2 - 2\tau_6\right)}{4\tau_7^2\sqrt{j\omega}} +$$
$$\frac{2\tau_6\left(-\sqrt{\tau_1^2 - 4\tau_3} + \tau_1 - 2\tau_5\right)}{4\tau_7^2\sqrt{j\omega}},$$

The terms of τ_i are described as

$$\tau_1 = Pp\rho_{22} - 2Qq\rho_{12} + \rho_{11}Rr,$$
$$\tau_2 = a(Pp + 2Qq + Rr)$$
$$\tau_3 = (PpRr - Qq^2)(\rho_{11}\rho_{22} - \rho_{12}^2)$$
$$\tau_4 = a(PpRr - Qq^2)(\rho_{11} - 2\rho_{12} + \rho_{22})$$
$$\tau_5 = \rho_{11}Rr - Qq\rho_{12}$$
$$\tau_6 = a(Qq + Rr)$$
$$\tau_7 = \rho_{12}Rr - Qq\rho_{22}$$

It should be noted that $\tilde{\varphi}(\omega)$ is the Fourier transform of the incident wave P^{inc}.

Appendix H

Waves used in Chapter 5

The harmonic incident plane wave in the cylindrical coordinate system can be expressed as (Morse and Ingard, 1986),

$$p_1^I(r,\theta,z,t) = p_0 \sum_{n=0}^{\infty} \varepsilon_n(-i)^n J_n(k_{1r}r)cos(n\theta)e^{i(\omega t - k_{1z}z)}$$

in which p_1^I is the acoustical pressure of the incident wave, p_0 is the amplitude of the incident wave, and

$$\varepsilon_n = \begin{cases} 1 & n = 0, \\ 2 & n \geq 1, \end{cases} k_{1r} = k_1 cos(\gamma), k_{1z} = k_1 sin(\gamma)$$

where ε_n, k_1, J_n, and ω stand for Neumann factor, wave number in the external acoustical medium, the cylindrical Bessel function of the first kind of integer order n, and the angular frequency amplitude of the incident wave, respectively. Furthermore, $k_1 = \frac{\omega}{c_1}$, $n = 0, 1, 2, ...$, and $i = \sqrt{-1}$.

The reflected wave p_1^R, from the cylindrical bone-like porous medium to the external fluid medium, and transmitted wave into the cavity p_3^T are given as (Morse and Ingard, 1986),

$$p_1^R(r,z,\theta,t) = \sum_{n=0}^{\infty} p_{1n}^R H_n^2(k_{1r}r)cos(n\theta)e^{i(\omega t - k_{1z}z)}$$

$$p_3^T(r,z,\theta,t) = \sum_{n=0}^{\infty} p_{3n}^R H_n^1(k_{3r}r)cos(n\theta)e^{i(\omega t - k_{3z}z)}$$

where H_n^1 and H_n^2 are the cylindrical Hankel functions of the first and second kind of integer order n, respectively. In addition, since the wave motion at the boundaries of the acoustical media and the cylindrical bone-like porous medium is driven by the incident-traveling wave, the wave numbers in z direction, k_{1z} and k_{3z}, are equated to each other, so $k_{1z} = k_{3z}$. Therefore, the following equations can be obtained as follows:

$$k_{jr} = \sqrt{k_j^2 - k_{jz}^2}, \quad k_j = \frac{\omega}{c_j}, \quad j = 1, 3$$

Appendix I

Eigenvalues and Eigenvectors Coefficients used in Chapter 5

$$M = \begin{pmatrix} M_{11} & M_{12} \\ M_{21} & M_{22} \end{pmatrix},$$

in which

$$M_{11} = \omega^2 \text{Qq} \left(\rho_{12} - \frac{A}{\sqrt{j\omega}} \right) - \omega^2 Rr \left(\rho_{11} + \frac{A}{\sqrt{j\omega}} \right),$$

$$M_{12} = \omega^2 \text{Qq} \left(\rho_{22} + \frac{A}{\sqrt{j\omega}} \right) - \omega^2 Rr \left(\rho_{12} - \frac{A}{\sqrt{j\omega}} \right),$$

$$M_{21} = \omega^2 \text{Qq} \left(\rho_{11} + \frac{A}{\sqrt{j\omega}} \right) - \omega^2 Pp \left(\rho_{12} - \frac{A}{\sqrt{j\omega}} \right),$$

$$M_{22} = \omega^2 \text{Qq} \left(\rho_{12} - \frac{A}{\sqrt{j\omega}} \right) - \omega^2 Pp \left(\rho_{22} + \frac{A}{\sqrt{j\omega}} \right).$$

where

$$Pp = \frac{P}{PQ - R^2}$$

and

$$Qq = \frac{Q}{PQ - R^2}$$

and

$$Rr = \frac{R}{PQ - R^2}$$

and

$$A = \frac{1}{\Lambda_f} 2\phi \rho_f \theta_\infty \sqrt{\frac{\eta}{\rho_f}}$$

Appendix J

Biot-JKD Theory Presented in Chapter 5

In Equation 5.2, P, Q, and R are poroelastic constants related to some measurable quantities such as bulk modulus of solid, K_s, bulk modulus of porous skeletal frame, K_b, bulk modulus of fluid, K_f and medium porosity, ϕ. The porosity of medium is defined by the ratio of the volume of the pore to the volume of elastic porous skeletal frame, $\phi = \frac{V_f}{V_b}$.

$$P = \frac{K_s \left(K_b \left((\phi - 1)K_f + \phi K_s \right) + (\phi - 1)^2 K_f K_s \right)}{K_s \left(\phi K_s - (\phi - 1)K_f \right) - K_b K_f} + \frac{4N}{3},$$

$$Q = \frac{\phi K_s \left(-\frac{K_b}{K_s} - \phi + 1 \right)}{-\frac{K_b}{K_s} + \frac{\phi K_s}{K_f} - \phi + 1},$$

$$R = \frac{\phi^2 K_s}{-\frac{K_b}{K_s} + \frac{\phi K_s}{K_f} - \phi + 1}.$$

The explicit relations between the mechanical properties of the medium and the measurable quantities in the laboratory are given by

$$K_s = \frac{\mathrm{E}_s}{3 - 6v_s}, \quad K_b = \frac{\mathrm{E}_b}{3 - 6v_b}, \quad N = \frac{\mathrm{E}_b}{2v_b + 2}. \tag{J.1}$$

where E_b, E_s and v_b, v_s are the modulus of elasticity and Poisson's ratio of the bulk of porous skeletal frame and the solid, respectively. The relation between the effective densities, ρ_{ij} $(i, j = 1, 2)$, and the densities of solid matrix, ρ_s, and the pore fluid, ρ_f, are

$$\rho_{11} + \rho_{12} = (1 - \phi)\rho_s, \quad \rho_{12} + \rho_{22} = \phi \rho_f \tag{J.2}$$

The mass coupling between the fluid and solid structure is described by ρ_{12} as,

$$\rho_{12} = -\phi \rho_f (\alpha_\infty - 1) \tag{J.3}$$

where α_∞ is defined as the medium turtuosity which relates the microscopic speed of flow inside the pores to macroscopic speed of flow through the medium.

The dynamic turtuosity and permeability of porous medium may have a significant effect on the acoustical response of the medium. They are related to the type of pore fluid and greatly dependent on the range of frequency. In addition, they are totally independent of the mechanical properties of the porous medium (Lafarge et al., 1997; Johnson, Koplik, and Dashen, 1987; Allard and Atalla, 1993). The theoretical formulation for the dynamic turtuosity developed by (Johnson, Koplik, and Dashen, 1987) for high frequency ranges is

expressed as

$$\tilde{\alpha}(\omega) = \alpha_\infty \left(1 + \frac{2}{\Lambda} \left(\frac{\eta}{\omega j \rho_f} \right)^{\frac{1}{2}} \right),$$ (J.3)

in which $j^2 = -1$, η is viscosity of the fluid, and Λ is the viscous characteristic length which controls the viscosity effect in the pores (Johnson, Koplik, and Dashen, 1987).

It is important to mention that $\tilde{\alpha}(\omega)$ indicating the interaction and viscous exchanges between the solid skeletal frame and pore fluid has a significant influence on the wave attenuation in porous media (Johnson, Koplik, and Dashen, 1987). Accordingly, the effective densities, $\rho_{ij}(\omega)$ in Equation 5.3 can be written for high frequency ranges by considering the dynamic tortuosity as,

$$\tilde{\rho}_{11}(\omega) = \rho_{11} + \mathfrak{J}(\omega)$$
$$\tilde{\rho}_{12}(\omega) = \rho_{12} - \mathfrak{J}(\omega)$$
$$\tilde{\rho}_{22}(\omega) = \rho_{22} + \mathfrak{J}(\omega)$$
$$\mathfrak{J}(\omega) = \frac{2\phi \, \alpha_\infty}{\Lambda} \left(\frac{\rho_f \eta}{j\omega} \right)^{\frac{1}{2}}$$

Appendix K

Eigenvalues of Matrix M used in Chapter 5

$$\tilde{\delta}_1^2(\omega) = \frac{\omega^2\left(-\sqrt{\Delta} + P\rho_{22} - 2Q\rho_{12} + \rho_{11}R\right)}{2\left(PR - Q^2\right)}$$

$$\tilde{\delta}_2^2(\omega) = \frac{\omega^2\left(+\sqrt{\Delta} + P\rho_{22} - 2Q\rho_{12} + \rho_{11}R\right)}{2\left(PR - Q^2\right)}$$

in which, Δ is given by

$$\Delta = \left(-P\rho_{22} + 2Q\rho_{12} + -R\rho_{11}\right)^2 - 4\left(\rho_{11}\rho_{12} - \rho_{12}{}^2\right)\left(PR - Q^2\right)$$

Appendix L

Solutions for Longitudinal and Transverse Waves used in Chapter 5

The general solutions for Equation 5.11 and Equation 5.15 in the cylindrical coordinate system are given in

$$\tilde{\phi}_1(\mathbf{r}, \omega) = \sum_{n=0}^{\infty} f_1(r) \cos(n\theta) e^{j(\omega t - k_z z)} \tag{L.1}$$

$$\tilde{\phi}_2(\mathbf{r}, \omega) = \sum_{n=0}^{\infty} f_2(r) \cos(n\theta) e^{j(\omega t - k_z z)} \tag{L.2}$$

$$\tilde{\psi}_r^s(\mathbf{r}, \omega) = \sum_{n=0}^{\infty} g_r(r) \sin(n\theta) e^{j(\omega t - k_z z)} \tag{L.3}$$

$$\tilde{\psi}_\theta^s(\mathbf{r}, \omega) = \sum_{n=0}^{\infty} g_\theta(r) \cos(n\theta) e^{j(\omega t - k_z z)} \tag{L.4}$$

$$\tilde{\psi}_z^s(\mathbf{r}, \omega) = \sum_{n=0}^{\infty} g_z(r) \sin(n\theta) e^{j(\omega t - k_z z)} \tag{L.5}$$

in which the integers n and k_z are the circumferential order of a wave mode and the axial wavenumber, respectively. Also, the relations between the components of the transverse wave vector potentials for the solid skeletal frame and fluid regarding Equation 5.17 can be obtained by

$$\psi_r^f(\mathbf{r}, \omega) = \mu_3 \psi_r^s(\mathbf{r}, \omega)$$

$$\psi_z^f(\mathbf{r}, \omega) = \mu_3 \psi_z^s(\mathbf{r}, \omega)$$

$$\psi_\theta^f(\mathbf{r}, \omega) = \mu_3 \psi_\theta^s(\mathbf{r}, \omega)$$

Note that the coefficients in Equation L.1 to Equation L.5, $f_1(r)$, $f_2(r)$, $g_r(r)$, $g_\theta(r)$, and $g_z(r)$, are obtained by substituting Equation L.1 to Equation L.5 into Equation 5.11 and Equation 5.15. Therefore, after some algebraic manipulations they are derived as

$$f_1(r) = C_1 J_n(a_1 r) + C_2 Y_n(a_1 r)$$

$$f_2(r) = C_3 J_n(a_2 r) + C_4 Y_n(a_2 r)$$

$$g_r(r) = A_1 J_{n+1}(a_3 r) + B_1 Y_{n+1}(a_3 r)$$

$$g_\theta(r) = -A_1 J_{n+1}(a_3 r) - B_1 Y_{n+1}(a_3 r)$$

$$g_z(r) = A_3 J_n(a_3 r) + B_3 Y_n(a_3 r)$$

where J_n and Y_n are the Bessel functions of the first and second type of order n in the cylindrical coordinate system, respectively. In addition, a_1, a_2, a_3 are the radial components of the wavenumber given

$$a_1 = \tilde{\delta}_1^2(\mathbf{r}, \omega) - k_z^2$$
$$a_2 = \tilde{\delta}_2^2(\mathbf{r}, \omega) - k_z^2$$
$$a_3 = \tilde{\delta}_3^2(\mathbf{r}, \omega) - k_z^2$$

Appendix M

Displacement Components in Radial Directions used in Chapter 5

$$u_r(r,\theta,z,t) = \frac{\partial \phi^s(\mathbf{r},t)}{\partial r} + \frac{1}{r}\frac{\partial \psi_z^s(\mathbf{r},t)}{\partial \theta} - \frac{\partial \psi_\theta^s(\mathbf{r},t)}{\partial z}$$

$$= \sum_{n=0}^{\infty} u_r^n(r)\cos(n\theta)e^{j(\omega t - K_z z)}$$

$$U_r(r,\theta,z,t) = \frac{\partial \phi^f(\mathbf{r},t)}{\partial r} + \frac{1}{r}\frac{\partial \psi_z^f(\mathbf{r},t)}{\partial \theta} - \frac{\partial \psi_\theta^f(\mathbf{r},t)}{\partial z}$$

$$= \sum_{n=0}^{\infty} U_r^n(r)\cos(n\theta)e^{j(\omega t - K_z z)}$$

$$u_\theta(r,\theta,z,t) = \frac{1}{r}\frac{\partial \phi^s(\mathbf{r},t)}{\partial \theta} + \frac{\partial \psi_r^s(\mathbf{r},t)}{\partial z} - \frac{\partial \psi_z^s(\mathbf{r},t)}{\partial r}$$

$$= \sum_{n=0}^{\infty} u_\theta^n(r)\sin(n\theta)e^{j(\omega t - K_z z)}$$

$$U_\theta(r,\theta,z,t) = \frac{1}{r}\frac{\partial \phi^f(\mathbf{r},t)}{\partial \theta} + \frac{\partial \psi_r^f(\mathbf{r},t)}{\partial z} - \frac{\partial \psi_z^f(\mathbf{r},t)}{\partial r}$$

$$= \sum_{n=0}^{\infty} U_\theta^n(r)\sin(n\theta)e^{j(\omega t - K_z z)}$$

$$u_z(r,\theta,z,t) = \frac{\partial \phi^s(\mathbf{r},t)}{\partial z} + \frac{1}{r}\left(\frac{\partial(r\psi_\theta^s(\mathbf{r},t))}{\partial r} - \frac{\partial \psi_r^s(\mathbf{r},t)}{\partial \theta}\right)$$

$$= \sum_{n=0}^{\infty} U_z^n(r)\cos(n\theta)e^{j(\omega t - K_z z)}$$

$$U_z(r,\theta,z,t) = \frac{\partial \phi^f(\mathbf{r},t)}{\partial z} + \frac{1}{r}\left(\frac{\partial(r\psi_\theta^f(\mathbf{r},t))}{\partial r} - \frac{\partial \psi_r^f(\mathbf{r},t)}{\partial \theta}\right)$$

$$= \sum_{n=0}^{\infty} U_z^n(r)\cos(n\theta)e^{j(\omega t - K_z z)}$$

in which,

$$u_r^n(r) = \frac{1}{r}\Big[(a_1 C_1 r J_{n-1}(a_1 r) + a_2 C_3 r J_{n-1}(a_2 r) + A_3 n J_n(a_3 r) -$$

$$n(C_1 J_n(a_1 r) + C_2 Y_n(a_1 r) + C_3 J_n(a_2 r) + C_4 Y_n(a_2 r)) +$$

$$B_3 n Y_n(a_3 r) + r(a_1 C_2 Y_{n-1}(a_1 r) + a_2 C_4 Y_{n-1}(a_2 r) - irkz(A_1 J_{n+1}(a_3 r) + B_1 Y_{n+1}(a_3 r)))\Big]$$

$$u_\theta^n(r) = \frac{1}{2}\Big((a_3A_3 - 2iA_1kz)J_{n+1}(a_3r) - a_3A_3J_{n-1}(a_3r) - a_3B_3Y_{n-1}(a_3r)\Big) -$$

$$\frac{n(C_1J_n(a_1r) + C_2Y_n(a_1r) + C_3J_n(a_2r) + C_4Y_n(a_2r))}{r} + (\frac{a_3}{2}B_3 - iB_1kz)Y_{n+1}(a_3r)$$

$$u_z^n(r) = -ikz(C_1J_n(a_1r) + C_2Y_n(a_1r) + C_3J_n(a_2r) + C_4Y_n(a_2r)) - a_3(A_1J_n(a_3r) + B_1Y_n(a_3r))$$

$$U_r^n(r) = \frac{1}{2r}\Big(a_1C_1\mu_1rJ_{n-1}(a_1r) + a_2C_3\mu_2rJ_{n-1}(a_2r) + 2A_3\mu_3nJ_n(a_3r) +$$

$$r(a_1C_1\mu_1J_{n+1}(a_1r) + a_2C_3\mu_2J_{n+1}(a_2r)) - 2iA_1kz\mu_3rJ_{n+1}(a_3r) +$$

$$a_1C_2\mu_1rY_{n-1}(a_1r) - a_1C_2\mu_1rY_{n+1}(a_1r) + a_2C_4\mu_2rY_{n-1}(a_2r) +$$

$$2B_3\mu_3nY_n(a_3r) - a_2C_4\mu_2rY_{n+1}(a_2r) - 2iB_1kz\mu_3rY_{n+1}(a_3r)\Big)$$

$$U_\theta^n(r) = \frac{-1}{r}\Big(C_1\mu_1nJ_n(a_1r) + C_3\mu_2nJ_n(a_2r) + a_3A_3\mu_3rJ_{n-1}(a_3r) - A_3\mu_3nJ_n(a_3r) +$$

$$C_2\mu_1nY_n(a_1r) + C_4\mu_2nY_n(a_2r) + a_3B_3\mu_3rY_{n-1}(a_3r) - B_3\mu_3nY_n(a_3r)\Big)$$

$$U_z^n(r) = -ikz(C_1\mu_1J_n(a_1r) + C_2\mu_1Y_n(a_1r) + C_3\mu_2J_n(a_2r) + C_4\mu_2Y_n(a_2r)) +$$

$$\frac{\mu_3(-A_1a_3rJ_n(a_3r) + A_1nJ_{n+1}(a_3r) - a_3B_1rY_n(a_3r) + B_1nY_{n+1}(a_3r))}{r}$$

Appendix N

Solid and Fluid Stresses used in Chapter 5

$$
\sigma_{rr}^n(r) = \frac{1}{r^2}\Big[-2a_2 C_3 N r J_{n-1}(a_2 r) - 2iNrJ_{n-1}(a_3 r)(A_1 kz(n+1) + ia_3 A_3 n) -
$$
$$
+ C_1 J_n(a_1 r)\left(-r^2\left(\delta_1^2(P - 2N + \mu_1 Q) + 2a_1{}^2 N\right) + 2n^2 N + 2nN\right) +
$$
$$
C_3 J_n(a_2 r)\left(-r^2\left(\delta_2^2(P - N + \mu_2 Q) + 2a_2{}^2 N\right) + 2n^2 N + 2nN\right) -
$$
$$
\frac{2N J_n(a_3 r)\left(iA_1 a_3{}^2 kzr^2 + n(n+1)(a_3 A_3 - 2iA_1 kz)\right)}{a_3} -
$$
$$
2iNrY_{n-1}(a_3 r)(+ia_3 B_3 n) + \left(-r^2\left(\delta_1^2(P - N + \mu_1 Q) + 2a_1{}^2 N\right)\right)C_2 Y_n(a_1 r)
$$
$$
+ C_2 Y_n(a_1 r)(2n^2 N + 2nN) - 2a_1 C_1 N r J_{n-1}(a_1 r) - 2a_1 C_2 N r Y_{n-1}(a_1 r)
$$
$$
- 2a_2 C_4 N r Y_{n-1}(a_2 r) + 2iNrY_{n-1}(a_3 r)(B_1 kz(n+1))
$$
$$
C_4 Y_n(a_2 r)\left(-r^2\left(\delta_2^2(P - N + \mu_2 Q) + 2a_2{}^2 N\right) + 2n^2 N + 2nN\right) -
$$
$$
\frac{2N Y_n(a_3 r)\left(ia_3{}^2 B_1 kzr^2 + n(n+1)(a_3 B_3 - 2iB_1 kz)\right)}{a_3}\Big]
$$

$$
\sigma_{r\theta}^n(r) = \frac{N}{r^2}\Big[-2a_2 C_3 n r J_{n-1}(a_2 r) + 2r J_{n-1}(a_3 r)(a_3 A_3 - iA_1 kz(n+1)) -
$$
$$
2a_1 C_1 n r J_{n-1}(a_1 r) + 2C_1 n(n+1) J_n(a_1 r) + 2C_3 n(n+1) J_n(a_2 r) +
$$
$$
\frac{J_n(a_3 r)\left(a_3{}^2 r^2(a_3 A_3 - iA_1 kz) - 2n(n+1)(a3 A_3 - 2iA_1 kz)\right)}{a_3} -
$$
$$
2a_1 C_2 n r Y_{n-1}(a_1 r) - 2a_2 C_4 n r Y_{n-1}(a_2 r) + 2C_2 n(n+1) Y_n(a_1 r) +
$$
$$
2r Y_{n-1}(a_3 r)(a_3 B_3 - iB_1 kz(n+1)) + 2C_4 n(n+1) Y_n(a_2 r)
$$
$$
\frac{Y_n(a_3 r)\left(a_3{}^2 r^2(a_3 B_3 - iB_1 kz) - 2n(n+1)(a_3 B_3 - 2iB_1 kz)\right)}{a_3}\Big]
$$

$$\sigma_{rz}^n(r) = \frac{-iN}{a_3 r}\left[2a_1 a_3 C_1 \mathrm{k}zr J_{n-1}(a_1 r) + 2a_2 a_3 C_3 \mathrm{k}zr J_{n-1}(a_2 r) - \right.$$

$$2a_3 C_1 \mathrm{k}zn J_n(a_1 r) + (-i)A_1 a_3 r(a_3 - \mathrm{k}z)(a_3 + \mathrm{k}z)J_{n-1}(a_3 r) -$$

$$2a_3 C_3 \mathrm{k}zn J_n(a_2 r) + n\left(a_3 A_3 \mathrm{k}z + iA_1\left(a_3{}^2 - 2\mathrm{k}z^2\right)\right)J_n(a_3 r) +$$

$$2a_1 a_3 C_2 \mathrm{k}zr Y_{n-1}(a_1 r) + 2a_2 a_3 C_4 \mathrm{k}zr Y_{n-1}(a_2 r) -$$

$$-2a_3 C_2 \mathrm{k}zn Y_n(a_1 r) - 2a_3 C_4 \mathrm{k}zn Y_n(a_2 r) + ia_3 B_1 r(a_3 - \mathrm{k}z)(a_3 + \mathrm{k}z)Y_{n-1}(a_3 r) +$$

$$\left. \left(ia_3{}^2 B_1 + a_3 B_3 \mathrm{k}z - 2iB_1 \mathrm{k}z^2\right)Y_n(a_3 r)\right]$$

$$S^n(r) = -C_1 \delta_1{}^2(Q + \mu_1 R)J_n(a_1 r) - C_3 \delta_2^2(Q + \mu_2 R)J_n(a_2 r) -$$

$$C_2 \delta_1^2(Q + \mu_1 R)Y_n(a_1 r) - C_4 \delta_2^2(Q + \mu_2 R)Y_n(a_2 r)$$

Appendix O

Displacements and Stresses used in Chapter 5

$$[Q]_{8\times 8} = [\Gamma]_{8\times 8}[\Upsilon]^{-1}_{8\times 8}$$

$$[\Gamma]_{8\times 8} = \begin{bmatrix} \Gamma_{11} & \cdots & \Gamma_{18} \\ \vdots & \ddots & \vdots \\ \Gamma_{81} & \cdots & \Gamma_{88} \end{bmatrix}$$

in which,

$$\Gamma_{11} = \frac{a_1 b J_{n-1}(a_1 b) - n J_n(a_1 b)}{b}, \quad \Gamma_{12} = \frac{a_1 b Y_{n-1}(a_1 b) - n Y_n(a_1 b)}{b}$$

$$\Gamma_{13} = \frac{a_2 b J_{n-1}(a_2 b) - n J_n(a_2 b)}{b}, \quad \Gamma_{14} = \frac{a_2 b Y_{n-1}(a_2 b) - n Y_n(a_2 b)}{b}$$

$$\Gamma_{15} = -ikzJ_{n+1}(a_3 b), \quad \Gamma_{16} = -ikzY_{n+1}(a_3 b), \quad \Gamma_{17} = \frac{n J_n(a_3 b)}{b}$$

$$\Gamma_{18} = \frac{n Y_n(a_3 b)}{b}, \quad \Gamma_{21} = -\frac{n J_n(a_1 b)}{b}, \quad \Gamma_{22} = -\frac{n Y_n(a_1 b)}{b}, \quad \Gamma_{23} = -\frac{n J_n(a_2 b)}{b}$$

$$\Gamma_{24} = -\frac{n Y_n(a_2 b)}{b}, \quad \Gamma_{25} = -ikzJ_{n+1}(a_3 b), \quad \Gamma_{26} = -ikzY_{n+1}(a_3 b)$$

$$\Gamma_{27} = \frac{1}{2}(a_3 J_{n+1}(a_3 b) - a_3 J_{n-1}(a_3 b)), \quad \Gamma_{28} = \frac{1}{2}(a_3 Y_{n+1}(a_3 b) - a_3 Y_{n-1}(a_3 b))$$

$$\Gamma_{31} = -ikzJ_n(a_1 b), \quad \Gamma_{32} = -ikzY_n(a_1 b), \quad \Gamma_{33} = -ikzJ_n(a_2 b)$$

$$\Gamma_{34} = -ikzY_n(a_2 b), \quad \Gamma_{35} = -a_3 J_n(a_3 b), \quad \Gamma_{36} = -a_3 Y_n(a_3 b), \quad \Gamma_{37} = 0, \quad \Gamma_{38} = 0$$

$$\Gamma_{41} = \frac{a_1 b \mu_1 J_{n-1}(a_1 b) - a_1 b \mu_1 J_{n+1}(a_1 b)}{2b}, \quad \Gamma_{42} = \frac{a_1 b \mu_1 Y_{n-1}(a_1 b) - a_1 b \mu_1 Y_{n+1}(a_1 b)}{2b}$$

$$\Gamma_{43} = \frac{a_2 b \mu_2 J_{n-1}(a_2 b) - a_2 b \mu_2 J_{n+1}(a_2 b)}{2b}, \quad \Gamma_{44} = \frac{a_2 b \mu_2 Y_{n-1}(a_2 b) - a_2 b \mu_2 Y_{n+1}(a_2 b)}{2b}$$

$$\Gamma_{45} = -ikz\mu_3 J_{n+1}(a_3 b), \quad \Gamma_{46} = -ikz\mu_3 Y_{n+1}(a_3 b), \quad \Gamma_{47} = \frac{\mu_3 n J_n(a_3 b)}{b}, \quad \Gamma_{48} = \frac{\mu_3 n Y_n(a_3 b)}{b}$$

$$\Gamma_{51} = \frac{aa_1 J_{n-1}(aa_1) - nJ_n(aa_1)}{a}, \quad \Gamma_{52} = \frac{aa_1 Y_{n-1}(aa_1) - nY_n(aa_1)}{a}$$

$$\Gamma_{53} = \frac{aa_2 J_{n-1}(aa_2) - nJ_n(aa_2)}{a}, \quad \Gamma_{54} = \frac{aa_2 Y_{n-1}(aa_2) - nY_n(aa_2)}{a}$$

$$\Gamma_{55} = -ikzJ_{n+1}(aa_3), \quad \Gamma_{56} = -ikzY_{n+1}(aa_3), \quad \Gamma_{57} = \frac{nJ_n(aa_3)}{a}, \quad \Gamma_{58} = \frac{nY_n(aa_3)}{a}$$

$$\Gamma_{61} = -\frac{nJ_n(aa_1)}{a}, \quad \Gamma_{62} = -\frac{nY_n(aa_1)}{a}, \quad \Gamma_{63} = -\frac{nJ_n(aa_2)}{a}, \quad \Gamma_{64} = -\frac{nY_n(aa_2)}{a}$$

$$\Gamma_{65} = -ikzJ_{n+1}(aa_3), \quad \Gamma_{66} = -ikzY_{n+1}(aa_3), \quad \Gamma_{67} = \frac{1}{2}(a_3 J_{n+1}(aa_3) - a_3 J_{n-1}(aa_3))$$

$$\Gamma_{68} = \frac{1}{2}(a_3 Y_{n+1}(aa_3) - a_3 Y_{n-1}(aa_3)), \quad \Gamma_{71} = -ikzJ_n(aa_1), \quad \Gamma_{72} = -ikzY_n(aa_1)$$

$$\Gamma_{73} = -ikzJ_n(aa_2), \quad \Gamma_{74} = -ikzY_n(aa_2), \quad \Gamma_{75} = -a_3 J_n(aa_3), \quad \Gamma_{76} = -a_3 Y_n(aa_3)$$

$$\Gamma_{77} = 0, \quad \Gamma_{78} = 0, \quad \Gamma_{81} = \frac{aa_1 \mu_1 J_{n-1}(aa_1) - aa_1 \mu_1 J_{n+1}(aa_1)}{2a}$$

$$\Gamma_{82} = \frac{aa_1 \mu_1 Y_{n-1}(aa_1) - aa_1 \mu_1 Y_{n+1}(aa_1)}{2a}, \quad \Gamma_{83} = \frac{aa_2 \mu_2 J_{n-1}(aa_2) - aa_2 \mu_2 J_{n+1}(aa_2)}{2a}$$

$$\Gamma_{84} = \frac{aa_2 \mu_2 Y_{n-1}(aa_2) - aa_2 \mu_2 Y_{n+1}(aa_2)}{2a}, \quad \Gamma_{85} = -ikz\mu_3 J_{n+1}(aa_3), \quad \Gamma_{86} = -ikz\mu_3 Y_{n+1}(aa_3)$$

$$\Gamma_{87} = \frac{\mu_3 nJ_n(aa_3)}{a}, \quad \Gamma_{88} = \frac{\mu_3 nY_n(aa_3)}{a}$$

and

$$[\Upsilon]_{8\times 8}^{-1} = \begin{bmatrix} \Upsilon_{11} & \cdots & \Upsilon_{18} \\ \vdots & \ddots & \vdots \\ \Upsilon_{81} & \cdots & \Upsilon_{88} \end{bmatrix}^{-1}$$

in which,

$$\Upsilon_{11} = \frac{J_n(a_1 b)\left(b^2\left(-\left(\delta_1^2(P - N + \mu_1 Q) + 2a_1^2 N\right)\right) + 2n^2 N + 2nN\right)}{b^2} - \\ \frac{-2a_1 bNJ_{n-1}(a_1 b)}{b^2}$$

$$\Upsilon_{12} = \frac{Y_n(a_1b)\left(b^2\left(-\left(\delta_1{}^2(P-N+\mu_1 Q)+2a_1{}^2N\right)\right)+2n^2N+2nN\right)}{b^2}+$$
$$\frac{-2a_1NY_{n-1}(a_1b)}{b}$$

$$\Upsilon_{13} = \frac{J_n(a2b)\left(b^2\left(-\left(\delta_2{}^2(P-N+\mu_2 Q)+2a_2{}^2N\right)\right)+2n^2N+2nN\right)}{b^2}+$$
$$\frac{-2a_2NJ_{n-1}(a_2b)}{b}$$

$$\Upsilon_{14} = \frac{Y_n(a_2b)\left(b^2\left(-\left(\delta_2{}^2(P-N+\mu_2 Q)+2a_2{}^2N\right)\right)+2n^2N+2nN\right)}{b^2}+$$
$$\frac{-2a_2NY_{n-1}(a_2b)}{b}$$

$$\Upsilon_{15} = \frac{4ikzn^2NJ_n(a_3b)}{b^2a_3}+\frac{4iknNJ_n(a_3b)}{b^2a_3}\frac{-2ibkzNJ_{n-1}(a_3b)}{b^2}+$$
$$\frac{-2ia_3b^2kzNJ_n(a_3b)-2ibkznNJ_{n-1}(a_3b)}{b^2}$$

$$\Upsilon_{16} = \frac{4ikzn^2NY_n(a_3b)}{b^2a_3}+\frac{4iknNY_n(a_3b)}{b^2a_3}\frac{-2ibkzNY_{n-1}(a_3b)}{b^2}+$$
$$\frac{-2ia_3b^2kzNY_n(a_3b)-2ibkznNY_{n-1}(a_3b)}{b^2}$$

$$\Upsilon_{17} = \frac{2a_3bnNJ_{n-1}(a_3b)-2nNJ_n(a_3b)-2n^2NJ_n(a_3b)}{b^2}$$

$$\Upsilon_{18} = \frac{2a_3bnNY_{n-1}(a_3b)-2nNY_n(a_3b)-2n^2NJ_n(a_3b)}{b^2}$$

$$\Upsilon_{21} = \frac{N(2n(n+1)J_n(a_1b)-2a_1bnJ_{n-1}(a_1b))}{b^2}, \quad \Upsilon_{22} = \frac{N(2n(n+1)Y_n(a_1b)-2a_1bnY_{n-1}(a_1b))}{b^2}$$

$$\Upsilon_{23} = \frac{N(2n(n+1)J_n(a_2b)-2a_2bnJ_{n-1}(a_2b))}{b^2}, \quad \Upsilon_{24} = \frac{N(2n(n+1)Y_n(a_2b)-2a_2bnY_{n-1}(a_2b))}{b^2}$$

$$\Upsilon_{25} = \frac{4ikzn^2NJ_n(a_3b)}{b^2a_3}+\frac{4iknNJ_n(a_3b)}{b^2a_3}\frac{-2ibkzNJ_{n-1}(a_3b)}{b^2}+$$
$$\frac{-ia_3b^2kzNJ_n(a_3b)-ibkznNJ_{n-1}(a_3b)}{b^2}$$

$$\Upsilon_{26} = \frac{4ikzn^2NY_n(a_3b)}{b^2a_3} + \frac{4ikznNY_n(a_3b)}{b^2a_3} \frac{-2ibkzNY_{n-1}(a_3b)}{b^2} +$$
$$\frac{-ia_3b^2kzNY_n(a_3b) - ibkznNY_{n-1}(a_3b)}{b^2}$$

$$\Upsilon_{27} = N\left(a_3{}^2b^2J_n(a_3b) - 2n^2J_n(a_3b) + 2a_3bJ_{n-1}(a_3b) - 2nJ_n(a_3b)\right)$$

$$\Upsilon_{28} = N\left(a_3{}^2b^2Y_n(a_3b) - 2n^2Y_n(a_3b) + 2a_3bY_{n-1}(a_3b) - 2nJ_n(a_3b)\right)$$

$$\Upsilon_{31} = -\frac{iN(2a_1a_3bkzJ_{n-1}(a_1b) - 2a_3kznJ_n(a_1b))}{a_3b}, \quad \Upsilon_{32} = -\frac{iN(2a_1a_3bkzY_{n-1}(a_1b) - 2a_3kznY_n(a_1b))}{a_3b}$$

$$\Upsilon_{33} = -\frac{iN(2a_2a_3bkzJ_{n-1}(a_2b) - 2a_3kznJ_n(a_2b))}{a_3b}, \quad \Upsilon_{34} = -\frac{iN(2a_2a_3bkzY_{n-1}(a_2b) - 2a_3kznY_n(a_2b))}{a_3b}$$

$$\Upsilon_{35} = -\frac{iN\left((-i)a_3{}^3bJ_{n-1}(a_3b) + ia_3{}^2nJ_n(a_3b) + ia_3bkz^2J_{n-1}(a_3b)\right)}{a_3b}$$
$$\frac{-2ikz^2nJ_n(a_3b)}{a_3b}, \quad \Upsilon_{36} = -\frac{iN\left((-i)a_3{}^3bY_{n-1}(a_3b) + ia_3{}^2nY_n(a_3b) + ia_3bkz^2Y_{n-1}(a_3b)\right)}{a_3b}$$
$$\frac{-2ikz^2nY_n(a_3b)}{a_3b}$$

$$\Upsilon_{37} = -\frac{ikznNJ_n(a_3b)}{b}, \quad \Upsilon_{38} = -\frac{ikznNY_n(a_3b)}{b}, \quad \Upsilon_{41} = -\delta_1{}^2(Q+\mu_1R)J_n(a_1b)$$

$$\Upsilon_{42} = -\delta_1{}^2(Q+\mu_1R)Y_n(a_1b), \quad \Upsilon_{43} = -\delta_2{}^2(Q+\mu_2R)J_n(a_2b)$$

$$\Upsilon_{44} = -\delta_2{}^2(Q+\mu_2R)Y_n(a_2b), \quad \Upsilon_{45} = 0, \quad \Upsilon_{46} = 0, \quad \Upsilon_{47} = 0, \quad \Upsilon_{48} = 0$$

$$\Upsilon_{51} = \frac{J_n(a_1a)\left(a^2\left(-\left(\delta_1{}^2(P-N+\mu_1Q) + 2a_1{}^2N\right)\right) + 2n^2N + 2nN\right)}{a^2} -$$
$$\frac{-2a_1aNJ_{n-1}(a_1a)}{a^2}$$

$$\Upsilon_{52} = \frac{Y_n(a_1a)\left(a^2\left(-\left(\delta_1{}^2(P-N+\mu_1Q) + 2a_1{}^2N\right)\right) + 2n^2N + 2nN\right)}{a^2} -$$
$$\frac{-2a_1aNY_{n-1}(a_1a)}{a^2}$$

$$\Upsilon_{53} = \frac{J_n(a2a)\left(a^2\left(-\left(\delta_2{}^2(P-N+\mu_2 Q)+2a_2{}^2N\right)\right)+2n^2N+2nN\right)}{a^2}+$$
$$\frac{-2a_2NJ_{n-1}(a_2b)}{a}$$

$$\Upsilon_{54} = \frac{Y_n(a_2a)\left(a^2\left(-\left(\delta_2{}^2(P-N+\mu_2 Q)+2a_2{}^2N\right)\right)+2n^2N+2nN\right)}{a^2}+$$
$$\frac{-2a_2NY_{n-1}(a_2b)}{a}$$

$$\Upsilon_{55} = \frac{4ikzn^2NJ_n(a_3a)}{a^2a_3}+\frac{4ikznNJ_n(a_3a)}{a^2a_3}\frac{-2iakzNJ_{n-1}(a_3a)}{a^2}+$$
$$\frac{-2ia_3a^2kzNJ_n(a_3a)-2iakznNJ_{n-1}(a_3a)}{a^2}$$

$$\Upsilon_{56} = \frac{4ikzn^2NY_n(a_3a)}{a^2a_3}+\frac{4ikznNY_n(a_3a)}{a^2a_3}\frac{-2iakzNY_{n-1}(a_3a)}{a^2}+$$
$$\frac{-2ia_3a^2kzNY_n(a_3a)-2iakznNY_{n-1}(a_3a)}{a^2}$$

$$\Upsilon_{57} = \frac{-2n^2NJ_n(aa_3)+2aa_3nNJ_{n-1}(aa_3)-2nNJ_n(aa_3)}{a^2}$$

$$\Upsilon_{58} = \frac{-2n^2NY_n(aa_3)+2aa_3nNY_{n-1}(aa_3)-2nNJ_n(aa_3)}{a^2}$$

$$\Upsilon_{61} = \frac{N(2n(n+1)J_n(aa_1)-2aa_1nJ_{n-1}(aa_1))}{a^2}, \quad \Upsilon_{62} = \frac{N(2n(n+1)Y_n(aa_1)-2aa_1nY_{n-1}(aa_1))}{a^2}$$

$$\Upsilon_{63} = \frac{N(2n(n+1)J_n(aa_2)-2aa_2nJ_{n-1}(aa_2))}{a^2}, \quad \Upsilon_{64} = \frac{N(2n(n+1)Y_n(aa_2)-2aa_2nY_{n-1}(aa_2))}{a^2}$$

$$\Upsilon_{65} = \frac{4ikzn^2NJ_n(a_3a)}{a^2a_3}+\frac{4ikznNJ_n(a_3a)}{a^2a_3}\frac{-2iakzNJ_{n-1}(a_3a)}{a^2}+$$
$$\frac{-ia_3a^2kzNJ_n(a_3a)-2iakznNJ_{n-1}(a_3a)}{a^2}$$

$$\Upsilon_{66} = \frac{4ikzn^2NY_n(a_3a)}{a^2a_3}+\frac{4ikznNY_n(a_3a)}{a^2a_3}\frac{-2iakzNY_{n-1}(a_3a)}{a^2}+$$
$$\frac{-ia_3a^2kzNY_n(a_3a)-2iakznNY_{n-1}(a_3a)}{a^2}$$

$$\Upsilon_{67} = \frac{N\left(a^2a_3{}^2J_n(aa_3)-2n^2J_n(aa_3)+2aa_3J_{n-1}(aa_3)-2nJ_n(aa_3)\right)}{a^2}$$

$$\Upsilon_{68} = \frac{N\left(a^2 a_3{}^2 Y_n(aa_3) - 2n^2 Y_n(aa_3) + 2aa_3 Y_{n-1}(aa_3) - 2n Y_n(aa_3)\right)}{a^2}$$

$$\Upsilon_{71} = -\frac{iN(2aa_1 a_3 \mathrm{k} z J_{n-1}(aa_1) - 2a_3 \mathrm{k} z n J_n(aa_1))}{aa_3}, \quad \Upsilon_{72} = -\frac{iN(2aa_1 a_3 \mathrm{k} z Y_{n-1}(aa_1) - 2a_3 \mathrm{k} z n Y_n(aa_1))}{aa_3}$$

$$\Upsilon_{73} = -\frac{iN(2aa_2 a_3 \mathrm{k} z J_{n-1}(aa_2) - 2a_3 \mathrm{k} z n J_n(aa_2))}{aa_3}, \quad \Upsilon_{74} = -\frac{iN(2aa_2 a_3 \mathrm{k} z Y_{n-1}(aa_2) - 2a_3 \mathrm{k} z n Y_n(aa_2))}{aa_3}$$

$$\Upsilon_{75} = -iN \frac{\left((-i)aa_3{}^3 J_{n-1}(aa_3) + ia_3{}^2 n J_n(aa_3) + iaa_3 \mathrm{k} z^2 J_{n-1}(aa_3)\right)}{aa_3} + \frac{-2N\mathrm{k} z^2 n J_n(aa_3)}{aa_3}$$

$$\Upsilon_{76} = -iN \frac{\left((-i)aa_3{}^3 Y_{n-1}(aa_3) + ia_3{}^2 n Y_n(aa_3) + iaa_3 \mathrm{k} z^2 Y_{n-1}(aa_3)\right)}{aa_3} + \frac{-2N\mathrm{k} z^2 n Y_n(aa_3)}{aa_3}$$

$$\Upsilon_{77} = -\frac{i\mathrm{k} z n N J_n(aa_3)}{a}, \quad \Upsilon_{78} = -\frac{i\mathrm{k} z n N J_n(aa_3)}{a}$$

$$\Upsilon_{81} = -\delta_1{}^2 (Q + \mu_1 R) J_n(aa_1), \quad \Upsilon_{82} = -\delta_1{}^2 (Q + \mu_1 R) Y_n(aa_1)$$

$$\Upsilon_{83} = -\delta_2^2 (Q + \mu_2 R) J_n(aa_2), \quad \Upsilon_{84} = -\delta_2{}^2 (Q + \mu_2 R) Y_n(aa_2)$$

$$\Upsilon_{85} = 0, \quad \Upsilon_{86} = 0, \quad \Upsilon_{87} = 0, \quad \Upsilon_{88} = 0$$

Appendix P

Coefficients of H Matrix used in Chapter 5

$$H_{11} = \phi^2 \rho_1 Q_{51} \omega^2 H_n^{(1)}(bK_{3r}) - \phi^2 \rho_1 Q_{54} \omega^2 H_n^{(1)}(bK_{3r}) -$$
$$\phi^2 \rho_1 Q_{81} \omega^2 H_n^{(1)}(bK_{3r}) + \phi^2 \rho_1 Q_{84} \omega^2 H_n^{(1)}(bK_{3r}) -$$
$$2\phi \rho_1 Q_{51} \omega^2 H_n^{(1)}(bK_{3r}) + \phi \rho_1 Q_{54} \omega^2 H_n^{(1)}(bK_{3r}) +$$
$$\phi \rho_1 Q_{81} \omega^2 H_n^{(1)}(bK_{3r}) + Q_{51} \rho_1 \omega^2 H_n^{(1)}(bK_{3r})$$

$$H_{12} = \phi^2 \rho_1 Q_{55} \omega^2 H_n^{(2)}(aK_{1r}) - \phi^2 \rho_1 Q_{58} \omega^2 H_n^{(2)}(aK_{1r}) -$$
$$\phi^2 \rho_1 Q_{85} \omega^2 H_n^{(2)}(aK_{1r}) + \phi^2 \rho_1 Q_{88} \omega^2 H_n^{(2)}(aK_{1r}) -$$
$$2\phi \rho_1 Q_{55} \omega^2 H_n^{(2)}(aK_{1r}) + \phi \rho_1 Q_{58} \omega^2 H_n^{(2)}(aK_{1r}) +$$
$$\phi \rho_1 Q_{85} \omega^2 H_n^{(2)}(aK_{1r}) + \rho_1 Q_{55} \omega^2 H_n^{(2)}(aK_{1r}) +$$
$$\frac{1}{2} K_{1r} H_{n-1}^{(2)}(aK_{1r}) - \frac{1}{2} K_{1r} H_{n+1}^{(2)}(aK_{1r})$$

$$H_{21} = \phi^2 Q_{11} \rho_3 \omega^2 H_n^{(1)}(bK_{3r}) - \phi^2 Q_{14} \rho_3 \omega^2 H_n^{(1)}(bK_{3r}) -$$
$$\phi^2 \rho_3 Q_{41} \omega^2 H_n^{(1)}(bK_{3r}) + \phi^2 \rho_3 Q_{44} \omega^2 H_n^{(1)}(bK_{3r}) -$$
$$2\phi Q_{11} \rho_3 \omega^2 H_n^{(1)}(bK_{3r}) + \phi Q_{14} \rho_3 \omega^2 H_n^{(1)}(bK_{3r}) +$$
$$\phi \rho_3 Q_{41} \omega^2 H_n^{(1)}(bK_{3r}) + Q_{11} \rho_3 \omega^2 H_n^{(1)}(bK_{3r}) +$$
$$\frac{1}{2} K_{3r} H_{n-1}^{(1)}(bK_{3r}) - \frac{1}{2} K_{3r} H_{n+1}^{(1)}(bK_{3r})$$

$$H_{22} = \phi^2 Q_{15} \rho_3 \omega^2 H_n^{(2)}(aK_{1r}) - \phi^2 Q_{18} \rho_3 \omega^2 H_n^{(2)}(aK_{1r}) -$$
$$\phi^2 \rho_3 Q_{45} \omega^2 H_n^{(2)}(aK_{1r}) + \phi^2 \rho_3 Q_{48} \omega^2 H_n^{(2)}(aK_{1r}) -$$
$$2\phi Q_{15} \rho_3 \omega^2 H_n^{(2)}(aK_{1r}) + \phi Q_{18} \rho_3 \omega^2 H_n^{(2)}(aK_{1r}) +$$
$$\phi \rho_3 Q_{45} \omega^2 H_n^{(2)}(aK_{1r}) + Q_{15} \rho_3 \omega^2 H_n^{(2)}(aK_{1r})$$

$$\chi_{11} = \rho_1 \omega^2 \left((1-\phi)(\varepsilon_n p_0(\phi-1)Q_{55}(-i)^n(J_n(k_{1r}a)))-\right.$$
$$\rho_1 \omega^2 (1-\phi)(\varepsilon_n p_0 \phi Q_{58}(-i)^n(J_n(k_{1r}a))))+$$
$$\rho_1 \omega^2 (\phi)(\phi(\varepsilon_n p_0(\phi-1)Q_{85}(-i)^n(J_n(k_{1r}a)))-$$
$$\rho_1 \omega^2 (\phi)(\varepsilon_n p_0 \phi Q_{88}(-i)^n(J_n(k_{1r}a)))-$$
$$\frac{1}{2}\varepsilon_n k_{1r}(-i)^n p_0(J_{n-1}(k_{1r}a)-J_{n+1}(k_{1r}a))$$

$$\chi_{21} = \rho_3 \omega^2 (1-\phi)(\varepsilon_n p_0(\phi-1)Q_{15}(-i)^n(J_n(k_{1r}a)))-$$
$$\rho_3 \omega^2 (1-\phi)(\varepsilon_n p_0 \phi Q_{18}(-i)^n(J_n(k_{1r}a)))+$$
$$\phi(\varepsilon_n p_0(\phi-1)Q_{45}(-i)^n(J_n(k_{1r}a)))-$$
$$\phi(\varepsilon_n p_0 \phi Q_{48}(-i)^n(J_n(k_{1r}a)))$$

Appendix Q

Transmission Loss used in Chapter 5

The transmission loss due to the propagation of acoustical waves through a cylinder can be expressed as

$$TL = 10 \log_{10} \left(\frac{\Pi_I}{\Pi_T} \right)$$

in which Π_I and Π_T are the incident and transmitted acoustic powers, respectively, given by

$$\Pi_I = \frac{1}{2} Re(\int_A p^I v^* dA)$$

in which $Re(z)$, A, and v are the real part of complex number z, the domain of integration over the surface of the cylinder, and the radial particle velocity, respectively. Note that the superscript " $*$ " is related to the complex conjugate of a complex number. Similarly, the transmitted power is written as

$$\Pi_T = \frac{1}{2} Re(\int_A p^T v^* dS) = \frac{1}{2} Re \left[\int_A p^T \frac{\partial (u_r)^*}{\partial t} dS \right]$$

Bibliography

.

Abendschein, WALTER and GW Hyatt (1970). "33 Ultrasonics and Selected Physical Properties of Bone." In: *Clinical Orthopaedics and Related Research (1976-2007)* 69, pp. 294–301.

Adachi, Taiji et al. (2001). "Trabecular surface remodeling simulation for cancellous bone using microstructural voxel finite element models". In: *J. Biomech. Eng.* 123.5, pp. 403–409.

Allard, J-F and Gilles Daigle (1994). *Propagation of sound in porous media: Modeling sound absorbing materials.*

Allard, Jean and Noureddine Atalla (1993). *Propagation of sound in porous media: modelling sound absorbing materials 2e*. John Wiley & Sons.

Allard, Jean and Noureddine Atalla (2009). *Propagation of sound in porous media: modelling sound absorbing materials 2e*. John Wiley & Sons.

Alves, José Marcos et al. (1996). "Influence of marrow on ultrasonic velocity and attenuation in bovine trabecular bone". In: *Calcified tissue international* 58.5, pp. 362–367.

Anast, George T, THEODORE Fields, and IRWIN M Siegel (1958). "Ultrasonic technique for the evaluation of bone fractures". In: *American Journal of Physical Medicine & Rehabilitation* 37.3, pp. 157–159.

Anderson, Christian C et al. (2008). "Interference between wave modes may contribute to the apparent negative dispersion observed in cancellous bone". In: *The Journal of the Acoustical Society of America* 124.3, pp. 1781–1789.

André, Michael P et al. (1980). "Measurement of the velocity of ultrasound in the human femur in vivo". In: *Medical physics* 7.4, pp. 324–330.

Ashman, Richard B, James D Corin, and Charles H Turner (1987). "Elastic properties of cancellous bone: measurement by an ultrasonic technique". In: *Journal of Biomechanics* 20.10, pp. 979–986.

Ashman, Richard B and Jae Young Rho (1988). "Elastic modulus of trabecular bone material". In: *Journal of biomechanics* 21.3, pp. 177–181.

Attenborough, Keith (1983). "Acoustical characteristics of rigid fibrous absorbents and granular materials". In: *the Journal of the Acoustical Society of America* 73.3, pp. 785–799.

Avioli, LV (1988). "Ultrasound transmission velocity in screening for bone fragility". In: *J Bone Min Res* 3, p. 215.

Bagley, Ronald L and Peter J Torvik (1986). "On the fractional calculus model of viscoelastic behavior". In: *Journal of Rheology* 30.1, pp. 133–155.

Baran, Daniel T et al. (1988). "Ultrasound attenuation of the os calcis in women with osteoporosis and hip fractures". In: *Calcified tissue international* 43.3, pp. 138–142.

Barger, James E (1979). "Attenuation and dispersion of ultrasound in cancellous bone". In: *Ultrasonic Tissue Characterization* 11, pp. 197–201.

Behari, J and S Singh (1981). "Ultrasound propagation in 'in vivo'bone". In: *Ultrasonics* 19.2, pp. 87–90.

Belhocine, F, S Derible, and H Franklin (2007). "Transition term method for the analysis of the reflected and the transmitted acoustic signals from water-saturated porous plates". In: *The Journal of the Acoustical Society of America* 122.3, pp. 1518–1526.

Bennamane, Abderrazek and Tarek Boutkedjirt (2017). "Theoretical and experimental study of the ultrasonic attenuation in bovine cancellous bone". In: *Applied Acoustics* 115, pp. 50–60.

Berryman, James G (1980). "Confirmation of Biot's theory". In: *Applied Physics Letters* 37.4, pp. 382–384.

Biot, MA (1956a). "Theory of elastic waves in a fluid-saturated porous solid. 1. Low frequency range". In: *J. Acoust. Soc. Am.* 28, pp. 168–178.

Biot, Maurice A (1941). "General theory of three-dimensional consolidation". In: *Journal of applied physics* 12.2, pp. 155–164.

Biot, Maurice A (1955). "Theory of elasticity and consolidation for a porous anisotropic solid". In: *Journal of applied physics* 26.2, pp. 182–185.

Biot, Maurice A (1956b). "General solutions of the equations of elasticity and consolidation for a porous material". In: *J. appl. Mech* 23.1, pp. 91–96.

Biot, Maurice A (1956c). "Theory of propagation of elastic waves in a fluid-saturated porous solid. I. Low-Frequency Range". In: *The Journal of the acoustical Society of america* 28.2, pp. 179–191.

Biot, Maurice A (1956d). "Theory of propagation of elastic waves in a fluid-saturated porous solid. II. Higher frequency range". In: *The Journal of the acoustical Society of america* 28.2, pp. 179–191.

Biot, Maurice A (1956e). "Theory of propagation of elastic waves in a fluid-saturated porous solid. II. Higher frequency range". In: *The Journal of the acoustical Society of america* 28.2, pp. 179–191.

Biot, Maurice A (1962a). "Generalized theory of acoustic propagation in porous dissipative media". In: *The Journal of the Acoustical Society of America* 34.9A, pp. 1254–1264.

Biot, Maurice A (1962b). "Mechanics of deformation and acoustic propagation in porous media". In: *Journal of applied physics* 33.4, pp. 1482–1498.

Biot, Maurice A and DG Willis (1957). "The elastic coeff cients of the theory of consolidation". In: *J Appl Mech* 15, pp. 594–601.

Bohr, H and O Schaadt (1983). "Bone mineral content of femoral bone and the lumbar spine measured in women with fracture of the femoral neck by dual photon absorptiometry." In: *Clinical orthopaedics and related research* 179, pp. 240–245.

Bolton, JS, N-M Shiau, and YJ Kang (1996). "Sound transmission through multi-panel structures lined with elastic porous materials". In: *Journal of sound and vibration* 191.3, pp. 317–347.

Bossy, Emmanuel et al. (2005). "Three-dimensional simulation of ultrasound propagation through trabecular bone structures measured by synchrotron microtomography". In: *Physics in Medicine & Biology* 50.23, p. 5545.

Bourbie, T et al. (1987). "Acoustics of Porous Media". In: *The Journal of the Acoustical Society of America* 91.5, pp. 3080–3080.

Buchanan, James L and Robert P Gilbert (2007). "Determination of the parameters of cancellous bone using high frequency acoustic measurements". In: *Mathematical and computer modelling* 45.3-4, pp. 281–308.

Buchanan, JAMES L, ROBERT P Gilbert, and KHALDOUN Khashanah (2002). "Recovery of the poroelastic parameters of cancellous bone using low frequency acoustic interrogation". In: *Acoustics, Mechanics, and the Related Topics of Mathematical Analysis*. World Scientific, pp. 41–47.

Buchanan, James L, Robert P Gilbert, and Khaldoun Khashanah (2004). "Determination of the parameters of cancellous bone using low frequency acoustic measurements". In: *Journal of Computational Acoustics* 12.02, pp. 99–126.

Buchanan, James L, Robert P Gilbert, and Y Ou Miao-jung (2011). "Wavelet decomposition of transmitted ultrasound wave through a 1-D muscle–bone system". In: *Journal of biomechanics* 44.2, pp. 352–358.

Buchanan, James L, Robert P Gilbert, and Miao-jung Ou (2012). "Transfer functions for a one-dimensional fluid–poroelastic system subject to an ultrasonic pulse". In: *Nonlinear Analysis: Real World Applications* 13.3, pp. 1030–1043.

Buchanan, James L et al. (2003). "Transient reflection and transmission of ultrasonic wave in cancellous bone". In: *Applied mathematics and computation* 142.2-3, pp. 561–573.

Butzer, Paul L and Ursula Westphal (2000). "An introduction to fractional calculus". In: *Applications of Fractional Calculus in Physics*. World Scientific, pp. 1–85.

Caputo, Michele (1976). "Vibrations of an infinite plate with a frequency independent Q". In: *The Journal of the Acoustical Society of America* 60.3, pp. 634–639.

Cardoso, Luis and Stephen C Cowin (2011). "Fabric dependence of quasi-waves in anisotropic porous media". In: *The Journal of the Acoustical Society of America* 129.5, pp. 3302–3316.

Cardoso, Luis et al. (2003). "In vitro acoustic waves propagation in human and bovine cancellous bone". In: *Journal of Bone and Mineral Research* 18.10, pp. 1803–1812.

Caviglia, G and A Morro (2004). "A closed-form solution for reflection and transmission of transient waves in multilayers". In: *The Journal of the Acoustical Society of America* 116.2, pp. 643–654.

Cepollaro, Chiara et al. (2005). "In vivo performance evaluation of the Achilles Insight QUS device". In: *Journal of Clinical Densitometry* 8.3, pp. 341–346.

Chaffaı, S et al. (2000). "Frequency dependence of ultrasonic backscattering in cancellous bone: Autocorrelation model and experimental results". In: *The journal of the Acoustical Society of America* 108.5, pp. 2403–2411.

Chaffaı, S et al. (2002). "Ultrasonic characterization of human cancellous bone using transmission and backscatter measurements: relationships to density and microstructure". In: *Bone* 30.1, pp. 229–237.

Chen, Hua, Robert P Gilbert, and Philippe Guyenne (2018). "A Biot model for the determination of material parameters of cancellous bone from acoustic measurements". In: *Inverse Problems* 34.8, p. 085009.

Cummings, Steven R et al. (1993). "Bone density at various sites for prediction of hip fractures". In: *The Lancet* 341.8837, pp. 72–75.

Daneshjou, K, R Talebitooti, and A Tarkashvand (2017). "An exact solution of three-dimensional elasticity for sound transmission loss through FG cylinder in presence of subsonic external flow". In: *International Journal of Mechanical Sciences* 120, pp. 105–119.

Daneshjou, K et al. (2010). "Analytical model of sound transmission through relatively thick FGM cylindrical shells considering third order shear deformation theory". In: *Composite Structures* 93.1, pp. 67–78.

Depollier, Claude, Jean F Allard, and Walter Lauriks (1988). "Biot theory and stress–strain equations in porous sound-absorbing materials". In: *The Journal of the Acoustical Society of America* 84.6, pp. 2277–2279.

Durbin, F (1974). "Numerical inversion of Laplace transforms: an efficient improvement to Dubner and Abate's method". In: *The Computer Journal* 17.4, pp. 371–376.

Evans, JA and MB Tavakoli (1990). "Ultrasonic attenuation and velocity in bone". In: *Physics in Medicine & Biology* 35.10, p. 1387.

Evans, WD et al. (1988). "Ultrasonic attenuation and bone mineral density". In: *Clin Phys Physiol Meas* 9, pp. 163–165.

Fan, SC, SM Li, and GY Yu (2005). "Dynamic fluid-structure interaction analysis using boundary finite element method–Finite element method". In: *Journal of Applied Mechanics* 72.4, pp. 591–598.

Fellah, M, Zine El Abiddine Fellah, and C Depollier (2008). "Generalized hyperbolic fractional equation for transient-wave propagation in layered rigid-frame porous materials". In: *Physical Review E* 77.1, p. 016601.

Fellah, Mohamed et al. (2013). "Transient ultrasound propagation in porous media using Biot theory and fractional calculus: Application to human cancellous bone". In: *The Journal of the Acoustical Society of America* 133.4, pp. 1867–1881.

Fellah, ZE A et al. (2010). "Ultrasonic characterization of air-saturated double-layered porous media in time domain". In: *Journal of Applied Physics* 108.1, p. 014909.

Fellah, ZEA and C Depollier (2000). "Transient acoustic wave propagation in rigid porous media: A time-domain approach". In: *The Journal of the Acoustical Society of America* 107.2, pp. 683–688.

Fellah, ZEA, C Depollier, and M Fellah (2002). "Application of fractional calculus to the sound waves propagation in rigid porous materials: validation via ultrasonic measurements". In: *Acta Acustica united with Acustica* 88.1, pp. 34–39.

Fellah, Zine El Abiddine et al. (2004a). "Ultrasonic wave propagation in human cancellous bone: Application of Biot theory". In: *The Journal of the Acoustical Society of America* 116.1, pp. 61–73.

Fellah, Zine El Abiddine et al. (2005). "A time-domain model of transient acoustic wave propagation in double-layered porous media". In: *The Journal of the Acoustical Society of America* 118.2, pp. 661–670.

Fellah, Zine El Abidine et al. (2003). "Direct and inverse scattering of transient acoustic waves by a slab of rigid porous material". In: *The Journal of the Acoustical Society of America* 113.1, pp. 61–72.

Fellah, Zine El Abidine et al. (2004b). "Verification of Kramers–Kronig relationship in porous materials having a rigid frame". In: *Journal of sound and vibration* 270.4-5, pp. 865–885.

Floriani, LP, NT Debervoise, and GW Hyatt (1967). "Mechanical properties of healing bone by the use of ultrasound". In: *Surg. Forum*. Vol. 18, pp. 468–470.

Fritsch, Andreas and Christian Hellmich (2007). "'Universal'microstructural patterns in cortical and trabecular, extracellular and extravascular bone materials: micromechanics-based prediction of anisotropic elasticity". In: *Journal of Theoretical Biology* 244.4, pp. 597–620.

Fry, FJ and JE Barger (1978). "Acoustical properties of the human skull". In: *The Journal of the Acoustical Society of America* 63.5, pp. 1576–1590.

Garcia, BJ et al. (1978). "Ultrasonic attenuation in bone". In: *1978 Ultrasonics Symposium*. IEEE, pp. 327–330.

Gilbert, Robert P, Philippe Guyenne, and Jing Li (2013a). "A viscoelastic model for random ultrasound propagation in cancellous bone". In: *Computers & Mathematics with Applications* 66.6, pp. 943–964.

Gilbert, Robert P, Philippe Guyenne, and Jing Li (2013b). "Simulation of a mixture model for ultrasound propagation through cancellous bone using staggered-grid finite differences". In: *Journal of Computational Acoustics* 21.01, p. 1250017.

Gilbert, Robert P, Philippe Guyenne, and Jing Li (2014). "Numerical investigation of ultrasonic attenuation through 2D trabecular bone structures reconstructed from CT scans and random realizations". In: *Computers in biology and medicine* 45, pp. 143–156.

Gilbert, Robert P, Philippe Guyenne, and M Yvonne Ou (2012). "A quantitative ultrasound model of the bone with blood as the interstitial fluid". In: *Mathematical and Computer Modelling* 55.9-10, pp. 2029–2039.

Gilbert, Robert P et al. (2009). "Computing porosity of cancellous bone using ultrasonic waves, II: The muscle, cortical, cancellous bone system". In: *Mathematical and computer modelling* 50.3-4, pp. 421–429.

Goossens, Liesbet et al. (2008). "The correlation between the SOS in trabecular bone and stiffness and density studied by finite-element analysis". In: *IEEE transactions on ultrasonics, ferroelectrics, and frequency control* 55.6, pp. 1234–1242.

Gorenflo, Rudolf and Francesco Mainardi (2008). "Fractional calculus: Integral and differential equations of fractional order". In: *arXiv preprint arXiv:0805.3823*.

Greenfield, MA et al. (1981). "Measurement of the velocity of ultrasound in human cortical bone in vivo. Estimation of its potential value in the diagnosis of osteoporosis and metabolic bone disease." In: *Radiology* 138.3, pp. 701–710.

Grimes, Morad et al. (2012). "In vitro estimation of fast and slow wave parameters of thin trabecular bone using space-alternating generalized expectation–maximization algorithm". In: *Ultrasonics* 52.5, pp. 614–621.

Haïat, G et al. (2007a). "Modeling of velocity dispersion in trabecular bone: effect of multiple scattering and of viscous absorption." In:

Haïat, Guillaume et al. (2007b). "Variation of ultrasonic parameters with microstructure and material properties of trabecular bone: a 3D model simulation". In: *Journal of Bone and Mineral Research* 22.5, pp. 665–674.

Haire, TJ and CM Langton (1999). "Biot theory: a review of its application to ultrasound propagation through cancellous bone". In: *Bone* 24.4, pp. 291–295.

Hanyga, Andrzej and Vladimir E Rok (2000). "Wave propagation in micro-heterogeneous porous media: A model based on an integro-differential wave equation". In: *The Journal of the Acoustical Society of America* 107.6, pp. 2965–2972.

Hasheminejad, Seyyed M and Mahdi Alaei-Varnosfaderani (2012). "Vibroacoustic response and active control of a fluid-filled functionally graded piezoelectric material composite cylinder". In: *Journal of Intelligent Material Systems and Structures* 23.7, pp. 775–790.

Hasheminejad, Seyyed M and Hessam Mousavi-Akbarzadeh (2013). "Three dimensional non-axisymmetric transient acoustic radiation from an eccentric hollow cylinder". In: *Wave Motion* 50.4, pp. 723–738.

Hodaei, M, P Maghoul, and N Popplewell (2020). "An overview of the acoustic studies of bone-like porous materials, and the effect of transverse acoustic waves". In: *International Journal of Engineering Science* 147, p. 103189.

Hodaei, M, V Rabbani, and P Maghoul (2020). "Transient acoustic wave propagation in bone-like porous materials using the theory of poroelasticity and fractional derivative: a sensitivity analysis". In: *Acta Mechanica* 231.1, pp. 179–203.

Hoffmeister, BK, SA Whitten, and JY Rho (2000). "Low-megahertz ultrasonic properties of bovine cancellous bone". In: *Bone* 26.6, pp. 635–642.

Horn, CA and D Robinson (1965). "Assessment of fracture healing by ultrasonics". In: *Australasian Radiology* 9.2, pp. 165–167.

Hosie, CJ et al. (1987). "Comparison of broadband ultrasonic attenuation of the os calcis and quantitative computed tomography of the distal radius". In: *Clinical Physics and Physiological Measurement* 8.4, p. 303.

Hosokawa, A (2005). "Simulation of ultrasound propagation through bovine cancellous bone using elastic and Biot's finite-difference time-domain methods". In: *The Journal of the Acoustical Society of America* 118.3, pp. 1782–1789.

Hosokawa, A and T Otani (1998). "Acoustic anisotropy in bovine cancellous bone". In: *The Journal of the Acoustical Society of America* 103.5, pp. 2718–2722.

Hosokawa, Atsushi and Takahiko Otani (1997). "Ultrasonic wave propagation in bovine cancellous bone". In: *The Journal of the Acoustical Society of America* 101.1, pp. 558–562.

Hughes, Elinor R et al. (2003). "Estimation of critical and viscous frequencies for Biot theory in cancellous bone". In: *Ultrasonics* 41.5, pp. 365–368.

Hughes, Elinor R et al. (2007). "Investigation of an anisotropic tortuosity in a Biot model of ultrasonic propagation in cancellous bone". In: *The Journal of the Acoustical Society of America* 121.1, pp. 568–574.

Hughes, Elinor Ruth et al. (1999). "Ultrasonic propagation in cancellous bone: A new stratified model". In: *Ultrasound in medicine & biology* 25.5, pp. 811–821.

Hui, Siu L, Charles W Slemenda, and C Conrad Johnston (1988). "Age and bone mass as predictors of fracture in a prospective study." In: *The Journal of clinical investigation* 81.6, pp. 1804–1809.

Hui, Siu L, Charles W Slemenda, and C Conrad Johnston (1989). "Baseline measurement of bone mass predicts fracture in white women". In: *Annals of internal medicine* 111.5, pp. 355–361.

Ilic, S, K Hackl, and RP Gilbert (2011). "Application of a biphasic representative volume element to the simulation of wave propagation through cancellous bone". In: *Journal of Computational Acoustics* 19.02, pp. 111–138.

Ilić, Sandra and Klaus Hackl (2004). "Homogenisation of random composites via the multiscale finite-element method". In: *PAMM: Proceedings in Applied Mathematics and Mechanics*. Vol. 4. 1. Wiley Online Library, pp. 326–327.

Ilic, Sandra, Klaus Hackl, and Robert Gilbert (2010). "Application of the multiscale FEM to the modeling of cancellous bone". In: *Biomechanics and modeling in mechanobiology* 9.1, pp. 87–102.

Jacobs, Christopher R (2000). "The mechanobiology of cancellous bone structural adaptation". In: *Journal of rehabilitation research and development* 37.2, pp. 209–216.

Johnson, David Linton, Joel Koplik, and Roger Dashen (1987). "Theory of dynamic permeability and tortuosity in fluid-saturated porous media". In: *Journal of fluid mechanics* 176, pp. 379–402.

Johnson, David Linton, Thomas J Plona, and Haruo Kojima (1994). "Probing porous media with first and second sound. II. Acoustic properties of water-saturated porous media". In: *Journal of Applied Physics* 76.1, pp. 115–125.

Jurist, John M (1970). "In vivo determination of the elastic response of bone. I. Method of ulnar resonant frequency determination". In: *Physics in Medicine & Biology* 15.3, p. 417.

Kaczmarek, M, J Kubik, and M Pakula (2002). "Short ultrasonic waves in cancellous bone". In: *Ultrasonics* 40.1-8, pp. 95–100.

Kaczmarek, M, J Kubik, and M Pakula (2005). *Wave propagation in saturated high porosity materials*. Taylor and Francis Group, London.

Kaufman, Jonathan J, Gangming Luo, and Robert S Siffert (2003). "On the relative contributions of absorption and scattering to ultrasound attenuation in trabecular bone: A simulation study". In: *IEEE Symposium on Ultrasonics, 2003*. Vol. 2. IEEE, pp. 1519–1523.

Krolner, B and S Pors Nielsen (1982). "Bone mineral content of the lumbar spine in normal and osteoporotic women: cross-sectional and longitudinal studies". In: *Clin Sci* 62.3, pp. 329–336.

Lafarge, Denis et al. (1997). "Dynamic compressibility of air in porous structures at audible frequencies". In: *The Journal of the Acoustical Society of America* 102.4, pp. 1995–2006.

Lakes, Roderic, Hyo Sub Yoon, and J Lawrence Katz (1983). "Slow compressional wave propagation in wet human and bovine cortical bone". In: *Science* 220.4596, pp. 513–515.

Lang, Sidney B (1970). "Ultrasonic method for measuring elastic coefficients of bone and results on fresh and dried bovine bones". In: *IEEE transactions on Biomedical Engineering* 2, pp. 101–105.

Langton, CM, SB Palmer, and RW Porter (1984). "The measurement of broadband ultrasonic attenuation in cancellous bone". In: *Engineering in medicine* 13.2, pp. 89–91.

Lauriks, Walter et al. (1994). "Propagation of ultrasonic pulses through trabecular bone". In: *Le Journal de Physique IV* 4.C5, pp. C5–1255.

Leclaire, Ph, L Kelders W Lauriks C Glorieux, and J Thoen (1997). "Ultrasonic wave propagation in porous media: Determination of acoustic". In: *Bone Research in Biomechanics* 40, p. 139.

Lee, J-H and J Kim (2002). "Analysis and measurement of sound transmission through a double-walled cylindrical shell". In: *Journal of sound and vibration* 251.4, pp. 631–649.

Lee, Joon-Hyun and J Kim (2003). "Study on sound transmission characteristics of a cylindrical shell using analytical and experimental models". In: *Applied acoustics* 64.6, pp. 611–632.

Lee, Kang Il, Heui-Seol Roh, and Suk Wang Yoon (2003). "Acoustic wave propagation in bovine cancellous bone: application of the modified Biot–Attenborough model". In: *The Journal of the acoustical Society of america* 114.4, pp. 2284–2293.

Li, Jun and Martin Ostoja-Starzewski (2019). "Application of fractional calculus to fractal media". In: *Applications in Physics,Part A, pp.263-276.*

Lin, Julie T and Joseph M Lane (2004). "Osteoporosis: a review". In: *Clinical Orthopaedics and Related Research*® 425, pp. 126–134.

Luo, Gangming et al. (1999). "Computational methods for ultrasonic bone assessment". In: *Ultrasound in medicine & biology* 25.5, pp. 823–830.

Luppé, Francine, Jean-Marc Conoir, and Hervé Franklin (2002). "Scattering by a fluid cylinder in a porous medium: Application to trabecular bone". In: *The Journal of the Acoustical Society of America* 111.6, pp. 2573–2582.

Maghoul, Pooneh, Behrouz Gatmiri, and Denis Duhamel (2011a). "Boundary integral formulation and two-dimensional fundamental solutions for dynamic behavior analysis of unsaturated soils". In: *Soil Dynamics and Earthquake Engineering* 31.11, pp. 1480–1495.

Maghoul, Pooneh, Behrouz Gatmiri, and Denis Duhamel (2011b). "Wave propagation in unsaturated poroelastic media: Boundary integral formulation and three-dimensional fundamental solution". In: *Computer Modelling in Engineering and Sciences* 78.1, pp. 51–76.

Mano, Isao et al. (2006). "Development of novel ultrasonic bone densitometry using acoustic parameters of cancellous bone for fast and slow waves". In: *Japanese journal of applied physics* 45.5S, p. 4700.

Marfurt, Kurt J (1984). "Accuracy of finite-difference and finite-element modeling of the scalar and elastic wave equations". In: *Geophysics* 49.5, pp. 533–549.

Marutyan, Karen R, Mark R Holland, and James G Miller (2006). "Anomalous negative dispersion in bone can result from the interference of fast and slow waves". In: *The Journal of the Acoustical Society of America* 120.5, EL55–EL61.

McCartney, RN and LB Jeffcott (1987). "Combined 2.25 MHz ultrasound velocity and bone mineral density measurements in the equine metacarpus and theirin vivo applications". In: *Medical and Biological Engineering and Computing* 25.6, pp. 620–626.

McCloskey, EV et al. (1990). "Broadband ultrasound attenuation in the os calcis: relationship to bone mineral at other skeletal sites". In: *Clinical Science* 78.2, pp. 227–233.

McKelvie, ML and SB Palmer (1991). "The interaction of ultrasound with cancellous bone". In: *Physics in Medicine & Biology* 36.10, p. 1331.

Meunier, A et al. (1982). "Ultrasonic characterization of some pathological human femora". In: *1982 Ultrasonics Symposium*. IEEE, pp. 713–717.

Miehe, C, Jacques Schotte, and M Lambrecht (2002). "Homogenization of inelastic solid materials at finite strains based on incremental minimization principles. Application to the texture analysis of polycrystals". In: *Journal of the Mechanics and Physics of Solids* 50.10, pp. 2123–2167.

Miller, Kenneth S and Bertram Ross (1993). "An introduction to the fractional calculus and fractional differential equations". In:

Mizuno, Katsunori et al. (2009). "Propagation of two longitudinal waves in human cancellous bone: An in vitro study". In: *The Journal of the Acoustical Society of America* 125.5, pp. 3460–3466.

Morse, Philip McCord and K Uno Ingard (1986). *Theoretical acoustics*. Princeton university press.

Multiphysics, COMSOL (1998). "Introduction to COMSOL Multiphysics®". In: *COMSOL Multiphysics, Burlington, MA, accessed Feb* 9, p. 2018.

Nagatani, Yoshiki et al. (2006). "Applicability of finite-difference time-domain method to simulation of wave propagation in cancellous bone". In: *Japanese journal of applied physics* 45.9R, p. 7186.

Nagatani, Yoshiki et al. (2008). "Numerical and experimental study on the wave attenuation in bone–FDTD simulation of ultrasound propagation in cancellous bone". In: *Ultrasonics* 48.6-7, pp. 607–612.

Nelson, Amber M et al. (2011). "Determining attenuation properties of interfering fast and slow ultrasonic waves in cancellous bone". In: *The Journal of the Acoustical Society of America* 130.4, pp. 2233–2240.

Nguyen, Vu-Hieu and Salah Naili (2012). "Simulation of ultrasonic wave propagation in anisotropic poroelastic bone plate using hybrid spectral/finite element method". In: *International journal for numerical methods in biomedical engineering* 28.8, pp. 861–876.

Nguyen, Vu-Hieu, Salah Naili, and Vittorio Sansalone (2010). "Simulation of ultrasonic wave propagation in anisotropic cancellous bone immersed in fluid". In: *Wave Motion* 47.2, pp. 117–129.

Nicholson, Patrick HF and Mary L Bouxsein (2002). "Bone marrow influences quantitative ultrasound measurements in human cancellous bone". In: *Ultrasound in medicine & biology* 28.3, pp. 369–375.

Niebur, Glen L et al. (2000). "High-resolution finite element models with tissue strength asymmetry accurately predict failure of trabecular bone". In: *Journal of biomechanics* 33.12, pp. 1575–1583.

Norton, Guy V and Jorge C Novarini (2003). "Including dispersion and attenuation directly in the time domain for wave propagation in isotropic media". In: *The Journal of the Acoustical Society of America* 113.6, pp. 3024–3031.

Ogam, Erick et al. (2011). "Non-ambiguous recovery of Biot poroelastic parameters of cellular panels using ultrasonicwaves". In: *Journal of sound and vibration* 330.6, pp. 1074–1090.

Oldham, Keith and Jerome Spanier (1974). *The fractional calculus theory and applications of differentiation and integration to arbitrary order*. Vol. 111. Elsevier.

Osterhoff, Georg et al. (2016). "Bone mechanical properties and changes with osteoporosis". In: *Injury* 47, S11–S20.

Ostoja-Starzewski, Martin and Jun Zhang (2018). "Does a Fractal Microstructure Require a Fractional Viscoelastic Model?" In: *Fractal and Fractional* 2.1, p. 12.

Otani, Takahiko (2005). "Quantitative estimation of bone density and bone quality using acoustic parameters of cancellous bone for fast and slow waves". In: *Japanese journal of applied physics* 44.6S, p. 4578.

Ott, Susan M, RF Kilcoyne, and Charles H Chesnut III (1987). "Ability of four different techniques of measuring bone mass to diagnose vertebral fractures in postmenopausal women". In: *Journal of Bone and Mineral Research* 2.3, pp. 201–210.

Padilla, F et al. (2005). "Numerical simulation of ultrasound transmission in cancellous bone". In: *Proceedings-IEEE Ultrasonics Symposium*. Vol. 4, pp. 2022–2025.

Padilla, F et al. (2008). "Relationships of trabecular bone structure with quantitative ultrasound parameters: In vitro study on human proximal femur using transmission and backscatter measurements". In: *Bone* 42.6, pp. 1193–1202.

Padilla, Frederic, Emmanuel Bossy, and Pascal Laugier (2006). "Simulation of ultrasound propagation through three-dimensional trabecular bone structures: Comparison with experimental data". In: *Japanese journal of applied physics* 45.8R, p. 6496.

Padilla, Frédéric and Pascal Laugier (2000). "Phase and group velocities of fast and slow compressional waves in trabecular bone". In: *The Journal of the Acoustical Society of America* 108.4, pp. 1949–1952.

Pahr, Dieter H and Philippe K Zysset (2008). "Influence of boundary conditions on computed apparent elastic properties of cancellous bone". In: *Biomechanics and modeling in mechanobiology* 7.6, pp. 463–476.

Pakula, Michal, Frederic Padilla, and Pascal Laugier (2009). "Influence of the filling fluid on frequency-dependent velocity and attenuation in cancellous bones between 0.35 and 2.5 MHz". In: *The Journal of the Acoustical Society of America* 126.6, pp. 3301–3310.

Pakula, Michal et al. (2008). "Application of Biot's theory to ultrasonic characterization of human cancellous bones: determination of structural, material, and mechanical properties". In: *The Journal of the acoustical Society of america* 123.4, pp. 2415–2423.

Poll, V, C Cooper, and MID Cawley (1986). "Broadband ultrasonic attenuation in the os calcis and single photon absorptiometry in the distal forearm: a comparative study". In: *Clinical Physics and Physiological Measurement* 7.4, p. 375.

Rich, Clayton et al. (1966). "Measurement of bone mass from ultrasonic transmission time." In: *Proceedings of the Society for Experimental Biology and Medicine* 123.1, pp. 282–285.

Ridha, Hambli and Philipp J Thurner (2013). "Finite element prediction with experimental validation of damage distribution in single trabeculae during three-point bending tests". In: *Journal of the Mechanical Behavior of Biomedical Materials* 27, pp. 94–106.

Riekkinen, Ossi et al. (2007). "Acoustic properties of trabecular bone—relationships to tissue composition". In: *Ultrasound in medicine & biology* 33.9, pp. 1438–1444.

Roh, Heui-Seol, Kang Il Lee, and Suk Wang Yoon (2003). "Acoustic characteristics of a non-rigid porous medium with circular cylindrical pores". In: *JOURNAL-KOREAN PHYSICAL SOCIETY* 43, pp. 55–65.

Ross, Philip D et al. (1991). "Pre-existing fractures and bone mass predict vertebral fracture incidence in women". In: *Annals of internal medicine* 114.11, pp. 919–923.

Rossikhin, Yuriy A and Marina V Shitikova (1997). "Applications of fractional calculus to dynamic problems of linear and nonlinear hereditary mechanics of solids". In: *Applied Mechanics Reviews* 50.1, pp. 15–67.

Rossman, P et al. (1989). "Comparison of speed of sound and ultrasound attenuation in the os calcis to bone density of the radius, femur and lumbar spine". In: *Clinical Physics and Physiological Measurement* 10.4, p. 353.

Sadouki, M et al. (2015). "Ultrasonic propagation of reflected waves in cancellous bone: Application of Biot theory". In: *2015 6th European Symposium on Ultrasonic Characterization of Bone*. IEEE, pp. 1–4.

Sadouki, Mustapha (2020). "Experimental characterization of human cancellous bone via the first ultrasonic reflected wave–Application of Biot's theory". In: *Applied Acoustics* 163, p. 107237.

Saha, S and R Shafkey (1987). "Relationship between ultrasonic and mechanical properties of cancellous bone from human distal tibia". In: *ASME Biomechanics Symposium AMD*. Vol. 84, pp. 105–107.

Samko, Stefan G, Anatoly A Kilbas, and Oleg I Marichev (1993). "Fractional integrals and derivatives: theory and applications". In:

Schoenberg, Michael (1984). "Wave propagation in alternating solid and fluid layers". In: *Wave motion* 6.3, pp. 303–320.

Sebaa, Naima et al. (2006a). "Application of fractional calculus to ultrasonic wave propagation in human cancellous bone". In: *Signal Processing* 86.10, pp. 2668–2677.

Sebaa, Naima et al. (2006b). "Ultrasonic characterization of human cancellous bone using the Biot theory: Inverse problem". In: *The Journal of the Acoustical Society of America* 120.4, pp. 1816–1824.

Selle, WA and JM Jurist (1966). "Acoustical detection of senile osteoporosis". In: *Proceedings of the Society for Experimental Biology and Medicine* 121.1, pp. 150–152.

Shalanskii, I et al. (1976). "Propagation of ultrasonics in bones". In: *Polymer Mechanics* 12.6, pp. 946–949.

Sharma, Gaurav and Jos Martin (2009). "MATLAB®: a language for parallel computing". In: *International Journal of Parallel Programming* 37.1, pp. 3–36.

Siegel, IM, GT Anast, and Th Fields (1958). "The determination of fracture healing by measurement of sound velocity across the fracture site." In: *Surgery, gynecology & obstetrics* 107.3, pp. 327–332.

Smeulders, David Maria Jacobus (1992). "On wave propagation in saturated and partially saturated porous media". PhD thesis. Citeseer.

Smith, DM, MR Khairi, and CC Johnston (1975). "The loss of bone mineral with aging and its relationship to risk of fracture." In: *The Journal of clinical investigation* 56.2, pp. 311–318.

Smith, SW et al. (1979). "Some advances in acoustic imaging through the skull". In: *Ultrasonic tissue characterization II* 525, pp. 209–218.

Stegman, MR et al. (1992). "Fracture risk as determined by prospective and retrospective study designs". In: *Osteoporosis International* 2.6, pp. 290–297.

Szabo, Thomas L (1994). "Time domain wave equations for lossy media obeying a frequency power law". In: *The Journal of the Acoustical Society of America* 96.1, pp. 491–500.

Talebitooti, R, K Daneshjou, and M Kornokar (2016). "Three dimensional sound transmission through poroelastic cylindrical shells in the presence of subsonic flow". In: *Journal of Sound and Vibration* 363, pp. 380–406.

Thomson, William (2018). *Theory of vibration with applications*. CrC Press.

Vafaeian, B et al. (2014). "The finite element method for micro-scale modeling of ultrasound propagation in cancellous bone". In: *Ultrasonics* 54.6, pp. 1663–1676.

Waters, Kendall R et al. (2000). "On a time-domain representation of the Kramers–Krönig dispersion relations". In: *The Journal of the Acoustical Society of America* 108.5, pp. 2114–2119.

Wear, KA, BK Hoffmeister, and P Laugier (2018). "Quantitative ultrasound and the management of osteoporosis". In: *Acoust. Today* 14.2, pp. 34–42.

Wear, Keith A (1999). "Frequency dependence of ultrasonic backscatter from human trabecular bone: Theory and experiment". In: *The Journal of the Acoustical Society of America* 106.6, pp. 3659–3664.

Wear, Keith A (2000). "Anisotropy of ultrasonic backscatter and attenuation from human calcaneus: Implications for relative roles of absorption and scattering in determining attenuation". In: *The Journal of the Acoustical Society of America* 107.6, pp. 3474–3479.

Wear, Keith A (2007). "Group velocity, phase velocity, and dispersion in human calcaneus in vivo". In: *The Journal of the Acoustical Society of America* 121.4, pp. 2431–2437.

Wear, Keith A (2010). "Cancellous bone analysis with modified least squares Prony's method and chirp filter: Phantom experiments and simulation". In: *The Journal of the Acoustical Society of America* 128.4, pp. 2191–2203.

Wear, Keith A et al. (2005). "Comparison of measurements of phase velocity in human calcaneus to Biot theory". In: *The Journal of the Acoustical Society of America* 117.5, pp. 3319–3324.

Williams, JL et al. (1996). "Prediction of frequency and pore size dependent attenuation of ultrasound in trabecular bone using Biot's theory". In: *Mechanics of Poroelastic Media*. Springer, pp. 263–271.

Williams, John L (1992). "Ultrasonic wave propagation in cancellous and cortical bone: Prediction of some experimental results by Biot's theory". In: *The Journal of the Acoustical Society of America* 91.2, pp. 1106–1112.

Wu, Kunyu, Qiang Xue, and Laszlo Adler (1990). "Reflection and transmission of elastic waves from a fluid-saturated porous solid boundary". In: *The Journal of the Acoustical Society of America* 87.6, pp. 2349–2358.

YANG, Xiao Jun (2018). "New rheological problems involving general fractional derivatives with nonsingular power-law kernels". In: *Proceedings Of The Romanian Academy Series A-Mathematics Physics Technican*, pp. 45–52.

Yang, Xiao-Jun (2019). "New General Calculi with Respect to Another Functions Applied to Describe the Newton-like Dashpot Models in Anomalous Viscoelasticity". In: *Thermal Science*.

Yang, Xiao Jun, Gao Feng, and Jing Hong-Wen (2019). "New mathematical models in anomalous viscoelasticity from the derivative with respect to another function view point". In: *Thermal Science*.

Yang, Xiao Jun, Minvydas Ragulskis, and Thiab Taha (2019). "A new general fractional-order derivative with Rabotnov fractional-exponential Kernel". In: *Thermal Science*.

Yang, Xiao-Jun et al. (2017). "New general fractional-order rheological models with kernels of Mittag-Leffler functions". In: *Rom. Rep. Phys* 69.4, p. 118.

Yoon, Hyo Sub and J Lawrence Katz (1976). "Ultrasonic wave propagation in human cortical bone—II. Measurements of elastic properties and microhardness". In: *Journal of biomechanics* 9.7, pp. 459–464.

Yousefian, Omid et al. (2018). "The effect of pore size and density on ultrasonic attenuation in porous structures with mono-disperse random pore distribution: A two-dimensional in-silico study". In: *The Journal of the Acoustical Society of America* 144.2, pp. 709–719.

Zhang, Jianfeng and DJ Verschuur (2002). "Elastic wave propagation in heterogeneous anisotropic media using the lumped finite-element method". In: *Geophysics* 67.2, pp. 625–638.

Zhang, Qing-Hang, Gianluca Tozzi, and Jie Tong (2014). "Micro-mechanical damage of trabecular bone–cement interface under selected loading conditions: a finite element study". In: *Computer methods in biomechanics and biomedical engineering* 17.3, pp. 230–238.